A NUMERICAL SIMULATION OF UNDERWATER SHOCK-CAVITATION-STRUCTURE INTERACTION

XIE WENFENG

NATIONAL UNIVERSITY OF SINGAPORE

2005

A NUMERICAL SIMULATION OF UNDERWATER SHOCK-CAVITATION-STRUCTURE INTERACTION

BY

XIE WENFENG

(***B. Eng., M. Eng, Dalian Maritime University***)

DEPARTMENT OF MECHANICAL ENGINEERING

A THESIS SUBMITTED

FOR THE DEGREE OF DOCTOR OF PHILOSIPHY OF ENGINEERING

NATIONAL UNIVERSITY OF SINGAPORE

2005

ACKNOWLEDGEMENT

I express my deepest gratitude to my supervisors A/Prof. B. C. Khoo and Dr. T. G. Liu for their invaluable direction, support and encouragement throughout the course of this work.

I am very grateful for the research scholarship from the Institute of High Performance Computing and National University of Singapore. I would like to thank the staff in Supercomputing and Visualization of NUS and IT Division of IHPC for the support of supercomputer resources. These resources accelerate the progress of this work.

Special thanks are also due to Dr. C. W. Wang and Dr. X. Y. Hu for their enlightening consultations. Many thanks are given to the staff and my friends in the Fluid Mechanics Lab for offering help and cooperation during the course of this work.

Finally, I want to dedicate all my success to my wife for her constant support and encouragement in my academic pursuits at the National University of Singapore.

Table of Contents

SUMMARY

Accurate treatment of material interfaces and accurate modeling of unsteady cavitation are critical for simulating shock-cavitation-structure interaction. The Ghost Fluid Method (GFM)-based algorithms (the original GFM and the new version GFM) developed by Fedkiw et al (1999, 2002) are cost-effective techniques but do not work well in the simulation of compressible multi-medium flows involving strong shock wave or jet impact. A modified GFM, with an approximate Riemann problem solver (ARPS) coupled, has been proposed and developed by Liu et al (2003) and can work effectively for gas-gas and gas-liquid compressible flows. The iteration required in the ARPS is, however, found to take quite many steps and sometimes may fail to converge efficiently especially in the low pressure situation when applied to fluid-flexible structure interaction. This is because the solid medium is governed by a very stiff equation of state and the pressure (stress) to the solid density is extremely sensitive. To reduce the computational cost, an explicit characteristic method is developed to predict the interfacial status in this work where only an algebraic equation is solved and no iteration is required. The resultant algorithm (called the present GFM) is more accurate than the original GFM because the interfacial status is solved to define ghost fluids. To define the application ranges of each GFM-based algorithm, some analysis for gas/liquid-solid flows is carried out. The present algorithm is able to reduce the computational cost and is accurate for the gas/liquid-solid simulations.

The transient cavitation, as usually occurring in underwater explosions, can be simulated via a one-fluid cavitation model where no additional governing equation is required. A few commonly employed one-fluid cavitation models can be found in the literature to date. These are the Cut-off model, the Vacuum model and the Schmidt

model. To remove the mathematical/physical inconsistency in these models or achieve wider application, we proposed a mathematically self-consistent isentropic one-fluid cavitation model where a model parameter should be determined (see also Liu et al, 2004a). To obtain a faster and more straightforward application of the Schmidt model, we further developed a modified Schmidt model without undetermined model parameters (see also Xie et al, 2005a). Extensive analysis and tests show that those models capture different cavitation sizes and have different application ranges (i.e. density ratio of liquid to vapor). The numerical results demonstrate that the proposed isentropic one-fluid model and the modified Schmidt model work much more consistently and have much wider applications than the others.

In this work, it has been found that the various one-fluid cavitation models mentioned above produce different periods and peak pressures of cavitation collapse for 1D cases like water hammer problem while provide similar solutions for 1D cavitating flow of large surrounding flow pressure. The present GFM and the various cavitation models are further extended to underwater explosion applications where there is the presence of large surrounding flow pressure. The present algorithm for 2D Euler system is derived and those one-fluid cavitation models are directly applied to multi-dimensions without any additional technique/modification. In addition, a fix is proposed to prevent the possible negative (water-solid) interface pressure. The present GFM is shown to be fast and robust for treating the material interface of multi-dimensions and the Isentropic model or the modified Schmidt model is able to simulate the dynamics of 2D cavitation well.

Nomenclature

English alphabets

a	Speed of sound
$\tilde{a}$	Roe average speed of sound
A	Constant in Tait's Equation
B	Constant in Tait's Equation
$\overline{B}$	$B - A$
c	Speed of sound for gas, water or solid
CFL	CFL number
d	Derivative operator
D	The diameter of pipe
e	Internal energy per unit volume
E	Total flow energy
f	Function of density or some heat conduction constants in EOS; Darcy friction factor
F	Inviscid flow flux in the x or radial (r) direction
g	Function of density or some heat conduction constants
G	Inviscid flow flux in the y or z direction; Modulus of rigidity
H	Numerical flux
i	Grid point in x direction
I	Pressure impulse on structure surface
j	Grid point in y direction
k	Grid point in z direction; A model constant in the Isentropic model
K	The marker of medium
m	Modulus for steel

M	Partial terms to be discretized; Mach number
n	The constant of source term for Euler equations
$\vec{N}$	Unit normal vector
p	Flow pressure
$\bar{p}$	$p + B$
p_a	Atmosphere pressure
s	Interface velocity
S	Source term in the 2D symmetric Euler equation; Identification matrix for mediums
t	Time interval
u	Flow velocity component in the x or radial direction
U	Conservative variable vector in the Cartesian system
v	Flow velocity component in the y direction
$\vec{V}$	Velocity vector
w	Flow velocity component in the z direction
W	Variable related interface information
x	x coordinate
y	y coordinate
Y	Young's stress
z	z coordinate

Greek alphabets

α	Void fraction
β	A model constant for hydro-elasto-plastic solid EOS
γ	specific heat Ratio of for gas

	EOS constants for water and solid
ρ	Flow density
τ	Shear stress
ϕ	Flow composition
Δt	Time step size
Δx	Spatial step size
λ	$\Delta t/\Delta x$

Superscripts

1	Fluid/medium one
2	Fluid/medium two
c	Index of a liquid flow status
cav	cavitation
G	Ghost fluid index
I	Index of interface
n	Temporal index
sat	Saturated status
'	A reference status

Subscripts

0	Index of initial flow status
a	Flow status under atmosphere pressure
A, B	End cell boundaries
BB	Bottom boundary
C	The center point of the solid wall
g	index of Gas

h	Index of Hooke's law
i	Index of a grid in x direction
I	Interface position
IL	Left side of the interface
IR	Right side of the interface
j	Index of a grid in y direction
l	Index of the fluid flow in the left side of the interface; Index of liquid
L	Left side
l_0	Initial liquid status
m	Index of mixture medium
max	Maximum
min	minimum
N	Index of normal direction
r	Index of the fluid flow in the right side of the interface
R	Right side
s	Index of solid
s_0	Initial solid status
sat	Index of saturated status
S	Surface of the solid wall
TB	Top boundary

List of Figures

List of Tables

Chapter 1

Introduction

1.1 Fundamentals of Cavitation in Underwater Explosion

Fluid flows with cavitation are of practical importance in many fields where the main working liquid is water. One typical example is the flow generated by the underwater explosions near structures and a sea surface. The underwater explosion is a very complicated process but its initial effects on nearby structures can be taken as a high-pressured shock and a cavitation collapse. The highly-pressured shock wave in an underwater explosion has been investigated in several previous studies [Sedov, 1959; Cole, 1965; Holt, 1977], where analytical and experimental solutions for the underwater explosion were presented and the process of shock was described very well. Behind the high-pressured shock, cavitation forms near the structure and the fluid-flow becomes a cavitating flow. This cavitating flow occurs since the low pressure in the liquid reaches towards the limit of vapor pressure. A few studies have been carried out to compute the flows with cavitation and describe the cavitation zone in detail. To obtain a more insight into the cavitating flow the knowledge of cavitation physics and classifications is essential.

1.1.1 Physics of cavitation

Minute particles are always present in liquid which serve as initiation for vapor bubbles when the local pressure is low enough or temperature is sufficiently high. The bubbles could grow and collapse dynamically and have strong interactions with the surrounding liquid and structures. Such interactions may have significant desirable or undesirable effects on nearby floating or submerged structures. Desirable effects come from supercavitation that is associated with viscous drag reduction and lift force on

hydrofoils enhancement. Undesirable effects are major characteristics of cavitation such as surface erosion, excessive noise generation and structure devastation. For example, an underwater explosion near a structure or a free surface (Liu et al, 2003a), where (bulk) cavitation just below the free surface and (hull) cavitation nearby the structure surface are usually created and collapse very violently, can have serious damage to nearby structures. The shock wave, produced by the explosion, travels in water at a high speed and reaches the structures in a short time if structures are close to the explosion center. Consequently, the shock will impact on the structures at a very high pressure. Normally this process is taken as the main damage effect of an underwater explosion on nearby structures. When rarefaction wave reflects from the free surface or structures, the cavitation occurs at the adjacent water and may prevent the structures from full shock wave loading since it separates the structures from the water. Although this reduces the damage caused by shock wave, the structure has to subsequently withstand the high pressure caused by cavitation collapse. Sometimes the cavitation between the structures and water can be seen as a high-pressured bubble, whose dynamics are related to the structural damage. When the cavitation is compressed, the decrease of the cavitation dimension or collapse of cavitation leads to rapid increase of the pressure in the original cavitation region, thereby resulting in the emission of pressure pulse into the surrounding water. Although the peak pressure of this pulse is lower than that of shock wave generated by the explosion, its duration of exertion is much longer than the shock wave and therefore the damage can be comparable to that caused by the shock wave.

1.1.2 Classifications of Cavitation

In fluid flow, different kinds of cavitations can be observed and each of them has its distinct shape and physical characteristics. Therefore, the employed numerical method

and model to compute for the cavitating flow are highly dependent on the different kinds of cavitation. Generally no single model can be used to simulate all kinds of cavitation. Knapp et al (1970) classified five types of cavitation in their papers and presented the underpinning basis or source of formation for each type of cavitation. In the same paper, the effects of each type of cavitation were described. In Table 1.1, an overview of the cavitation types and characteristics is presented. Here some types of cavitation posed in Knapp's paper are described briefly, and the bulk/hull cavitation that usually occurs in an underwater explosion is also introduced.

Bulk/Hull cavitation is the disruption of what would otherwise be a continuous water phase, which is typically observed in an underwater explosion near a structure or a free surface and in some pipe flows. Such cavitation collapses very violently and may cause great damage to the nearby structure and pipe. The major characteristics of such cavitation are that cavitation region is relatively large and interaction between cavitation and structure is violent. Bulk cavitation in pipe flows is shown in the work of Qin et al (1999, 2000, and 2001).

Traveling cavitation moves in the liquid while it expands and shrinks. Sometimes the geometries of such cavitations are dependent on the amount of nuclei present in the incoming flow (Lecoffre, 1999). Cloud cavitation is generated by vorticity shed into the flow field and it can cause vibration, noise and erosion (Knapp et al, 1970). Sheet cavitation is a type of cavitation like attached cavity or pocket cavitation. Such cavitation normally has a well-shaped cavity and is stable in a quasi-steady sense (Senocak, 2002). The effect of sheet cavitation on downstream flow is introduced in detail in Gopalan and Katz (2000). Supercavitation occurs when the whole solid body is overlaid by the sheet cavity. Supercavitation can be observed on an underwater high-speed vehicle. To achieve viscous drag reduction and increase the lift force on

underwater hydrofoils, the supercavitation is created and enhanced. One application of supercavitation, the supersonic operation of underwater projectiles, is reported in Kirschner (2001). The tip vortex cavitation occurs at the tips of lifting surfaces and at the hubs of propellers and hydraulic turbines. Tip vortex cavitation can be viewed as a canonical problem that captures many of the essential physics associated with vortex cavitation in general. Franc et al (1995) produced the visualization of different types of cavitation, in which the shape and process of the different types of cavitation can be distinguished clearly. To capture these cavitations, a robust numerical algorithm and a cavitation model are compulsory.

1.2 Numerical Method Studies

As high resolution schemes for compressible flows, present commonly used numerical methods can be roughly classified into two groups. The first one is Total-Variation-Diminishing (TVD) schemes. The original idea and some examples of TVD schemes can be found in many papers (Harten, 1983, 1984; Yee, 1987, 1989; Zalesak 1987). The other one is Essentially Non-Oscillatory (ENO) schemes, about which one can refer to the work of Harten and Osher (1987). The main contributions of ENO reconstruction can be retrieved from the work of Shu and Osher (1988, 1989). All of these methods work well in a single phase. To simulate multi-medium compressible flows with a material interface, an additional numerical algorithm should be developed for treating material interface. In general, there are two basic approaches to treat material interfaces in the solution of hyperbolic system of conservation laws. One is Front capturing methods and the other is Front tracking methods. Front capturing methods solve the discontinuities (material interfaces) over a few grid cells and the algorithm construction is relatively simple. The application of Front capturing methods to multidimensional problems is straightforward. In the numerical algorithms

associated with front capturing methods, the interfaces are usually tracked through volume of fluid (Hirt and Nichols, 1981), mass fraction (Larrouturou, 1991), ratio of specific heats (Karni, 1994; Abgrall, 1996), or level set function (Osher and Sethain, 1988). However, numerical inaccuracies and oscillations may occur at the contact discontinuity and a sharp interface may not be obtained due to numerical dissipation. To overcome these difficulties, treating an interface using Lagrangian method is reasonable when the deformation of the interface is not large. But when the interface has large deformation this method may give rise to inaccuracy in the computation near the interfaces. Therefore, Farhat and Roux (1991) develop a robust method called Arbitrary Lagrangian-Eulerian (ALE) to reduce the mesh distortions of Lagrangian method but the effect is still limited. Also, Lagrangian methods and ALE methods need more computation time when compared to Euler method. To avoid this difficulty the idea that the interface is tracked in a fixed grid system is developed. The resultant technique is now usually called front tracking methods. Hyman (1984) did a detailed survey on the early front tracking methods. Front tracking, where discontinuities are treated as internal moving boundaries, is still quite complicated to use although it can solve discontinuities very well. This problem can be seen from the studies by Youngs (1984), Lafaurie et al (1994), Mao (1995), and Glimm et al (1998). Another disadvantage arising from the front tracking methods is the possible numerical instability caused by the presence of extremely small grid sizes/volumes when the interface moves towards a fixed grid node. Some examples of novel front tracking methods to avoid such instability can be found in (Falcovitz and Birman, 1994; Hilditch and Colella, 1995; Mao, 1995 and Shyy et al, 1996). Recently, Liu et al (2001a) developed a local solver based on the integral conservation laws over variable intervals which is used to solve for the flow field near the interface. Liu's method can

work well in underwater shock bubble interaction and underwater explosions near a free surface which can lead to a very strong shock to impact on the material interface.

One notable method proposed by Fedkiw et al (1999b) is the Ghost Fluid Method (the original GFM). They use a level set function (Osher and Sethian, 1988; Mulder and Osher, 1992) to track the motion of a multi-material interface in an Eulerian framework, and then use the ghost cells and an isobaric fix technique to obtain the flow field near the interface. The original GFM is very robust and easy to program. However, the original GFM may not work consistently using isentropic fix when applied to a strong shock impacting on a material interface (Liu et al, 2003b). Liu et al (2003b) analyses such inapplicability of the original GFM and develop a more robust and consistent method (the modified GFM). The modified GFM (henceforth called MGFM) is to solve an approximate Riemann problem (ARPS) at the interface for better prediction of the interface information (pressure and velocity). Iteration is needed to obtain the solution of the approvimate Riemann problem. It has been found that it may take many steps to obtain converged solution for such iteration when the MGFM is applied to water-solid compressible flows where the equation of state for solid is very stiff and the pressure is not high. Also, the MGFM is apparently more complex than the original GFM due to the employment of the approximate Riemann solver. Therefore, an explicit characteristic method will be developed to replace ARPS as for the MGFM in this work.

1.3 Cavitation Model Studies

Due to complex physics involved in cavitating flows and limitation of current computational capabilities, it is still impossible to simulate cavitations by resolving each tiny bubble. Therefore, some viable cavitation models which can simulate salient features of cavitation have to be employed. The dominant difficulties of modeling

cavitating flows lie in the complicated cavitation physics involved in the phase change, high gradients of flow variables and unsteadiness. Generally transient cavitating flows includes three main processes: cavitation creation, cavitation evolution and cavitation collapse. Therefore, the employed models should be able to capture all three processes and suppress the possible pressure oscillation.

In numerical modeling of cavitating flow so far, most of the works are focused on the attached/sheet cavitation. Such cavitation normally has a fairly well-defined cavity full of vapor at saturated pressure together with a mixed wake part. The wake part consists of bubbly flow and is fully turbulent. For the attached cavity, its shape is usually under steady/quasi-steady conditions or changes relatively slowly and/or periodically. Furthermore, the ambient liquid flow is generally taken as incompressible. Due to the steady state status or relatively slow change of the cavity shape, the velocity slip conditions and the continuity of pressure and normal velocity across the cavity boundary are imposed (Chen and Heister, 1994). Wesseling and co-authors has also developed models to simulate the attached cavitation (Wesseling et al, 1999; Duncan et al, 2000). The numerical simulation for the attached/sheet cavitation can be broadly divided into two categories: the interface tracking method and the continuum modeling method. Interface tracking method assumes that there is a clear and distinct interface between the liquid and vapor (Chen and Heister, 1994; Deshpande et al, 1994, 1997). For the said method, there is no calculation made inside the cavity. On the other hand, the treatment for the wake part is usually required and the liquid-vapour interface (cavity boundary) is determined via an iterative procedure. Besides these models, there are other cavitation models or techniques have been developed to simulate attached and sheet cavitating flow. More specifically, Mazel et al (1996) developed a bubble dynamic model based on Rayleigh equation for vapor

bubbles, which have to be assumed present initially. To model the cavitation pockets around airfoils, a VOF technique is developed in (Molin et al, 1997). This technique is suitable for the simulation of cavitation pockets but it cannot model the unsteady transient cavitation of present interest because the new interface creation is not allowed. In practice, there may be much less distinction or even no distinct interface between the liquid and vapor in the cavitation region. Therefore, it is also reasonable to build continuum models for the cavitating flows.

One continuum cavitation model was developed by Delannoy and Kueny (1990) who used a simple method to close the hydrodynamic equations. They assumed a barotropic equation of state where density is a function of pressure. The densities of two phases were considered as constant and joined by a sine function whose maximum slope was chosen to represent the speed of two-phase mixture. Delannoy and Kueny improved the stability of the model but their method was limited to density ratios of one hundred to one. Kubota et al (1992) developed one of the earliest continuum models for a cavitating flow, in which a constitutive relation for pressure is built based on the assumption that the fluid was a uniform mixture of liquid and very small, spherical bubbles. This model encountered severe stability problems and thus their methods were limited to small void fractions. Avva and Singhal (1995) used an energy equation to replace constitutive relation for closure. They assumed a homogenous flow of no velocity slip and thermodynamic equilibrium. Based on these assumptions the energy equation was simplified to a single fluid energy equation as a function of mean cell density. However, this model also suffered from problems of instability. To overcome this instability, Senocak and Shyy (2002), based on the work of Kunz et al (2000), developed a set of governing equations consists of the conservative form of the Reynolds averaged Navier–Stokes equations, plus a volume fraction transport equation

to account for the cavitation dynamics. The cavitation process is governed by the thermodynamics and the kinetics of the phase change dynamics occurring in the system. Song (2003) applied the same method to simulate unsteady compressible flow. The only difference between Song's method and Senocak's method is that the fifth order polynomial is used to simulate the cavitating process. Such type of model was also used to compute high speed cavitating flows (Owis and Nayfeh, 2003).

A continuum method as mentioned above makes no attempt to track the cavity interface but instead treats the flow as two-phase with an averaged mixture density. Such an approach is to apply a single continuity equation for both phases, with the fluid density being described as a continuous function varying between the vapor and liquid phases (Merkle et al, 1998; Song and Chen, 1998). This model is also sometimes called a two-phase model. In the two-phase model, liquid and vapor phases co-exist in the flow field and transform from one to the other, depending on the local conditions. The two-phase model is becoming more and more popular in recent times because it is able to include all the possible physics of cavitating flows and no special wake treatment is required. In its implementation, there are generally two different approaches. One is called the two-fluid method. The other is the one-fluid method. The former one assumes that both phases co-exist at every point in the flow field and each phase is governed by its own set of differential equations. Recently, Saurel and co-workers (1999a, 1999b, and 2001) developed a multiphase two-fluid model and showed applications of this model to compressible multi-medium/multiphase flows. A satisfactory application of such a two-fluid model is for multi-medium problems and problems of phase change caused by temperature difference and chemical reaction at a well-defined interface (Allaire et al, 2002; Evje, 2002). However, this model is quite complex and involves non-conservative terms in the momentum and energy equations

with quantities related to phase exchange. A 1D computation using this model already involves six equations plus a seventh equation for the evolution of volume fraction necessarily to close the system. Because the exchange of mass, momentum and energy is treated explicitly as transfer terms in this approach, some quantities such as exchange rates (Ahuja, 2001; Kunz, 2000; Lindau, 2002; Senocak, 2002; Venkateswaran, 2002) and the viscous friction between the two phases (Kubota, 1992; Senocak, 2002) have to be known *a priori* to represent the phase-change phenomena. Such quantities, however, are usually very difficult to measure whether experimentally or otherwise. To simulate the unsteady cavitation using this two-fluid model, the initial pure liquid has to be supposedly mixed with a negligible amount of vapor. Thus far, we are only aware that this model has been used to simulate cavitating flow of Case 1 as detailed in Chapter 3. On the other hand, the one-fluid method treats the cavitating flow as a mixture of two fluids behaving as one. Thus, one set of differential equations similar to the single-phase flow are used to govern the whole fluid motion. The most challenging task of this category of approach is to define a proper constitutive relation (equation of state) for the mixture to close the system. A barotropic or homogeneous assumption can be used to develop a reasonable constitutive relationship. Coutier-Delgosha et al (2002, 2003) developed a very simple barotropic relationship associated with a turbulence model for the simulation of cavitating flows. The main idea of this work was to define a minimum speed of sound in the mixture depends on the two-phase structure of the medium and remains an adjustable parameter of the model. Felipe (2003), in the parallel effort, built a consistent thermodynamic homogeneous model to describe the vaporous cavitation phenomenon by means of an internal variable theory. In this model, the temperature is supposed to be the same for both phases and the cavitation process assumed to be an isothermal transformation, and then

the constitutive equations of this model are derived within the framework of the thermodynamics of irreversible processes. Other recent works in homogeneous cavitation models can be found in Clerc (2000) and Shin et al (2003). On the other hand, another kind of constitutive relationship can be obtained if the mixture is usually supposed or assumed to be both homogeneous and barotropic (Delannoy and Kueny, 1990; Schmidt et al, 1999; Ventikos and Tzabiras, 2000). Such kind of cavitation model is effective for simulation of unsteady cavitation generated from pressure drop. If possible, one can also define this relation using the well-tabled mixture properties similar to that carried out in by Ventikos and Tzabiras (2000) for simulating water and vapor mixture.

The interest of this work lies in the unsteady cavitation caused by pressure jump across the cavitation boundary. Such unsteady cavitation is commonly observed in the underwater explosion, where both the ambient liquid and the mixture have to be considered as compressible. In contrast to the attached/sheet cavitation, where relatively extensive studies have been carried out, there is much less work on the latter in literature. For simulation of such cavitation the one-fluid models are efficient and straightforward. Table 1.2 give an overview of past one-fluid models for such unsteady cavitation. In the following, selected studies are summarized.

One commonly used model is the Cutoff model which is essentially pure-fluid model and no phase exchange is taken into account. In the Cutoff model like those used by Aanhold et al (1998) and Wardlaw and Luton (2000), flow pressure is simply re-instated as a given value and computation continues whenever the liquid pressure is detected lower than a given critical level. In the pressure-cut-off (cavitation) region, the flow medium is still taken as liquid and no phase change is considered. The Cutoff model is quite easy to implement and use. However, there are obvious physical

violations because the conservation law may not be maintained and the hyperbolic system of equations is non-physically degenerated due to the pressure and the associated density cut-off. As a result, errors can incur in the cavitation region, as shown later in Chapter 3. The Vacuum model as developed by Tang and Huang (1996) treats the cavitation zone of zero mass inside and is an ideal approximation of cavitation. This model is physically reasonable because usually only a small amount of liquid transfers into vapor and the vapor density is about O (10^{-4}) of the liquid density. The idea of neglecting the amount of vapor is also used in the simulation of sheet cavitation (Kubota et al, 1992). The vacuum model is presently only applied to study 1D inviscid cavitating flow because it was based on the solution of a local gas-water-vacuum Riemann problem which is quite complex. The extension of this model to multi-dimensions, as we are aware, has yet to be established probably due to the requirement of constructing a local Riemann solver, where the vacuum boundary needs to be tracked and a special Riemann problem in the neighborhood of the vacuum region has to be solved. Schmidt (1997) developed a one-fluid model for modeling high-speed cavitating nozzles. This method can be considered as an isentropic model associated with phase change, where the sound speed is given by Wallis (1969). The pressure is given by an analytical function of density. This closure means that no partial differential equation is required and the pressure can be found analytically from the cell density which reduces the computational cost of a time step. Schmidt et al used this model to simulate small scale high speed cavitating nozzle flow and then obtained some reasonable results. However Schmidt developed a constitutive relation based on the assumption of constant sound speeds and densities for the respective saturated vapor and liquid in the cavitation zones, which contradicted Wallis' sound speed equation. Moreover this method has not been used for large scale, low speed cavitation

calculations. To extend the application of this model, Qin et al (1999, 2001) incorporated a model constant into the Schmidt model to prevent the pressure from becoming lower than the vapor pressure. However, by a strict mathematical analysis, this model constant, which was chosen to range from 10^{-3} to 10^{-5} should be determinable and equal to one. To remove the mathematical and physical inconsistencies in the one-fluid models as mentioned above, we proposed an Isentropic one-fluid model which is mathematical self-consistent and able to capture the transient cavitation in various flow conditions (see also Liu et al, 2004a). Before the Isentropic model can be employed, a model parameter has to be determined, which is a major limitation of the Isentropic one-fluid model. The modified Schmidt model is, therefore, proposed for a straightforward engineering application (see also Xie et al, 2005a) where no model parameter is required to be solved.

1.4 Objectives and Organizations of This Work

As mentioned above, the GFM-based algorithms are simple and flexible for multi-medium/multiphase compressible flows. However, the application of the GFM-based algorithms developed by Fedkiw et al (1999b, 2002) is limited as applied to a strong shock impacting a gas-water interface (Liu et al, 2003b). The MGFM is able to overcome the difficulties as for the original GFM-based algorithms but application of the MGFM to water-solid simulation is costly as the converged solution is not easy to obtain via iteration for the Riemann problem at the interface when the pressure is not high in the solid medium. On the other hand, the main drawbacks of the existing one-fluid cavitation models are: mathematical inconsistency and physical inconsistency. Therefore, the main goal of this research is to propose a newly developed GFM-based algorithm and compare four one-fluid cavitation models by simulating various transient cavitating flows. The more specific objectives are as follow:

►To propose a GFM-based method to achieve higher level of accuracy and wider application than the original GFM and the new version GFM, and to obtain faster computation than the MGFM for water-solid compressible flows. The range of applicability of this GFM-based algorithm is also defined via mathematical analysis.

►To analyze and compare the existing one-fluid models. The range of applicability for each one-fluid model is then defined.

►To apply the present GFM and four one-fluid cavitation models as mentioned above to simulate 1D unsteady cavitation flows. The different cavitation sizes, periods and peak pressure of cavitation collapse are observed and analyzed as well.

►To apply the present GFM and various one-fluid cavitation models to 2D underwater shock-cavitation-structure interactions. Especially, the response of the flexible wall is investigated in our computations to observe its effect on cavitation dynamics.

The scope of this research focuses on the simulation of unsteady cavitating flows where cavitation is caused by a sudden pressure drop such that there is insufficient time for heat transfer to take place like the cavitation occurring in underwater explosions. Such cavitation usually consists of an unsteady and dynamically developing boundary and can evolve to a certain dimension before collapsing. In such situations, the variation of pressure with temperature, thermal non-equilibrium and cavitation surface tension can be neglected.

The thesis is organized as follows. Chapter 2 describes the numerical methods for multiphase compressible flows. Firstly, the equation of state (EOS) for each medium is presented, and then the employed numerical method for the regions away from the interface is introduced, followed by the existing various GFM-based algorithms. The present GFM is also developed and presented in detail in this chapter. The

comparisons of these GFM-based algorithms are carried out via mathematical analysis and numerical examples with analytical solutions.

Chapter 3 introduces the one-fluid cavitation models using the 1D Euler equations. Four one-fluid cavitation models besides the very recently developed Isentropic model and the newly developed modified Schmidt model are described and compared in detail. Also, some numerical examples with analytical solutions are also calculated to verify the analysis.

In Chapter 4, the numerical methodology is applied to model several 1D cavitating flows where the experimental results or numerical results are available. Chapter 4 investigates two pipe/tunnel cavitation problems in detail. One is a water hammer problem where the cavitation may occur at the different locations of tube under different initial conditions. The other is a cavitating flow in a close tunnel with the complex wave propagation and shock-cavitation interaction.

Chapter 5 extends numerical methodology to multi-dimensional cavitating flows. The cavitating flows generated by underwater explosions nearly structures are investigated. The solid walls are considered as rigid or flexible for comparisons to investigate the effect of solid deformation on cavitation dynamics. To better observe such effect, the pressure histories at the center point of the solid surface, the pressure impulses and overall forces exerted on the solid surface are calculated for both rigid and flexible walls. A method to suppress the possible negative pressure in solid next to interface is also proposed.

The overall conclusions and recommendations for further work are provided in Chapter 6.

Cavitation type	Major characteristics
Bulk/Hull cavitation	Has large cavitation region
Traveling cavitation	Moves in the liquid while expand and shrink
Cloud cavitation	Causes vibration, noise and erosion
Sheet cavitation	Has a well-shaped cavity and relatively stable
Supercavitation	Achieves viscous drag reduction and increase the lift force
Tip vortex cavitation	Occurs at rotating blades

Table 1.1 An overview of the cavitation types and major characteristics.

Author & Reference	Methodology	Main characteristic
1.Chen and Heister(1994)	Interface tracking scheme associated with $p = p_v$ when $p \le p_v$	Easy to apply and not fully conservative
2. Tang and Huang(1996)	Vacuum model based on local gas-water-vacuum Riemann solver	Physically conservative but difficult to extend to multidimensional.
3.Deshpande et al (1997)	Interface tracking scheme associated with $p = p_v$ when $p \le p_v$ and cavity shape determination	More accurate than model 1 but conservation limited
4.Schmidt et al (1997)	Mixture analysis. Cavitation pressure is analytically obtained from density	Pressure is a sole function of density. Strictly for high speed nozzle cavitating flows
5.Qin et al (1999)	Mixture analysis. The cavitation pressure is artificially reduced via a model constant.	Wider application than model 3 but mathematically inconsistent.

Table 1.2 An overview of the past one-fluid cavitation models.

Chapter 2

Mathematical Formulation: Numerical Methods

In this chapter, the numerical methodology for multi-medium or multiphase compressible flows is presented using 1D Euler equation. Various equations of state (EOS) are described in detail. The numerical method consists of two parts. One is a high-resolution numerical scheme for the fluid flow away from the material interface. Such numerical scheme has been extensively analyzed and reviewed in Toro (1997) and therefore only a brief introduction is presented here. The other is the numerical technique for treating the material interface, which is the major work to simulate the multiphase compressible flows using the Eulerian method. A recently developed method called the Ghost Fluid Method (henceforth called the original GFM for ease of referral) by Fedkiw et al (1999b) has been found to be inaccurate to simulate a strong shock impacting a gas-water interface (Liu et al, 2003b). In this chapter, the two conditions developed by Liu et al (2005) are extended to analyze the main characteristics and shortcomings of various GFM-based algorithms for the compressible gas-solid and liquid-solid Riemann problems, and then the possible application ranges for each GFM-based algorithm are determined. An explicit characteristic method based GFM is then proposed and analyzed as well.

2.1 Introduction

The high-resolution conservative Eulerian algorithms like TVD and ENO as mentioned in Chapter 1 are very robust when applied to single-medium compressible flows. Such an algorithm can obtain high-order numerical accuracy and capture the wave position and motion in the single-medium flow accurately with low computational cost. When these algorithms are applied to the multi-medium/

multiphase compressible flows, computations invariably run into unexpected difficulties due to numerical oscillations generated at material interfaces. Such oscillations are arisen from the different specific ratio of heat for different materials, which are analyzed mathematically by Abgrall and Karni (2001). To suppress oscillations, some non-conservative discretization techniques have been developed by Abgrall (1996), Karni (1994, 1996), Shyue (1998) and Saurel and Abgrall (1999b). With these techniques, numerical oscillations are greatly suppressed but may not vanish completely at the material interface partly because the conservative property at the interface can not be maintained. Much effort has been made to develop a conservative numerical method for material interfaces (Liu et al, 2001a, 2001b; Van Brummelen, 2003). Conservative methods, however, are relatively much more complex in the treatment of material interfaces and computationally costly. Furthermore, the extension of conservative methods to multi-dimensions is not trivial.

To maintain the simplicity of Eulerian algorithms while still able to remove possible numerical oscillations at the material interface, the original GFM is developed recently by Fedkiw et al (1999b) to overcome the difficulties associated with using Eulerian-based algorithm for multi-medium compressible flows. The original GFM assumes that both the real fluid and ghost fluid coexist at each grid point in the computational domain. The pressure and (normal) velocity of the ghost fluid are defined with the pressure and (normal) velocity as for the real fluid while the density is obtained via isobaric fix (Fedkiw et al, 1999a) which is developed to suppress the “overheating effect” phenomenon which may occur at solid wall boundaries (Glaister, 1988). In (Fedkiw et al, 1999a), three types of isobaric fixes called internal energy fix, temperature fix and isentropic fix are developed. Once the ghost fluid is properly defined, the standard Eulerian algorithm for the single-medium flows as mentioned

above can be applied directly to multi-medium flows. The numerical oscillations at the material interface are then expected to be eliminated. One main advantage of the original GFM is that only a single phase solver is needed and thus the extension to multidimensional applications is fairly straightforward. The original GFM has been found to be workable for shock tube problems and even for a not very strong shock wave interaction with the material interface. The application of the original GFM for a strong shock wave impacting on a material interface has been found to suffer from numerical inaccuracy at the material interfaces. Such numerical inaccuracy arises due to the GFM Riemann problems not being able to provide for the correct Riemann waves at the respective real fluid where the effects of material properties and wave interactions with the interface should be taken into account (Liu et al, 2003b).

To overcome the difficulties of the original GFM applied to gas-liquid flow, a subsequent new version GFM was proposed by Fedkiw (2002) (henceforth called the new version GFM for ease of referral) where the effect of material properties on interface status is partly considered using extrapolation, i.e. the interface pressure is determined by the fluid on one side of interface while the interface normal velocity is determined by the fluid on the other side. Generally, the interface normal velocity is obtained from the fluid with stiff equation of state (water or solid) while the interface pressure is obtained from the other fluid (gas). By using the new version GFM, the material properties are partially taken into account resulting in a better performance compared to the original GFM when applied to the gas-water and gas-solid flows. However, it has been found by Liu et al (2003b) that the new version GFM is not as effective as the original GFM when applied to gas-gas flows. A problem may arise as to which GFM-based algorithm is most appropriate is obviously problem-related. To taken into account the influence of the material properties, an approximate Riemann

problem at the interface is solved to predict the interface status and this leads to the modified Ghost Fluid Method (henceforth called the MGFM for ease of referral) as proposed by Liu et al (2003b), which is able to overcome the difficulties encountered by the original GFM in the application of a strong shock impacting on material interfaces. Unlike the original GFM or even the new version GFM, the MGFM is more universally applicable. To understand better the underlying cause(s) for the differences between the mentioned GFMs, Liu et al (2005) compare the GFM Riemann waves generated from the original GFM and the new version GFM to the original Riemann waves generated from gas-water Riemann problems. All the possible wave patterns at the material interface for gas-water flows are analyzed in Liu et al (2005) which then leads to two necessary conditions imposed to identify the ranges of conditions of inapplicability for the various GFM-based algorithms. It is found that the approximate Riemann problem solver (ARPS) in Liu et al (2003) can provide the correct interface status except for nearly cavitating flows where a double rarefaction wave solver has to be developed to obtain the correct interface status. However, it is found that the converged solution of the ARPS can be (very) difficult to obtain when the MGFM is applied to gas-solid or water-solid simulations where the hydro-elasto-plastic EOS (Tang and Sotiropoulos, 1999) is used for the solid medium. This is because the iteration required for ARPS does not converge effectively when a low pressure is employed to solve for the density as in the hydro-elasto-plastic solid EOS. In this chapter, an explicit characteristic method is applied to replace the ARPS for the calculation of interface status without any iteration. Based on the explicit characteristic method, a GFM-based algorithm (henceforth called the present GFM for ease of referral) is developed for modeling of gas-solid or gas-water flows (see also Xie et al,

2005b, 2005c). The applicability of the present GFM is verified by comparing to the MGFM and the analytical results in this chapter.

The remaining text of this chapter is organized as follows. The 1D Euler equations with the EOS for gas, water, and solid are presented in Section 2.2. A high-resolution numerical scheme is used to discretize the governing equations in Section 2.3. The various GFM-based algorithms are presented and compared in Section 2.4. The two conditions proposed by Liu et al (2005) are applied to analyze the applicability of various GFM-based algorithms in Section 2.5. Various tests are carried out in Section 2.6 for further discussion and analysis. A brief summary is presented in Section 2.7.

2.2 Equation of State (EOS)

The 1D conservative equations for inviscid gas, water, solid or bubbly flow can be written in a consistent form as

$$\frac{\partial U}{\partial t}+\frac{\partial F(U)}{\partial x}=0, \tag{2.1}$$

where $U=[\rho,\rho u,E]^T$ and $F(U)=[\rho u,\rho u^2+p,(E+p)u]^T$. Here ρ is the density, u is the velocity, p is the pressure. E is the total energy and given as $E=\rho e+0.5\rho u^2$, where e is the internal energy per unit mass. For the closure of (2.1), the equations of state are required for all mediums (phases). We assume the materials are characterized with an equation of state developed by Cochran and Chan (1979) and this EOS can be written as the Mie-Gruneisen-type form

$$\rho e=f(\rho)p+g(\rho). \tag{2.2}$$

Here, f and g are functions of density or some constants associated with heat conductivity. A commonly used EOS called stiffened gas equation of state (Godunov

et al, 1979) can be seen as a simplification of the Mie-Gruneison type EOS and can be expressed as

$$\rho e = \frac{p + \gamma p_\infty}{\gamma - 1}, \tag{2.3}$$

where γ and p_∞ are constant parameters of EOS which are different for each material and are discontinuous across the material interface . If $p_\infty = 0$, (2.3) recovers to the ideal gas medium. Equation (2.3) has been extensively used for modeling of various fluid materials (Saurel and Abgrall, 1999a; Abgrall and Karni, 2001; Saurel and Lemetayer, 2001; Gavrilyuk and Saurel, 2002; van Brummelen and Koren, 2003). The generalization of the stiffened gas EOS to the Mie-Gruneisen-type EOS can be found in Massoni et al (1999). In this work, the focuses lie in three types of EOS for gas, water and solid, which can be expressed as the form of (2.2). The γ-law for a prefect gas with $f = 1/(\gamma_g - 1)$ and $g = 0.0$ can be rewritten as

$$\rho e = \frac{p}{\gamma_g - 1}, \tag{2.4}$$

where γ_g is the ratio of specific heats for gases and set to be 1.4 in this work except for the explosive gases where γ_g is set to be 2.0. The EOS for water employed in this work is Tait's equation (Wardlaw, 1998) and given as

$$p = B\left(\frac{\rho_l}{\rho_{l0}}\right)^{\gamma_l} - B + A \text{ or } \frac{\overline{p}}{\overline{p}_0} = \left(\frac{\rho_l}{\rho_{l0}}\right)^{\gamma_l}. \tag{2.5a}$$

Here B and A are constants and set equal to $3.31\times10^8\,Pa$ and $10^5\,Pa$, respectively, $p_0 = A$ and $\rho_{l0} = 1000 kg/m^3$ are the initial pressure and density for water, $\overline{p} = p + \overline{B}$, $\overline{p}_0 = p_0 + \overline{B}$, $\overline{B} = B - A$, and γ_l is set to be 7.15. Equation (2.5a) can be

rewritten in the form of (2.2) if we set $f = 1/(\gamma_l - 1)$ and $g = \gamma_l (B - A)/(\gamma_l - 1)$. Thus, we have

$$\rho e = \frac{p}{\gamma_l - 1} + \frac{\gamma_l (B - A)}{\gamma_l - 1}. \tag{2.5b}$$

Several commonly used EOS for solid materials are summarized here:

(1) Tait' EOS for solid-EOSS1 (Fedkiw, 1999a)

Tait's EOS can be directly used as the EOS for solid with different parameters when compared to (2.5a). Such EOS for solid can be written as follows

$$\frac{p + p_\infty}{p_0 + p_\infty} = \left(\frac{\rho_s}{\rho_{s0}} \right)^{\gamma_s}. \tag{2.6a}$$

Here γ_s is a constant parameter to be determined by the solid property. It takes on the value of 3.7 for steel in the present computation. p_0 and ρ_{s0} are the initial pressure and density of solid. Similar to (2.5b), (2.6a) can be rewritten in the form of (2.3) as

$$\rho e = \frac{p}{\gamma_s - 1} + \frac{\gamma_s (B_s - A_s)}{\gamma_s - 1}. \tag{2.6b}$$

Here, the values of B_s and A_s are determined by the solid properties and different from those of (2.5). B and A are set equal to $6.01351 \times 10^{10} Pa$ and $10^5 Pa$, respectively. It should be noted that Tait's EOS is a special example of the stiffened gas EOS and the generalization of Tait's EOS to stiffened gas EOS is straightforward. Thus, the stiffened gas EOS is obviously able to be used as the EOS for solid if the solids are not under very high-pressure shock wave. Otherwise, the Mie-Gruneisen EOS is better used to describe the solid medium.

(2) Mie-Gruneisen EOS for solid-EOSS2 (Shyue, 2001)

This EOS is a relatively general EOS for flow materials and it can be written as

$$p = p_\infty(\rho,\phi) + \gamma(\phi)(\rho e - e_\infty(\rho,\phi)), \tag{2.7}$$

where ϕ is a variable to describe the flow composition; $\gamma(\phi)$ is the Gruneisen coefficient decided by $\gamma = (1/\rho)(\partial p/\partial\rho)\big|_\rho$ for each material; p_∞ and e_∞ are properly chosen parameters for each material. For the properties of solid material for the Mie-Gruneisen EOS, one can refer to Shyue (2001) and Saurel and Abgrall (1999b).

(3) Hydro-elasto-plastic EOS-EOSS3 (Tang and Sotiropoulos, 1999)

The Murnagham equation and Hooke's law are used for the hydrostatic pressure and the shear stress, respectively. Thus, the EOS can be written as

$$p = p_h(\rho) + \frac{4}{3}s(\rho_s,\tau_s,\rho), \tag{2.8a}$$

where $p_h(\rho)$ and $s(\rho_s,\tau_s,\rho)$ are the hydrostatic pressure and shear stress, respectively. The subscript "s" refers to an initial state. Hydrostatic pressure $p_h(\rho)$ is written as a form similar to Tait's EOS

$$p_h(\rho) = \frac{m}{\beta}\left(\left(\frac{\rho}{\rho_a}\right)^\beta - 1\right) + p_a, \tag{2.8b}$$

and shear stress is described by Hooke's law,

$$s = \begin{cases} \tau & |\tau| < Y/2, \\ Y sign(\tau)/2, & |\tau| \geq Y/2. \end{cases} \tag{2.8c}$$

In (2.8b) and (2.8c), m, Y and β are the bulk modulus, yield stress, and a model constant, respectively. Equation (2.8a) can be rewritten as

$$p = \begin{cases} p_h(\rho) + \dfrac{2}{3}Y, & \rho \geq \rho_2 \\ p_h(\rho) + \dfrac{4}{3}\left(G \ln \dfrac{\rho}{\rho_s} + \tau_s \right) & \rho_1 < \rho \leq \rho_2 \\ p_h(\rho) - \dfrac{2}{3}Y, & \rho < \rho_1 \end{cases}, \tag{2.8d}$$

where G is the modulus of rigidity. ρ_1 and ρ_2 are given densities (or defined for) pure elastic deformation, elastic and plastic deformation, and pure plastic deformation, respectively. It may be noted that the three EOS for solid (Henceforth called EOSS1, EOSS2, and EOSS3 for reference) are used under different conditions. In this chapter, the EOSS1 for solid is preferred for ease of analysis for the various GFM-based algorithms in the next section. With EOSS1, the sound speeds for gas, water and solid can be written in the same forms. In this way, the techniques developed for gas can be applied directly to water and solid. The EOSS1 is a good approximation to stiffened gas EOS and EOSS2. When the flow is under a very strong shock, the EOSS2 is used to capture the elastic and plastic deformation of solid. The obvious drawback of EOSS1 and EOSS2 is the limited domain of validity. That is, the elastic and plastic deformations can not be accurately captured in the context of underwater explosions and/or high velocity impacts. Generally, the EOSS1 and EOSS2 may not be accurate if the pressure ratio across the interface is very high. Compared to EOSS1 and EOSS2, the EOSS3 is deemed more accurate when the solid sustains both elastic deformation and plastic deformation under the action of a strong shock-solid interaction. Two problems cases posed in Tang and Sotiropoulos (1999) are tested in this chapter by using the EOSS3 for solid.

2.3 Numerical algorithm for single-medium

The numerical method for the region away from the interface employed in this work is a high-resolution MUSCL-type TVD scheme with HLL approximate Riemann solvers (Harten et al, 1983) employed. The scheme is given briefly in this section. The numerical flux in the HLL approximation reads as

$$H^{hll} = \frac{S_R F_L - S_L F_R + S_L S_R (U_R - U_L)}{S_R - S_L} \ . \tag{2.9a}$$

The indexes R and L are related to the right and left sides of a cell boundary. In order to determine the numerical fluxes completely in HLL Riemann solver we need to provide an algorithm for computing the wave speeds (S_l, S_R). Various methods are available for wave speed estimate (Toro, 1997). We prefer the Roe average eigenvalues for the left and right non-linear waves for convenience, that is

$$S_L = \tilde{u} - \tilde{a} \ , S_R = \tilde{u} + \tilde{a} \, , \tag{2.9b}$$

where $\tilde{u}$ and $\tilde{a}$ are the Roe-averaged velocity and sound speed, respectively. It is now necessary to determine the discretization formulas for the conservative equations. To obtain these formulas, we develop the algorithm over a time step for 1D Euler governing equations. The scheme for 1D conservative system (Equation (2.1)) can be written as

$$U_i^{n+1} = U_i^n - \lambda \left(H_{i+1/2}^n - H_{i-1/2}^n \right), \tag{2.9c}$$

where $\lambda = \Delta t / \Delta x$, Δt and Δx are the time and spatial step-sizes, respectively. Numerical fluxes in the HLL approximation $\left(H_{i\pm 1/2}^n \right)$ are obtained via (2.9a) as

$$H_{i+1/2}^n = \frac{S_{R,i+1/2}^n F_{L,i+1/2}^n - S_{L,i+1/2}^n F_{R,i+1/2}^n + S_{R,i+1/2}^n S_{L,i+1/2}^n \left(U_{R,i+1/2}^n - U_{L,i+1/2}^n \right)}{S_{R,i+1/2}^n - S_{L,i+1/2}^n}.$$

(2.9d)

The parameters at the cell boundary as shown for the right hand side of Equation (2.9d) are calculated via the MUSCL method employed by Liu (2000) with 2-order accuracy. To ensure a stable computation, the stability condition (2.10) in the following should be satisfied

$$\Delta t = CFL \frac{\Delta x}{\max\left(|u_i| + c_i\right)}. \tag{2.10}$$

This scheme is stable under standard CFL number (generally from 0.1 to 0.9), based on the largest absolute wave speed.

2.4 GFM-based Algorithms for material interface

The level set equation is solved to keep track of the interface location as zero level of ϕ which is the signed distance function. With interface locations, the GFM defines ghost fluids and the computations are then carried out as for a single-medium manner via solving two respective single-medium GFM Riemann problems. In this section, various existing GFM-based schemes like the original GFM, the new version GFM and the MGFM are presented. The MGFM employs an ARPS to predict the interface information (pressure and normal velocity) which needs relatively more computations. To speed the computation, an explicit characteristic method is proposed to replace the ARPS for predicting interface information, resulting in the so-called present GFM.

2.4.1 The Original GFM with Isobaric Fix

The key point of any GFM-based algorithm is defining the ghost fluid properties where the real fluid and ghost fluid coexist (Fedkiw et al, 1999b). Generally, the pressure and velocity are continuous across the interface and thus the pressure and velocity of the ghost fluid are equal to the pressure and velocity of real fluid at ghost

cells. Consider two fluids called Fluid1 and Fluid2 are connected by a material interface which lies in between node i and node $i+1$ as shown in Fig. 2.1. In the computation of Fluid1, the real fluid and ghost fluid coexist in the domain of Fluid2. The pressure and velocity of the ghost cells are copied from the real fluid of Fluid2. The entropy is chosen as the third variable to complete the definition of the ghost cells. The entropy of the ghost cells at Fluid2 is extrapolated from the node $i-1$ of Fluid1. In this way, the ghost cells are defined and the interface conditions are determined. It should be noted that the entropy of node i of Fluid1 is updated by the entropy of node $i-1$ in this process to suppress "overheating" phenomenon where numerical results provide accepted pressure and velocity but can not predict an acceptable third variable, density or temperature. The overall process for the definition of the ghost cells can be written as

$$\begin{aligned} &p_{i+1}^{G} = p_{i+1}^{2} \qquad p_{i+2}^{G} = p_{i+2}^{2} \qquad p_{i+3}^{G} = p_{i+3}^{2}, \\ &u_{i+1}^{G} = u_{i+1}^{2} \qquad u_{i+2}^{G} = u_{i+2}^{2} \qquad u_{i+3}^{G} = u_{i+3}^{2}, \\ &s_{i}^{1} = s_{i-1}^{1} \qquad s_{i+1}^{G} = s_{i-1}^{1} \qquad s_{i+2}^{G} = s_{i-1}^{1} \qquad s_{i+3}^{G} = s_{i-1}^{1}, \end{aligned} \tag{2.11}$$

where the superscript "G", "1" and "2" express the ghost cell, Fluid1 and Fluid2, respectively. If Fluid2 is calculated, similar process as (2.11) can be used for the definition of ghost cells at Fluid1. The definition of ghost cells as mentioned above shows that the major advantage of the original GFM is its simplicity.

2.4.2 The New Version GFM with Isobaric Fix

The original GFM may not work well for some flows with different EOS across the interface like the gas-water and gas-solid flows. Such inapplicability is due to the fact that the pressure of water or solid is very sensitive to density. For (proper) definition of

ghost fluid for the material associated with a stiff equation of state, the material properties have to be taken into account because the pressure or velocity may not be continuous across the interface in the first several computational steps during a shock wave impacting on the interface. Fedkiw et al (2002) developed a new version GFM for solid computation in which the velocity of ghost fluid is determined by the fluid associated with the stiff EOS (water or solid) and the pressure of ghost fluid is determined by the other fluid (gas). In this way, the material property is partly taken into account and thus the new version GFM performs better than the original GFM in the computation of gas-water and gas-solid flows. Consider a gas-water flow where gas (Fluid1) lies in the left side of the interface and water (Fluid2) lies in the right side of the interface as Fig 2.2 shows. When defining the ghost fluid status for water, the pressure of gas is copied into the ghost cells while the entropy and velocity of water are extrapolated into the ghost cells from water side. When defining the ghost fluid status for gas, the velocity of water is copied into the ghost cells while the entropy and pressure of gas are extrapolated into the ghost cells from the gas side. Figure 2.2a shows the process of defining ghost fluid status for Fluid1 (gas). This process can be written as

$$
\begin{aligned}
&p_{i+1}^{G} = p_{i}^{1} \qquad p_{i+2}^{G} = p_{i}^{1} \qquad p_{i+3}^{G} = p_{i}^{1}, \\
&u_{i+1}^{G} = u_{i+1}^{2} \qquad u_{i+2}^{G} = u_{i+2}^{2} \qquad u_{i+3}^{G} = u_{i+3}^{2}, \\
&s_{i}^{1} = s_{i-1}^{1} \qquad s_{i+1}^{G} = s_{i-1}^{1} \qquad s_{i+2}^{G} = s_{i-1}^{1} \qquad s_{i+3}^{G} = s_{i-1}^{1}.
\end{aligned}
\tag{2.12a}
$$

Figure 2.2b shows that the process of defining ghost fluid status for Fluid2 (water), similar equations like (2.12a) can be written as follows

$$
\begin{aligned}
&p_{i}^{G} = p_{i}^{1} \qquad p_{i-1}^{G} = p_{i-1}^{1} \qquad p_{i-2}^{G} = p_{i-2}^{1}, \\
&u_{i}^{G} = u_{i+1}^{2} \qquad u_{i-1}^{G} = u_{i+1}^{2} \qquad u_{i-2}^{G} = u_{i+1}^{2},
\end{aligned}
\tag{2.12b}
$$

$$s_{i+1}^2 = s_{i+2}^2 \qquad s_i^G = s_{i+2}^2 \qquad s_{i-1}^G = s_{i+2}^2 \qquad s_{i-2}^G = s_{i+1}^2 .$$

It has been found that the new version GFM is not effective as the original GFM for some gas-gas flows and gas-water flows (Liu et al, 2005). That is, the employment of the original GFM or the new version GFM is very problem-related instead of universally effective. To overcome such non-generality, a modified GFM with more generality and accuracy is developed by Liu et al (2003b).

2.4.3 The Modified GFM

The modified GFM is developed for a strong shock impacting on a material interface where the pressure, velocity and entropy may not be continuous across the interface in the initial several steps of computation as a singularity is created at the interface (Liu et al, 2003b). That is, the assumption of pressure and velocity continuity for the original GFM may not be maintained under such condition. In the presence of a strong shock, a correct interface status has to be obtained before a GFM-based algorithm can be applied. For this purpose, the characteristic relationship associated with the shock-jump conditions is employed to predict the interface status (Liu et al, 2001a). The material properties and wave interactions with interface are taken into account for better prediction of the interface status. The modified GFM is described in detail in Liu et al (2003b). A brief summary is given here.

The system (2.1) can be rewritten at the interface in the characteristic form, and the two nonlinear characteristic equations intersecting with the material interface are expressed as

$$\frac{dp_I}{dt} + \rho_{IL} c_{IL} \frac{du_I}{dt} = 0, \quad \text{along } \frac{dx}{dt} = u_I + c_{IL} \ , \tag{2.13a}$$

$$\frac{dp_I}{dt} - \rho_{IR} c_{IR} \frac{du_I}{dt} = 0, \quad \text{along } \frac{dx}{dt} = u_I - c_{IR} \ , \tag{2.13b}$$

where subscripts " I ", " IL " and " IR " refer to the interface, the left side of the interface and the right side of the interface, respectively. ρ_{IL} (ρ_{IR}) and c_{IL} (c_{IR}) are the density and sound speed on the left (right) side of the interface; u_I and p_I are the velocity and density at the interface, respectively. Discretization of (2.13) via the implicit characteristic method leads to the modified GFM in which (2.13) is approximated by

$$\frac{p_I - p_{IL}}{W_{IL}} + (u_I - u_{IL}) = 0, \tag{2.14a}$$

$$\frac{p_I - p_{IR}}{W_{IR}} - (u_I - u_{IR}) = 0, \tag{2.14b}$$

where u_{IL} (u_{IR}) is the fluid velocity on the left (right) side of interface. W_L and W_R are related to the interface information and used to approximate $\rho_{IL}c_{IL}$ and $\rho_{IR}c_{IR}$. Equation (2.14) is solved via iteration to obtain the interface pressure and velocity. The detailed solver for (2.14) is presented in Liu et al (2001a, 2003b). Assume Fluid1 on the left and Fluid2 on the right are connected by an interface located between nodes i and $i+1$ as shown in Fig. 2.3. In the computation of Fluid1, (2.14a, b) are solved for prediction of the interface status. The predicted interface pressure and velocity are then copied into the ghost cell $i+1$ and the density of this ghost cell is determined by the predicted interface entropy. For the ghost cell $i+2$, the pressure and velocity can be copied from the predicted interface pressure and velocity while the predicted interface entropy is copied into ghost cell $i+2$ to fix the density. For suppressing the "overheating" phenomenon, the entropy of real Fluid1 i is updated by the predicted interface entropy to define a new density at this point. Similar to the Sections 2.4.1 and 2.4.2, we express this process as follows

$$p_{i+1}^G = p_I \qquad p_{i+2}^G = p_I ,$$

$$u_{i+1}^G = u_I \qquad u_{i+2}^G = u_I , \tag{2.15}$$

$$s_i^1 = s_I \qquad s_{i+1}^G = s_I \qquad s_{i+2}^G = s_I .$$

Similar procedures (2.15) for the ghost fluid status can be obtained in the computation of Fluid2. The MGFM preserves the simplicity of the original GFM and can be universally applicable. As an approximate Riemann problem solver (ARPS) is applied to predict the interface status and hence a little more computational cost than the original GFM is unavoidable. For the flows where one medium is a solid and EOSS3 is used for the solid medium, it may take much more computing time to obtain the solution of ARPS when the pressure is not high. To overcome this difficulty, as one of the purposes of this work, a simple explicit characteristic method is employed to replace the ARPS for predicting the interface status, thereby resulting in the so-called present GFM in the following.

2.4.4 The Present GFM

The explicit characteristic method proposed here is another method to discretize (2.14) (see also Xie et al, 2005b). If $\rho_{IL} c_{IL}$ and $\rho_{IR} c_{IR}$ are assumed as constants and thus (2.13) is approximated as

$$\frac{p_I - p_{IL}}{\rho_{IL} c_{IL}} + \left(u_I - u_{IL}\right) = 0 , \tag{2.16a}$$

$$\frac{p_I - p_{IR}}{\rho_{IR} c_{IR}} - \left(u_I - u_{IR}\right) = 0 , \tag{2.16b}$$

where p_{IL} (p_{IR}) is the pressure on the left (right) side of the interface. With simple derivation, the system (2.16) can be solved to obtain the interface pressure and velocity as follows:

$$p_I = \frac{(u_{IL} - u_{IR})\rho_{IL}c_{IL}\rho_{IR}c_{IR} + p_{IL}\rho_{IR}c_{IR} + p_{IR}\rho_{IL}c_{IL}}{\rho_{IL}c_{IL} + \rho_{IR}c_{IR}}, \tag{2.17a}$$

$$u_I = \frac{p_{IL} - p_{IR} + \rho_{IL}u_{IL}c_{IL} + \rho_{IR}u_{IR}c_{IR}}{\rho_{IL}c_{IL} + \rho_{IR}c_{IR}}. \tag{2.17b}$$

Assuming the interface lies between nodes i and $i+1$, the values of p_{IL}, ρ_{IL} and c_{IL} are taken from node $i-1$ while the values of p_{IR}, ρ_{IR} and c_{IR} are taken from node $i+2$, then (2.17) can be rewritten as

$$p_I = \frac{(u_{i-1} - u_{i+2})\rho_{i-1}c_{i-1}\rho_{i+2}c_{i+2} + p_{i-1}\rho_{i+2}c_{i+2} + p_{i+2}\rho_{i-1}c_{i-1}}{\rho_{i-1}c_{i-1} + \rho_{i+2}c_{i+2}}, \tag{2.18a}$$

$$u_I = \frac{p_{i-1} - p_{i+2} + \rho_{i-1}u_{i-1}c_{i-1} + \rho_{i+2}u_{i+2}c_{i+2}}{\rho_{i-1}c_{i-1} + \rho_{i+2}c_{i+2}}. \tag{2.18b}$$

On the explicit characteristic method we have the following conclusions.

Conclusion 2.1: *System (2.16) is an approximation to the exact Riemann solver with the initial condition of U_{IL} and U_{IR} on left and right sides of the interface. It approximates the exact Riemann solver with the accuracy of $O(p_I / p_{IL} - 1)$ or $O(p_I / p_{IR} - 1)$.*

Conclusion 2.1 states that (2.14) and (2.16) approximate the exact Riemann problem with different level of accuracy. That is, (2.14) approximates the exact Riemann problem with accuracy of $O(p_I / p_{IL} - 1)^2$ or $O(p_I / p_{IR} - 1)^2$ while (2.16) approximates the exact Riemann with accuracy of $O(p_I / p_{IL} - 1)$ or $O(p_I / p_{IR} - 1)$. The present GFM may not be so accurate if a strong rarefaction wave is propagating in the flow especially for gas-gas flows where the assumption of constants for $\rho_{IL}c_{IL}$ and $\rho_{IR}c_{IR}$ are not quite correct. Therefore, the main application of the present GFM is for gas-solid and water-solid flows where high pressure lies in the gas medium for gas-

solid flows and water medium for water-solid flows. A gas-steel and a water-steel flow are presented below to verify the accuracy of the present GFM for predicting the interface status where the hydro-elasto-plastic EOS (EOSS3) in Section 2.2 is employed for the steel. The main parameters for the steel are shown in Table 2.1. For the gas-steel flow, the pressure ratio of gas to steel ranges from 1000 to 10000 and gas densities are 0.320, 0.429 and 0.720, respectively. Other initial conditions are $\rho_g = 0.05, u_g = 0.0;\ p_s = 1.0, \rho_s = 7.8, u_s = 0.0$. Here the superscripts "g" and "s" refer to gas and steel mediums, respectively. Table 2.2 shows the comparison of the expected pressure and velocity at the interface for system (2.16) and the exact Riemann problem solver where the high pressure always lies in the gas medium. It is found that there is reasonably good concurrence for the predicted interface pressure and velocity via (2.16) and the exact Riemann problem solver when applied to the gas-steel flow. For the water-steel flow, a similar test is carried out to verify the explicit characteristic method. The pressure ratios of water to steel ranges from 5000 to 15000 and water densities are calculated from Tait's Equation. Other initial conditions are $u_w = 0.0;\ p_s = 1.0,\ \rho_s = 7.8,\ u_s = 0.0$. Once again, the explicit characteristic method provides close interface pressure and velocity to the exact Riemann problem solver. Such agreement will be further verified in the Section 2.6 via two further examples (Case 2.6.1 and Case 2.6.2). The required iteration steps to solve ARPS is also shown in Table 2.4 to investigate the relatively high computational cost of the MGFM when compared to the present GFM.

Compared to (2.14), the applicability of (2.16) is relatively more limited. This is mainly due to the assumption of constants for $\rho_{IL}c_{IL}$ and $\rho_{IR}c_{IR}$. In the case of gas-gas flows with a large pressure difference or a strong rarefaction wave present, the first-order accuracy of (2.16) is not sufficiently accurate to ensure a correct predicted

interface pressure and velocity. Furthermore, (2.16) may on occasions predict a negative interface pressure and thus no subsequent meaningful results can be obtained. That is, the breakdown of computation may occur if p_I in (2.16) become negative, and we have

$$u_{IL} - u_{IR} \le -\frac{p_{IL}}{\rho_{IL} c_{IL}} - \frac{p_{IR}}{\rho_{IR} c_{IR}} , \qquad \text{if } p_I \le 0 . \tag{2.19}$$

Conclusion 2.2: *The present explicit characteristic method is not applicable if the inequality (2.19) is satisfied. One necessary condition for application of (2.16) is to ensure* p_I *is positive.*

Conclusion 2.2 gives a necessary condition for the application of the present explicit characteristic method. It should be noted that this condition is not a sufficient condition. As mentioned above, the present GFM may meet difficulties when applied to gas-gas flows with a large pressure difference or gas-solid flows with a strong rarefaction in the gaseous medium. For those cases where the present GFM is inapplicable, the MGFM is used instead to replace the present GFM.

Another important condition for the application of the explicit characteristic method is that the pressure is continuous across the interface. That means that the pressures of both mediums have to be positive. As we are aware, the pressure on the solid may become negative if cavitation occurs in the water near the water-solid interface. In such case, a fix has to be developed for the present GFM. (2.17) can be rewritten as

$$p_I = \frac{u_{IL} - u_{IR} + \dfrac{p_{IL}}{\rho_{IL} c_{IL}} + \dfrac{p_{IR}}{\rho_{IR} c_{IR}}}{\dfrac{1}{\rho_{IL} c_{IL}} + \dfrac{1}{\rho_{IR} c_{IR}}}, \tag{2.20a}$$

$$u_I = \frac{\dfrac{p_{IL} - p_{IR}}{\rho_{IR} c_{IR}} + \dfrac{\rho_{IL} u_{IL}}{\rho_{IR} c_{IR}} c_{IL} + u_{IR}}{\dfrac{\rho_{IL} c_{IL}}{\rho_{IR} c_{IR}} + 1}. \tag{2.20b}$$

The medium with larger acoustic impedance is assumed to be located on the right side of interface (solid) and there is a small pressure and velocity change across the interface. When cavitation occurs near the water-solid interface, ρ_{IL} is a very small quantity (approximated as vapor density) and c_{IL} is the acoustic speed of cavitation mixture which is of even lower value than the acoustic speed of gas (Qin et al, 1999). Therefore, the acoustic impedance on the left side of the interface (i.e. $\rho_{IL} c_{IL}$) is much smaller than the corresponding value on the right side of the interface (i.e. $\rho_{IR} c_{IR}$). Moreover, there is a small pressure and velocity change across the interface when cavitation occurs because the pressure and velocity are continuous across the interface. As such, we have $|u_{IL} - u_{IR}| < \varepsilon$, $|p_{IL} - p_{IR}| < \varepsilon$ and $\rho_{IR} c_{IR} >> \rho_{IL} c_{IL}$, with ε being much smaller than acoustic impedance. (2.20a, b) are thus simplified as

$$p_I \approx p_{IL} + \rho_{IL} c_{IL} (u_{IL} - u_{IR}), \tag{2.21a}$$

$$u_I \approx u_{IR}. \tag{2.21b}$$

It should be noted the pressure calculated via (2.21a) is always positive. This is because $u_{IL} - u_{IR}$ is positive. Therefore, the potential presence of negative interface pressure can be suppressed because the ghost fluids are defined via (2.21a) which is positive.

Compared to the MGFM, the present GFM obtains the interface pressure and velocity by algebraic equation which largely reduces computational cost. Although Conclusion 2.2 shows the application of the present GFM is limited, it is still able to

simulate for numerous gas-solid and water-solid compressible flow problems like those in present work. This can be clearly shown based on the analysis carried out in Section 2.5 and numerical examples in Section 2.6.

2.5 Analysis for Various GFM-based Algorithms

In the above section, various GFM-based numerical algorithms are briefly introduced and an explicit characteristic method for prediction of interface status is developed. It has been discussed by Liu et al (2005) that the application range of each GFM-based algorithm can be very different. The original GFM, the new version GFM and the present GFM have its own limitations when applied to various multi-medium flows. To determine and summarize such range of applicability for each GFM-based algorithm, mathematical analysis is carried out in this chapter based on the work by Liu et al (2005).

In the computation of multi-medium Riemann problem (henceforth called original Riemann problem for ease of referral), the Riemann waves in the fluid flow have to be decomposed correctly. Such Riemann waves consist of a non-linear shock wave, a non-linear rarefaction wave and a linear contact discontinuity which generally is located between a shock wave and a rarefaction wave. With different initial conditions the structure of Riemann waves may be quite different but solutions of the original Riemann problem always consist of two non-linear waves and one linear contact discontinuity. When the GFM-based algorithm is employed (the original GFM or the new version GFM or otherwise), the structures of the Riemann waves (GFM Riemann waves) may be different from the original Riemann waves. In the GFM-based algorithm, the two single-medium Riemann problems (henceforth called GFM Riemann problems for ease of referral) can be constructed to calculate the value at the

interface. It has been found especially by Liu et al (2005) that the original GFM or the new version GFM may provide inconsistent Riemann waves as compared to the original Riemann waves in the respective real fluids, thereby resulting in inaccurate numerical results. Therefore, it is suggested that the consistency of GFM Riemann waves to the original Riemann waves to the respective real fluid can be taken as a criterion to evaluate the applicability or viability of any GFM-based algorithm. An original initial-value Riemann problem can be expressed as

$$U\big|_{t=0} = \begin{cases} U_l & x < x_0 \\ U_r & x > x_0 \end{cases}, \tag{2.22}$$

where U is the conservative variable in (2.1) and the subscripts "l" and "r" indicate the flow at the left and right sides of the interface, respectively. x_0 is the initial interface location. The solution of system (2.1) with initial condition (2.22) is a shock wave-contact discontinuity- rarefaction wave or a shock wave-contact discontinuity-shock wave or a rarefaction wave-contact discontinuity-rarefaction wave. Physically, the pressure and velocity across the interface are continuous but it takes several steps for the numerical computation to reach such continuity. In the application of a GFM-based algorithm, two initial-value GFM Riemann problems are constructed after the ghost fluid status is defined, they can be written as

$$U\big|_{t=0} = \begin{cases} U_l & x < x_0 \\ U_r^G & x > x_0 \end{cases}, \qquad \text{for left flow} \tag{2.23a}$$

and

$$U\big|_{t=0} = \begin{cases} U_l^G & x < x_0 \\ U_r & x > x_0 \end{cases}, \qquad \text{for right flow} \tag{2.23b}$$

where the superscript "G" indicates the ghost fluid. In general, the pressure and velocity will be continuous across the interface after several steps of computation. Thus, the applicability of a GFM-based algorithm is determined primarily by the computation at the first several steps when an initial singularity exists at the interface. To decompose such singularity correctly is the key to obtain the consistent Riemann waves and correct pressure and velocity at the interface. This is particularly important for the GFM-based algorithm to obtain reasonable numerical results. Unfortunately, the original GFM and the new version GFM may not correctly decompose the singularity in many cases. It is found that such difficulty arises mainly because the GFM Riemann waves generated by (2.23a) or (2.23b) are not consistent with those by (2.22). To ensure consistent GFM Riemann waves during the decomposition of the singularity, two conditions proposed by Liu et al (2005) have to be satisfied:

Condition (I): the GFM Riemann wave in the real fluid side for both GFM Riemann problems is initially consistent with that for the same side as for the original Riemann problem.

Condition (II): the new Riemann problem formed from the GFM computation maintains the same type of solution as that for the original Riemann problem during the decomposition of the singularity.

The violation of any of these two conditions leads to numerical error at the interface. One should note that the satisfaction of Condition (I) does not necessary mean the Condition (II) is satisfied automatically. To obtain consistent GFM Riemann waves, both conditions have to be satisfied simultaneously. The evaluation of Condition (I) is straightforward for the GFM-based algorithms. That is, after the ghost fluid status is defined, if the Riemann waves at the real fluid side generated from the GFM Riemann problem (2.23) are consistent with the Riemann waves generated from the original

Riemann problem (2.22), Condition (I) is satisfied. Otherwise, Condition (I) is violated and Condition (II) need not be evaluated because numerical error has appeared at the interface due to violation of Condition (I). On the other hand, the evaluation of Condition (II) is relatively much more complex. This is because the evaluation of Condition (II) involves the numerical scheme and relates to the interface status at the first few steps of computation. In Liu et al (2005), the interface pressure and velocity provided by the GFM Riemann problems (2.23a) and (2.23b) are employed to evaluate the Condition (II). If the interface pressure and velocity obtained from the GFM Riemann problem (2.23a) are close to those obtained from the GFM Riemann problem (2.23b), Condition (II) is assumed to be satisfied under the prior satisfaction of Condition (I). Otherwise, Condition (II) is likely to be violated with the ensuing large difference between the interface pressure and velocity predicted by the GFM Riemann problem (2.23a) and (2.23b). Such evaluation criterion for Condition (II) has been shown to be effective by numerous numerical examples in Liu et al (2005).

Conditions (I) and (II) have been applied to analyze the various GFM-based algorithms for compressible gas-water flows (Liu et al, 2005). Such analysis can be extended to other multi-medium flows like gas-solid and water-solid compressible flows. In the following, the analysis on the different GFM-based algorithms for gas-water, gas-solid and water-solid flows is given.

2.5.1 Analysis for Gas-Water Compressible Flows

For all solution types of gas-water compressible flows, the ranges where the original GFM and the new version GFM are unable to provide the correct numerical results have been identified by Liu et al (2005). In the same paper, various numerical examples, where Condition (I) or Condition (II) is violated by either the original GFM or the new version GFM, are constructed to support the analysis for gas-water flows.

At the same time, the MGFM is shown to be able to calculate reasonably for the same numerical examples. It is found that the MGFM with a double shock wave solver are able to produce reasonable results for comparison to the analytical solutions.

The analysis for gas-water flows is not repeated in this section. For details, one can refer to the series of papers by Liu et al (2003b, 2005). As mentioned in Section 2.4.4, the explicit characteristic method is a first-order approximation to the exact Riemann problem solver. Four numerical examples of gas-water flows, which the original GFM and the new version GFM are unable to produce reasonable results, are calculated by both the MGFM and the present GFM in Section 2.6 (Case 2.6.3-2.6.6) for comparison and analysis. Furthermore, Conclusion (2.2) states a necessary condition to assure the applicability of the present GFM and thus violation of this necessary condition will lead to a breakdown of numerical computation. A numerical example for such inapplicability of the present GFM is also given in Section 2.6 (Case 2.6.7).

2.5.2 Analysis for Gas-Solid Compressible Flows

For ease of analysis, the Tait EOS (EOSS1) is used for the solid medium. Obviously, the analysis of such gas-solid flows is similar to that of gas-water flows because the EOS for water and solid take on the same form. Thus, the analysis for gas-water flows in Liu et al (2005) can be applied directly to the analysis for gas-solid flows. In this section, we only analyze the gas-solid flows with high pressure in the gaseous medium assuming that the gas medium is located on the left side of the interface. Thus we have $p_l > p_r$ and only three solution types are possible: a rarefaction wave in gas and a shock wave in solid (called R-S); a shock wave in gas and a shock wave in solid (called S-S); a rarefaction wave in gas and a rarefaction wave in solid (called R-R). The following conclusions can be obtained:

Conclusion 2.3 (for the R-S solution type): *If the initial status of U_l and U_r satisfies*

$$\frac{2c_l}{\gamma_g-1}\left[\left(\frac{p_r}{p_l}\right)^{\frac{\gamma_g-1}{2\gamma_g}}-1\right]<u_l-u_r<\sqrt{\frac{\overline{p}_r}{\rho_r}}\sqrt{\frac{\overline{p}_l}{\overline{p}_r}-1}\sqrt{1-\left(\frac{\overline{p}_l}{\overline{p}_r}\right)^{-1/\gamma_s}}, \qquad (2.24)$$

then the solution type of Riemann problem (2.22) is a rarefaction wave in gas and a shock wave in solid (R-S). Here, c_l is sound speed of the medium on the left side.

Conclusion 2.4 (for the S-S solution type): *If the initial status of U_l and U_r satisfies*

$$u_l-u_r>\sqrt{\frac{\overline{p}_r}{\rho_r}}\sqrt{\frac{\overline{p}_l}{\overline{p}_r}-1}\sqrt{1-\left(\frac{\overline{p}_l}{\overline{p}_r}\right)^{-1/N}}>0, \qquad (2.25)$$

then the solution type of Riemann problem (2.22) is a shock wave in gas and a shock wave in solid (S-S).

Conclusion 2.5 (for the R-R solution type): *If the initial status of U_l and U_r satisfies*

$$-\frac{2c_l}{\gamma_g-1}-\frac{2\overline{c}_r k_{cr}}{\gamma_s-1}<u_l-u_r<\frac{2c_l}{\gamma_g-1}\left[\left(\frac{p_r}{p_l}\right)^{\frac{\gamma_g-1}{2\gamma_g}}-1\right]<0, \qquad (2.26)$$

then the solution type of Riemann problem (2.22) is a rarefaction wave in gas and a rarefaction wave in solid (R-R).

Here $\overline{c}_r$ is the sound speed of solid and $k_{cr}=\left[1-\left(B/\overline{p}_r\right)^{\frac{\gamma_s-1}{2\gamma_s}}\right]$ where $\overline{p}=p+B$. It should be noted that B in Tait's EOS for solid is a magnitude of $O\left(10^{10}\right)$ which is much larger than B ($O\left(10^{8}\right)$) in Tait's EOS for water. From Conclusions 2.3, 2.4 and 2.5 we have the (required) relationship between the interface status and flow status at both sides of the interface as follows:

1) $u_I > \max(u_l, u_r)$ *and* $p_r < p_I < p_l$ *for R-S solution.*

2) $u_r < u_I < u_l$ *and* $p_I > \max(p_l, p_r)$ *for S-S solution.*

3) $u_l < u_I < u_r$ *and* $p_I < \min(p_l, p_r)$ *for R-R solution.*

These three relationships are very useful to evaluate if a GFM-based algorithm satisfies Condition (II). Here, the analysis on various GFM-based algorithms is given briefly.

(1) On the original GFM, we have $p_r^G = p_r$, $u_r^G = u_r$, $p_l^G = p_l$ and $u_l^G = u_l$. Using the analysis similar as in Liu et al (2005), the range where the original GFM is unable to provide the consistent Riemann wave at the respective real fluid (i.e. violation of Condition (I)) for gas-solid flows can be defined as

1) If the solution type of Riemann problem (2.22) is R-S, this range is defined by

$$\frac{2c_l}{\gamma-1}\left[\left(\frac{p_r}{p_l}\right)^{\frac{\gamma-1}{2\gamma}}-1\right] < u_l - u_r < \frac{2\bar{c}_l^G}{\gamma_s-1}\left[\left(\frac{\bar{p}_r}{\bar{p}_l}\right)^{\frac{\gamma_s-1}{2\gamma_s}}-1\right], \tag{2.27a}$$

2) If the solution type of Riemann problem (2.22) is S-S, this range is defined by

$$\sqrt{\frac{\bar{p}_r}{\rho_r}}\sqrt{\frac{\bar{p}_l}{\bar{p}_r}-1}\sqrt{1-\left(\frac{\bar{p}_l}{\bar{p}_r}\right)^{-1/\gamma_s}} < u_l - u_r < \sqrt{\frac{\beta p_r}{\rho_r^G}}\frac{p_l/p_r-1}{\sqrt{1+\tau p_l/p_r}}, \tag{2.27b}$$

where $\beta = 2/(\gamma_g - 1)$, $\tau = (\gamma_g + 1)/(\gamma_g - 1)$.

3) If the solution type of Riemann problem (2.22) is R-R, the original GFM generally provides inconsistent Riemann waves in either one of the real flow sides.

For a double-rarefaction wave problem, Condition (I) is initially satisfied by the original GFM. However, Condition (II) is very difficult to be maintained except the initial gas density is far larger than solid which is apparently unrealistic. Difficulties

may also arise from the numerical method itself. It has been found by Einfeldt et al (1991) that a non-positive preserving scheme such as Roe-type schemes does not work well in a double-rarefaction problem especially when the flow condition approaches cavitation. To overcome such difficulty, a double rarefaction wave solver has been developed by Liu et al (2005).

(2) On the new version GFM, we have $p_r^G = p_l, u_r^G = u_r$, $p_l^G = p_l$ and $u_l^G = u_r$. Doing so, the pressure of ghost fluid is provided by the gas medium and the velocity of ghost fluid is provided by the solid medium. The range where the new version GFM is unable to satisfy both Conditions (I) and (II) simultaneously can be defined as

1) If the solution type of Riemann problem (2.22) is R-S: Condition (I) is violated if $u_l - u_r > 0$ *; Condition (I) is satisfied if* $u_l - u_r < 0$ *but Condition (II) is violated if* u_l *is much different from* u_r.

2) If the solution type of Riemann problem (2.22) is S-S: Condition (I) is satisfied while Condition (II) is violated. This is because the interface velocity obtained from the GFM Riemann problem (2.23a) is always less than the interface velocity obtained from the GFM Riemann problem (2.23b) while the interface pressure from (2.23a) is always larger than the interface pressure from (2.23b).

3) If the solution of Riemann problem (2.22) is R-R: Condition (I) is always violated because we assume $p_l > p_r$.

(3) On the MGFM and the present GFM, we have $p_r^G = p_I, u_r^G = u_I$, $p_l^G = p_I$ and $u_l^G = u_I$ where the interface pressure and velocity are solved via an (interface) approximate Riemann problem solver (ARPS). This ARPS considers the wave interaction and refraction at the interface and thus is able to provide consistent GFM

Riemann waves to the original Riemann waves. Numerical examples show that the MGFM is able to produce reasonable numerical results compared to analysis. If the pressure and velocity change across the gas-solid interface is small and a low pressure region appears next to the gas-solid interface, the ARPS takes more time to obtain the density of the solid medium from the pressure quantity. This is especially so if the solid medium is governed by hydro-elasto-plastic EOS, resulting in much more computational cost for the MGFM. The present GFM is able to greatly reduce the computational cost because only an algebraic equation is solved for the interface status as shown in (2.16). Case 2.6.1 is a gas-solid (steel) flow where the present GFM computes much faster than for the MGFM.

Various numerical examples, where at least one of Conditions (I) and (II) is violated, are calculated by the four GFM-based algorithms (Case 2.6.8-Case 2.6.10).

2.5.3 Analysis for Water-Solid Compressible Flows

Similar to the gas-solid compressible flows as discussed above, the analysis for the water-solid compressible flows is based on Tait's EOS (EOSS1) used for the solid medium. If EOSS2 or EOSS3 in Section 2.2 is used for the solid medium, similar analysis can be carried out but the closed form may not be obtained. This is because the relationship between the pressure and density in EOSS2 and EOSS3 is implicit. In the computation of water-solid flows, the high pressure invariably lies in the water medium and initial water velocity is usually much larger than the solid velocity. Based on the assumption that the water is on the left side of the interface and the solid is on the right side of the interface we therefore have

$$p_l > p_r, u_l \geq u_r, \tag{2.28}$$

The water-solid flows we consider are a high pressure and high speed water stream impacting on the solid where the water pressure and velocity are much larger than solid pressure and velocity. In such case, the only possible solution type of interest is S-S. Therefore, we have Conclusion 2.6:

Conclusion 2.6: *If the initial status of* U_l *and* U_r *satisfies*

$$u_l - u_r > \sqrt{\frac{\bar{p}_r}{\rho_r}}\sqrt{\frac{\bar{p}_l}{\bar{p}_r}-1}\sqrt{1-(\frac{\bar{p}_l}{\bar{p}_r})^{-1/\gamma_s}}\ , \tag{2.29}$$

then the solution type of Riemann problem (2.22) is a shock wave in water and a shock wave in solid (S-S).

Next, the performance of various GFM-based algorithms is discussed for this particular solution type.

(1) On the original GFM, to satisfy Condition (I), the only acceptable solution type of the GFM Riemann problem (2.23a) is S-S. Thus we have

$$u_l - u_r > \sqrt{\frac{\bar{p}_r}{\rho_r^G}}\sqrt{\frac{\bar{p}_l}{\bar{p}_r}-1}\sqrt{1-(\frac{\bar{p}_l}{\bar{p}_r})^{-1/\gamma_l}} > 0\,. \tag{2.30}$$

On the other hand, the GFM Riemann problem (2.23b) should have a solution of either R-S or S-S. If the following inequality (2.31a) is held,

$$\frac{2\bar{c}_l}{\gamma_l - 1}\left[(\frac{\bar{p}_r}{\bar{p}_l})^{\frac{\gamma_l-1}{2\gamma_l}}-1\right] < u_l - u_r < \sqrt{\frac{\bar{p}_r}{\rho_r^G}}\sqrt{\frac{\bar{p}_l}{\bar{p}_r}-1}\sqrt{1-(\frac{\bar{p}_l}{\bar{p}_r})^{-1/\gamma_s}}\ , \tag{2.31a}$$

then the solution type of (2.23b) is R-S, where ρ_r^G is the density of ghost fluid. Otherwise, if inequality (2.31b) is held

$$u_l - u_r > \sqrt{\frac{\bar{p}_r}{\rho_r^G}}\sqrt{\frac{\bar{p}_l}{\bar{p}_r}-1}\sqrt{1-(\frac{\bar{p}_l}{\bar{p}_r})^{-1/\gamma_s}}\ , \tag{2.31b}$$

the solution type of (2.23b) is S-S. Inequality (2.31a) is excluded due to (2.28) and (2.29). Therefore, the only acceptable solution type for (2.23b) is S-S. It is clearly shown that (2.31b) is always true due to inequality (2.29). But (2.30) may not be true in this case. Condition (I) is violated if following inequality (2.32) is held

$$0 < u_l - u_r < \sqrt{\frac{\overline{p}_r}{\rho_r^G}}\sqrt{\frac{\overline{p}_l}{\overline{p}_r} - 1}\sqrt{1 - (\frac{\overline{p}_l}{\overline{p}_r})^{-1/\gamma_l}} \,. \tag{2.32}$$

It has also been found that Condition (II) is difficult to be maintained because the EOS for water and solid are very stiff and the interface pressure and velocity predicted by the GFM Riemann problem (2.23a) are not close to those predicted by GFM Riemann problem (2.23b). Therefore, the original GFM is generally unable to obtain reasonable results for such water-solid flows.

(2) On the new version GFM, if $u_l > u_r$, Condition (I) can be easily fulfilled. It is interesting to find that Condition (II) is always violated in the application of the new version GFM for the present water-solid flows. For the GFM Riemann problem (2.23a) solved using the new version GFM, the interface velocity is

$$u_I = \frac{u_l + u_r}{2} < \max(u_l, u_r) \,. \tag{2.33}$$

On the other hand, for the GFM Riemann problem (2.23b), the interface velocity satisfies the following inequality

$$u_I > \max(u_l, u_r) \,. \tag{2.34}$$

The conflict or inconsistency between (2.33) and (2.34) leads to numerical errors incurred at the interface in the application of the new version GFM.

(3) On the MGFM and the present GFM, similar to gas-solid flows, numerical examples show that the MGFM is able to produce reasonable numerical results

compared to analytical results when a strong shock makes impact on the water-solid interface. Once again, the present GFM achieves the converged solution with much less time than the MGFM especially when the hydro-elasto-plastic EOS is employed for the solid medium. Case 2.6.2 is a (typical) water-solid (steel) flow where the present GFM computes much faster than the MGFM.

In next section, three numerical examples (2.6.11 to 2.6.13) will be calculated to compare the performance of four GFM-based algorithms for water-solid flows.

2.6 Numerical Examples

Various tests are implemented for the GFM-based algorithms as discussed in Section 2.4. The Euler equations are solved by MUSCL-type scheme with HLL approximate Riemann solver (Harten et al, 1983; Toro, 1997). A detailed discussion and analysis on this method can be found in (Toro, 1997). To ensure stable computation, the stability condition should satisfy

$$\Delta t = CFL \frac{\Delta x}{\max\left(|u_i| + c_i\right)}, \tag{2.35}$$

and the CFL number is taken to be between 0 and 1. It may be noted that actual numerical accuracy of the GFM-based algorithms may be different if other numerical schemes like ENO or WENO or otherwise are employed. Isentropic fix is employed for the various GFM-based algorithms. The numerical results may also depend on the different fix but it will not be discussed here. Whatsoever, the relative merit of a given numerical scheme for the different GFM-based algorithms stays generally true; difficulties arise primarily when one tries to compare the accuracy of a particular numerical scheme as applied to a given GFM-based algorithm to another numerical scheme employed in a different GFM-based algorithm. Below, the CFL number is set

to be 0.9 over 201 uniform mesh points in domain [0,1] for all the examples except for Cases 2.6.1 and 2.6.2 with CFL=0.8 over 101 uniform mesh points in domain [-5,5]. All the initial interface is located at 0.4 unless specially noted otherwise. γ_g is set to 1.4 while γ_l is set to be 7.15 and γ_s (β)is taken to be 3.7 for solid and steel. Other parameters for steel are shown in Table 2.1. All the parameters in the computation are non-dimensional.

Cases 2.6.1 and 2.6.2 are provided for validating the present GFM with comparing to the MGFM and analysis. The EOS for solid in these two cases is the Hydro-elasto-plastic EOS (EOSS3). Cases 2.6.3 to 2.6.13, where either Condition (I) or (II) is violated by the original GFM or new version GFM, are computed for further validation of the present GFM and verification of the analysis carried out on the gas-water flows in Section 2.5.1, gas-solid flows in Section 2.5.2 and water-solid flows in Section 2.5.3.

Case 2.6.1 (Gas-Steel). This case is taken from Tang and Sotiropoulos (1999) where a high pressurized air stream impact the stationary steel. The main parameters for the steel are shown in Table 2.1. The initial conditions are $u_l = 50.0$, $p_l = 10000.0$, $\rho_l = 0.05$; $u_r = 0.0$, $p_r = 1.0$, $\rho_r = 7.8$. Initial interface is located at 0.0. We ran the computation to a final time of 4.04×10^{-4} . Figures 2.4a, 2.4b and 2.4c show that the present GFM can obtain reasonable results when compared to the MGFM. This supports the analysis in Section 2.4.4 that the present GFM is able to predict the interface status even with 1st-order accuracy. For this case, the present GFM provides almost the same results as the MGFM. The present GFM also, with much less computational cost, produces very comparable results to the approximate Riemann solver developed by Tang and Sotiropoulos (1999).

Case 2.6.2 (Water-Steel). This case is also taken from Tang and Sotiropoulos (1999) where a high pressurized water stream impacts on steel at a very high velocity. The initial conditions are $u_l = 30.0$, $p_l = 25000.0$; $u_r = -30.0$, $p_r = 25.0$, $\rho_r = 7.80006$. Initial interface is located at 0.0. We ran the code to a time of 5.46×10^{-4}. In this case, there are two shock waves propagating in the steel, one is an elastic shock wave and the other is a plastic shock wave. Another shock wave is observed propagating in the water. The EOSS3 can capture both the elastic and plastic shock waves in the solid which is apparently different from the EOSS1 where only one wave is captured. It is clearly shown in Figs. 2.5a to 2.5c that the present GFM again provides very similar results to the MGFM. Once again, the present GFM needs less computation cost to achieve sufficient level of accuracy in contrast to the MGFM (Liu et al, 2003) and the approximate Riemann solver (Tang and Sotiropoulos, 1999).

Case 2.6.3 (Gas-Water). The solution type of this case is a rarefaction wave in gas and a shock wave in water. For this case, Condition (II) is violated by the original GFM and Condition (I) is violated by the new version GFM. Therefore, both the original GFM and new version GFM are unable to provide reasonable results. The initial conditions for this case are $u_l = 10.0$, $p_l = 1800.0$, $\rho_l = 0.2$; $u_r = 0.0$, $p_r = 1.0$, $\rho_r = 1.0$. We ran the computation to a final time of 2.0×10^{-3}. The results of MGFM and present GFM are provided for comparison to the analytical solution; no meaningful result is obtained via original or new version GFM (not shown). Figures 2.6a and 2.6b show that the velocity profile provided by the present GFM is quite close to the MGFM while there is a little difference at the position of the rarefaction wave in gas. Such observation supports the analysis that the present GFM is not as accurate as the MGFM if a strong rarefaction wave propagates in the gas

medium as mentioned in Section 2.4.4. Figure 2.6c and 2.6d provide similar pressure profiles for the MGFM and the present GFM.

Case 2.6.4 (Gas-Water). The solution type of this case is a shock wave in gas and a rarefaction wave in water. For this case, Condition (I) is violated by the new version GFM. Therefore, the new version GFM can not provide reasonable results The initial conditions are $u_l = 0.0$, $p_l = 1000.0$, $\rho_l = 0.5$; $u_r = 0.0$, $p_r = 2000.0$, $\rho_r = 1.076$. We ran the computation to a final time of 2.0×10^{-3}. In this case, the shock wave in gas and the rarefaction wave in water are captured well by both the MGFM and the present GFM as shown in Figs. 2.7a to 2.7d. Note that the original GFM is able to provide the correct GFM Riemann waves and thus reasonable results are also obtained for this case due to a large gas density comparable to the water density (Liu et al, 2005).

Case 2.6.5 (Gas-Water). The solution type of this case is a shock wave in gas and a shock wave in water. For this case, Condition (I) is violated by the original GFM and Condition (II) is violated by the new version GFM. Thus, both methods are unable to provide any meaningful results. The initial conditions are $u_l = 50.0$, $p_l = 1000.0$, $\rho_l = 0.5$; $u_r = 0.0$, $p_r = 1.0$, $\rho_r = 1.0$. We ran the computation to a final time of 2.0×10^{-3}. Similar pressure and velocity profiles are provided by the MGFM and the present GFM as shown in Figs. 2.8a to 2.8d.

Case 2.6.6 (Gas-Water). The solution type of this case is a rarefaction wave in gas and a rarefaction wave in water. Condition (I) is satisfied while Condition (II) is violated by the original GFM and Condition (II) is violated by the new version GFM. The initial conditions for this case are $u_l = -10.0$, $p_l = 8000.0$, $\rho_l = 1.2$; $u_r = 0.0$, $p_r = 8000.0$, $\rho_r = 1.199$. We ran the computation to a final time of 2.0×10^{-3}. The original GFM is unable to provide any meaningful results for this case

while pressure oscillations appear in the neighborhood of the rarefaction wave in the water when the new version GFM is used. It may be noted that a little pressure undershoot produced by the present GFM near the right rarefaction wave if we see closely into Fig. 2.9d, while it is still able to capture the rarefaction wave and provide a reasonable velocity profile when compared to the analytical solution and the MGFM.

Case 2.6.7 (Gas-Water). The solution type of this case is the same as Case 2.6.3. Condition (I) is violated by the original GFM and Condition (II) is violated by the new version GFM. The initial conditions are $u_l = -100.0$, $p_l = 8000.0$, $\rho_l = 1.2$; $u_r = 0.0$, $p_r = 1.0$, $\rho_r = 1.0$. The initial interface is located at 0.5. We ran the computation to a final time of 2.0×10^{-3}. This case is difficult for most of the GFM-based algorithms because a very strong rarefaction wave is propagating in the gas. A spurious cavitation is provided by the original GFM and the present GFM while a severe numerical inaccuracy is experienced by the new version GFM. The present GFM is also unable to provide any meaningful results because (2.19) is held and thus a negative interface pressure is produced. As mentioned in Section 2.5.2, such difficulty may arise because the numerical algorithm itself is unable to solve for a double rarefaction wave problem. It should be noted that such inapplicability may occur if solution type of (2.22) comprises a strong rarefaction wave and a wave (shock or rarefaction wave) connected by a discontinuity or two relatively strong rarefaction waves connected by a discontinuity. For such case, however, the MGFM is still able to provide a reasonable pressure and velocity profile as shown in Fig. 2.10a and 2.10b if a double rarefaction wave solver is incorporated into the MGFM as found in Liu et al (2005).

Case 2.6.8 (Gas-Solid). The solution type of this case is a rarefaction in gas and a shock wave in solid. Similar to Case 2.6.3, Condition (I) is violated by the original

GFM and Condition (II) is violated by the new version GFM. The initial conditions for this case are $u_l = -10.0$, $p_l = 1800.0$, $\rho_l = 0.2$; $u_r = 0.0$, $p_r = 1.0$, $\rho_r = 7.8$. We ran the computation to a final time of 5.0×10^{-4}. No meaningful result is provided by the original GFM while a pressure overshoot is found in Fig. 2.11a provided by the new version GFM. On the other hand, Figure 2.11c shows a reasonable pressure profile provided by the present GFM when compared to the analytical solution. A more accurate result is observed in Fig. 2.11b obtained from the MGFM due to higher order approximation to the exact Riemann problem solver than the present GFM when the interface singularity is decomposed in the first few steps of computation.

Case 2.6.9 (Gas-Solid). The solution type of this case is a shock wave in gas and a shock wave in solid. Condition (I) is violated by the original GFM and Condition (I) is satisfied but Condition (II) is violated by the new version GFM. The initial conditions for this case are $u_l = 20.0$, $p_l = 1800.0$, $\rho_l = 0.2$; $u_r = 0.0$, $p_r = 1.0$, $\rho_r = 7.8$. The computation is allowed to run to a final time of 5.0×10^{-4}. Once again, the original GFM is unable to produce any meaningful results due to large density difference across the interface, while the new version GFM provides an inaccurate shock location in the solid medium as shown in Fig. 2.12a. Both the MGFM and the present GFM compare reasonably with the analytical solution as shown in Fig. 2.12b and 2.12c although the MGFM shows better concurrence.

Case 2.6.10 (Gas-Solid). The solution type of this case is a rarefaction wave in gas and a rarefaction wave in solid. Condition (I) is satisfied and Condition (II) is violated by the original GFM while Condition (II) is violated by the new version GFM. The initial conditions for this case are $u_l = -10.0$, $p_l = 8000.0$, $\rho_l = 1.2$; $u_r = 0.0$, $p_r = 8000.0$. The computation is allowed to run to a final time of 1.0×10^{-3}.

The original GFM is still unable to provide an acceptable pressure profile for this case. Also, a severe inaccuracy of the rarefaction wave location produced by the new version GFM is observed in Fig. 2.13a. The MGFM with a double rarefaction wave solver is able to provide a very reasonable pressure profile. The present GFM, however, produces a pressure undershoot near the rarefaction wave in solid even if a double rarefaction wave solver is incorporated.

Case 2.6.11 (Water-Solid). This is a case where a water stream is impacting a stationary solid. For such a case, if (2.28) is held, the solution type is always a shock wave in water and a shock wave in solid. The initial conditions for this case are $u_l = 10.0$, $p_l = 2000.0$; $u_r = 0.0$, $p_r = 1.0$, $\rho_r = 7.8$. The computation is allowed to run to a final time of 5.0×10^{-3}. Condition (I) is violated by the original GFM due to upholding of (2.32) while Condition (II) is violated by the new version GFM. No meaningful results are provided by the original GFM due to severe oscillations in the computation. Such oscillations in water-solid flows are much more severe than those in gas-water or gas-solid flows because the EOS for water and solid are much stiffer such that the magnitude of pressure oscillation is very quickly magnified. On the other hand, Condition (II) is generally violated by the new version GFM for this case due to the incompatibility of (2.33) and (2.34). An unacceptable shock location in solid is produced by the new version GFM as shown in Fig. 2.14a while Figs. 2.14b and 2.14c show that the MGFM and the present GFM are both able to provide reasonable pressure profile when compared to the analytical solution.

Case 2.6.12 (Water-Solid). The solution type is also a shock wave in water and a shock wave in solid. The initial conditions for this case are $u_l = 10.0$, $p_l = 1000.0$; $u_r = 0.0$, $p_r = 1.0$, $\rho_r = 7.8$. The computation is allowed to run to a final time of

5.0×10^{-3}. Condition (I) is satisfied and Condition (II) is violated by the original GFM while Condition (II) is violated by the new version GFM. Similar to Case 2.6.11, no meaningful results are provided by the original GFM due to severe oscillations in the computation. Figure 2.15a shows that the shock location in the solid medium provided by the new version GFM is always lagging. The present GFM is still able to produce reasonable results with a little dissipation at the region of the shock in solid as shown in Fig. 2.15c while Fig. 2.15b shows that the MGFM provides the closest pressure profile to the analytical solution.

Case 2.6.13 (Water-Solid). This is a case where both water and solid are impacting each other at a very high speed. The solution type is a shock wave in water and a shock wave in solid. The initial conditions for this case are $u_l = 50.0$, $p_l = 25000.0$; $u_r = -5.0$, $p_r = 25.0$, $\rho_r = 7.800088$. The computation is allowed to run to a final time of 5.0×10^{-3}. Condition (I) and Condition (II) are satisfied by the original GFM because (2.30) and (2.31b) are upheld simultaneously while Condition (II) is violated by the new version GFM. It is found that the interface pressure and velocity calculated by (2.23a) and (2.23b) are relatively close to each other. That is why the original GFM is able to provide acceptable result as shown in Fig. 2.16a. The new version GFM however leads to a lagging shock location in solid as shown in Fig. 2.16b. It is shown in Fig. 2.16c that the pressure profile provided by the MGFM is quite comparable to the analytical results. Also, the pressure profile produced by the present GFM in Fig. 2.16b is in substantial agreement with the MGFM and the analytical solutions.

2.7 Summary for Chapter 2

In this chapter, various GFM-based algorithms are introduced and analyzed briefly for gas-water and gas-solid flows. A detailed analysis on water-solid flows is also

carried out for application of each GFM-based algorithm. Based on the two conditions proposed by Liu et al (2005), it has been found that there is a range of applicability where the original GFM and the new version GFM are unable to provide reasonable results, while the MGFM with a double shock wave solver is robust for all the challenging numerical examples presented in this chapter. The MGFM consists of two parts: one is the approximate Riemann problem solver for predicting the interface status where the iteration solver is needed and the other is to define the ghost status using predicted interface status. To reduce the computational cost, an explicit characteristic method (the present GFM) is proposed to replace the MGFM. The advantage and limitation of the present GFM are analyzed and then various numerical examples are calculated using various GFM-based algorithms for further comparison and verification of the present GFM. It is clearly shown that the present GFM is able to provide reasonable results for most of problems when compared to the MGFM and analytical solutions. It is also found that the present GFM is inapplicable for the problems where the solution type comprises two rarefaction wave connected by a discontinuity or a strong rarefaction wave and a shock wave connected by a discontinuity. Such inapplicability is due to the negative interface pressure predicted by the present GFM. It may be noted that both the MGFM and the present GFM can successfully simulate the water-solid flows with high pressure on the water side while the original GFM and the new version GFM meet severe difficulties for such problems.

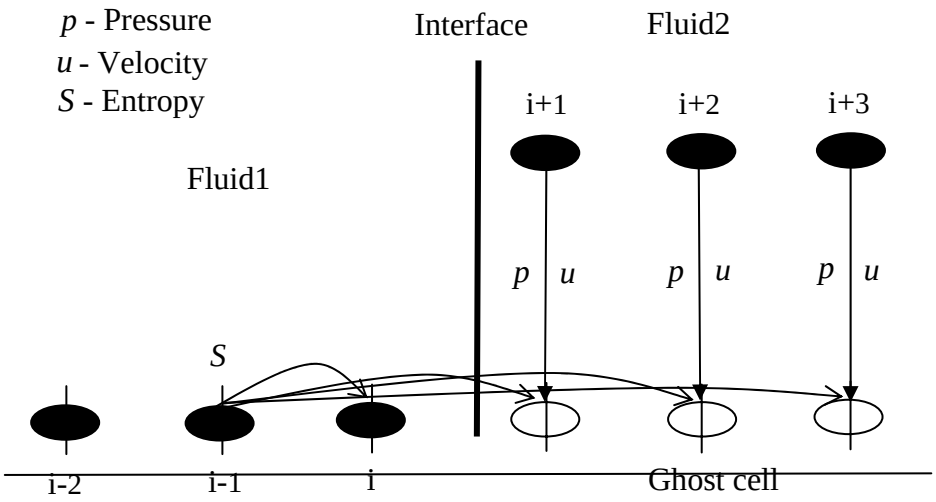

Fig. 2.1 Isobaric fix for the ghost fluid method (the original GFM).

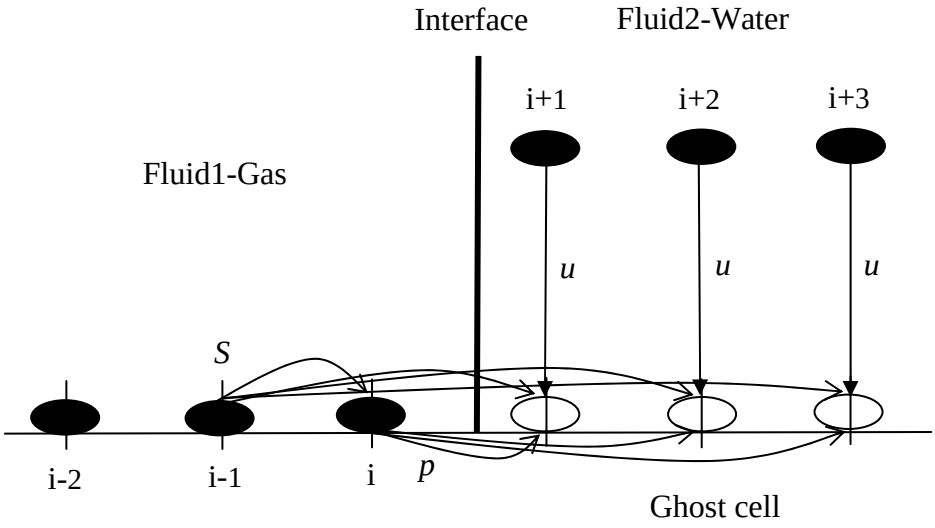

Fig. 2.2a Ghost fluid status for the new version ghost fluid method (Fluid1).

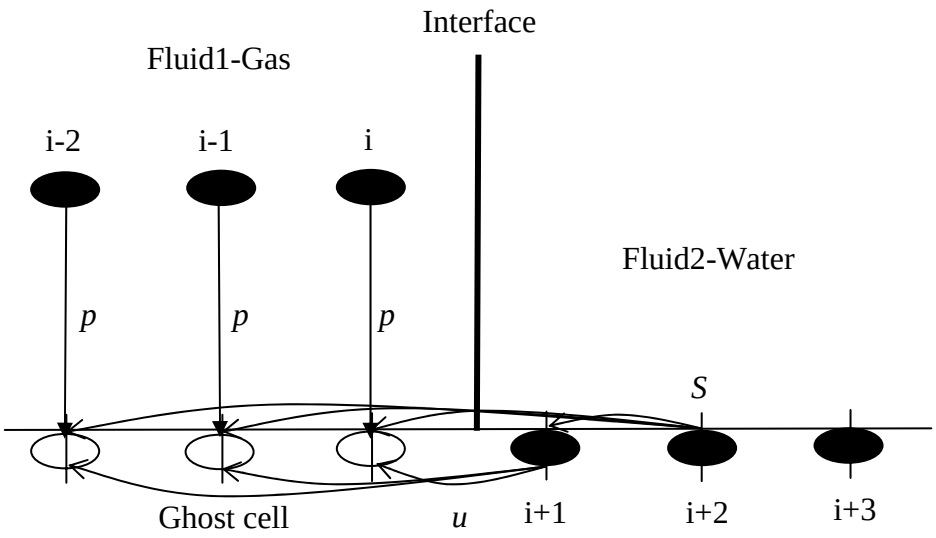

Fig. 2.2b Ghost fluid status for the new version ghost fluid method (Fluid2).

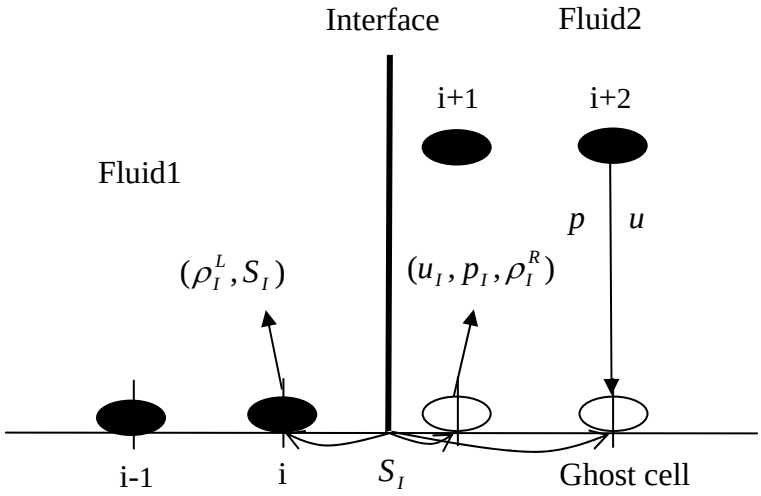

Fig. 2.3 Isentropic fix for the modified ghost fluid method (the MGFM).

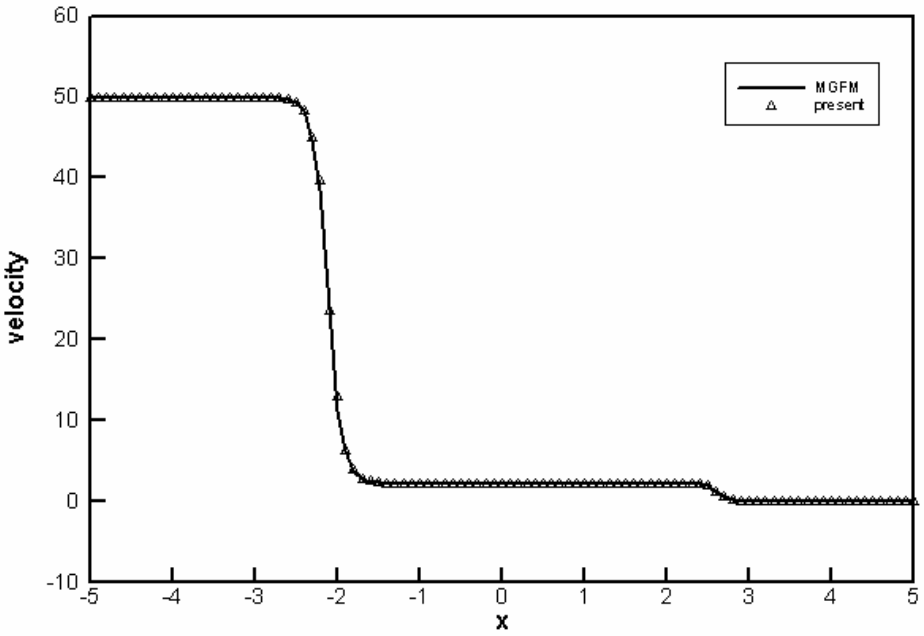

Fig. 2.4a Velocity profile for Case 2.6.1 by the MGFM and the present GFM.

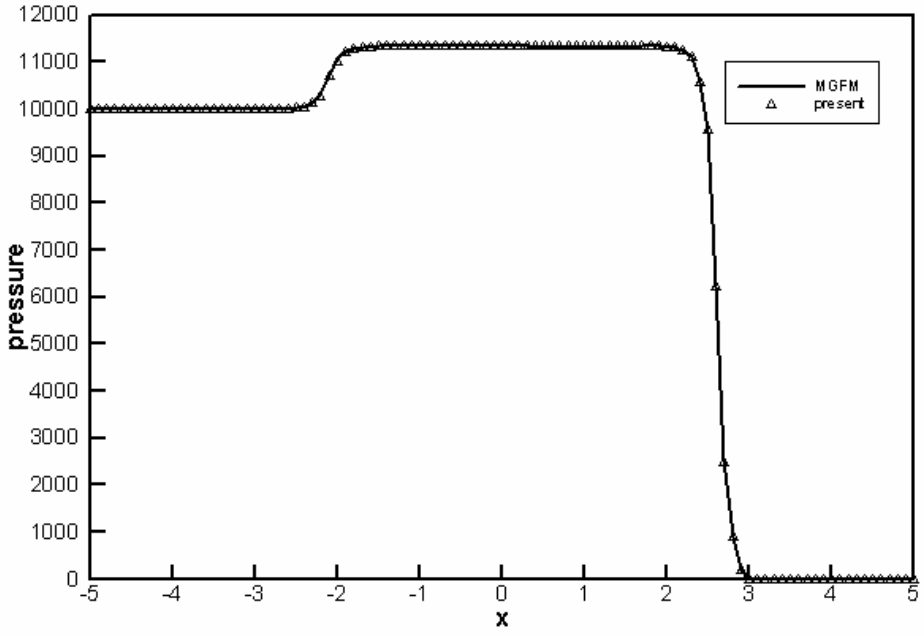

Fig. 2.4b Pressure profile for Case 2.6.1 by the MGFM and the present GFM.

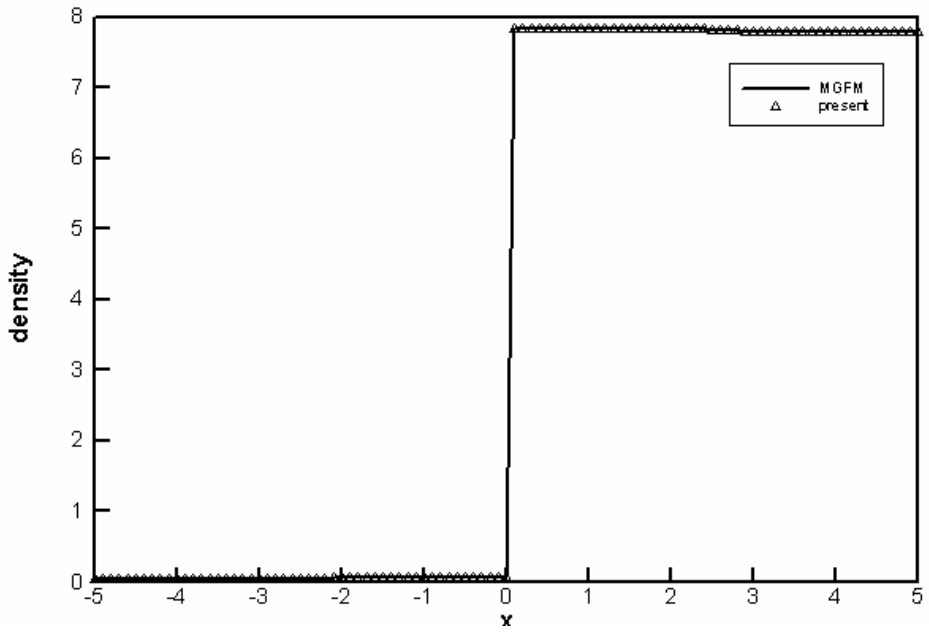

Fig. 2.4c Density profile for Case 2.6.1 by the MGFM and the present GFM.

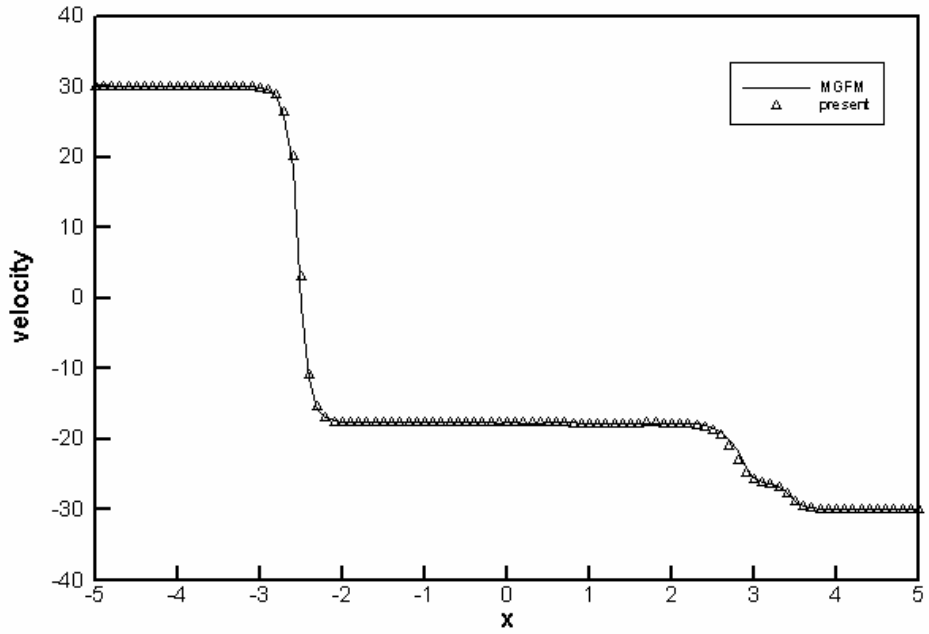

Fig. 2.5a Velocity profile for Case 2.6.2 by the MGFM and the present GFM.

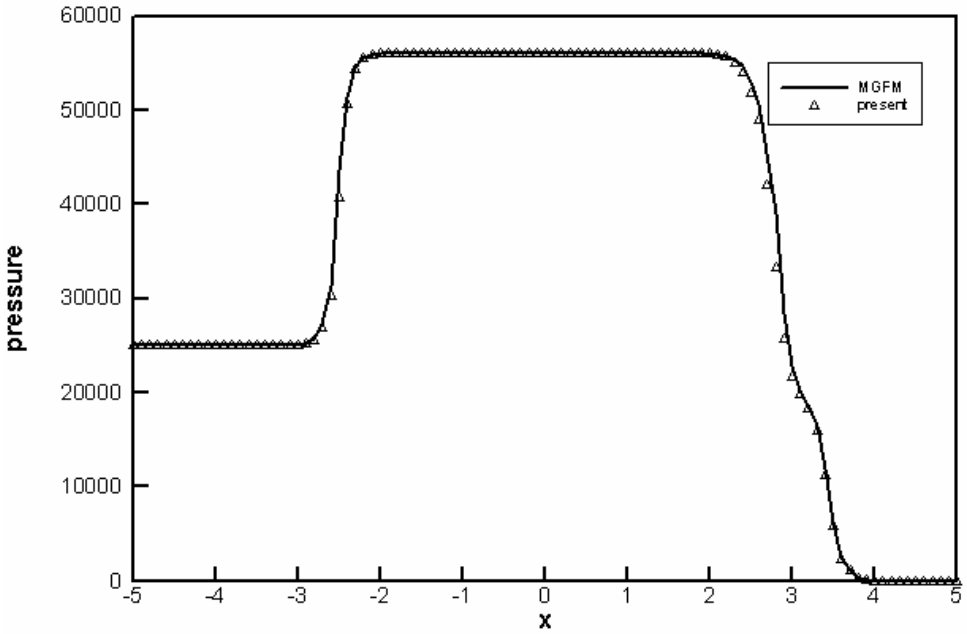

Fig. 2.5b Pressure profile for Case 2.6.2 by the MGFM and the present GFM.

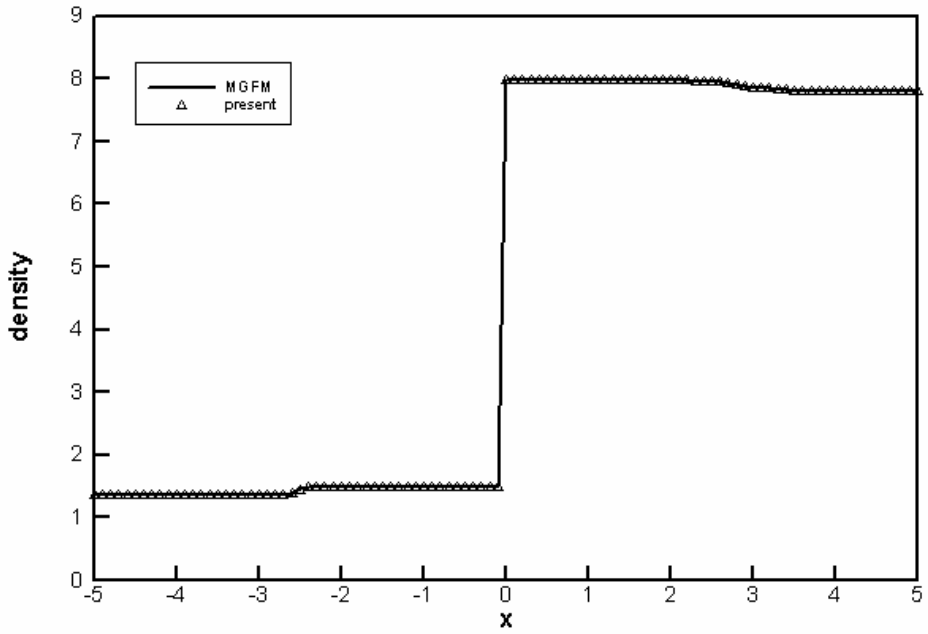

Fig. 2.5c Density profile for Case 2.6.2 by the MGFM and the present GFM.

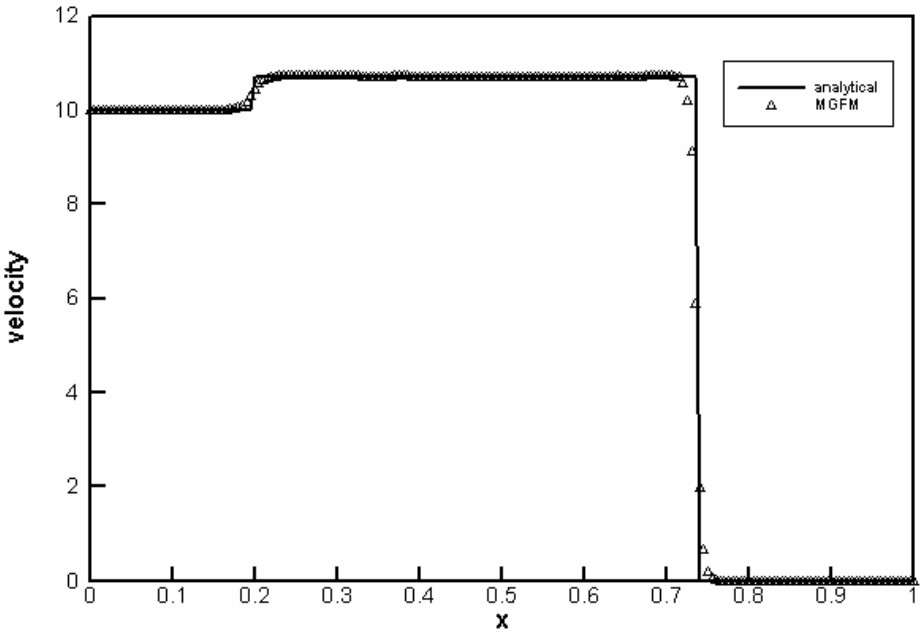

Fig. 2.6a Velocity profile for Case 2.6.3 by the MGFM.

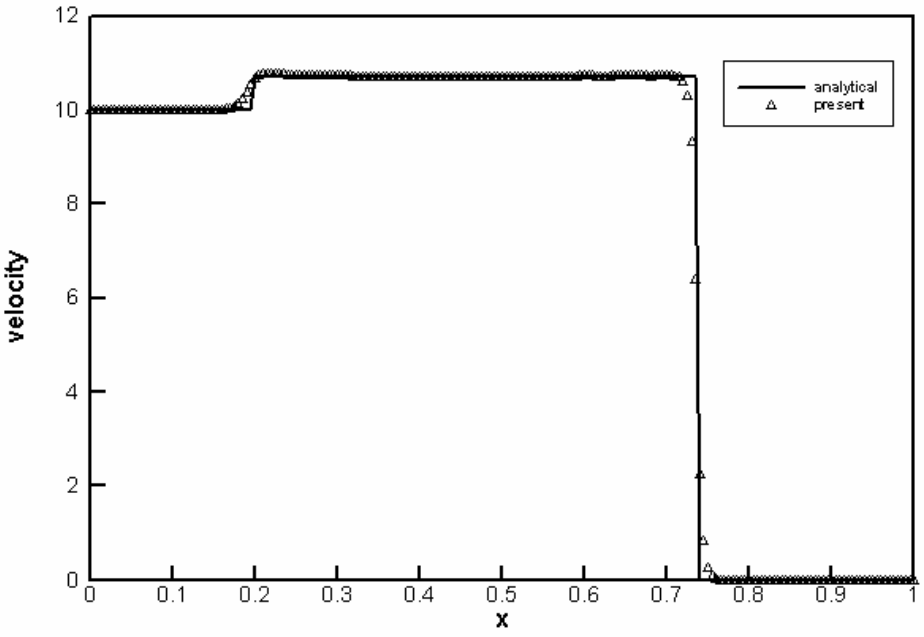

Fig. 2.6b Velocity profile for Case 2.6.3 by the present GFM.

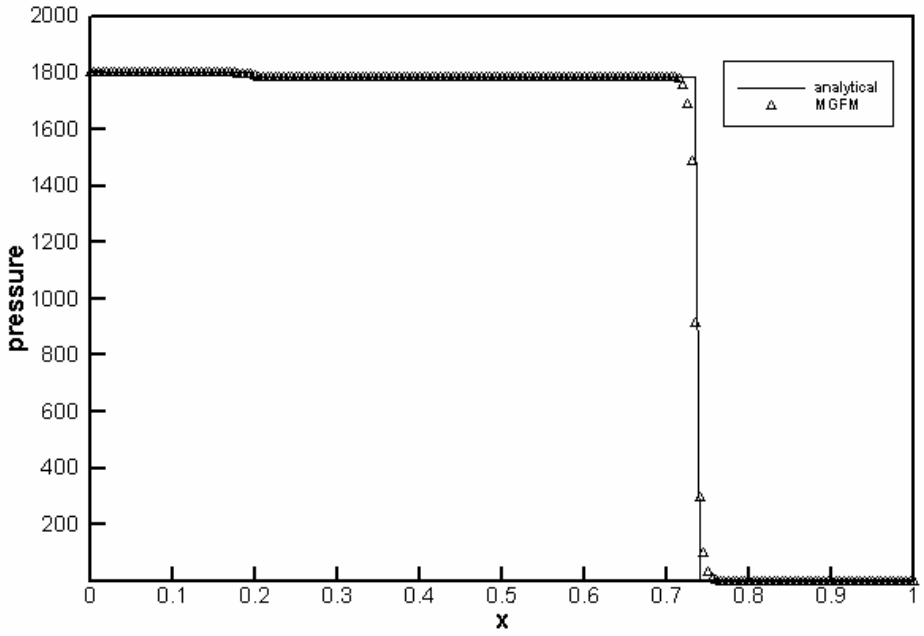

Fig. 2.6c Pressure profile for Case 2.6.3 by the MGFM.

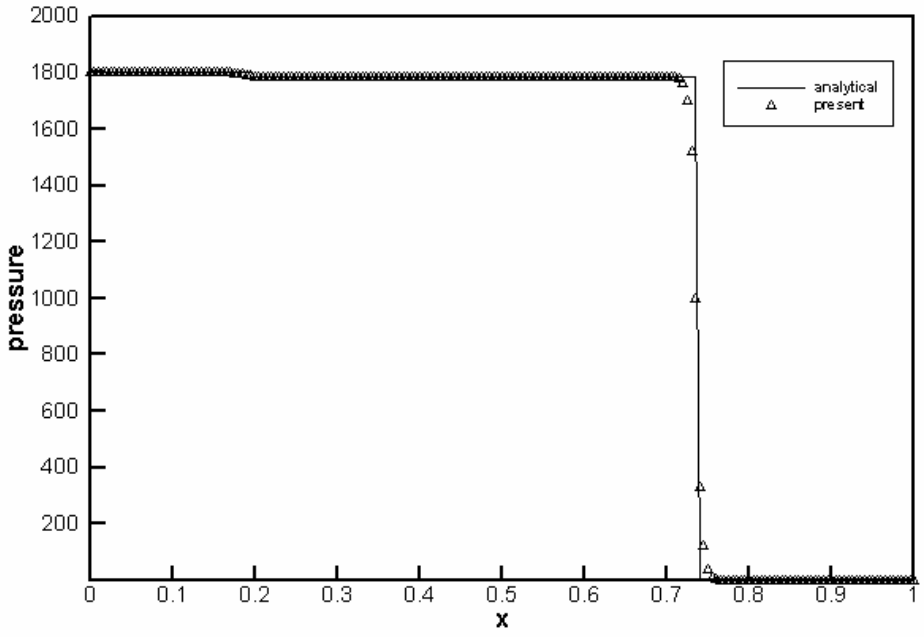

Fig. 2.6d Pressure profile for Case 2.6.3 by the present GFM.

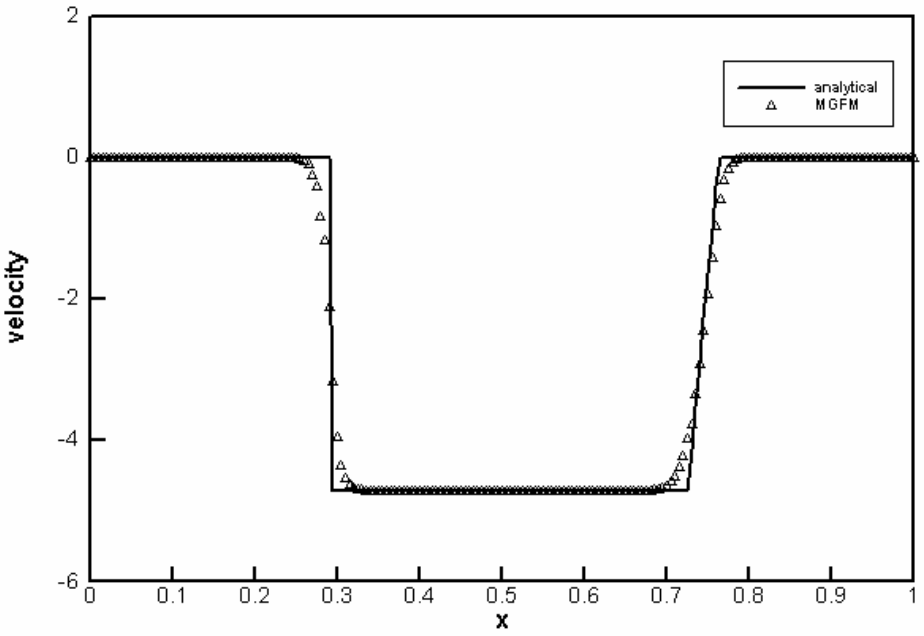

Fig. 2.7a Velocity profile for Case 2.6.4 by the MGFM.

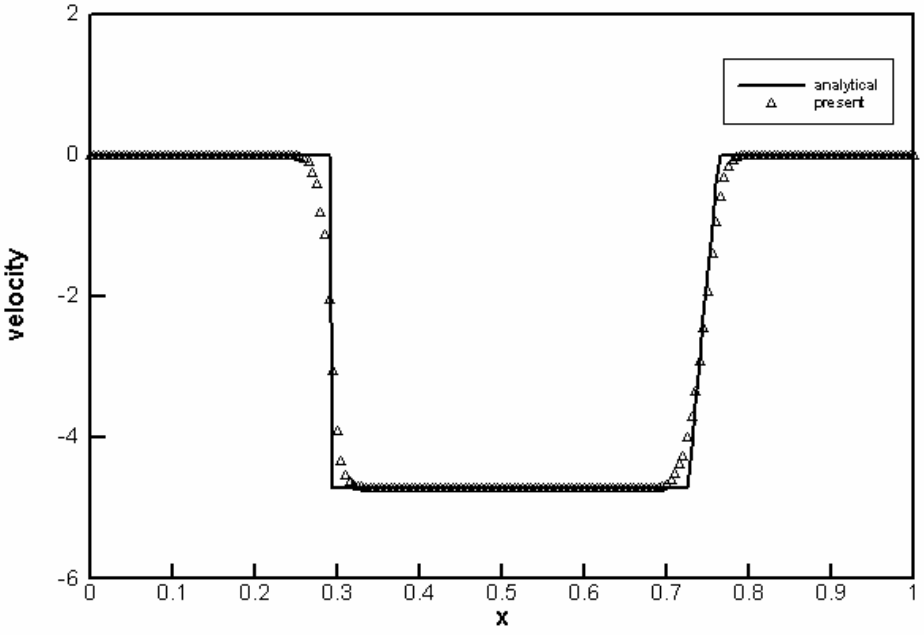

Fig. 2.7b Velocity profile for Case 2.6.4 by the present GFM.

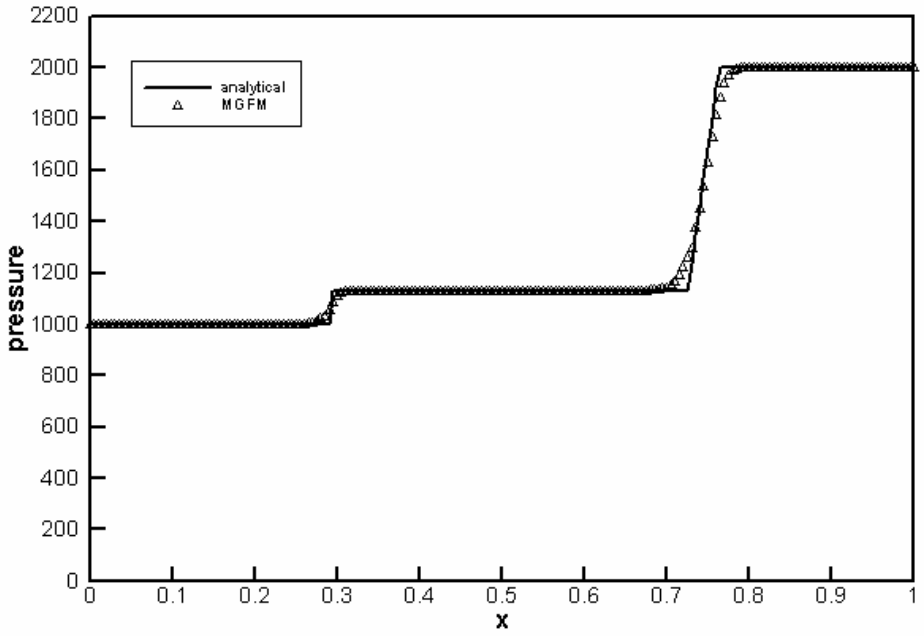

Fig. 2.7c Pressure profile for Case 2.6.4 by the MGFM.

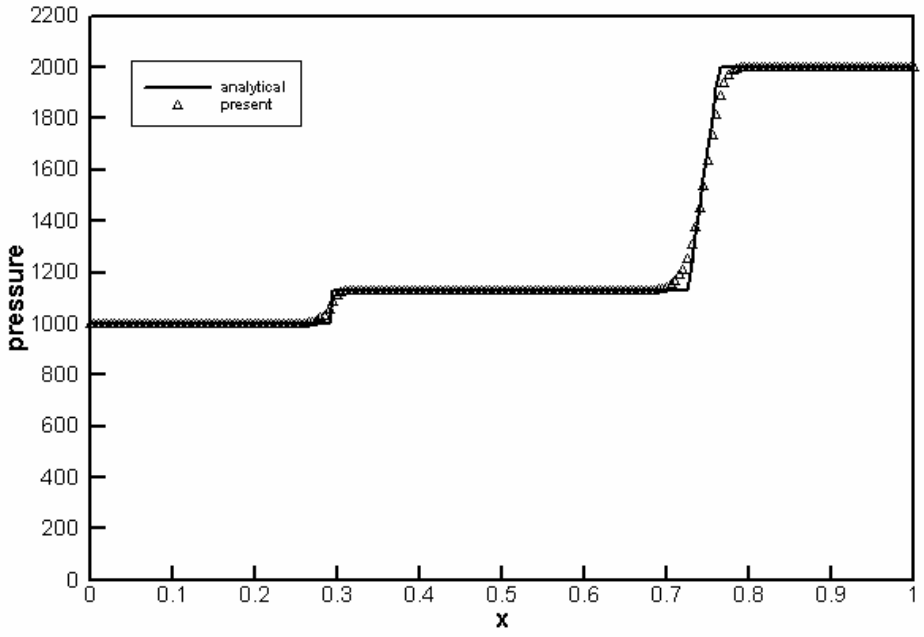

Fig. 2.7d Pressure profile for Case 2.6.4 by the present GFM.

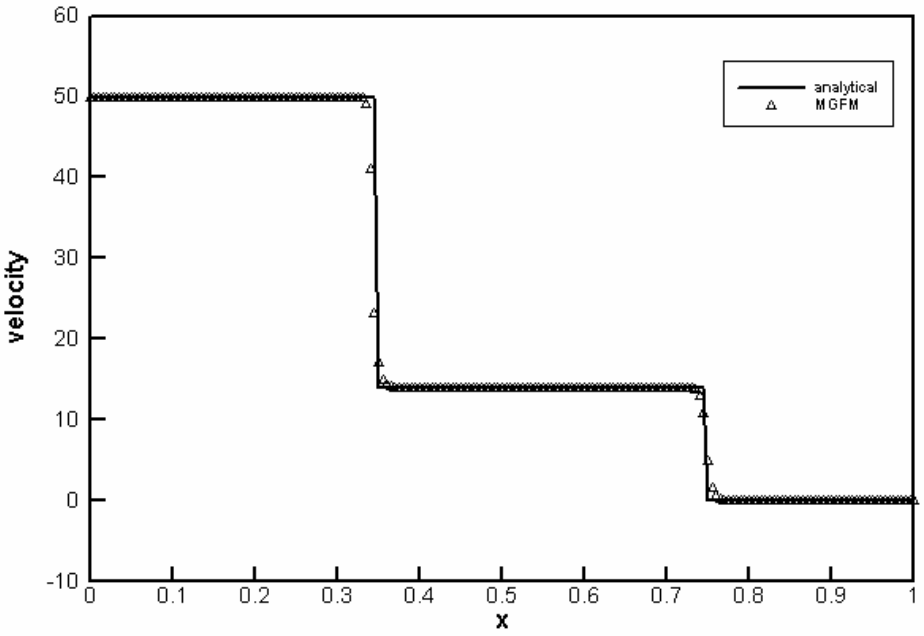

Fig. 2.8a Velocity profile for Case 2.6.5 by the MGFM.

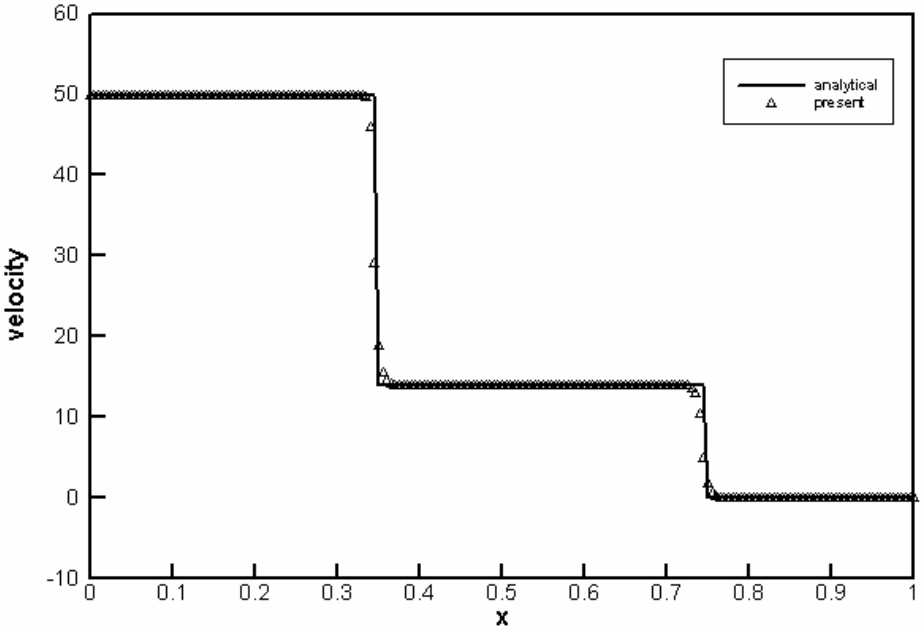

Fig. 2.8b Velocity profile for Case 2.6.5 by the present GFM.

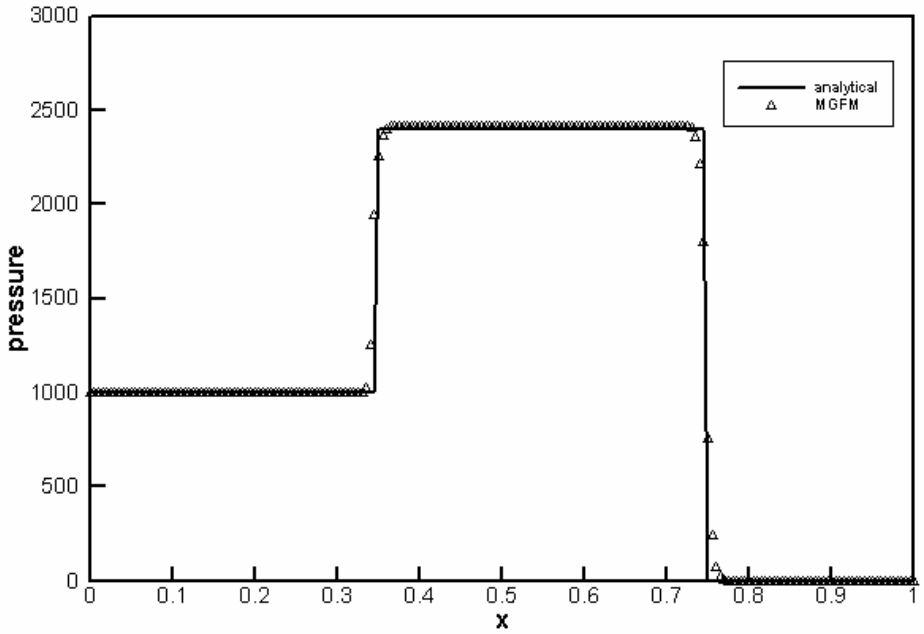

Fig. 2.8c Pressure profile for Case 2.6.5 by the MGFM.

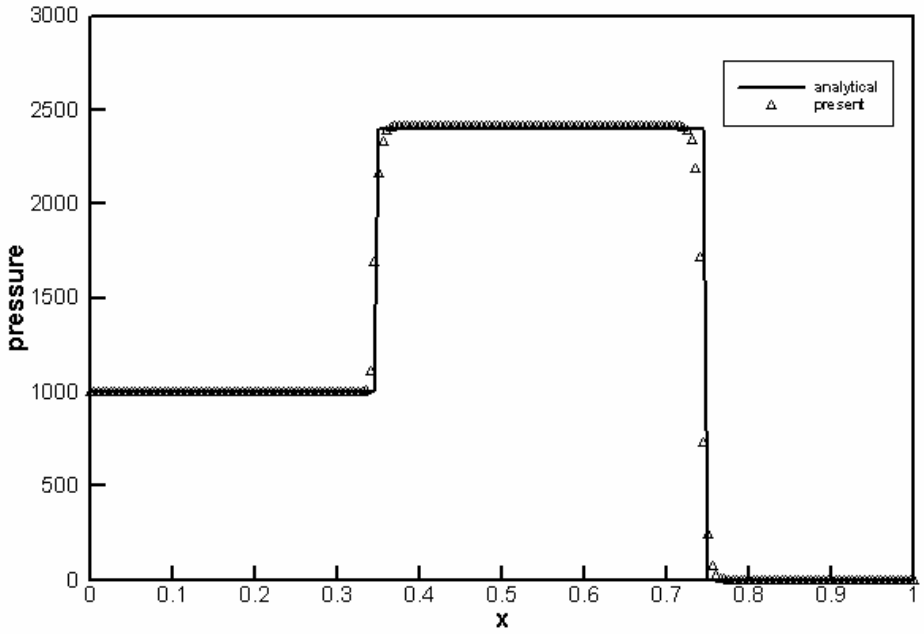

Fig. 2.8d Pressure profile for Case 2.6.5 by the present GFM.

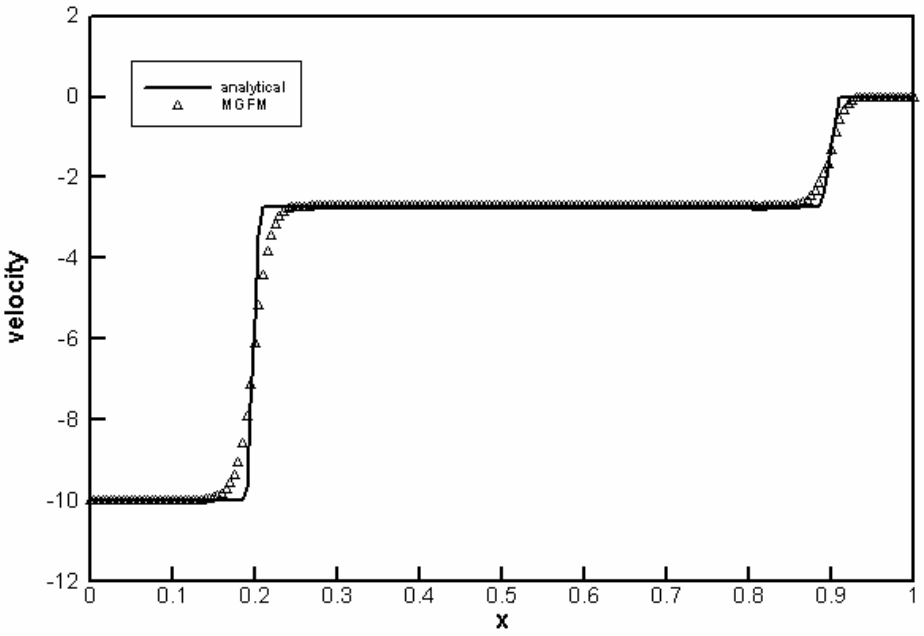

Fig. 2.9a Velocity profile for Case 2.6.6 by the MGFM.

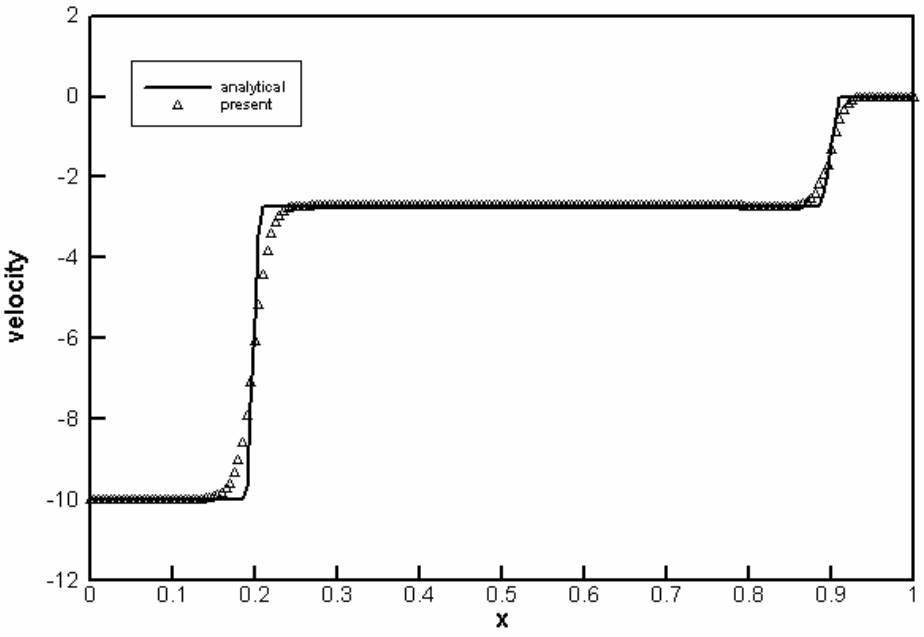

Fig. 2.9b Velocity profile for Case 2.6.6 by the present GFM.

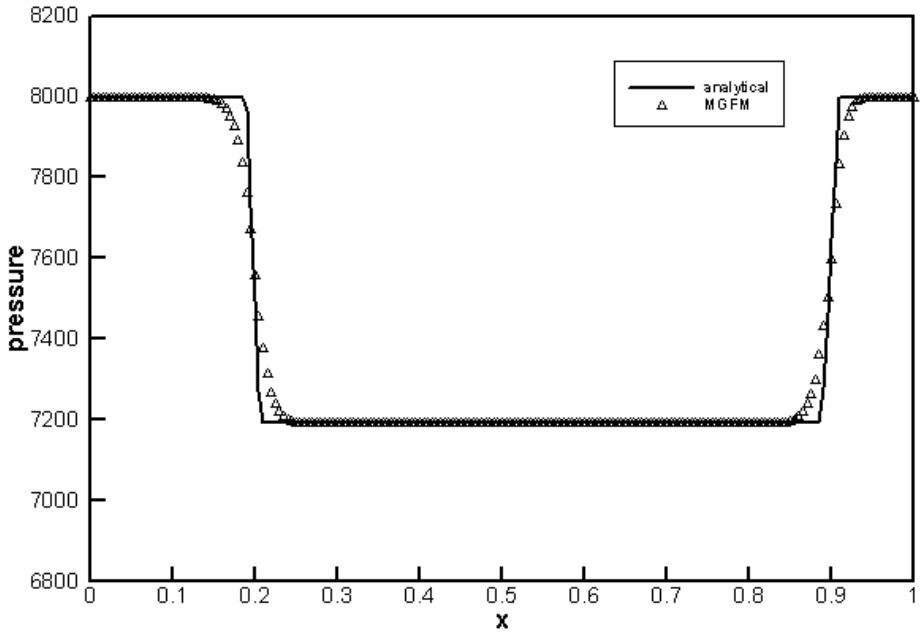

Fig. 2.9c Pressure profile for Case 2.6.6 by the MGFM.

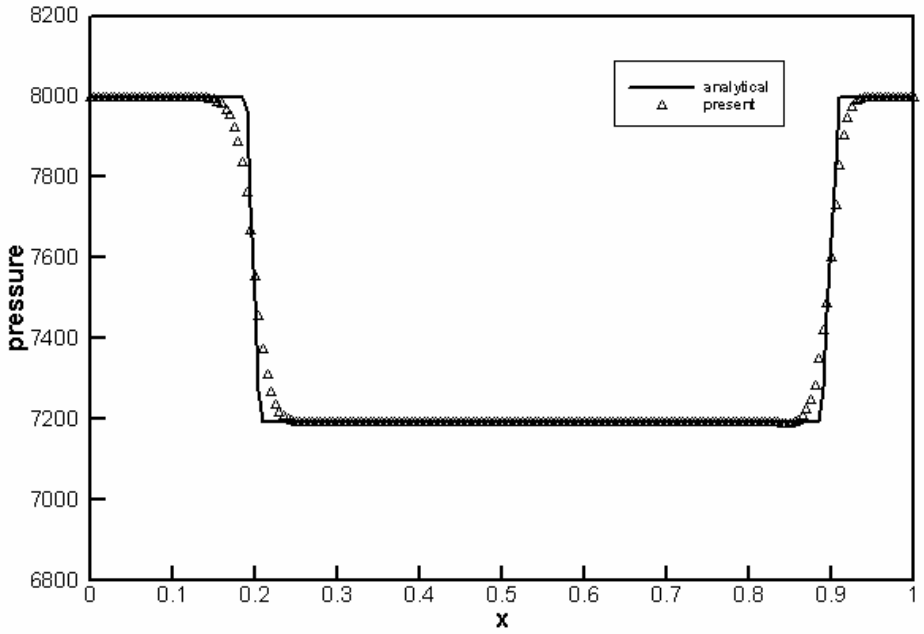

Fig. 2.9d Pressure profile for Case 2.6.6 by the present GFM.

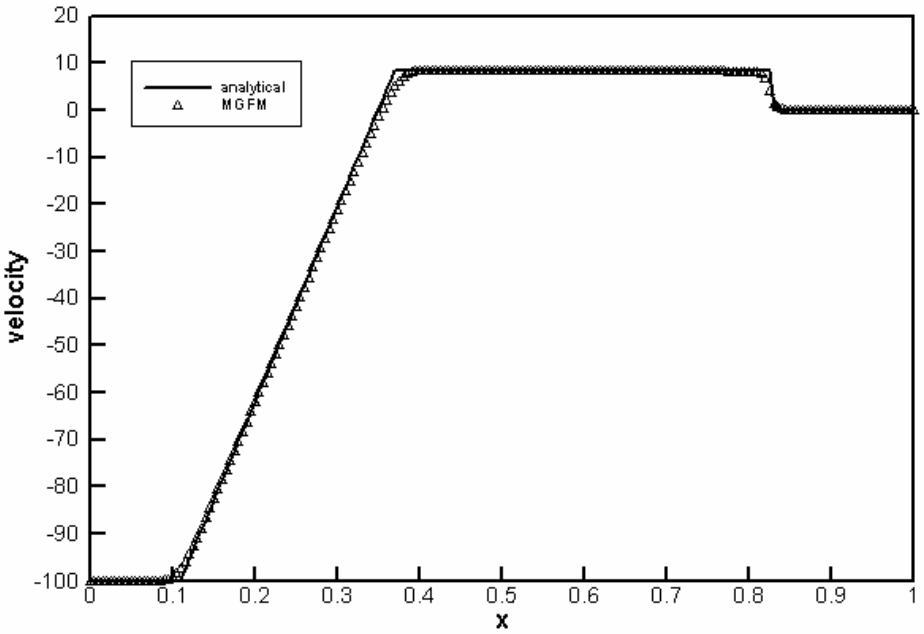

Fig. 2.10a Velocity profile for Case 2.6.7 by the MGFM.

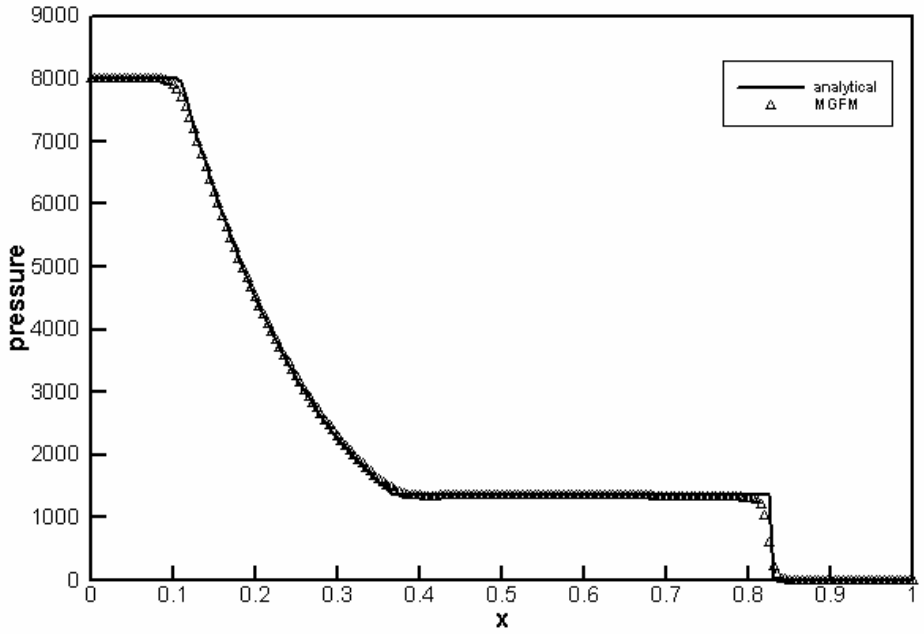

Fig. 2.10b Pressure profile for Case 2.6.7 by the MGFM.

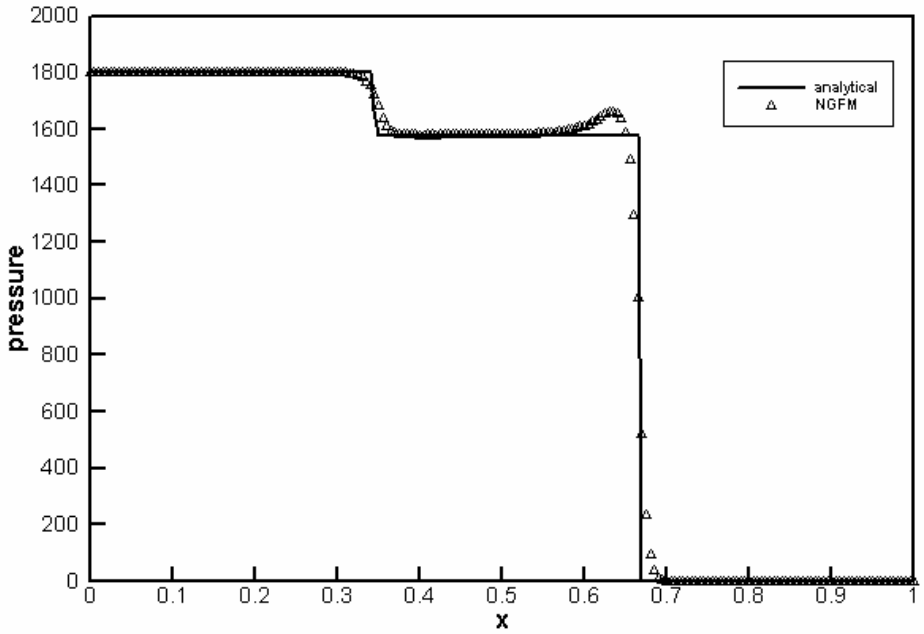

Fig. 2.11a Pressure profile for Case 2.6.8 by the new version GFM.

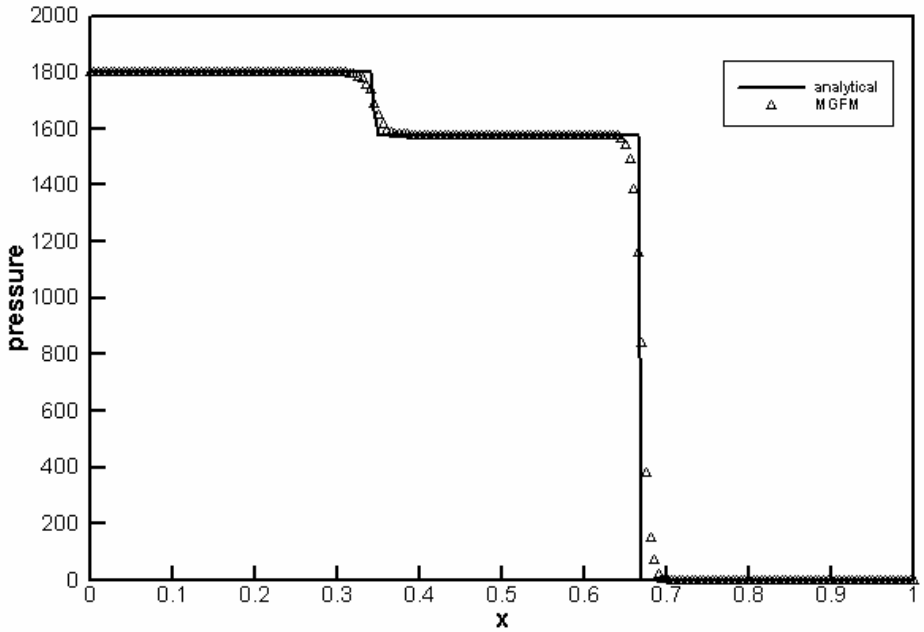

Fig. 2.11b Pressure profile for Case 2.6.8 by the MGFM.

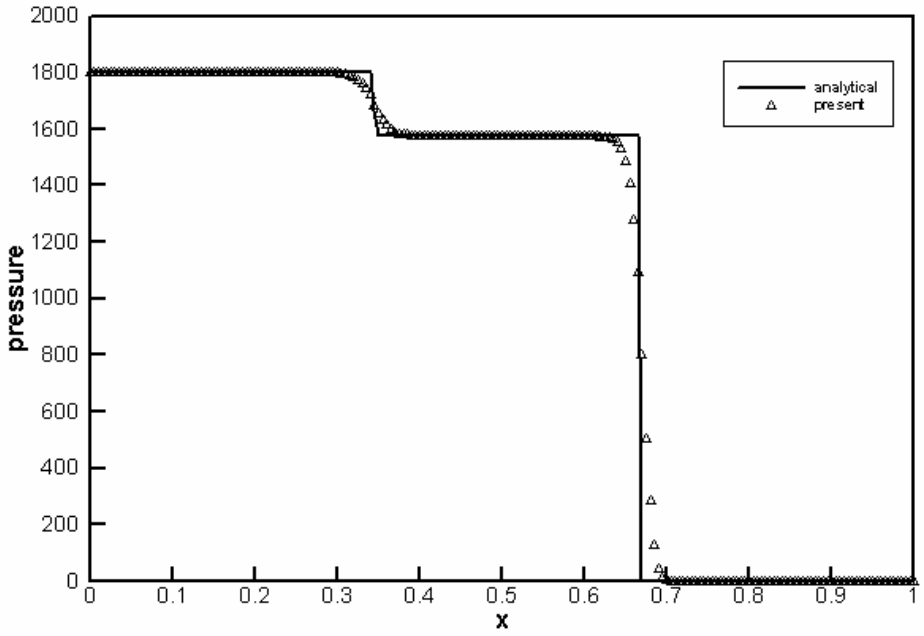

Fig. 2.11c Pressure profile for Case 2.6.8 by the present GFM.

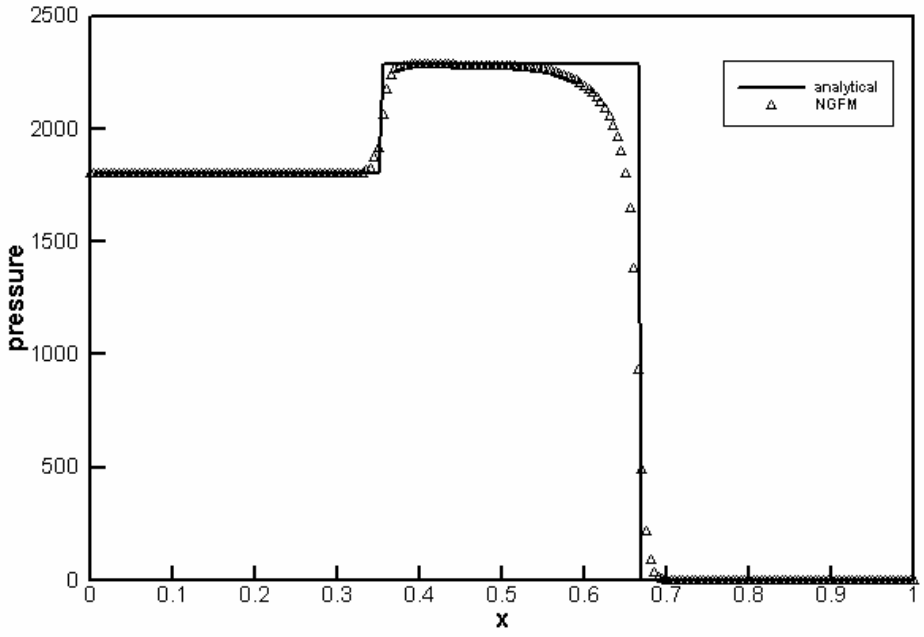

Fig. 2.12a Pressure profile for Case 2.6.9 by the new version GFM.

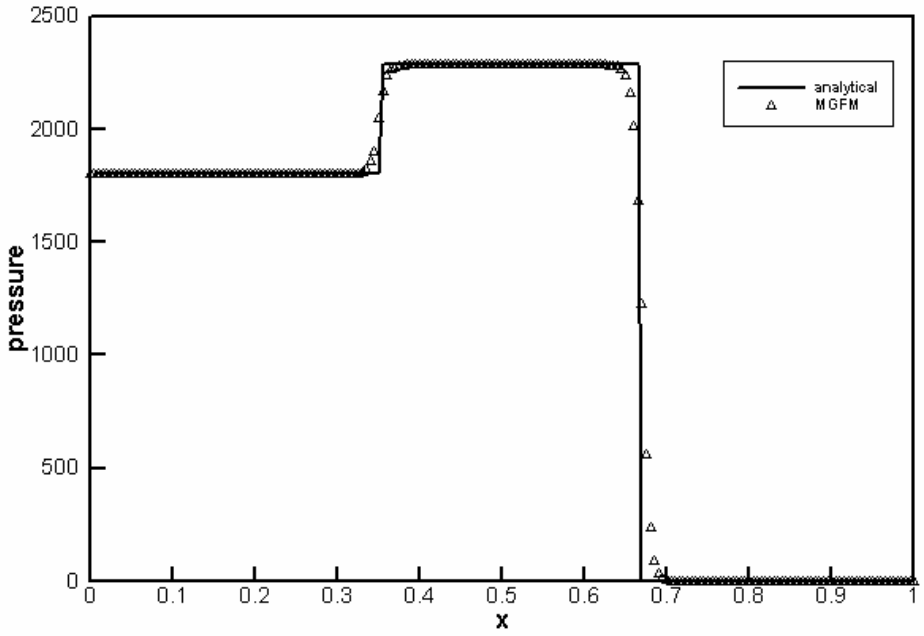

Fig. 2.12b Pressure profile for Case 2.6.9 by the MGFM.

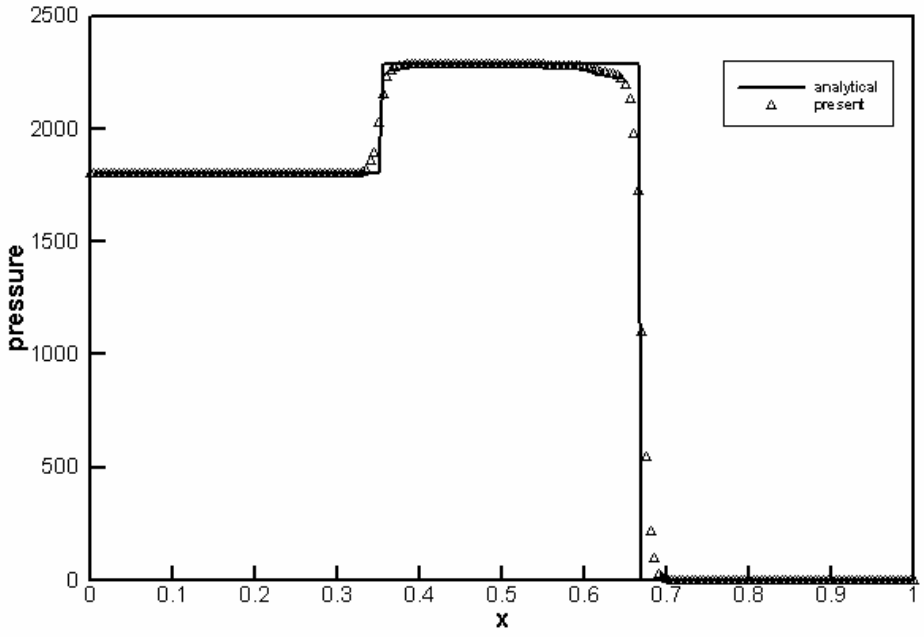

Fig. 2.12c Pressure profile for Case 2.6.9 by the present GFM.

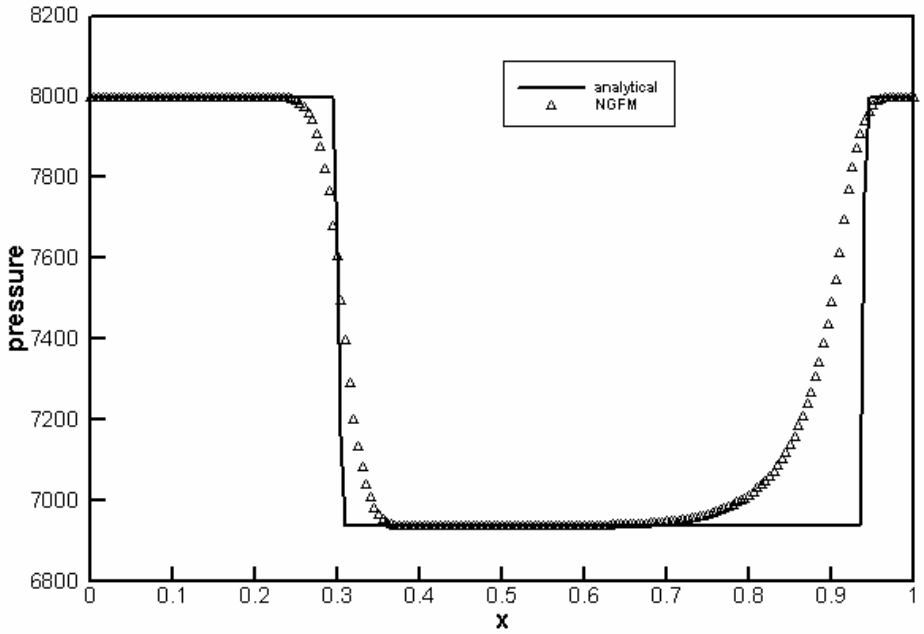

Fig. 2.13a Pressure profile for Case 2.6.10 by the new version GFM.

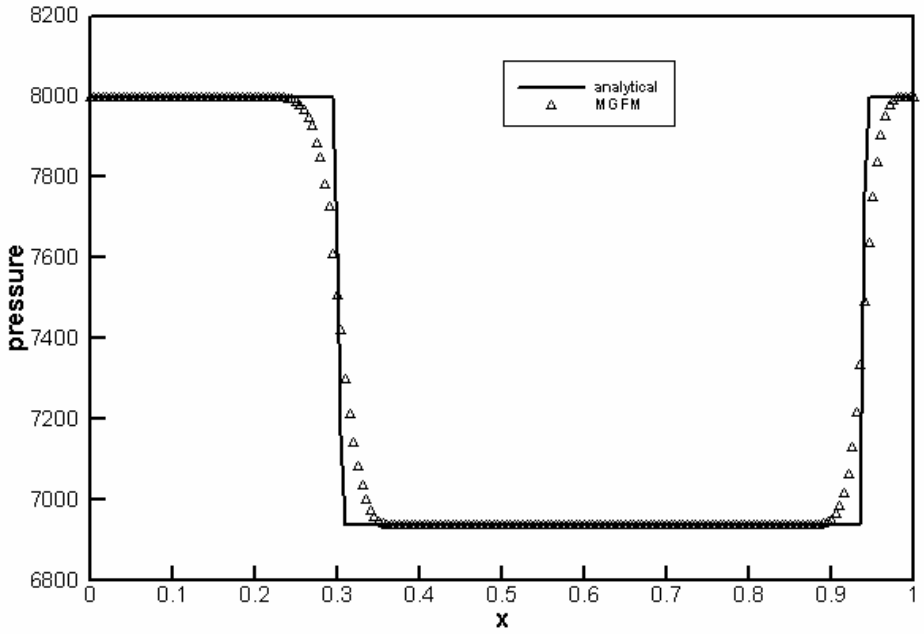

Fig. 2.13b Pressure profile for Case 2.6.10 by the MGFM.

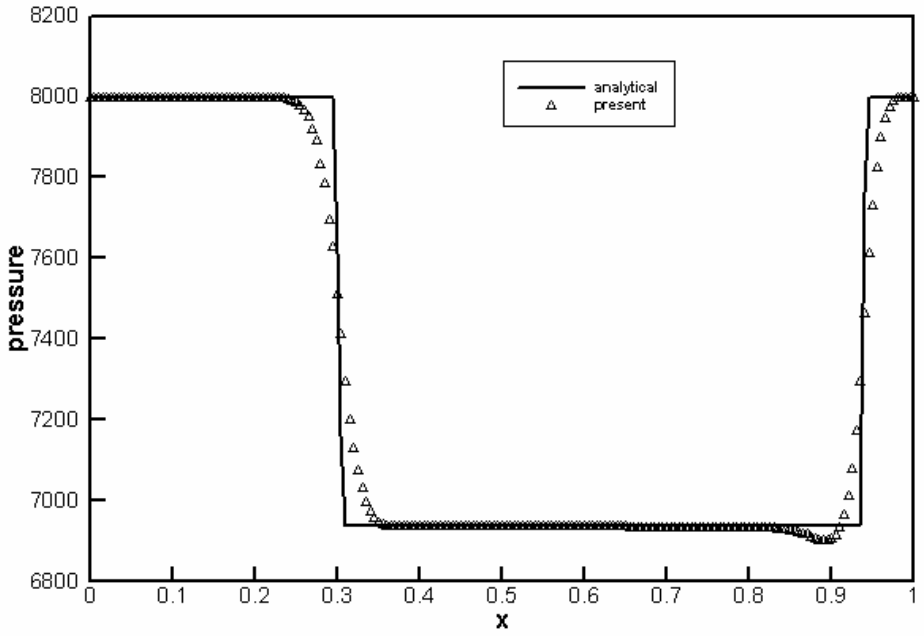

Fig. 2.13c Pressure profile for Case 2.6.10 by the present GFM.

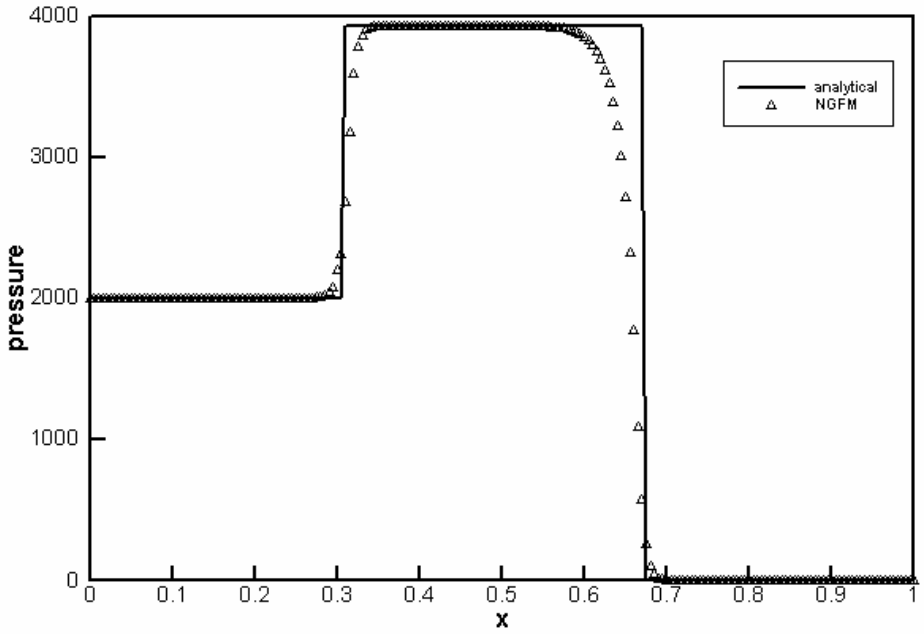

Fig. 2.14a Pressure profile for Case 2.6.11 by the new version GFM.

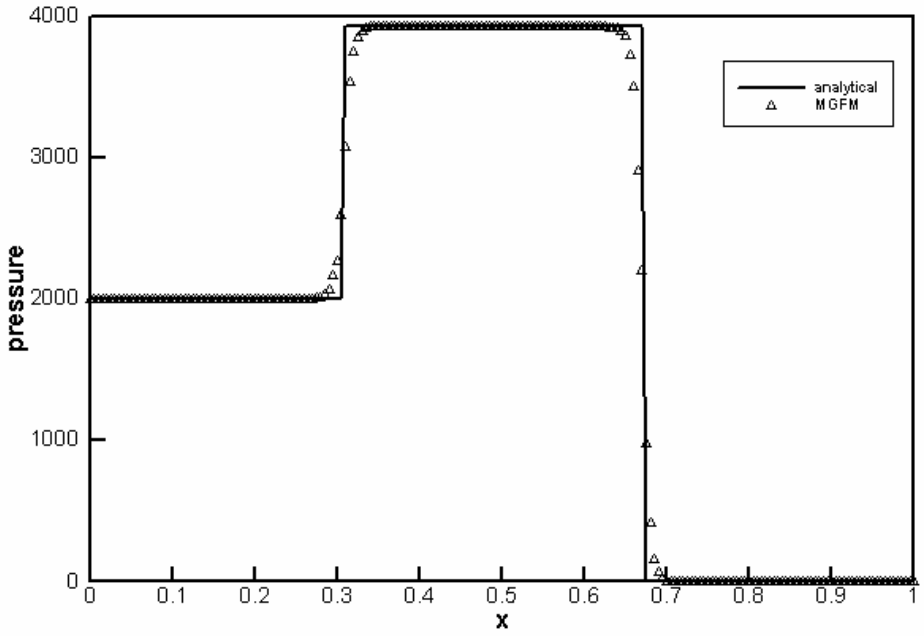

Fig. 2.14b Pressure profile for Case 2.6.11 by the MGFM.

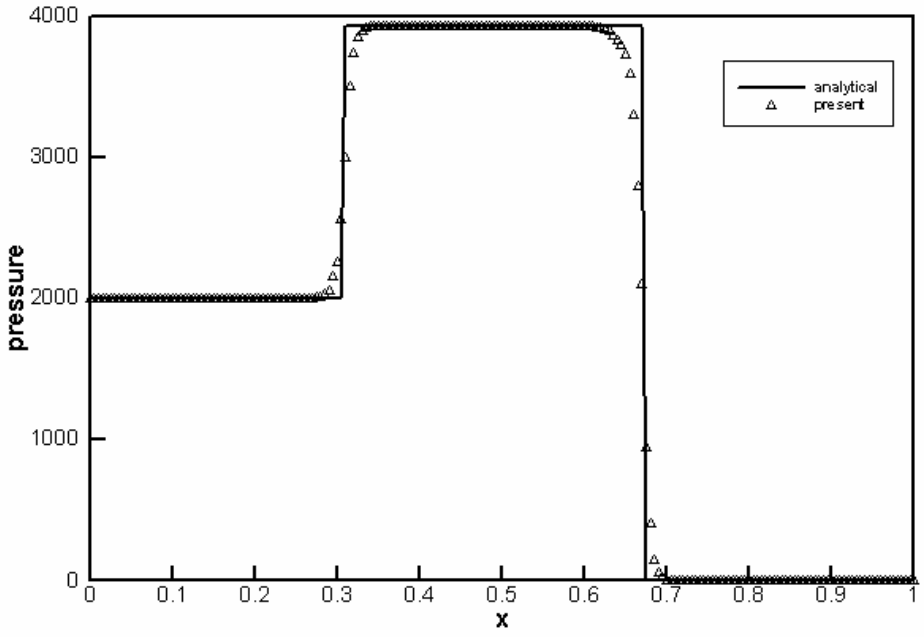

Fig. 2.14c Pressure profile for Case 2.6.11 by the present GFM.

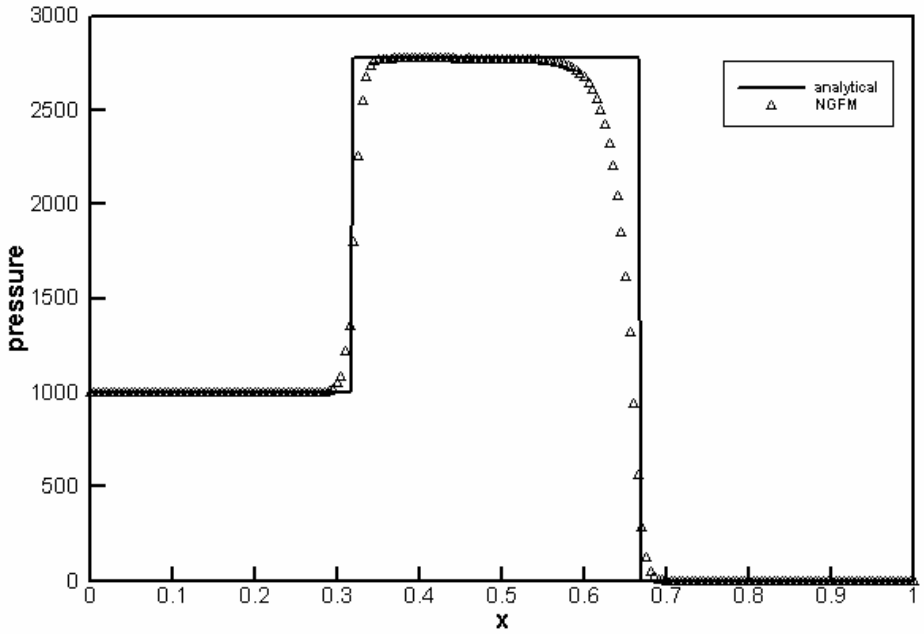

Fig. 2.15a Pressure profile for Case 2.6.12 by the new version GFM.

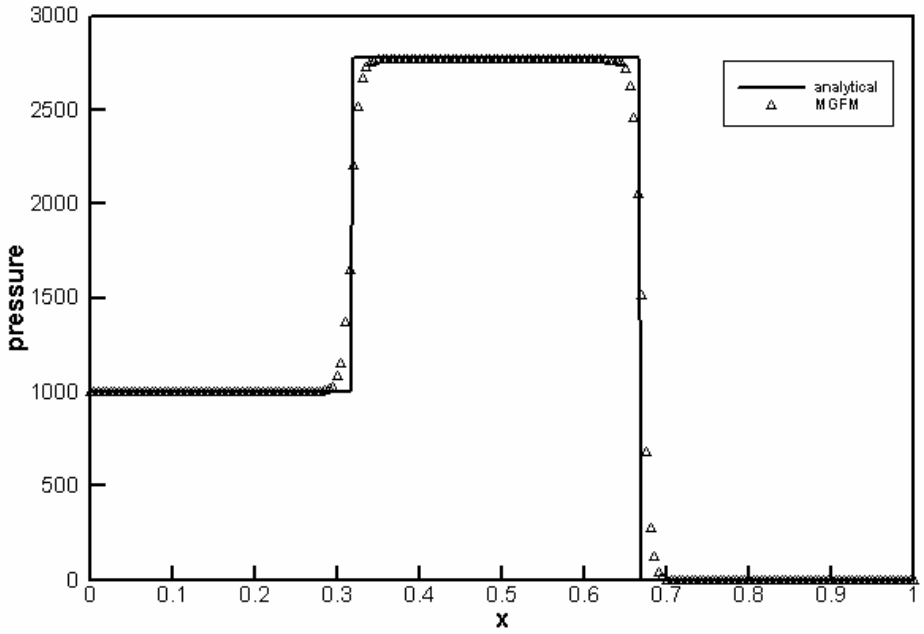

Fig. 2.15b Pressure profile for Case 2.6.12 by the MGFM.

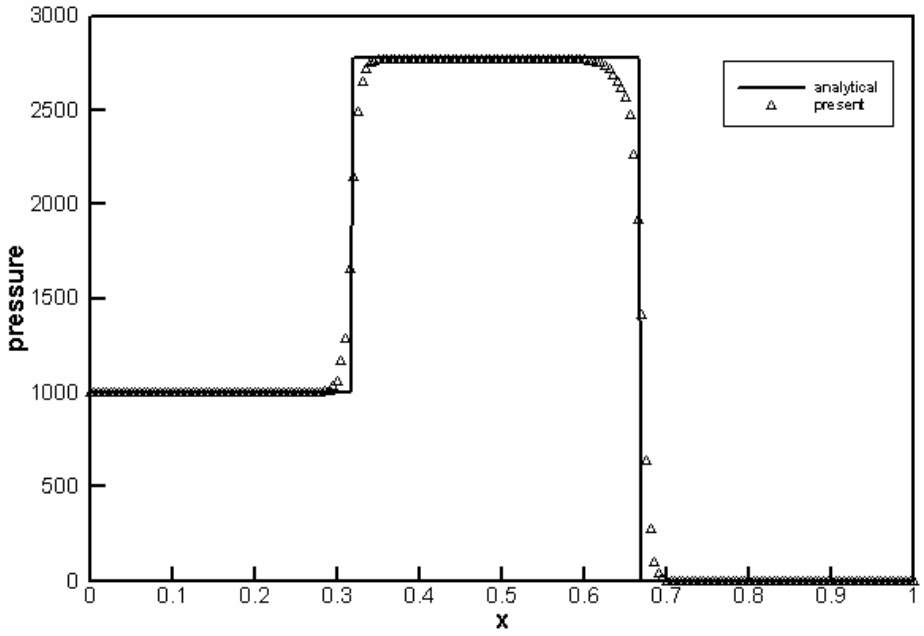

Fig. 2.15c Pressure profile for Case 2.6.12 by the present GFM.

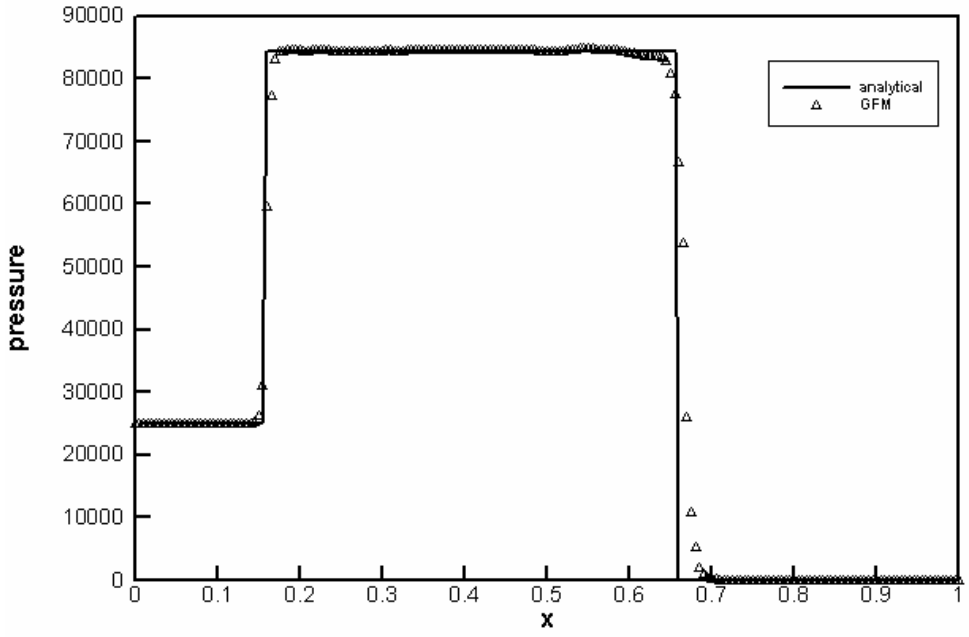

Fig. 2.16a Pressure profile for Case 2.6.13 by the original GFM.

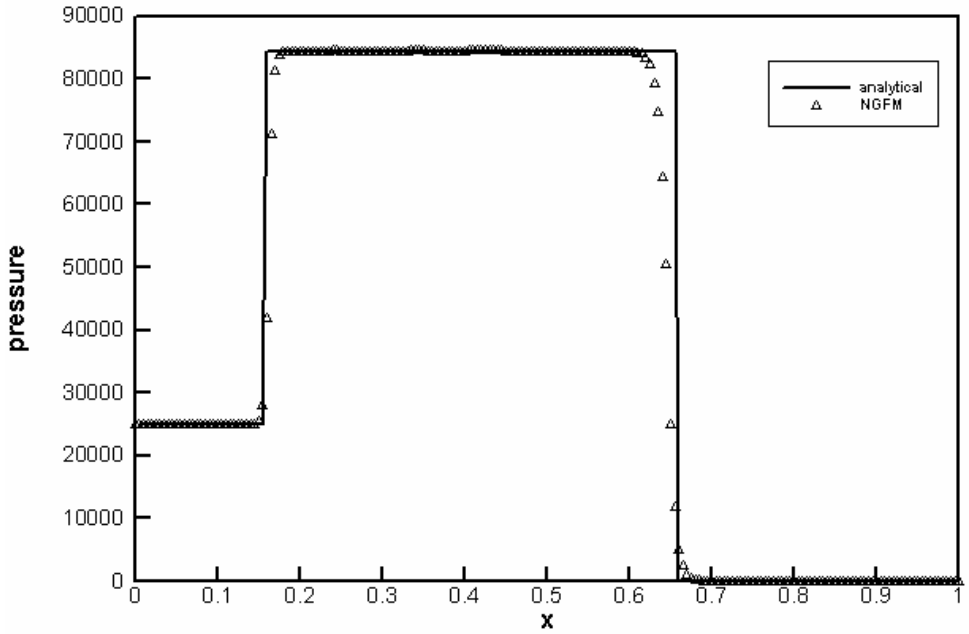

Fig. 2.16b Pressure profile for Case 2.6.13 by the new version GFM.

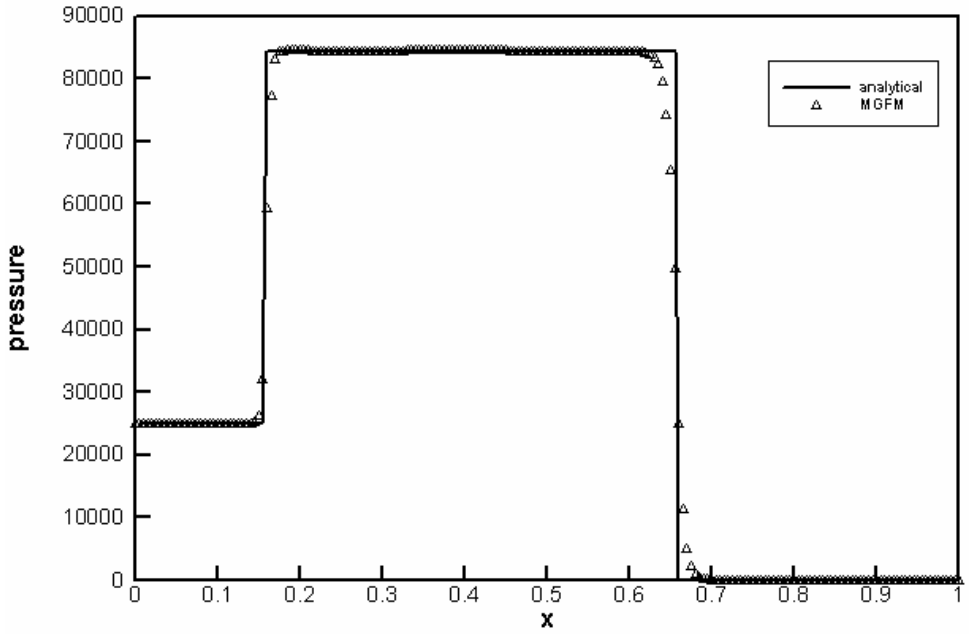

Fig. 2.16c Pressure profile for Case 2.6.13 by the MGFM.

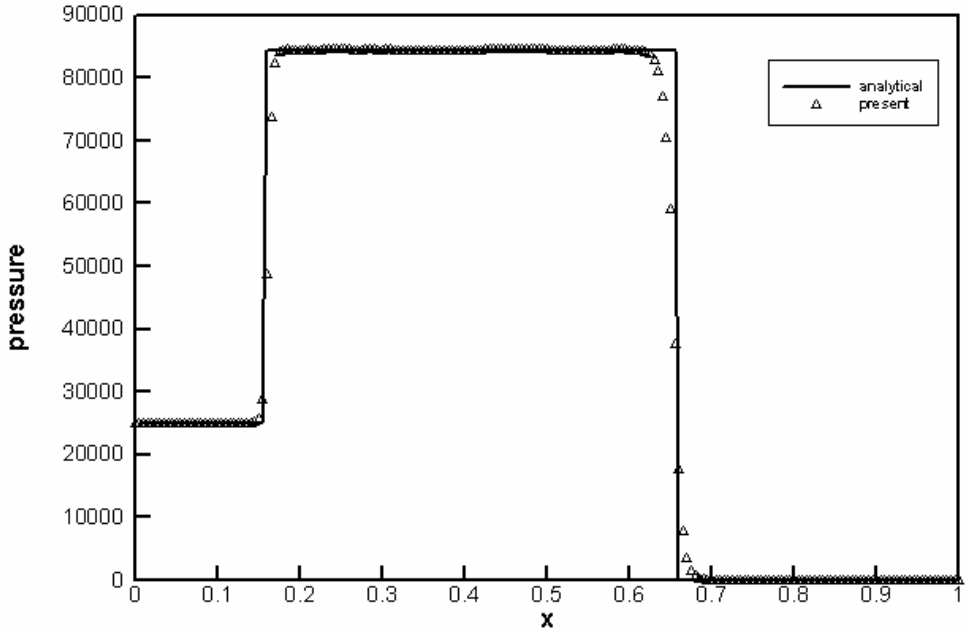

Fig. 2.16d Pressure profile for Case 2.6.13 by the present GFM.

Parameter	Values	Dimension
p_a	1.0	*bar*
ρ_a	7800	kg/m^3
β	3.7	Non-dimensional
m	2.225×10^{11}	p_a (Pascal)
G	8.53×10^{10}	p_a (Pascal)
Y	9.79×10^{8}	p_a (Pascal)

Table 2.1 Material properties of steel for hydro-elasto-elastic EOS.

Pressure ratio p_g/p_s	Exact interface pressure	Predicted interface pressure	Exact interface velocity	Predicted interface velocity
1000	998.37	998.37	0.1948	0.1948
5000	4981.86	4981.80	0.9711	0.9725
10000	9948.84	9948.61	1.9378	1.9425

Table 2.2 The predicted interface status via the explicit characteristic method and accurate Riemann problem solver with various pressure ratios of gas and steel.

Pressure ratio p_w/p_s	Exact interface pressure	Predicted interface pressure	Exact interface velocity	Predicted interface velocity
5000	4760.68	4758.51	0.9283	0.9290
10000	9386.59	9377.47	1.8283	1.8309
15000	13914.88	13893.75	2.7073	2.7128

Table 2.3 The predicted interface status via the explicit characteristic method and accurate Riemann problem solver with various pressure ratios of water and steel.

Pressure ratio p_g/p_s	Iteration steps	Pressure ratio p_w/p_s	Iteration steps
1000	124	5000	112
5000	121	10000	119
10000	119	15000	125

Table 2.4 The required iteration steps for ARPS with various pressure ratios of gas to steel and water to steel ($\varepsilon = 10^{-7}$).

Chapter 3

Mathematical Formulation: Unsteady Cavitation Models

The numerical methods presented in last chapter are unable to simulate cavitating flows without incorporation of a cavitation model. An unsteady cavitation consists of a dynamically developing boundary and can evolve to a certain dimension before collapsing very violently. The development and collapse of such cavitation is sustained mainly by the pressure jump across the cavitation boundary. For simulation of the unsteady cavitation, the one-fluid cavitation model is efficient to capture the cavitation creation, evolution and collapse. Several one-fluid models have been introduced briefly in Chapter 1. For ease of description, henceforth these models are called as the Cutoff model (Heister and Chen, 1994), the Vacuum model (Tang and Huang, 1996), the Schmidt model (Schmidt et al, 1997) and the Qin model (Qin et al, 1999). In this chapter, these models are analyzed and compared from both the mathematical point of view and physical point of view, and then a modification is proposed for the Schmidt model (henceforth called the modified Schmidt model) and a mathematically more consistent one-fluid model (henceforth called the Isentropic model) is presented to study the unsteady cavitation. The extensive comparisons of the one-fluid cavitation models are also carried out and presented by several water-tube numerical examples.

This chapter is organized as follows. We firstly present the physics of cavitation models and governing equations in Section 3.1. Some conclusions obtained from the jump condition across cavitation boundary are presented in Section 3.2 on the behaviors of the inviscid one-fluid cavitation models. The Cutoff model, the Schmidt model, the modified Schmidt model and the Isentropic model are analyzed and compared in Section 3.3. Several 1D cavitating flows occurred in water-tube are employed to test the modified Schmidt model and the Isentropic model and compare to

other existing one-fluid models in Section 3.4. A brief summary is presented in Section 3.5.

3.1 Model Physics

There is an important assumption that the mixture of liquid and vapor is homogenous, barotropic with no heat conductivity. This is the usual and realistic assumption for simulating cavitation occurring in cold water and under high pressure condition where the thermal effect and viscous loss are usually very much smaller than the mechanical (pressure) driving force of our system. The governing equations used in the present study are the inviscid Euler equations for compressible flows, thus effects of turbulence, surface tension of interfaces are also neglected. The 1D Euler systems can be written as

$$\frac{\partial U}{\partial t}+\frac{\partial F(U)}{\partial x}=0, \tag{3.1}$$

$$p=p(\rho), \tag{3.2}$$

$$\rho=\alpha\rho_g+(1-\alpha)\rho_l. \tag{3.3}$$

Here $U=[\rho,\rho u,E]^T$ and $F(U)=[\rho u,\rho u^2+p,(E+p)u]^T$. ρ, u and p are the average density, average velocity, average pressure, respectively. α is the void fraction determining the mixture ratio of the liquid to vapor, and ρ_g and ρ_l are the densities of pure vapor and pure liquid, respectively. In system (3.1), the total energy equation is only required to solve for gases. On the other hand, the EOS (3.2) is used to calculate the pressure from the density for liquid, solid and cavitation mixture so that the associated energy equation is excluded from the governing equation for liquid, solid and cavitation mixture. The averaged density is calculated by (3.3). For pure phase, the EOS provided in Chapter 2 is used to close the system (3.1). The sound speeds

associated with the EOS for the pure gas, liquid and solid can be written as follows if the flow is assumed as isentropic:

$$a_g = \left(\frac{dp}{d\rho_g} \right)^{\frac{1}{2}} = \left(\gamma_g \frac{p}{\rho_g} \right)^{\frac{1}{2}}, \qquad \text{for gas,} \tag{3.4}$$

and

$$a_l = \left(\frac{dp}{d\rho_l} \right)^{\frac{1}{2}} = \left(\gamma_l \frac{\overline{p}}{\rho_l} \right)^{\frac{1}{2}}, \qquad \text{for liquid,} \tag{3.5}$$

and

$$a_s = \left(\frac{dp}{d\rho_l} \right)^{\frac{1}{2}} = \left(\gamma_s \frac{\overline{p}}{\rho_l} \right)^{\frac{1}{2}}, \qquad \text{for solid.} \tag{3.6}$$

It should be noted that with the EOS presented in Chapter 2, the system of (3.1) is closed only for pure phases (gas, liquid and solid). Therefore, an EOS for mixture has to be developed to close the system for cavitating flows which is a major goal of this chapter. It should also be noted that the unsteady cavitation is assumed to be created by pressure jump across the cavitation boundary in the application of the system (3.1). The relationship across the cavitation boundary, like the Rankine-Hugoniot relationship, is thus developed (see also Liu et al, 2004a). Some of conclusions achieved from that article are summarized below.

3.2 Relationship across the Cavitation Boundary

As mentioned above, the unsteady cavitation investigated is caused by a pressure jump across the cavitation boundary which is governed via a local jump relation. Such local jump relationship similar to the Rankine-Hugoniot relationship can be written as

$$s(U_l^I - U_m^I) = F_l^I - F_m^I . \tag{3.7}$$

Here $U_l^I = \lim_{x \to x_I -} U(x,t)$ and $U_m^I = \lim_{x \to x_I +} U(x,t)$, $F_l^I = F(U_l^I)$, $F_m^I = F(U_m^I)$ and $s = \frac{dx_I}{dt}$. Hereafter, the subscripts "*l*" and "*m*" indicate the "liquid" and "mixture" media, respectively. The superscript "*I*" stands for "Interface" (cavitation boundary). For detailed derivation of (3.7), one can refer to (Liu et al, 2004a). (3.7) can be rewritten as

$$\rho_l^I v_l^I = \rho_m^I v_m^I, \tag{3.8a}$$

$$\rho_l^I (v_l^I)^2 + p_l^I = \rho_m^I (v_m^I)^2 + p_m^I, \tag{3.8b}$$

where $v_l^I = u_l^I - s$ and $v_m^I = u_m^I - s$. Some important conclusions can be deduced from (3.7) or (3.8) which are employed to analyze various one-fluid cavitation models. The verifications of these conclusions can be found in Liu et al (2004a) and all these conclusions are still valid in the normal direction of multi-dimensions.

Conclusion 3.1: *The inviscid one-fluid model allows the existence of a steady cavitation or cavitation convecting with the local flow velocity.*

For steady cavitation or cavitation convecting with the local fluid velocity, the relationship (3.8) degenerates to a relationship of "contact discontinuity". Conclusion 3.1 demonstrates the unsteady one-fluid cavitation model can possibly be applied to simulate for a steady cavitation like attached/sheet cavitation.

Conclusion 3.2: *With the exception of the Vacuum model, a pure liquid model of cavitation leads to the propagation of cavitation boundary with a "shock speed" if there is a pressure jump across the cavitation interface. Furthermore, relative to the cavitation interface, the local flow velocity is supersonic inside the cavitation, while it is subsonic in the liquid during cavitation collapse.*

In Conclusion 3.2, Tait's equation is employed for the liquid and the pressure (density) inside the cavitation is lower than the neighboring medium. Conclusion 3.2 shows that the fluid inside the cavity can be assumed as liquid of saturated pressure without significant effect on the final results as for the Cutoff model (see Section 3.3.1).

Conclusion 3.3: *If the sonic speed and density in the cavitation region are lower than those in the liquid at the vapor (saturated) pressure, then we have* $M_l^I < M_m^I$.

Here, M ($M = |u - s| / a$) is the Mach number relative to the propagating cavitation interface. This Conclusion implies that the flow relative to the cavitation motion may be transonic or even supersonic in the cavitation region. Therefore, the errors incurred inside the cavitation, although not negligible, are well confined during the rapid expansion phase of the cavitation. This conclusion is important to support that the pressure cut-off as employed in the modified Schmidt model (Section 3.3.3) does not affect the surrounding flows significantly.

Conclusion 3.4: *If the vapor pressure is set low enough but still positive and* $M_l^I < \sqrt{\overline{B} / \overline{p}_l^I}$ *, then there does not exist one liquid flow status (* ρ_l^c *,* p_l^c *,* u_l^c *) such that* $\rho_l^{sat} \le \rho_l^c < \rho_l^I$ *and* $p_l^{sat} \le p_l^c < p_l^I$ *with the provision of (a)* $\rho_l^I v_l^I = \rho_l^c v_l^c$ *and (b)* $\rho_l^I (v_l^I)^2 + p_l^I = \rho_l^c (v_l^c)^2 + p_l^c$.

Here $v_l^c = u_l^c - s$ and the pressure and density follows Tait's EOS. ρ_l^{sat} is the corresponding liquid density at the given vapor (saturated) pressure (p_l^{sat}). As mentioned in Chapter 2, numerical oscillations may occur in the vicinity of cavitation interface if the single-medium numerical solvers are directly employed to simulate the cavitating flow where the EOS for liquid and cavitation mixture are usually different. Furthermore, the ghost fluid status for GFM-based algorithms may not be properly

defined to maintain the Rankine-Hugoniot condition if there is a pressure jump across the cavitation interface. This means that the GFM-based algorithms as discussed in Chapter 2 may not able to capture such unsteady cavitation interface efficiently or accurately.

3.3 Unsteady Cavitation Models

The Cutoff model, the Schmidt model, the modified Schmidt model and the Isentropic model are introduced and presented below. The analysis and comparison of these four models are also carried out in this section.

3.3.1 Cutoff Model

The Cutoff model sets the local pressure equal to a given value (saturated vapor pressure) when the flow pressure falls down below a critical pressure level. If Tait's equation is employed for the pure water, the EOS for this model can then be described as

$$p = \begin{cases} B\left(\dfrac{\rho}{\rho_0}\right)^{\gamma_l} - B + A, & \rho > \rho_{sat} \\ p_{sat} & \rho \le \rho_{sat} \end{cases}. \tag{3.9}$$

Here, ρ_{sat} is the liquid density in association with the given critical pressure p_{sat}. The pressure cut-off causes that the EOS to degenerate from a convex type in the pure liquid region to a non-convex form in the pressure cut-off region. Furthermore, the Cutoff model assumes that the pressure in the cavitation region does not change or the density is set to ρ_{sat}, resulting in mass loss and thus system non-conservation. To maintain the conservative computation using the Cutoff model, a positive sound speed, which cannot be consistent with (3.9), has to be defined in the cavitation region. In the present computation, there are two ways to define a positive sound speed. The sound

speed in the cavitation zone is set equal to the sound speed in water under saturated pressure; the sound speed is calculated from the updated density via conservative computation under a fixed saturated water pressure. Some nonphysical consequences are arisen from these two definitions of sound speed for cavitation mixture as mentioned in Liu et al (2004a). Firstly, the numerical sound speed in the cavitation region contradicts the assumed EOS (3.9). Secondly, the flow status computed inside the cavitation region is not physical. Thirdly, the motion of cavitation boundary is forced to propagate with a "shock" speed (Conclusion 3.2). Fourthly, the inconsistency of above-mentioned *artificial* treatment of the sound speed with EOS (3.9) tends to exclude an "expansion shock", thereby resulting in the decomposition of this "expansion shock" under such said treatment. Lastly, the result of captured cavitation collapse may not be physical and possibly inaccurate.

The Cutoff model is easy to be implemented and employed to cavitation computation since it is an essentially a pure fluid model. This is why the Cutoff model is extensively applied and coupled into the commercial software. Furthermore, the numerical error generated from the pressure cut-off does not have significant effect on surrounding flow if the flow pressure is sufficiently high like in an underwater explosion. Numerical tests in Section 3.4 will also show that the inaccuracy caused by the non-physical and inconsistent treatment of the cavitation region does not affect too severely the calculated peak pressures. On the other hand, the limitation of the Cutoff model becomes very obvious when the surrounding flow pressure is relatively low. As such, the nonphysical computation of the flow status in the cavitation region as mentioned above will lead to wrong pressure jump across the cavitation boundary and cavitation collapse as will be shown in Sections 3.4 and 4.3.

3.3.2 Schmidt Model

This is another unsteady one-fluid compressible cavitation model in literature, which was developed and verified for high velocity and high pressure flow in a very small nozzle (Schmidt et al, 1999). In this model, the cavitating flow is assumed to be a homogeneous and barotropic mixture of gas and liquid, where the sound speed can theoretically be given (Brennen, 1995; Wallis, 1969) as

$$a = \left\{ \left[\alpha.\rho_g + (1-\alpha).\rho_l \right] \left[\frac{\alpha}{\rho_g.a_g^2} + \frac{(1-\alpha)}{\rho_l.a_l^2} \right] \right\}^{-1/2}. \tag{3.10}$$

To obtain the barotropic EOS for the mixture, Schmidt et al (1999) assumed the sound speeds for gas and liquid components as well as their respective densities to be constant, and the mixture follows the constitutive relation of $dp/d\rho = a^2$ because the cavitating flow is assumed to be homogeneous. As a result, the pressure can be obtained analytically as a function of void fraction or density by integrating $dp/d\rho = a^2$ using (3.10), giving rise to the EOS,

$$p = p'_{sat} + p_{gl}.\ln\left[\frac{\rho_g.a_g^2.(\rho_l + \alpha.(\rho_g - \rho_l))}{\rho_l.\left(\rho_g.a_g^2 - \alpha\left(\rho_g.a_g^2 - \rho_l.a_l^2\right)\right)} \right], \tag{3.11}$$

where p_{gl} is a parameter of the known surrounding fluid properties given as

$$p_{gl} = \frac{\rho_g.a_g^2.\rho_l.a_l^2.(\rho_g - \rho_l)}{\rho_g^2.a_g^2 - \rho_l^2.a_l^2}. \tag{3.12}$$

Equations (3.1) with (3.3) and (3.11) constitute a closed system for the mixture. The mixture density can be obtained by solving (3.1) and then the void fraction is calculated by using (3.3) to be followed by solving the pressure via (3.11).

The applicability of (3.11) to a large scale unsteady cavitation depends on the value of "saturated" pressure p'_{sat}. When the void fraction ranges from 0 to 1 and p'_{sat} in (3.11) is set to be the *physical* saturated pressure p_{sat} (generally tens to hundreds of Pa and thousands of Pa in an underwater explosion). The variation of the pressure with the void fraction using the Schmidt model is shown in Fig. 3.1 under p'_{sat} set to the physical saturated pressure of 2000Pa. It is found that the pressure in (3.11) can not be kept positive when the void fraction is larger than a small quantity of about $O(10^{-2})$ because the second term on the right side of (3.11) is negative for the void fraction ranging from 0 to 1. Therefore, to ensure that the pressure in (3.11) is always positive, p'_{sat} should be necessarily larger than the magnitude of the second term on the right side of (3.11). If p and α in (3.11) are set to 0 and 1, respectively, the minimum value of p'_{sat} that ensures no negative pressure in the cavitation region is obtained by

$$p'_{\min} = -p_{gl}.\ln\left[\frac{\rho_g^2.a_g^2.}{\rho_l^2 a_l^2.}\right]. \tag{3.13}$$

If $p'_{sat} \geq p'_{\min}$, which may be far larger than the *physical* saturated pressure (p_{sat}), the pressure obtained from (3.11) is always positive.

Now, we examine the applicability of the Schmidt model. (3.13) can be approximately simplified as

$$p'_{\min} \approx -2\rho_g.a_g^2.(\ln\frac{\rho_g}{\rho_l} + \ln\frac{a_g}{a_l}), \tag{3.14}$$

where $p_{gl} = \dfrac{\rho_g.a_g^2.\rho_l.a_l^2.(\rho_g - \rho_l)}{\rho_g^2.a_g^2 - \rho_l^2.a_l^2} = \rho_g.a_g^2\dfrac{(\rho_g.\rho_l.a_l^2 - \rho_l^2.a_l^2)}{(\rho_g^2.a_g^2 - \rho_l^2.a_l^2)} \approx \rho_g.a_g^2$ based on $\rho_g << \rho_l$ and $\rho_g^2.a_g^2 << \rho_l^2.a_l^2$. In (2.13), $\ln(a_g/a_l)$ takes on a value normally ranging from -3 to -1. If ρ_g/ρ_l takes on a value of 10^{-5}, $p'_{\min}$ is a quantity of about $5\,kPa$.

One can easily show that $p'_{\min}$ decreases to a physically reasonable value of hundreds to thousands of Pascal with the further decrease of ρ_g / ρ_l to below 10^{-5}. On the contrary, a larger ratio of ρ_g / ρ_l can lead $p'_{\min}$ to assume an unreasonable large quantity. Table 3.1 shows that $p'_{\min}$ can go beyond 1bar and reach even tens of bar if the ratio of ρ_g / ρ_l ranges from 10^{-4} to10^{-3}.

If one requires that the Schmidt model is applied to cavitation with a large vapor to liquid density ratio without negative pressure, $p'_{sat} \geq p'_{\min}$ should be satisfied. This may result in a large assumed p'_{sat}. We want to check the performance of the Schmidt model with the requirement of $p'_{sat} \geq p'_{\min}$ when applied to the situations where the initial surrounding liquid pressure is not very high. For such flow, the ratio of ρ_g / ρ_l can range from 10^{-4} to10^{-3}. In the numerical computation, one can use either p_{sat} or p'_{sat} as the criterion of flow starting cavitating. For the liquid flow under initially very high pressure and the cavitation dimension is small, p'_{sat} can be taken to be quite close to p_{sat} as the ratio of ρ_g / ρ_l can go below 10^{-5}. The results then have not much difference when using either value as the criterion of cavitation initiation. However, as the cavitation evolves to a large dimension or if the initial surrounding flow pressure is not very high, one will find (later) that the results obtained are very different in the cavitation region between using p'_{sat} or p_{sat} as the criterion. This is because the value of p'_{sat} satisfying the requirement of $p'_{sat} \geq p'_{\min}$ can be quite larger than the physical saturated pressure p_{sat} in such a situation. We call the former numerical implementation as **Implementation I**, while the latter numerical implementation as **Implementation II**. More specifically,

Implementation I (Schmidt-I): The liquid flow is assumed to cavitate when the pressure is lower than the nonphysical p'_{sat} under the requirement of $p'_{sat} \geq p'_{\min}$ or no negative pressure is present. Under this implementation, the calculated pressure in the cavitation region is always positive and lower than p'_{sat}. Moreover, the computed pressure in the surrounding flow will never be lower than p'_{sat}. Schmidt implemented the Schmidt model in this way or manner.

Implementation II (Schmidt-II): The liquid flow is assumed to cavitate when the pressure is lower than the physical p_{sat} under the requirement of $p'_{sat} \geq p'_{\min}$ or no negative pressure is present.

Under **Implementation II**, the calculated pressure in the cavitation region is positive and lower than p'_{sat} but may be higher than p_{sat}, while the computed pressure in the surrounding flow will never be lower than p_{sat}. If the initial surrounding flow pressure is sufficiently high or the density jump across cavitation boundary is large enough to ensure a vapor to liquid density ratio of about 10^{-5} or smaller, the Schmidt model can work properly or consistently under **Implementation II**. This is also the reason why the Schmidt model works rather effectively on small scale nozzle cavitating flows. With the cavitation evolution, however, the flow pressure in the neighborhood of the cavitation interface reduces rapidly to a very low value which then becomes much lower than p'_{sat} or even close to p_{sat} while the calculated pressure in the cavitation region by equation (3.11) may be larger than p_{sat}. As a result, *nonphysical* pressure oscillations occur in the vicinity of the cavitation interface.

Qin *et al* (1999) presented a modification of the Schmidt model by multiplying a parameter (β) ranging from $O(10^{-3})$ to $O(10^{-5})$ to the second term of (3.11) accordingly. Doing so, the "saturated" pressure p'_{sat} can be adjusted to the

physical p_{sat} . Such a modification also essentially makes the model takes on the characteristic of a pressure cut-off. This is because the product of β and the second non-constant term in (3.11) is negligibly small. On the other hand, such a modification makes the resultant EOS apparently to be inconsistent with (3.10) and parameter (β) should be unity based on strict mathematical derivation (see Appendix A).

There are mathematical inconsistencies between (3.10) and (3.11). In fact, the limitation of the Schmidt model arises from these inconsistencies. In the derivation of (3.10), both the gas and liquid components are assumed compressible; the sound speeds and densities of both components are functions of pressure. Thus, the assumption of constant component densities and sonic speeds utilized in obtaining (3.11) contradicts the premises of (3.10). Because the sound speed formulation used for the Schmidt model is mathematically sound and verified experimentally, it is the inconsistent way of deriving EOS (3.11) that leads to a very large p'_{sat} obtained, which results in inherent limitation when applied to large-size cavitation. This shortcoming causes very stringent CFL used especially for the low-pressure surrounding flow or large size cavitation, as will be shown in Section 3.4. To overcome these difficulties and extend the application of the Schmidt model to large scale unsteady cavitation, some modifications are proposed leading to a new model as described in the following.

Remark: *In this thesis, the Schmidt Model stands for the Schmidt-I except noted otherwise.*

3.3.3. The Modified Schmidt Model

It is important to declare that cavitation only occurs when the pressure falls below the *physical* saturated pressure. As such, we propose the following modification for the Schmidt model and the resulting EOS is

$$p = \begin{cases} Tait's \quad EOS, & p \geq p_{sat}, \\ p_{sat} + p_{gl}.\ln\left[\dfrac{\rho_g.a_g^2.\left(\rho_l + \alpha.\left(\rho_g - \rho_l\right)\right)}{\rho_l.\left(\rho_g.a_g^2 - \alpha.\left(\rho_g.a_g^2 - \rho_l.a_l^2\right)\right)}\right], & p_\varepsilon < p < p_{sat}, \\ p_\varepsilon, & p \leq p_\varepsilon. \end{cases} \qquad (3.15)$$

Here p_ε is a given small positive value close to zero (about10^{-9}), p_{sat} is the *physical* saturated pressure. The intention of $p \leq p_\varepsilon$ is to prevent the cavitation pressure from assuming a negative quantity. This model is based on the same assumption and derived by integrating (3.10) and $dp/d\rho = a^2$ as for the Schmidt model. Therefore, this model can be applied to model small scale cavitation which occurs in high-speed nozzles. The major differences between the Schmidt model and the modified Schmidt model are clearly shown in Table 3.2 and can be summarized as follows:

1) The *physical* saturated pressure p_{sat} is used in (3.15) and the flow is assumed to cavitate at p_{sat} for the modified Schmidt model, while a large pressure p'_{sat} is employed in (3.11) for the Schmidt model. Also the modified Schmidt model has no restraint on the vapor to liquid density ratio. It is apparent that the modified Schmidt model is able to capture the pressure jump across the cavitation boundary for more extensive vapor to liquid density ratio. The Schmidt model, however, is not applicable when vapor to liquid density ratio is larger than about10^{-5}.

2) The cavitation pressure as calculated by the modified Schmidt model (3.15) is always less than the *physical* saturated pressure, while the surrounding flow pressure is always larger than the *physical* saturated pressure. Therefore, the cavitation pressure can be physically kept below the surrounding pressure.

This is unlike the Schmidt model under Implementation II, in which the calculated cavitation pressure may become larger than the surrounding flow pressure near the cavitation interface, resulting in the numerical oscillation near the cavitation interface.

The modified Schmidt model removes such nonphysical phenomenon and makes the cavitation pressure always below the surrounding flow pressure. Therefore, the modified Schmidt model is able to remove the numerical oscillation which occurs in the application of the Schmidt model.

It should be noted that the modified Schmidt model allows for possible negative pressure inside the cavitation region due to employment of the *physical* saturated pressure. To remove such negative pressure, if any, a small p_ε is used in conjunction with the pressure cut-off when the calculated cavitation pressure is below p_ε. Such pressure cut-off leads to the *nonphysical* treatment in the central region of cavitation. Numerical tests, however, have shown that such treatment does not significantly affect the subsequent peak pressure caused by cavitation collapse. This is probably because the flow pressure and density in the central region of cavitation are so low that the flow motion relative to the cavitation interface (boundary) is supersonic as mentioned by Conclusion 3.3 (Section 3.2). As a result, the errors incurred inside the cavitation are confined largely to the central region of cavitation during the rapid expansion phase of the cavitation. In the phase of cavitation collapse, the cavitation interface moves rapidly across the centre of the cavitation region, where the flow pressure is not accurate due to the employment of pressure cutoff. Thus the motion of cavitation interface can be affected and suffered from some inaccuracies when moving across the cut-off region. This is why the predicted period of cavitation collapse by the modified Schmidt model is affected and found to have but still a well-confined discrepancy when compared to Liu et al's model (2004) (see Fig. 4.8 in Chapter 4). However, such effect is not overwhelming especially in the evaluation of the pressure surge caused by cavitation collapse. This is possibly so because the flow pressure in the cut-off region is physically very low already.

It is apparent that the modified Schmidt model has a wider application than the Schmidt model. However, the mathematical and physical inconsistency still exists in this model. In fact, besides the Schmidt EOS (3.11) and the modified Schmidt EOS (3.15), there are some other barotropic relations developed and discussed in Brennen (1995) by either assuming the density and sonic speed of the liquid component are constant or neglecting the density of the gas component or the volume of liquid component. Those barotropic relations did provide satisfactory results in the respective applicable ranges. However, the mathematical inconsistencies between the barotropic relations and the sound speed (3.10) invariably exist. We argue that these inconsistencies are removable for barotropic mixture. The Isentropic model below is able to remove such inconsistencies.

3.3.4 Isentropic Model

The inapplicability of the Schmidt model and modified Schmidt model arise from the inconsistency between these two models and sound speed equation (3.10). (3.10) has been verified to be mathematically sound and accurate via comparing to experimental results as shown in Wallis (1969) and Brennen (1995) under the assumptions of the homogenous and thermal equilibrium mixture with the neglect of the influence of mass transfer on the sound speed. Based on the same assumptions, the barotropic relation for the mixture is defined by Liu et al (2004a) without any contradiction with respect to (3.10). By taking the derivative of (3.3) with respect to pressure, the void fraction can only be a function of pressure alone as

$$\frac{d\alpha}{dp}(\rho_l - \rho_g) = \alpha\frac{d\rho_g}{dp} + (1-\alpha)\frac{d\rho_l}{dp} - \frac{d\rho}{dp}. \tag{3.16}$$

Here the compressibility of the mixture comes from the gas and liquid components as well as void fraction. Since (3.3) is always held, (3.16) is true and should be

maintained consistently with (3.10). By assuming both the gas and liquid components and the mixture follow the constitutive relation of $dp/d\rho = a^2$ and using (3.10), expression (3.16) can then be reduced to the form,

$$\frac{d\alpha}{dp} = \alpha(1-\alpha)\left(\frac{1}{\rho_l a_l^2} - \frac{1}{\rho_g a_g^2}\right). \tag{3.17}$$

If the gas and liquid components are assumed isentropic, with (3.17) and (3.10), we have

$$\frac{\alpha}{1-\alpha} = k\frac{(\overline{p}/\overline{p}_{cav})^{1/\gamma_l}}{(p/p_{cav})^{1/\gamma_g}}, \tag{3.18}$$

and

$$\rho = \frac{k\rho_g^{cav} + \rho_l^{cav}}{\left(\frac{\overline{p}}{\overline{p}_{cav}}\right)^{-1/\gamma_l} + k\left(\frac{p}{p_{cav}}\right)^{-1/\gamma_g}}, \tag{3.19}$$

where $k = \alpha_0/(1-\alpha_0)$. ρ_g^{cav} and ρ_l^{cav} are the associated gas and liquid density at the cavitation pressure p_{cav}, respectively, and α_0 is the known void fraction of the mixture density at p_{cav}. Sometimes it may not be easy to obtain α_0 experimentally or otherwise for certain problems due to the flow cavitating pressure being strongly related to the surrounding environment. A simple method ((Liu et al, 2004a) is used to define the initial void fraction (α_0) where k_{cav} or α_0 can be obtained via $k_{cav} = \dfrac{\rho_l^{cav} - \rho_{l\infty}}{\rho_{l\infty} - \rho_g^{cav}}$, ($\rho_{l\infty}$, $u_{l\infty}$, $p_{l\infty}$) is the flow status before cavitation occurs at the flow cavitating location. Using (3.4) and (3.5), (3.17) can be rewritten as

$$\frac{d\alpha}{dp} = \alpha(1-\alpha)\left(\frac{1}{\gamma_l \overline{p}} - \frac{1}{\gamma_g p}\right). \tag{3.20}$$

or

$$d(\ln\alpha) - d(\ln(1-\alpha)) = d(\ln \bar{p}^{1/\gamma_l}) - d(\ln p^{1/\gamma_g}). \tag{3.21}$$

From (3.21), it can be deduced that α is not allowed to be equal to 0 or 1. Physically a void fraction jump exists across the cavitation interface. Assuming that the pressure drops to p_{cav} ($p_{cav} \le p_{sat}$) and the void fraction takes on the value of α_0 simultaneously across the cavitation interface, (3.18) is obtained by integrating (3.21) from p_{cav}. Substituting of α from (3.18) into (3.3), EOS (3.19) is obtained and which is consistent with (3.10) regardless of k or α_0.

In cold water or under normal atmospheric condition, water is usually assumed to be isothermal and the sound speed for the surrounding flow is taken as a constant. The EOS for water becomes $p - p_0 = a_l^2(\rho_l - \rho_{l0})$ instead of Tait's EOS, where ρ_{l0} is the water density at pressure p_0. Therefore, we have

$$\frac{\alpha}{1-\alpha} = k\frac{(p+B')/(p_{cav}+B')}{(p/p_{cav})^{1/\gamma_g}}, \tag{3.22}$$

and

$$\rho = \frac{k\rho_g^{cav} + \rho_l^{cav}}{\dfrac{p_{cav}+B'}{p+B'} + k\left(\dfrac{p}{p_{cav}}\right)^{-1/\gamma_g}}, \tag{3.23}$$

where, $B' = \rho_{l0}a_l^2 - p_0$. (3.22) and (3.23) will be employed to calculate water-hammer problem in Chapter 4 where the flow is assumed isothermal.

Newton's iteration method can provide a viable way to obtain the pressure from (3.19) given a good starting value which is defined as

$$p = p_{cav}\left(\frac{k\rho}{k\rho_g^{cav} + \rho_l^{cav} - \rho}\right)^{\gamma_g}. \tag{3.24}$$

(3.24) is obtained directly from (3.22) since $(\overline{p}/\overline{p}_{cav})^{-1/\gamma_l}$ is very close to 1. This is due to the very low pressure inside the cavitation and the very large *B*. Numerical tests showed that a few iteration steps could generate satisfactory results using (3.24) to provide the starting value. Furthermore, (3.24) is also a very good approximation to (3.19). One, instead, can also use it directly to obtain the pressure.

Based on the derivation and analysis as done above, the major characteristics of the Isentropic one-fluid model can be summarized as

1) p is a one-to-one monotonous function of ρ and there is a unique positive p for each $\rho > 0$.

2) The mixture density approaches zero as the pressure goes to zero.

3) The void faction approaches 1 when the pressure goes to zero.

4) The sound speed approaches zero when the pressure goes to zero.

5) A void fraction jump must occur across the cavitation boundary.

6) The whole system (3.1) is hyperbolic and conservative.

3.3.5 Some Observations on the One-fluid Models

Barometric relationships are shown in Fig. 3.1 for the comparison among the Schmidt model, the modified Schmidt model, the Cut-off model and the Isentropic model. The difference among these models has been shown clearly in this figure. The Cut-off model can only provide a constant pressure of magnitude p_{sat}, which is taken to be 2000Pa—the amount usually assumed in underwater explosions, with respect to void fraction in the cavitation region. The Schmidt model with the restraint of $p'_{sat} \geq p'_{\min}$ (noted with "Schmidt with large saturated pressure" in Fig. 3.1) provides

pressure quite higher than the physical saturated pressure p_{sat}, while it provides negative pressure beyond α>0.01 if p'_{sat} is set to be equal to p_{sat} (noted with "Schmidt with physical saturated pressure" in Fig. 3.1). The Isentropic model always provides positive pressure in the cavitation region, which is also physically lower than p_{sat}. Compared to the Isentropic model, theoretically, there are mathematical inconsistencies for the modified Schmidt model, which mainly come from the pressure cut-off carried out to the negative pressure and the inconsistency with expression (3.10) as well; to obtain expression (3.10), both the vapor and liquid components are assumed compressible, while their density and sound speeds are assumed constant in the Schmidt model and the modified Schmidt model. However, it is interesting to observe from Fig. 3.1 that the behavior of the modified Schmidt model looks quite similar to that of the Isentropic model in the vicinity of the cavitation interface. This is why the modified Schmidt model can provide results compared very reasonably to those obtained using the Isentropic model, although the modified Schmidt model is not strictly mathematically consistent as the latter. It is also found that the region of pressure cut-off will become larger with the increase of the vapor to liquid density ratio because the calculated cavitation pressure by equation (3.15) is more likely to be negative. Thus, the region of having pressure cut-off treatment becomes large. As such, the discrepancy between the modified Schmidt model and the Isentropic model becomes observable, as the ratio of ρ_g / ρ_l is close to about10^{-3}. However, it is found that the discrepancy is well-limited and has well-confined effect on the final pressure surge caused by cavitation collapse.

More specifically, some observations on the four one-fluid models can be summarized as:

1). There are mathematical and physical inconsistencies in the Cutoff model, the Schmidt model and the modified Schmidt model which are not consistent with the sound speed equation (3.10). The Isentropic model is, however, developed based on the same assumptions as (3.10) and thus mathematical and physical consistent.

2). The Cutoff model is able to predict correct the peak pressure of cavitation collapse for most cases while fails to predict accurate periods of cavitation collapse; the Schmidt model is sufficiently accurate if the void fraction is below 10^{-5}; the modified Schmidt model can be applied to higher vapor to liquid density ratios, say 10^{-4}; there is no limitation on the ratio of ρ_g / ρ_l when one employs the Isentropic model.

3). There are no undetermined model parameters for the Cutoff model, the Schmidt model and the modified Schmidt model and the pressure is obtained algebraically from the density. In the application of the Isentropic model, iteration is required to find the pressure and a model parameter k has to be determined beforehand. Therefore, the Isentropic model needs more computational effort than the other three models.

4). One can (theoretically) apply the one-fluid models to simulate attached/sheet cavitation where usually the influence of turbulence must be taken into consideration by employing the (compressible) N-S equations instead of the Euler equations given in (3.1); this is attributed to the presence of the wake part for attached/sheet cavitation and the flow is usually turbulent. However, the discussion on the applicability and efficiency of the proposed one-fluid models as applied to the N-S equations is beyond the scope of the present work and will be pursued in future.

3.4 Numerical Examples for Testing Various Cavitation Model

Besides the difficulties arising from physically modeling cavitation flow, which is the focus of the present work, there are difficulties from the numerical aspect in

computing the cavitating flow. Because the coupled system of incompressible flow (the pure liquid phase) with compressible flow (the mixture) is very stiff in the vicinity of cavitation interface (boundary) during the simulation of attached/sheet cavitation, (severe) numerical instability and/or convergence problem can occur. Thus, additional numerical techniques are usually required to overcome such difficulties (Kunz, 2000; Senocak, 2002). In the present study, both the surrounding medium (liquid) and the mixture are considered as compressible, the resultant system is therefore mathematically well-posed. When a high-resolution numerical scheme developed for the compressible single phase flow is directly applied to multi-phase flow and the present cavitating flow, the numerical oscillations may occur because of the employment of different EOS across the interface. However, such difficulties may not be so severe and overwhelming since the jumps across the cavitation interface are relatively small, and a high-resolution numerical scheme developed for compressible single phase flow with well-designed limiter (Schmidt et al, 1999) can still give satisfactory results. The numerical experiments to be carried out in this section will also show that a well-developed high-resolution numerical scheme can prevent or greatly suppress these oscillations but may not be able to remove them completely. It is found that there is no numerical oscillation encountered using the Isentropic model with *full* CFL number in the present study.

For purpose of testing the validity of the four one-fluid models as discussed in Section 3.3, the results obtained via the Vacuum model and the Multiphase model will also be presented. The comparisons between the Schmidt model and the modified Schmidt model are also carried out to investigate the performance of the modified Schmidt model under various ratios of vapor to liquid density. It should be noted that the Cutoff model and the Vacuum model are pure phase models. The usual *full* CFL

number at, say, 0.8 to 0.9 can be used without incurring numerical oscillations. The Vacuum model developed in (Tang and Huang, 1996) has been shown to be reasonable both mathematically and physically except for the difficulties in extending to multi-dimensions. Wherever possible, the 1D analytical solutions based on the Vacuum model will be employed to verify the numerical results of various one-fluid models.

The numerical scheme selected and used to solve system (3.1) is the well-developed MUSCL scheme with HLL approximate Riemann solver as mentioned in Chapter 2 with CFL=0.8 and 401 uniform mesh points in domain [0,1]. All the parameters are dimensional unless otherwise noted and all the results in figures are dimensional in the international standard units (i.e. pressure is in $Pascal$, density is in kg/m^3 and velocity is in m/s) except for those with their own units. In this section, various cavitation models will be tested and verified by either comparing to the *analytical* solution, experiments or numerical results. As α_0 is unknown for each problem to be discussed in the tests, we use the procedure developed in Section 3.3.4 to determine α_0 and adjustment made to k accordingly. In the present computation, p_{sat} is set to 62.5Pa and the local cavitation number σ is set to $0.1\sigma_{\max}$ in the computation of the initial k for the Isentropic model unless otherwise noted.

Case 3.4.1. This is a Riemann problem of two highly-pressurized water streams moving with the same magnitude of velocity in the opposite direction away from the centre of a tube. The initial pressure of the two water streams is set to 10^8. The two water streams initially meet at x=0.5. If the magnitude of the initial two-water stream velocity is not sufficiently high, two opposite centered rarefaction waves are generated and expand from the centre without cavitation. In such a situation, exact solution can be obtained by solving a Riemann problem of double rarefaction waves. Our cavitation models associated codes can automatically treat the flow as single phase. Figures 3.2a,

b show the velocity and pressure results obtained by our codes for a velocity magnitude of two streams initially set to 50m/s and compare well to the analytical solution at 0.2ms.

Case 3.4.2. This case is similar to Case 3.4.1 except the velocity magnitude of two streams is set to 100m/s. Thus, cavitation immediately starts at the centre. The *exact* solution can also be obtained by solving a Riemann problem of double rarefaction waves connected to a vacuum at the centre (Tang and Huang, 1996) (i.e. the exact solution based on the Vacuum model for this problem). Due to p_{sat} set to be negligibly small physically at least relative to the initial very high surrounding pressure, the results provided by the Isentropic model can be directly compared to the exact solution of the Vacuum model. Figures 3.3a, b shows the velocity profiles and pressure profiles obtained by the Cutoff model and the modified Schmidt model and the Isentropic model at time t=0.2ms. It is observed from Fig. 3.3 that the three models provide the same results in the region beyond the cavitation. In particular, the Cut-off model provides a result with a larger cavitation dimension, while the Isentropic model and the modified Schmidt model provide results very close to the analytical solution at this very earlier stage.

Case 3.4.3. This is a Riemann problem where two water streams have different pressures and velocities. This case is used to test the performance of the different models for the water streams with different strength. The initial conditions are $u_l = -10$, $p_l = 10^6$; $u_r = 100$, $p_r = 10^8$. For this case, a strong rarefaction wave propagates to the right and a relatively weaker rarefaction wave propagates to left. Figure 3.4a at t=0.1ms shows that there is a region (0.5-0.68) where the velocity is approximately constant due to the fully developed cavitation. The pressure distributions are given in Fig. 3.4b. The velocity and pressure profiles obtained by the

Isentropic and the modified Schmidt model are very comparable to the analytical results while the Cutoff model provides relatively less accurate results.

Case 3.4.4. This case is used to test the performance of the different models for the water streams with low flow speed and thus small Mach number. The computation of low Mach number compressible flows is always challenging (Guillard and Viozat, 1999). The initial conditions are $u_l = -1.0$, $p_l = 10^6$; $u_r = 1.0$, $p_r = 10^6$. The computation is allowed to run to a final time of 0.2ms. Figures 3.5a and b show that the present numerical algorithm is able to simulate such low Mach number compressible flow very well. It is also found that the Isentropic model and the modified Schmidt model provide slightly yet perceptibly a little more accurate results than the Cutoff model.

Case 3.4.5. This case is also similar to Case 3.4.1 except that the pressure and velocity magnitude of both water streams are much higher. Such case is calculated here to test the performance of the different models in the computation of high-pressured and high-velocity compressible flows. The initial conditions are $u_l = -1000.0$, $p_l = 10^9$; $u_r = 1000.0$, $p_r = 10^9$. We ran the computation to a final time of 0.1ms. It has been shown in Fig. 3.6a that two very strong rarefaction waves propagate into the water streams at a very high velocity. The pressure distributions are provided in Fig. 3.6b. The cavitation very quickly evolved into a large dimension and rarefaction waves appear from the center of the cavitation region. Once again, the Isentropic model and the modified Schmidt model provide close results to analytical solution while the Cutoff model is a little different from analytical solution at the cavitation region.

Case 3.4.6. This case is presented in detail to compare various cavitation models and to show the limitation of the Schmidt model when applied to large scale cavitation. This case was previously investigated by Saurel and Abgrall (1999b) using a

multiphase model comprising seven governing equations. The initial conditions are $u_l = -100.0$, $p_l = 10^5$; $u_r = 100.0$, $p_r = 10^5$. Figure 3.7 shows the comparison of the results obtained respectively by the Isentropic model, the modified Schmidt model and the Cutoff model at 0.2ms. The results between the Isentropic model and the modified Schmidt model look very similar, while obvious discrepancies in the density and velocity profiles can be observed for the Cutoff model. An almost twice cavitation size is provided by the latter in contrast to that provided by the former two models (see density profile in Fig. 3.7c). The lowest density obtained by the latter is also doubly higher than those provided by the former two models. Figure 3.8 shows the comparison of pressures obtained by the Isentropic model, the modified Schmidt model, and the Schmidt model under Implementations I and II with $\rho_g : \rho_l = 10^{-5}$ as denoted by Schmidt-I and Schmidt II, respectively (see Section 3.3.2) (hereafter, Schmidt-I and Schmidt-II imply the employment of the Schmidt model under implementation I and implementation II, respectively). The results from Schmidt-I and Schmidt-II look fairly similar in shape except for the presence of pressure oscillations in the vicinity of the cavitation interface for Schmidt-II. This is because Schmidt-I assumes that the flow cavitates at the saturated pressure p'_{sat} which thereby ensures the cavitation pressure is less than the surrounding flow pressure. Although there is no oscillation observed as discussed in Section 3.3.2, the cavitation pressure next to the cavitation interface is still unreasonably high relative to the initial pressure of 1 bar even when the ratio of ρ_g / ρ_l is set to be 10^{-5}. Under Schmidt-II, the calculated cavitation pressure next to the cavitation interface takes on a more acceptable value but is still quite higher than the given *physical* cavitating pressure of 62.5 Pa. Moreover, obvious numerical oscillations are observed across the cavitation interface, which supports the analysis as discussed in Section 3.3.2. Such oscillations indeed hamper

the possible wider application of this model. On the other hand, a pressure jump across the cavitation boundary is well captured by the modified Schmidt model, and the cavitation pressure is always below the surrounding flow pressure. It is clearly shown in Fig. 3.7 that the result obtained by the modified Schmidt model compares favorably with results obtained by the Isentropic model, and the modified Schmidt model produces far reasonable results than the Schmidt model. It may be reiterated that this case is calculated under the condition of $\rho_g : \rho_l = 10^{-5}$. As analyzed in Section 3.3.2, the Schmidt model is inapplicable when $\rho_g : \rho_l > 10^{-5}$. To further verify this analysis, the ratio $\rho_g : \rho_l$ is set to 10^{-4} and the results obtained by Schmidt-I and Schmidt-II are shown in Fig. 3.9 at t=0.2ms. It is found that the cavitation pressures as calculated by both models take on a magnitude of tens of thousand of Pa since a very large "saturated" pressure p'_{sat} (close to $1 bar$) is employed to keep the cavitation pressure positive. Such *nonphysical* large cavitation pressure results in *nonphysical* flow profiles as shown in Fig. 3.9. The result by Schmidt-II indicates some rather severe *nonphysical* pressure oscillations. The modified Schmidt model, however, provides a much lower cavitation pressure which is kept below the physical saturated pressure (when the ratio of $\rho_g : \rho_l$ increases to a value larger than 10^{-4}, no meaningful result whether under Schmidt-I or Schmidt-II is obtained)

The present computation is also carried out to t=2.5ms for comparing to the numerical results obtained by Multiphase model (Saurel and Abgrall, 1999b). Figure 3.10 shows the flow profiles at five different instances of 0.5ms, 1.0ms, 1.5ms, 2.0ms and 2.5 ms, where the left column and right column indicate the results obtained by Multiphase model and the Isentropic model, respectively. The results obtained by the Isentropic model are in reasonable agreement with those by Multiphase model. It is

also found that the Isentropic model provides lower cavitation density when compared to Multiphase model. This is possibly because Multiphase model (Saurel and Abgrall, 1999b) assumes that the gas and water coexist initially.

3.5 Summary for Chapter 3

Four one-fluid cavitation models, called the Cutoff model, the Schmidt model, the modified Schmidt model and the Isentropic model, have been analyzed and compared in this chapter. The Cutoff model results in some nonphysical consequences in the computation of cavitation pressure. The modified Schmidt model, as well as the Schmidt model, is inconsistent with the sound speed formulation (3.10). Numerical results, however, show that the modified Schmidt model is able to produce reasonable results for all 1D cavitating flows in this chapter when compared to the mathematical self-consistent Isentropic one-fluid model. This is because the barometric relations for the modified Schmidt model and the Isentropic model are close to each other. It is also found that the Isentropic model is able to completely remove the mathematical and physical inconsistency with a little more computational cost than the other three models. The analytical solutions as well as other published numerical data are then presented to verify the analysis and comparisons. The further application of these one-fluid models, where some experimental results are available, will be carried out in next chapter.

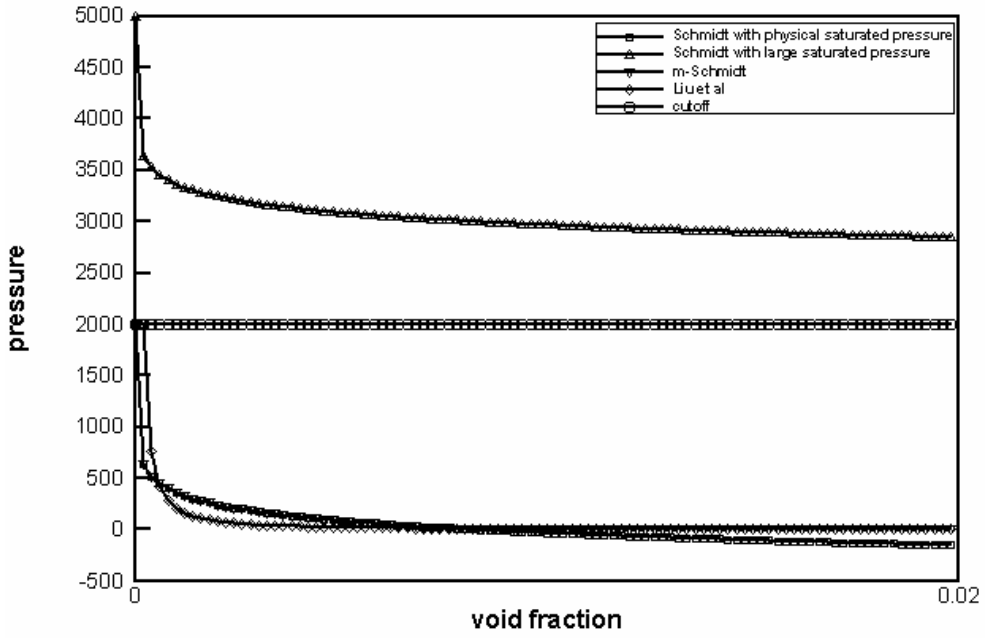

Fig. 3.1 Pressure of mixture with void fraction changes. The densities of gas and liquid are 1000kg/m^3 and 1kg/m^3 while the sonic speeds of gas and liquid are 1538m/s and 208m/s, respectively.

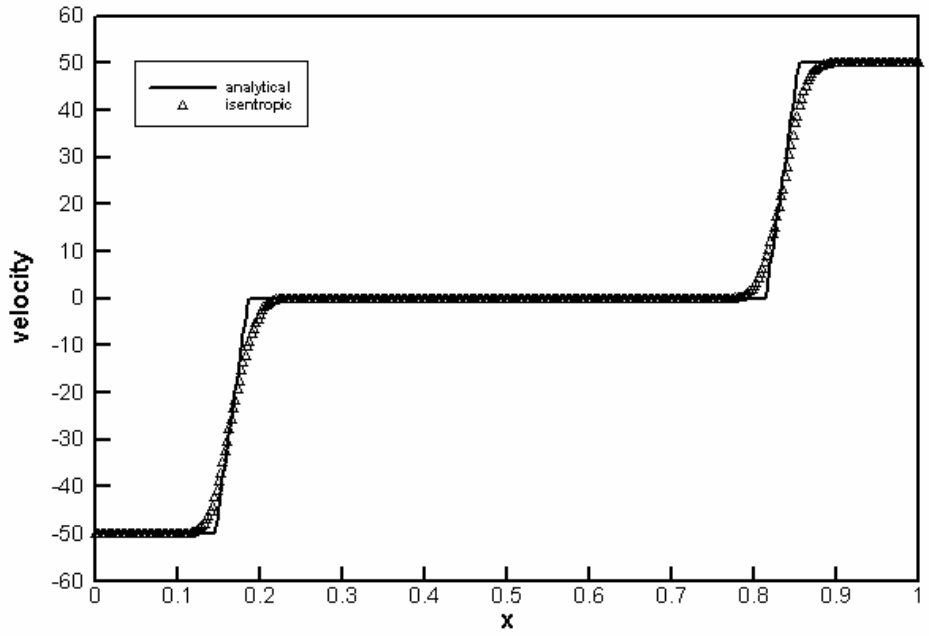

Fig. 3.2a Velocity profile for Case 3.4.1 (without cavitation).

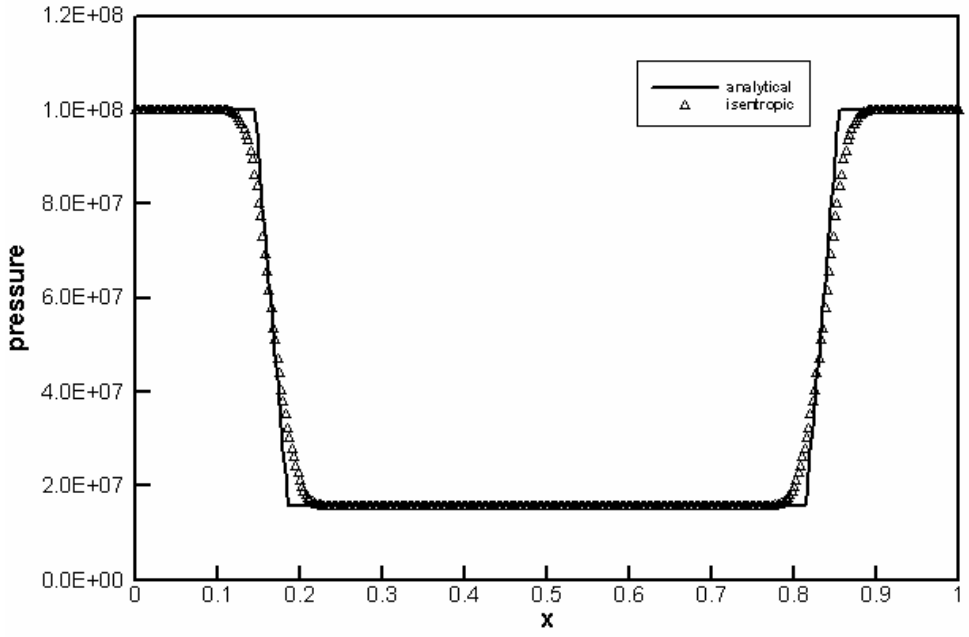

Fig. 3.2b Pressure profile for Case 3.4.1 (without cavitation).

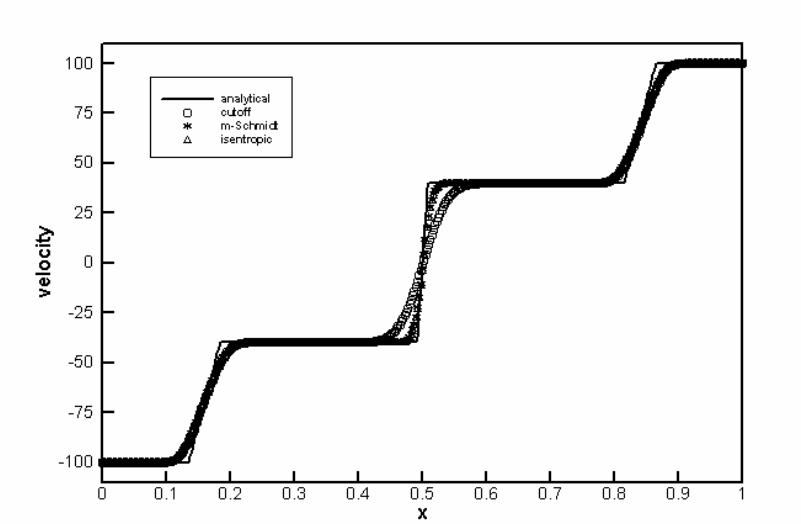

Fig. 3.3a Velocity profiles for Case 3.4.2 by the Isentropic model, the modified Schmidt model and the Cutoff model (with cavitation).

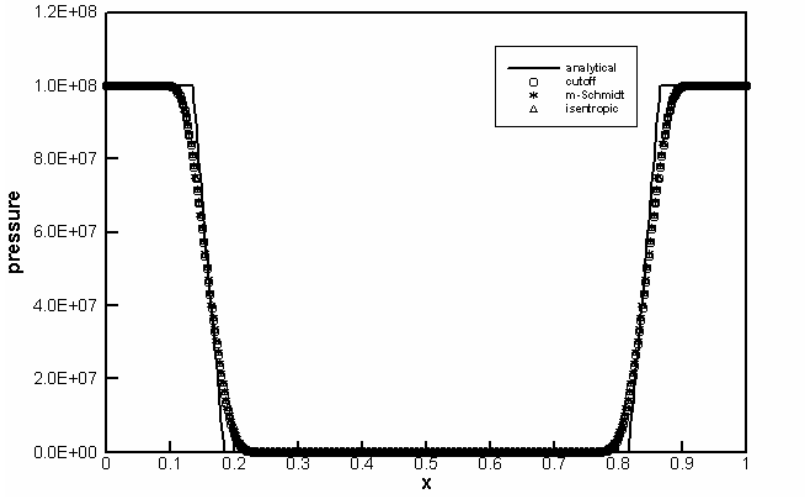

Fig. 3.3b Pressure profiles for Case 3.4.2 by the Isentropic model, the modified Schmidt model and the Cutoff model (with cavitation).

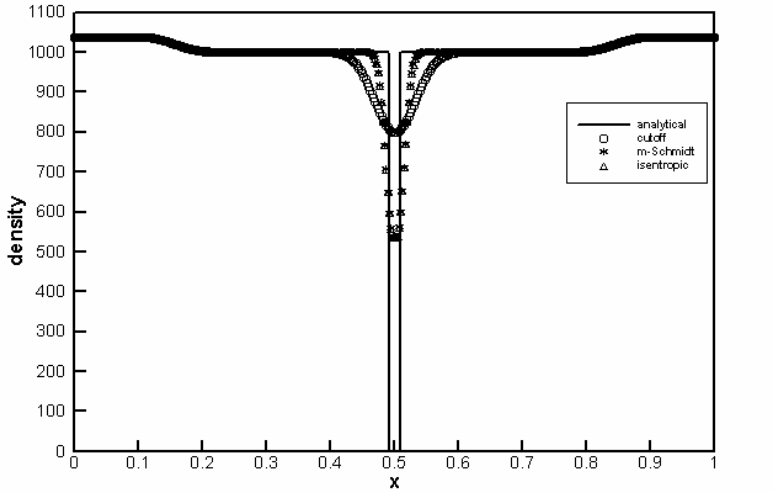

Fig. 3.3c Density profiles for Case 3.4.2 by the Isentropic model, the modified Schmidt model and the Cutoff model (with cavitation).

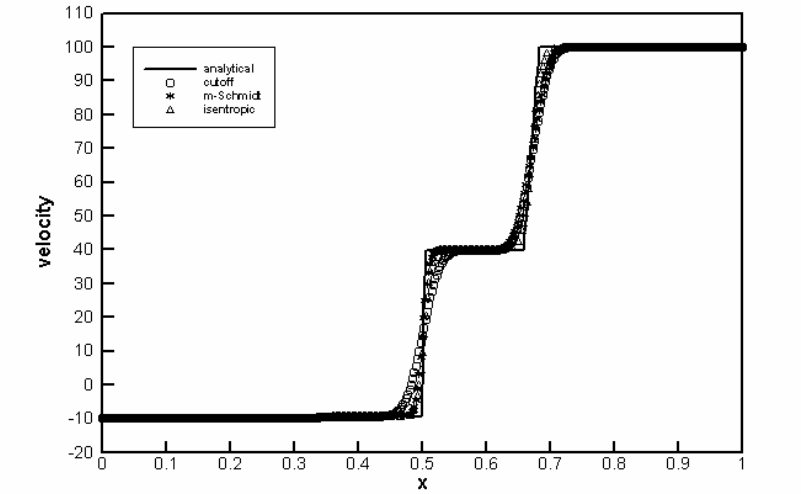

Fig. 3.4a Velocity profiles for Case 3.4.3 by the Isentropic model, the modified Schmidt model and the Cutoff model (with cavitation).

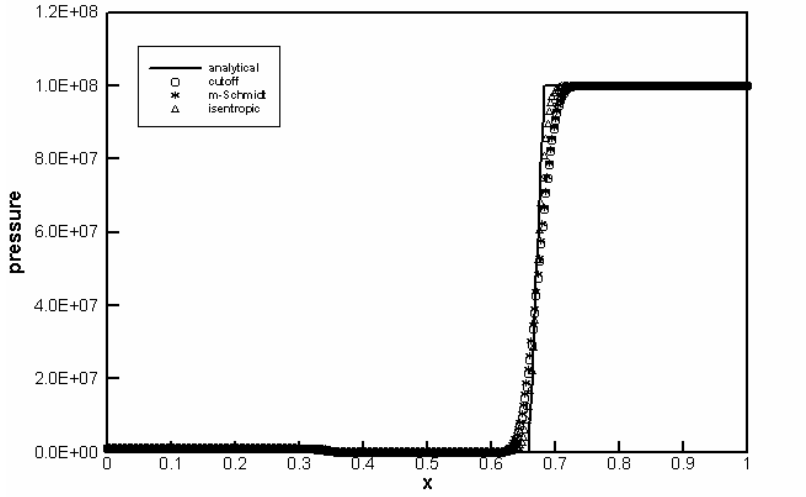

Fig. 3.4b Pressure profiles for Case 3.4.3 by the Isentropic model, the modified Schmidt model and the Cutoff model (with cavitation).

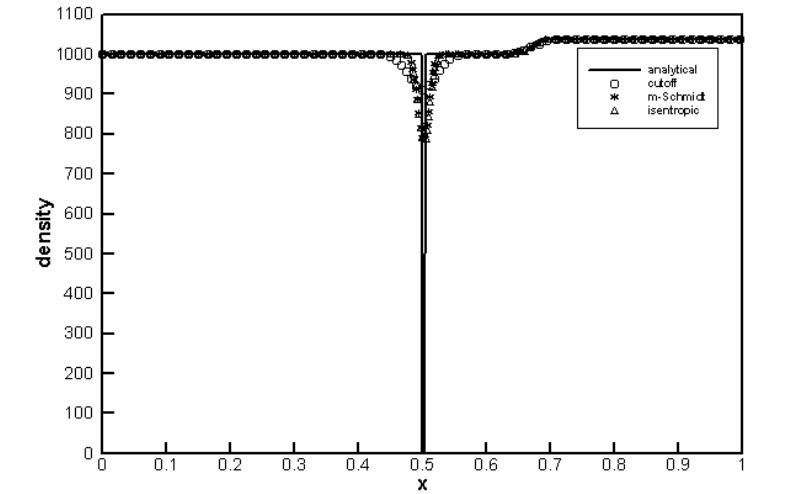

Fig. 3.4c Density profiles for Case 3.4.3 by the Isentropic model, the modified Schmidt model and the Cutoff model (with cavitation).

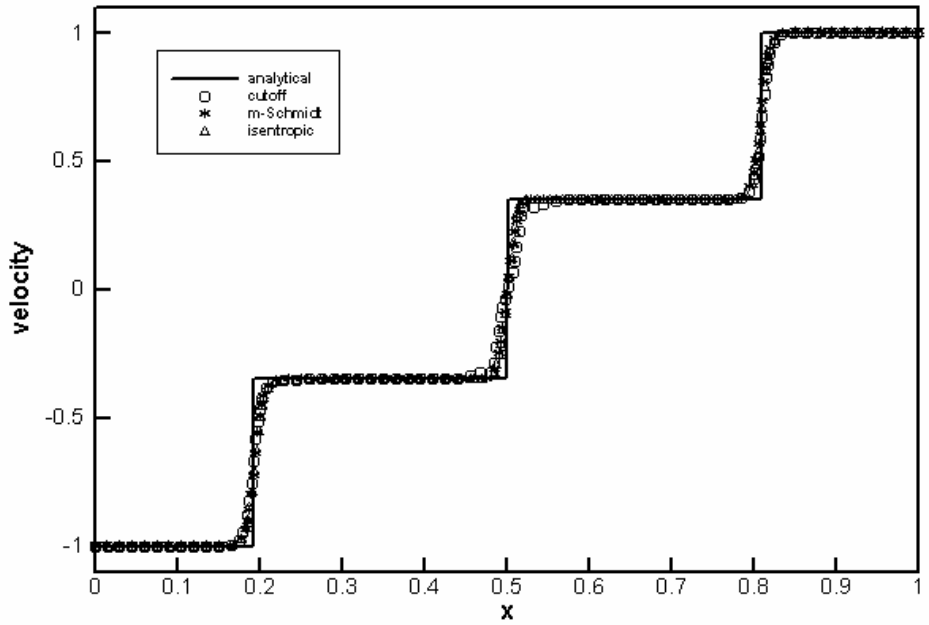

Fig. 3.5a Velocity profiles for Case 3.4.4 by the Isentropic model, the modified Schmidt model and the Cutoff model (with cavitation).

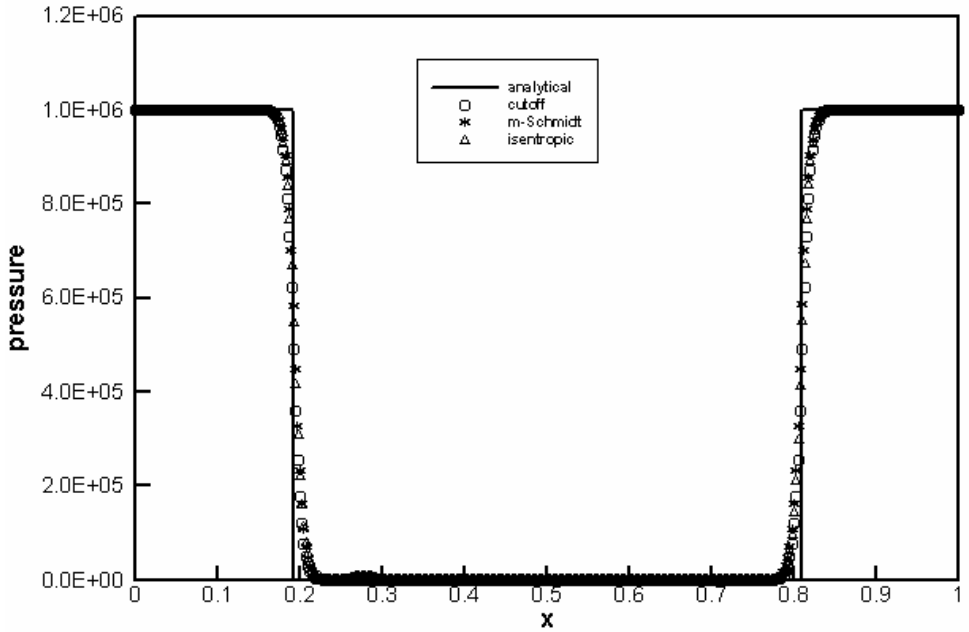

Fig. 3.5b Pressure profiles for Case 3.4.4 by the Isentropic model, the modified Schmidt model and the Cutoff model (with cavitation).

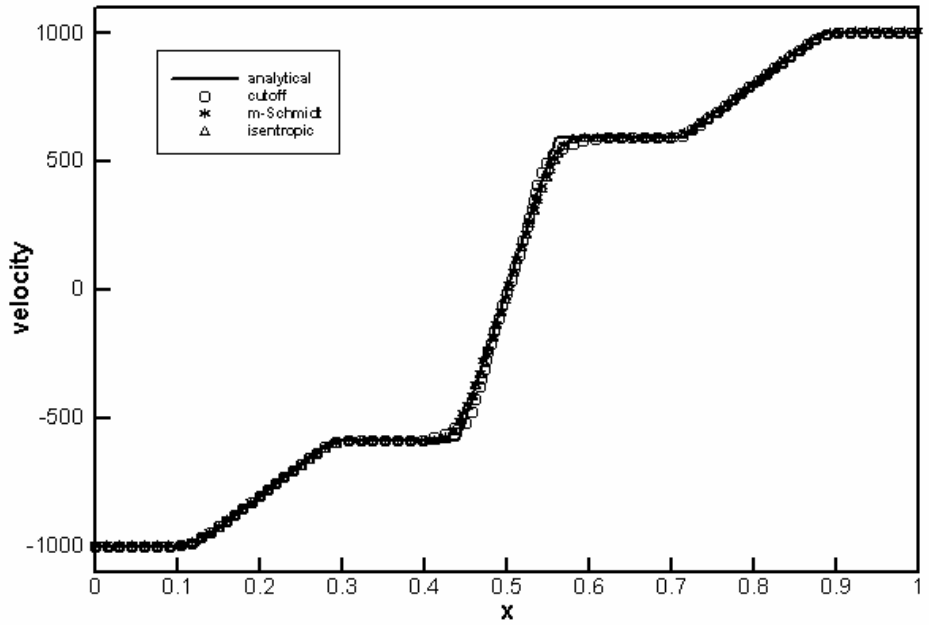

Fig. 3.6a Velocity profiles for Case 3.4.5 by the Isentropic model, the modified Schmidt model and the Cutoff model (with cavitation).

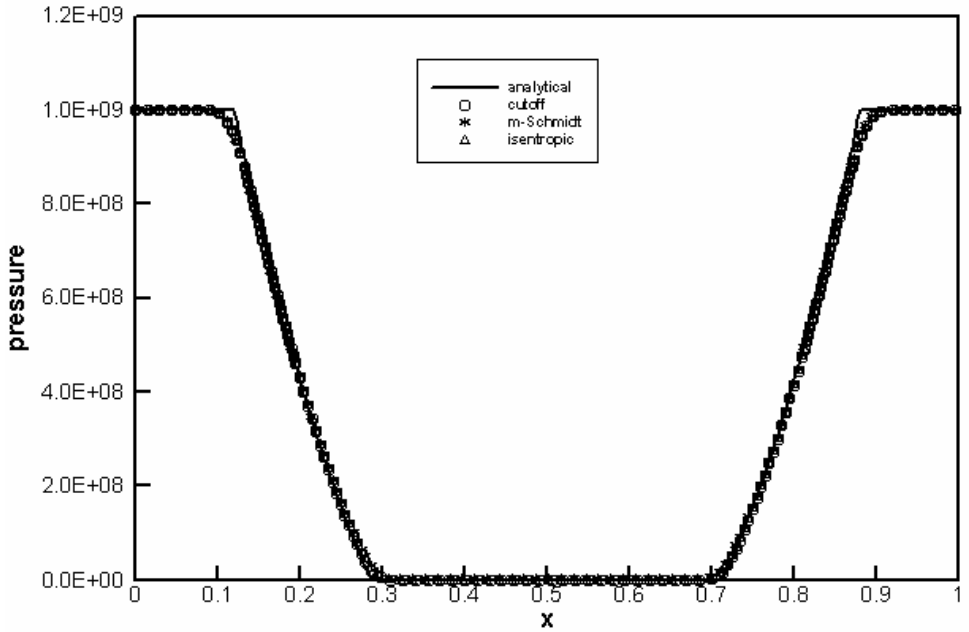

Fig. 3.6b Pressure profiles for Case 3.4.5 by the Isentropic model, the modified Schmidt model and the Cutoff model (with cavitation).

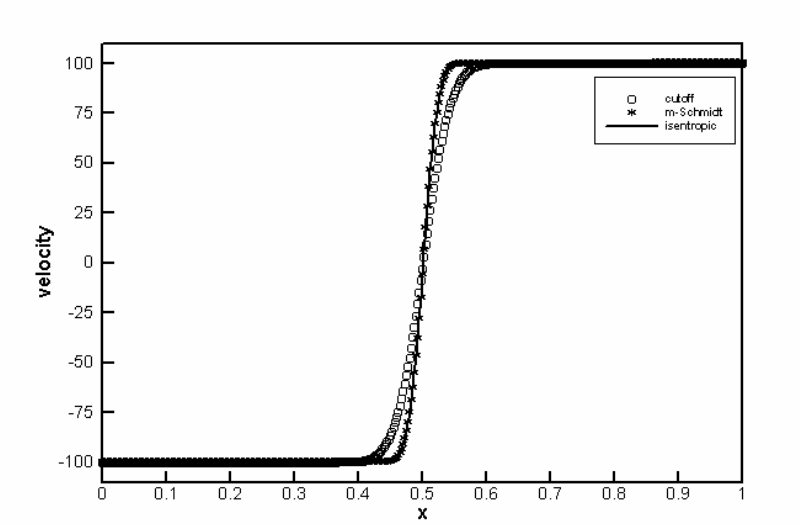

(a)

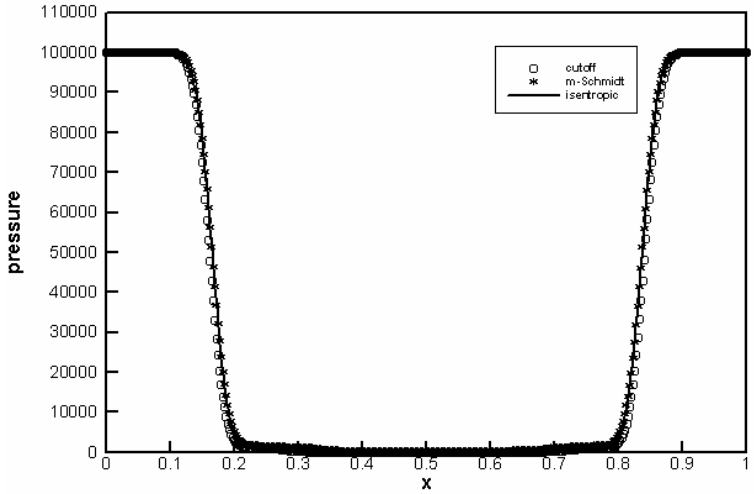

(b)

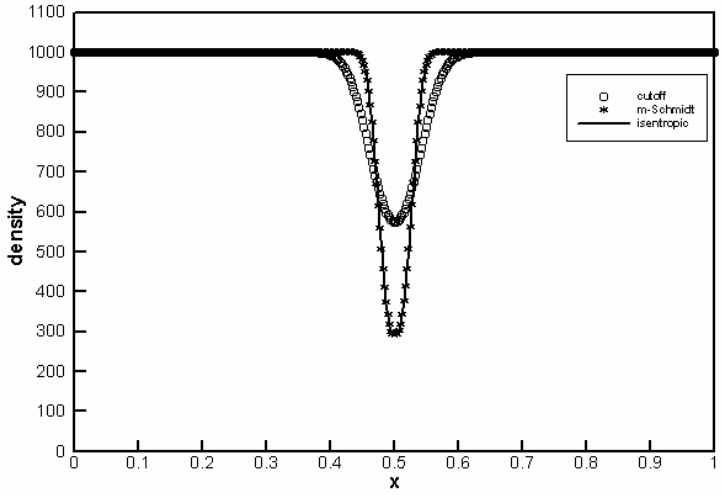

(c)

Fig. 3.7 Flow profiles for Case 3.4.6 by the isentropic model, the modified Schmidt model and the Cutoff model.

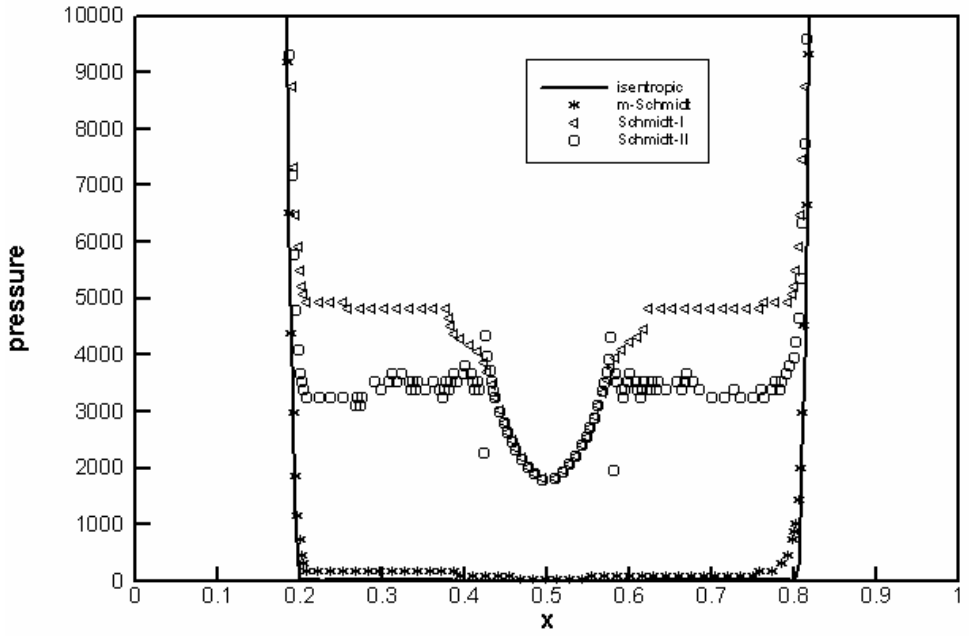

Fig. 3.8 The close-up view of pressure profiles for Case 3.4.6 by the Isentropic model, the modified Schmidt model and the Schmidt model (I & II) with a vapor to liquid density ratio of 10^{-5}.

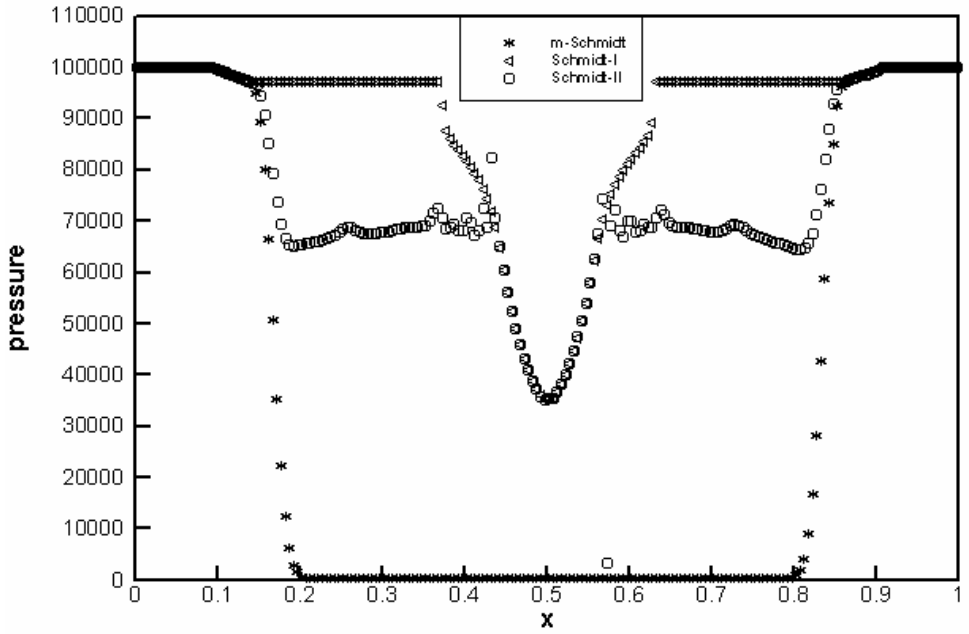

Fig. 3.9 The comparison of closed-up view of pressure profiles for Case 3.4.6 by the Schmidt-I to the Schmidt-II with a vapor to liquid density ratio of 10^{-4}.

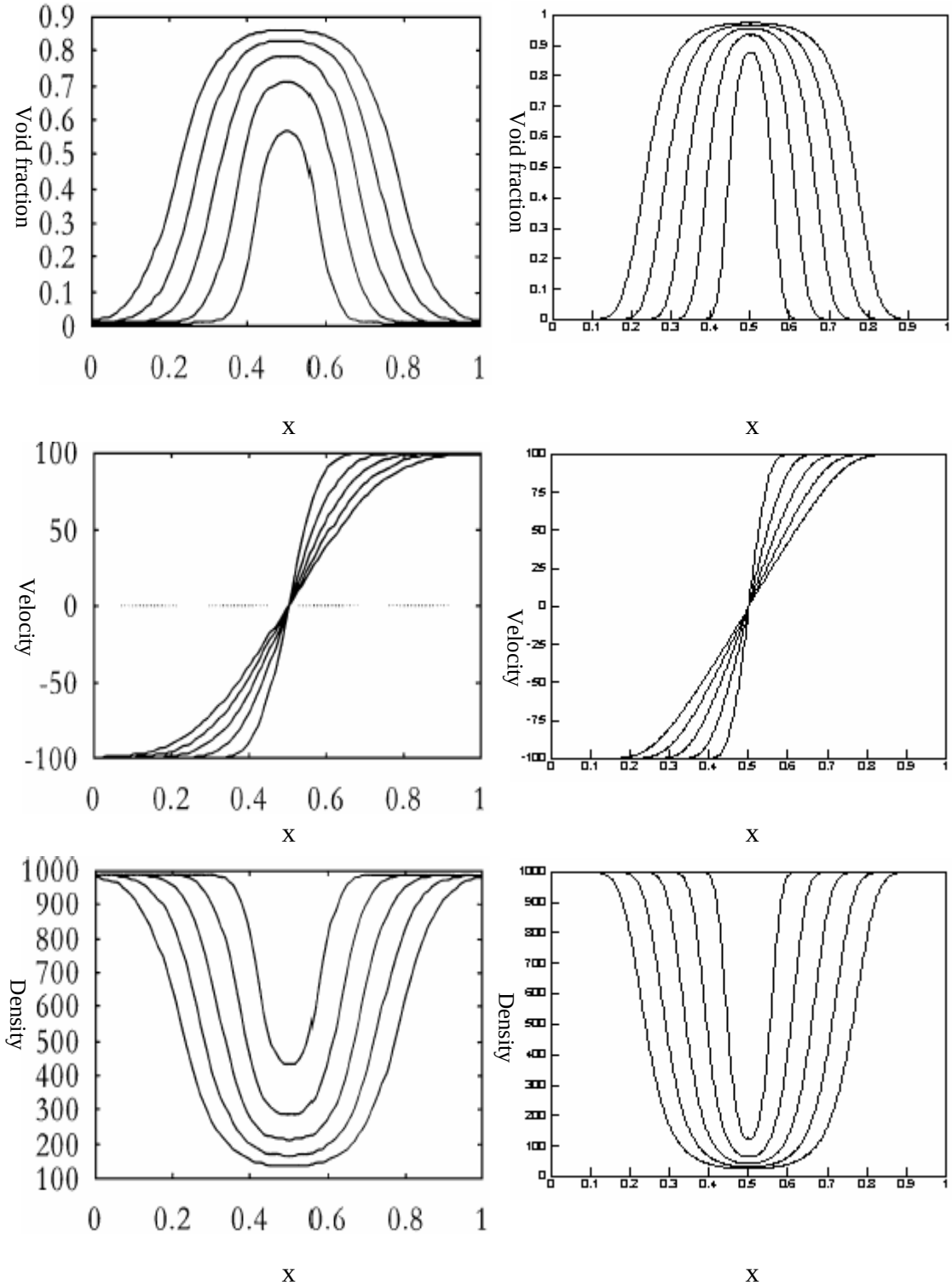

Fig. 3.10 Comparison of flow variables for Case 3.4.6 at times 0.5, 1.0, 1.5, 2.0, and 2.5ms between Saurel's Multiphase model (left) (Saurel et al, 1999) and the Isentropic model (right).

$\rho_g : \rho_l$	ρ_g	$p'_{\min} \approx -2\rho_g . a_g^2 . (\ln \frac{\rho_g}{\rho_l} + \ln \frac{a_g}{a_l})$
10^{-5}	$0.01 kg/m^3$	$0.05 bar$
10^{-4}	$0.1 kg/m^3$	$0.97 bar$
10^{-3}	$1.0 kg/m^3$	$18.3 bar$

Table 3.1 The variation of the approximate value of $p'_{\min}$ with the vapor to liquid density ratio.

The Schmidt model	***Physical status***	***The Modified Schmidt model***	***Physical status***
p'_{sat} is far higher than p_{sat}	nonphysical	p'_{sat} can be set to be not larger than p_{sat}	physical
Negative pressure dose not appear	physical	Negative Pressure appears	nonphysical
No pressure cut-off is needed	physical	Pressure cut-off is used to remove the negative pressure	nonphysical
Pressure inside the cavitation region can allow being far higher than p_{sat}	nonphysical	pressure inside the cavitation region does not allow to be higher than the surrounding pressure	physical
there is no inconsistency between the EOS and the formulation of the sound speed used under the assumption of gas and liquid components with constant density and sound speed	physical	There are inconsistencies between the EOS and the formulation of the sound speed used.	nonphysical

Table 3.2 Comparison of physical status between the Schmidt model and the modified Schmidt model.

Chapter 4

Applications: 1D Pipe/Tube Cavitating Flows

The numerical methods presented in Chapter 2 and the cavitation models presented in Chapter 3 will be applied to simulate several cavitating flows in a tube. The cavitation creation, evolution and collapse, occurred in a pipe or tube, will be studied in detail to better understand the underlying physics of large dimension unsteady cavitations. The cavitation may cause severe damage to a pipe due to the pressure surges caused by cavitation collapse. For analysis of such damage, three problems are considered here. The first one is a Riemann problem in a closed tube where the cavitation phenomenon can be captured and observed clearly and the performances of four one-fluid cavitation models as presented in Chapter 3 are clearly shown. The second one is a water-hammer problem with wide application in engineering design. Under different initial conditions, the cavitation may occur at different locations of the pipe and will cause different damages to the pipe. Both experiments and numerical results can be found in literature for comparison. The third problem is an initially multiphase (gas-water) compressible flow in a closed tube. The cavitation arises from the region near the gas-water interface and travels towards the end wall. In this case, the interface is tracked by the present GFM developed and the cavitation is simulated by various one-fluid cavitation models as presented in Chapter 3. The main purpose of this chapter is to study the cavitation physics in a pipe/tube flow and to test the proposed numerical methods and cavitation models.

4.1 Introduction

Cavitation plays an important role in practical engineering problems and development of modern hydraulic tools and injection systems. Cavitation is a relevant

feature in structural failure prediction of pipelines transporting liquids (Freitas Rachid and Costa Mattos, 1998a, 1998b) and in the analysis of the response of submerged structures excited by transient acoustic waves (Fellipa and Deruntz, 1984). It can also form at the surface of a high speed submerged body (supercavitation) and affect the motion of the body (Owis and Nayfeh, 2003). Furthermore, the performance of an oil nozzle is highly dependent on the cavitation physics (Schmidt et al, 1999). Extensive research has been carried out for the cavitation generated from a flow passing through a body, like hydrofoil, plate and venturi type duct (Ventikos and Tzabiras, 2000; Ahuja et al, 2001 ; Lohrberg et al, 2002; Coutier-Delgosha et al, 2002, 2003). Such cavitation, generally a cloud cavitation or a sheet cavitation, is relatively steady with relative regular collapse cycles. The simulation of this type of cavitation usually takes the N-S equation as governing system and the main fluid flow is assumed to be incompressible. On the other hand, in the computation of internal flows through nozzle injectors with high flow pressure and velocity (high Mach number) the liquid compressibility may be significant and has to be taken into account (Schmidt et al, 1999). Some work in the nozzle cavitating flow can be found in Soteriou et al (1995). The size of such cavitation is relatively small and the ratio of liquid to vapor of the flow is more than 10000: 1.

Compared to the cavitation mentioned above, the cavitation occurred in a pipe/tube may have a large dimension. The motion of such cavitation leads to severe pressure transient which may cause pipe failure. For example, a cavitation/vapor bubble is created from the surface of the check valve, as the fluid momentum is arrested, over-compression of the cavitation can produce a reverse flow in the pipe thereby leading the check valve to be slammed closed, resulting in a water-hammer transient. The water-hammer transient has been studied in detail by Sanada et al (1990) and Chaiko

and Brinckman (2002). The cavitation models used to capture these cavitations have been reviewed in Chapter 1. The present computation of the pipe cavitating flows and water-hammer problems will be shown in Section 4.4. It will be found that our simulation can capture the cavitation period and collapse pressure reasonably when compared to the experiments and other numerical solutions.

The rest of this chapter will be organized as follows. The governing equation with source term for the water-hammer problem and the boundary condition used in the present computation are presented in Section 4.2. The solution procedures and numerical examples are shown in Section 4.3. A brief summary is presented in Section 4.4.

4.2 1D Boundary Treatment

The usual treatments of complete reflecting boundary, non-reflecting inlet and outlet boundaries are necessary for the present one-dimensional and multi-dimensional computations. More specially, a reservoir boundary has to be enacted or imposed in the computation of water-hammer problem (see Case 4.3.2). For all stationary rigid walls (boundaries), the complete reflecting boundary condition is used (see Case 4.3.1). When an underwater explosion is simulated, the shock should, physically, travel to the region beyond the computational domain. Thus, a non-reflecting boundary is generally employed. The application of such boundary condition based on the characteristic method has been described in detail by Liu (2000). In the computation of a water-hammer problem, the following governing system is employed:

$$\frac{\partial U}{\partial t}+\frac{\partial F(U)}{\partial x}=S\,, \tag{4.1}$$

where $S=[S_1,S_2]^T=[0,-f\rho u|u|/2D]^T$, f is the Darcy friction factor and D is the diameter of the pipe. The ratio of f/D is determined by initial conditions. The source

term S is used to simulate the pipe friction force. It should be noted that this source term is set to be zero for all cases in the present computation except for the water-hammer problem. The characteristic form of (4.1) can be written as

$$\left(a\frac{\partial \rho}{\partial t}-\rho\frac{\partial u}{\partial t}\right)-(u-a)\left(a\frac{\partial \rho}{\partial x}-\rho\frac{\partial u}{\partial x}\right)=2aS_1^m, \tag{4.2a}$$

$$\left(a\frac{\partial \rho}{\partial t}+\rho\frac{\partial u}{\partial t}\right)+(u+a)\left(a\frac{\partial \rho}{\partial x}+\rho\frac{\partial u}{\partial x}\right)=2aS_2^m, \tag{4.2b}$$

where $\left[S_1^m, S_2^m\right]^T=\frac{1}{2a}\left[(u+a)S_1-S_2, -(u-a)S_1+S_2\right]^T$. If we assume the reservoir is connected to the left/right end of the pipe and thus the pressure and density at the left/right end of the pipe are assumed as constants. (4.2) leads to

$$\frac{\partial u}{\partial t}-(u-a)\left(\frac{a}{\rho}\frac{\partial \rho}{\partial x}-\frac{\partial u}{\partial x}\right)=2aS_1^m=-S_2, \tag{4.3a}$$

$$\frac{\partial u}{\partial t}+(u+a)\left(\frac{a}{\rho}\frac{\partial \rho}{\partial x}+\frac{\partial u}{\partial x}\right)=2aS_2^m=S_2, \tag{4.3b}$$

(4.3a) or (4.3b) is solved to obtain the velocity at the left or right end of the pipe for water-hammer problem as in Case 4.3.2.

4.3 1D Applications to Flows in Pipeline and Multi-medium Tube

If we assume the flow variables at $t=t^n$ are known, the numerical procedures to obtain flow variables at the next time step t^{n+1} can be summarized as follows:

1. Initialize flow field and level set distance function (if any).

2. Solve (4.1) to obtain flow variables at the new time step.

3. Evaluate the value of pressure (p) to check if the pressure is less than the *physical* saturated pressure (p_{sat}) (cavitation occurs).

4. Obtain the flow pressure. If $p \geq p_{sat}$, pressure can be solved from Tait's equation with known density. Otherwise, the selected cavitation model is employed to obtain the cavitation pressure.

5. Proceed to 2 and iterate from 2 to 4 until the desired time duration is simulated.

The Cutoff model, the modified Schmidt model and the Isentropic model as mentioned in Chapter 3 are employed in the numerical examples for comparison and analysis. The present GFM (see Chapter 2) is used to calculate the numerical example where two phases exist initially (Case 4.3.3). For the cases in which the possible oscillation occurs, a relatively small CFL number is used. As a result, a CFL number of 0.5 will be used to calculate for the Case 4.3.1. For Case 4.3.2 (water-hammer problem), a CFL number of 0.8 is used and reasonable results are obtained when compares with experimental results. Case 4.3.3 is a challenging problem not amendable to a large CFL number, and thus a much smaller value at 0.1 is used; this prevents the oscillations from dominating the flow physics. Similar to Chapter 3, the *physical* saturated pressure p_{sat} is set to be $62.5Pa$ and all the results in figures are dimensional in the international standard units (i.e. pressure is in $Pascal$, density is in kg/m^3 and velocity is in m/s) except for those with their own units.

Case 4.3.1: 1D Cavitating Flow in a Closed Tube. This case is similar to Case 3.4.6 as mentioned in Chapter 3, except that the two ends of the tube are closed before the flow starts. Therefore, a shock created at each end moves towards the center, resulting in shock-cavitation interaction and cavitation collapse. The flow initial status and computational conditions are kept the same as for Case 3.4.6. The walls at the two ends are treated as complete reflecting boundaries. The purpose of this model is to study the shock-cavitation interaction and cavitation collapse. In this model, the flow is initially pure water and soon changes phase into a vapor-water mixture at the center,

and then reverting back into a pure liquid after the cavitation collapse. Figures 4.1 and 4.2 depict a series of plots for the three one-fluid cavitation models at the time instance of 0.3ms and 0.5ms, respectively. The results between the Isentropic model and the modified Schmidt model are close to each other during the whole computation for this problem except for the differences as observed and discussed in Case 3.4.6 during the cavitation expansion. The results provided by the Cutoff model, however, are very different from those provided by the former two models. It is observed that the shocks created at the ends propagate towards the center and meet the outward propagating rarefaction generated at the center. The shock then propagates through the rarefaction region with a mitigated strength and then interacts with the expanding cavitation interface. As a result, a stronger discontinuity forms at the cavitation interface, where larger pressure and velocity jumps occur. This leads to the cavitation interface moving like a “genuine shock” in the evolution of cavitation collapse. The plots shown in Figs. 4.1a to 4.1c are the results just before the cavitation collapse, while the plots in Fig.4.2a to 4.2c are the results after cavitation collapse when the flow returns back to being a pure liquid. The cavitation collapse generates two shocks which propagate outwards with equal strength as that for the shocks generated initially at the two ends. The Cutoff model provided a larger dimension of cavitation, resulting in a far later cavitation collapse for this problem. Such discrepancy for the Cutoff model, the modified Schmidt model, and the Isentropic model are apparently due to the different cavitation pressures and dimensions predicted by different models.

Case 4.3.2: 1D Water Hammer Cavitating Flows. In cold water or under the normal atmospheric condition, water is usually assumed to be isothermal and the sound speed for the surrounding flow is taken as a constant. The EOS for water becomes

$p - p_0 = a_l^2(\rho_l - \rho_{l0})$ instead of Tait's EOS, where ρ_{l0} is the water density at pressure p_0. Therefore, we have $p = \rho a_l^2 + B'$ where $B' = p_0 - \rho_{l0} a_l^2$.

Selected cases were previously investigated experimentally in detail by Sanada et al (1990) where the flow is assumed as isothermal. It should be noted that a source term $S = [0, -f\rho u|u|/2D]^T$ in the right side of Equation (4.1) is added to account for the viscous friction of the pipe. The pipe used in this computation is 200 meters long and each end of the pipe is connected to a water tank and equipped with a valve. To facilitate a thorough comparison of the present computation and experimental results, this problem is divided into three sub-cases: a) upstream cavitating flow; b) midstream cavitating flow; c) downstream cavitating flow. The schematic diagrams for there three sub-cases are shown in Fig. 4.3 and the possible cavitation located are also shown in this figure. The comparison among the Cutoff model, the Schmidt model, the modified Schmidt model and the Isentropic model at x=0m is carried out for Case 4.3.2a, and then the Isentropic model is used to calculate Case 4.3.2b and Case 4.3.2c. For Case 4.3.2a and Case 4.3.2c, the pressure at both the upstream and downstream tanks is kept constant and one of the valves will be closed suddenly to generate cavitation starting from either end of the pipe. In the computation of Case 4.3.2b, both valves are always open and pressure in the upstream tank will be decreased rapidly to generate cavitation starting away from the pipe ends. For more details, one can refer to the experimental setup of Sanada et al (1990). A uniform mesh of 1000 cells is distributed and CFL number is set to be 0.8 for all computations. It should be noted that all the experimental results (pressure and velocity histories) are reproduced by the present computation. However, only a (experimental) pressure history is presented for each sub-case. For more experimental results, one can refer to Sanada et al (1990).

The initial flow states of Case 4.3.2a are given as follows: the upstream pressure at the water tank is 5.49164bar and the downstream pressure at the reservoir is 0.98065bar. The water density is 1000kg/m^3 and the fluid flow moves at a constant speed of 1.5m/s before the valve is closed. From the given conditions, it can be deduced that $f/D = 2m^{-1}$ and the constant B' is -6.723E8 Pa. Reflecting boundary condition is used for the left closed valve and the reservoir boundary condition is employed to treat the right boundary. The sudden closing of the upstream valve leads to the occurrence of cavitation starting from the surface of the valve. Such cavitation can evolve to a large dimension as time progresses and then the pressure in the cavitation region becomes very low to generate a large pressure jump across the liquid-cavitation interface. Therefore, the flow will move back from the right water reservoir to compress the cavitation and make the cavitation collapse, resulting in a pressure surge. This is the process of cavitation creation, evolution and collapse of the water-hammer problem. To capture this process, the pressure histories at the left end of the tube (valve surface) are recorded as shown in Figs. 4.4a to 4.4e. It is found that the Cutoff model fails to capture the correct periods of cavitation collapse when compared to experimental result (see Fig. 4.4b). The Cutoff model provides an earlier collapse time and one more collapse than the experimental result. Figure 4.4.c shows that the Schmidt model produces close periods peak pressures of cavitation collapse to experiments. However, the apparent pressure oscillation can be observed before the first cavitation collapse. Such oscillation, as mentioned in Chapter 3, is caused by employed large saturated pressure and possible larger cavitation pressure than surrounding flow pressure. Compared to the Schmidt model, the modified Schmidt model and the Isentropic model are able to capture the period of cavitation collapse and peak pressure accurately as shown in Figs. 4.4d and 4.4e. For both models, the

first collapse pressure head at x=0m is 62m which is very close to experimental result of 66m. The small discrepancy may be attributed to the employed source term which can not completely simulate the viscous friction of the pipe. Another possible reason for the discrepancy is the 1D assumption may not be quite accurate due to end effect. For further verification of the Isentropic model, the pressure histories at x=40m and x=120m are recorded (see Figs. 4.4f and 4.4g) and compared well with the experimental results as shown in Sanada et al (1990); it is also found that the velocity histories obtained by the Isentropic model at various locations of the pipe (see Figs. 4.5a-4.5c) are quite comparable to experimental results (see Sanada et al, 1990).

The initial upstream and downstream pressures of Case 4.3.2b are the same as those of Case 4.3.2a except that the valves at both ends are always open during the computation. The upstream pressure at x=0m decreases rapidly from the initial value of 5.49164bar to a standard atmosphere pressure and then remains as a constant. Such rapid pressure drop generates a rarefaction wave traveling through the pipe and causes the flow pressure to decrease. Associated with the effect of friction, the flow pressure at some locations of the pipe will become lower than the saturated pressure to generate cavitation. The history of such cavitation creation and collapse at x=120m is recorded and compared to experimental result as shown in Fig. 4.6a and 4.6b. The first two collapse pressure heads of the present computation at x=120m are 25m and 20m, respectively (Fig. 4.6b). Meanwhile, the results from the experiments at the same location are 22m and 18m, respectively (Fig. 4.6a). Once again, the results obtained by the Isentropic model are in substantial agreement with those from experiments for both peak pressure and periods. Similar to Case 4.3.2a, the pressure histories at x=0m and x=40m (Figs. 4.6c and 4.6d), as well as the velocity histories at x=40m, x=120m and x=200m (Figs. 4.7a to 4.7c), are also comparable to experiments in Sanada et al (1990).

In Case 4.3.2c, the initial downstream pressures are set to 0.98065bar. When the downstream valve is suddenly closed, a strong shock wave impacts and reflects from the valve. This shock wave interacts with the upstream water tank and then a rarefaction wave is generated and travels from upstream to downstream. The cavitation occurs initially from the downstream valve when this said rarefaction wave interacts and reflects from the downstream valve. Figures 4.8a and 4.8b show the pressure histories at x=200m by the experiment and the Isentropic model. It is apparent that the flow pressure before cavitation occurs for this case is higher than that either of the former two cases due to the downstream shock. Therefore, the first collapse pressure head of this case are much higher than those of the former two cases. Similar to the former two cases, Fig. 4.8b shows that the result obtained by the Isentropic model compares well with the experimental result (Fig. 4.8a). The Isentropic model also gives similar pressure and velocity histories as the experiments (see Figs. 4.8c-4.9a and Sanada et al (1990)).

Numerical results of pressure profile by the modified Schmidt model are also presented for comparison to the results by the Isentropic model for Case 4.3.2a. Figure 4.10 shows the pressure profiles by the modified Schmidt model and the Isentropic model before the cavitation collapse when the flow returns from the right reservoir and begins to compress the cavitation. The pressure oscillation at the region of interface is due to the different EOS used as pointed out also in Liu et al (2004a). It is found that the modified Schmidt model compares rather well with Liu et al's model even when we examine very closely the region of the interface as depicted in the small figure embedded within Fig. 4.10. That is because both models use physical saturated pressure to evaluate if cavitation occurs and the cavitation pressure has relatively trivial effect on the magnitude of surrounding pressure before cavitation collapse.

After the cavitation collapses, there is a greater discrepancy of pressure profile between the modified Schmidt model and the Isentropic model as shown in Fig. 4.11. This difference can be partly attributed to the pressure cut-off as utilized in the modified Schmidt model. Such pressure cut-off causes the motion of the cavitation boundary captured by the modified Schmidt model to be slower than that by the Isentropic model. Therefore, the cavitation collapse as calculated by the Isentropic model is generally earlier than that captured by the modified Schmidt model as shown in Fig. 4.11.

Case 4.3.3: 1D Gas-Water Cavitating Flows in a Closed Tube. This case is taken from Tang and Huang (1996). In their work, a vacuum model was developed and employed to model 1D inviscid cavitating flows. The tube is occupied by a highly pressurized gas on the left and low-pressure water on the right, and the length of tube occupied by the gas is much smaller than that by the water. The initial conditions are $\rho_g = 70.735 kg/m^3$, $p_g = 100692985.3 Pa$, $u_g = 0.0$, $\gamma_g = 2.0$, (x<0.001); $\rho_l = 1000 kg/m^3$, $p_l = 101325 Pa$, $u_l = 0.0$, $\gamma_l = 7.15$, (0.001≤x<0.275). A uniform mesh of 1100 cells is distributed and the CFL number is set to 0.1, which is nearly the maximum workable CFL for the Schmidt model for this problem. The explosive gas-water interface is treated with the present GFM developed in Chapter 2. One purpose of this study is to analyze the shock-cavitation-structure interaction. After the diaphragm separating the explosive gas and water is removed, a strong shock is generated and propagates in the water and a strong rarefaction wave simultaneously propagates towards the left end. As time progresses, the shock impacts the right-end wall and reflects from the wall. The reflected shock wave from the right end meets and goes through the reflected rarefaction from the left wall with a slightly mitigated strength and finally impacts the explosive gas-water interface, resulting in a relatively

weak shock transmitted into the explosive gas and a relatively strong rarefaction wave back into water, which leads to the creation of a cavitation region next to the gas-liquid interface. The cavitation right boundary moves with a speed faster than the local flow velocity and rapidly expands towards the right end. Simultaneously, the reflection of the transmitted shock wave from the left wall soon propagates through the interface and interacts with the left expanding cavitation boundary. Such shock-cavitation interaction causes the left cavitation boundary to move towards the right with an enhanced pressure jump. As a result, the whole cavitation region moves towards the right with an expansion at the right side and compression at the left side. With the left cavitation boundary impacting on the right wall, the cavitation finally collapses at the right end wall, resulting in a strong shock propagating towards the left. Similar cavitation creation and collapse subsequently occur many times. Figures. 4.12b to 4.12e show the pressure history at the right end obtained with the Cutoff model, the Schmidt model, the modified Schmidt model and the Isentropic model. Among the four models, the respective pressure history curves looks very similar because the pressure of surrounding flow is always much higher than cavitation pressure. The result by the Vacuum model is reproduced in Fig. 4.12a for comparison. The comparison looks reasonable except for the smaller initial peak pressure as registered by the Vacuum model. This is possibly due to less grid points used in Tang and Huang (1996). Although the curves of pressure history in Figs. 4.12b to 4.12e indicate no significant difference, there are obvious differences among the detailed flow profiles during the cavitation collapse. Figures 4.13 and 4.14 show the pressure profiles provided by the four models just before and after the first cavitation collapses, respectively. The Schmidt model, the modified Schmidt model and the Isentropic model provide very similar results, while there is relatively flatter pressure profile

provided by the Cutoff model. The magnitude of pressure jump across the cavitation interface and the location of cavitation boundary captured among the four models, however, are very similar for this problem due to large pressure difference between surrounding flow and cavitation region. This is possibly one reason the Cutoff model is able to provide reasonable end pressure history for this specific problem.

4.4 Summary for Chapter 4

In this chapter, the present GFM and one-fluid cavitation models as mentioned in Chapter 2 and Chapter 3 are used to simulate several 1D cavitating flows. The numerical results are quite comparable to experimental results and other published numerical data. The water-hammer problem is investigated in detail by the Isentropic method. It is clearly shown that the Isentropic model is able to provide reasonable peak pressure and periods of collapse for all three sub-cases when compared to experiments. Also, the modified Schmidt model produces very similar results to the Isentropic model while the Cutoff model fails to capture the periods of collapse and apparent oscillations have been observed in the application of the Schmidt model. For the multiphase tube cavitating flow, however, the four models obtain very similar peak pressure and cavitation periods because the presence of high pressure of surrounding flow ensures a large pressure jump across the cavitation boundary. It is obviously shown from this problem that the Cutoff model is applicable in some simulation. The conclusion we can make from this chapter is that the one-fluid cavitation model is relatively simple and easy to implementation. Such simplicity will be further verified in the next chapter when one-fluid models are applied to multi-dimensions.

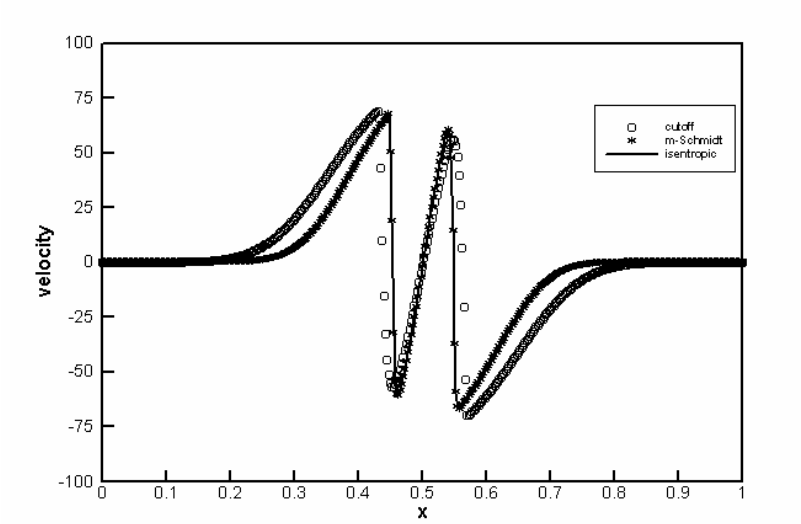

Fig. 4.1a The velocity profile for Case 4.3.1 at t=0.3ms just before cavitation collapse.

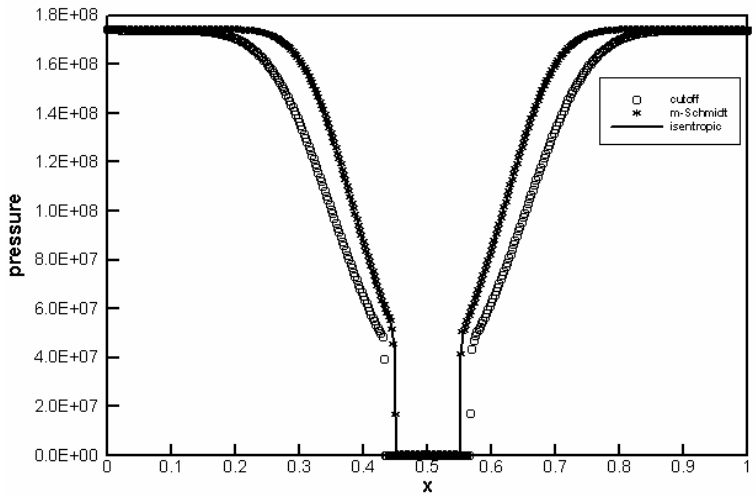

Fig. 4.1b The pressure profile for Case 4.3.1 at t=0.3ms just before cavitation collapse.

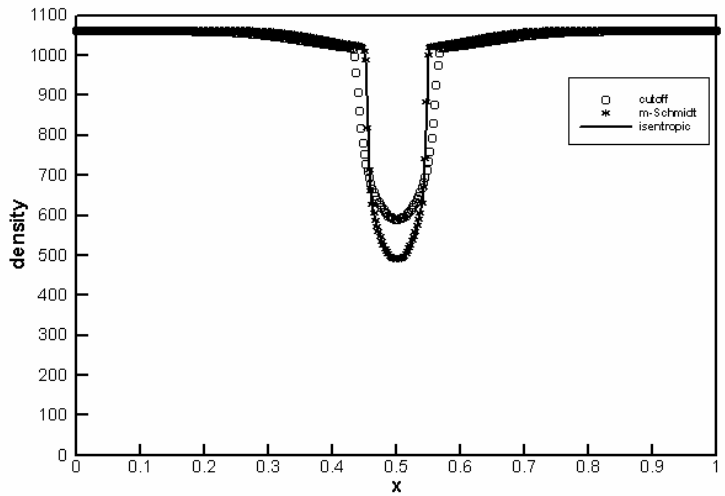

Fig. 4.1c The density profile for Case 4.3.1 at t=0.3ms just before cavitation collapse.

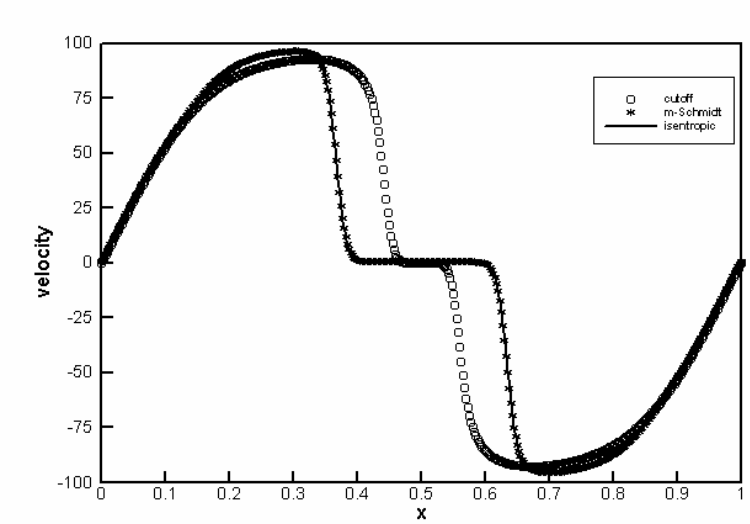

Fig. 4.2a The velocity profile for Case 4.3.1 at t=0.5ms after cavitation collapse.

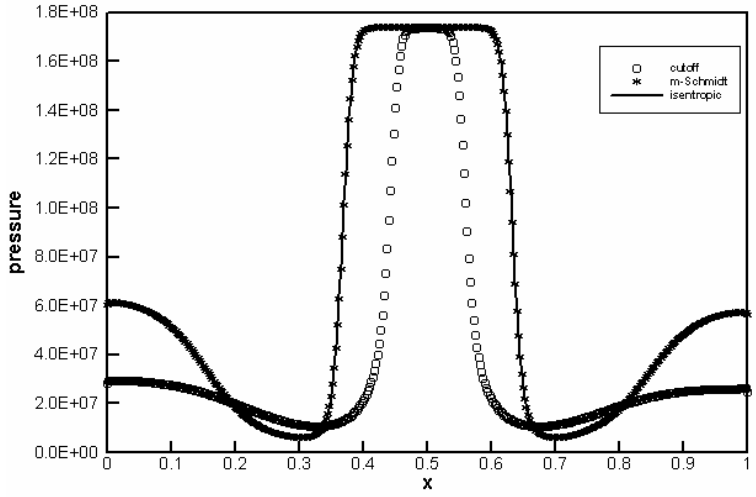

Fig. 4.2b The pressure profile for Case 4.3.1 at t=0.5ms after cavitation collapse.

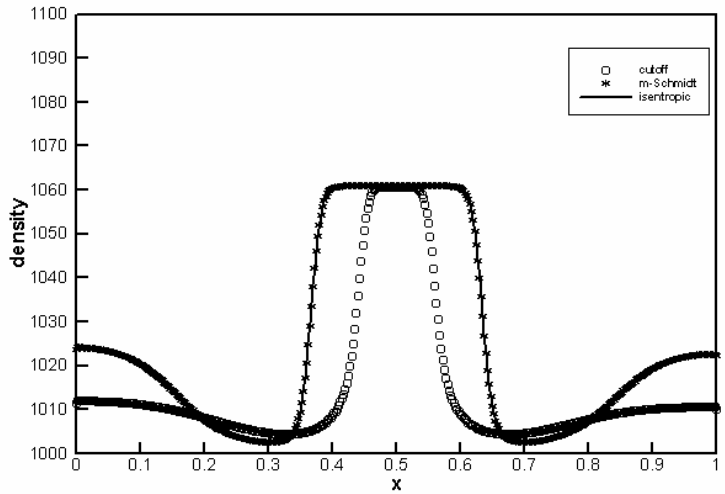

Fig. 4.2c The density profile for Case 4.3.1 at t=0.5ms after cavitation collapse.

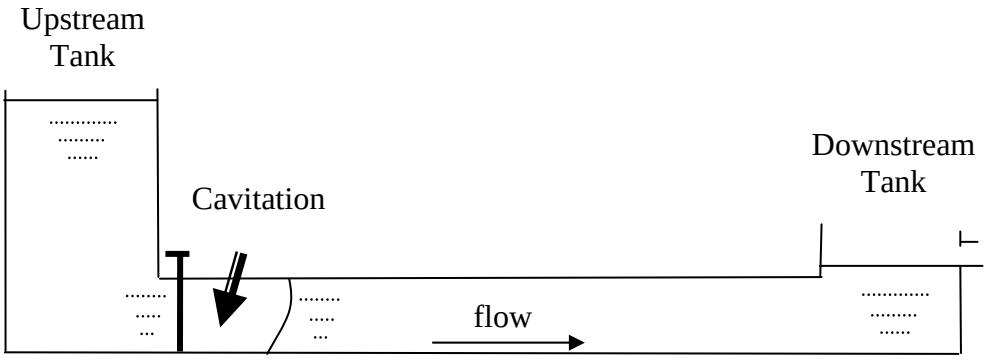

(a) Case 4.3.2a- Upstream type

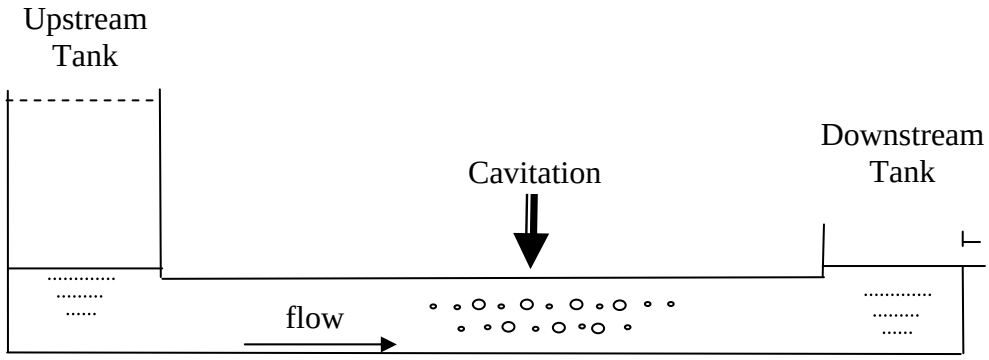

(b) Case 4.3.2b- Midstream type

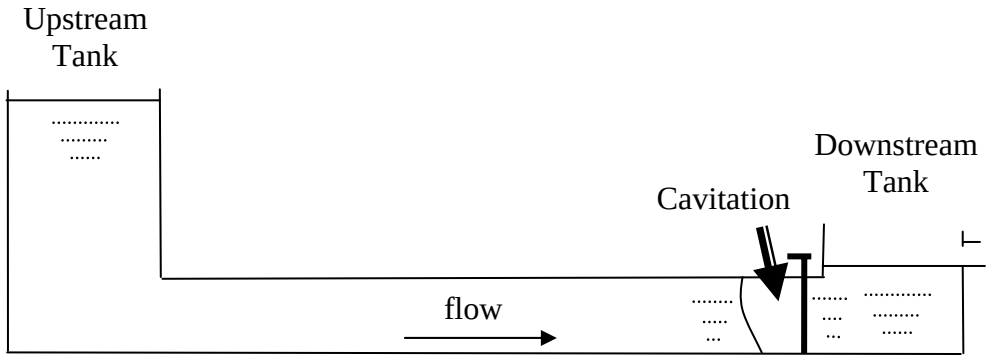

(c) Case 4.3.2c- Downstream type

Fig.4.3 The schematic diagram of water hammer problem for Case 4.3.2 (a) upstream type cavitating flow (Case 4.3.2a); (b) midstream type cavitating flow (Case 4.3.2b); (c) downstream type cavitating flow (Case 4.3.2c).

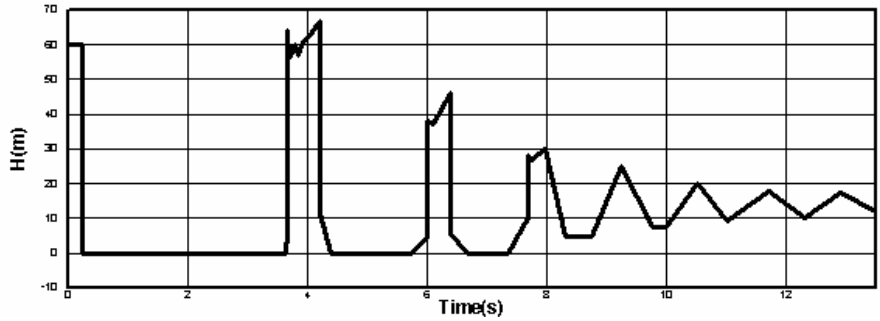

Fig. 4.4a The experimental pressure history for upstream cavitating flow for Case 4.3.2 at x=0m duplicated from (Sanada, 1990).

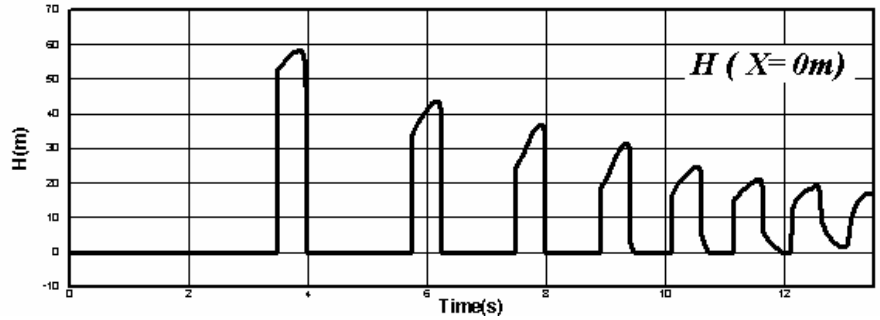

Fig. 4.4b The pressure history for upstream cavitating flow for Case 4.3.2 at x=0m by the Cutoff model.

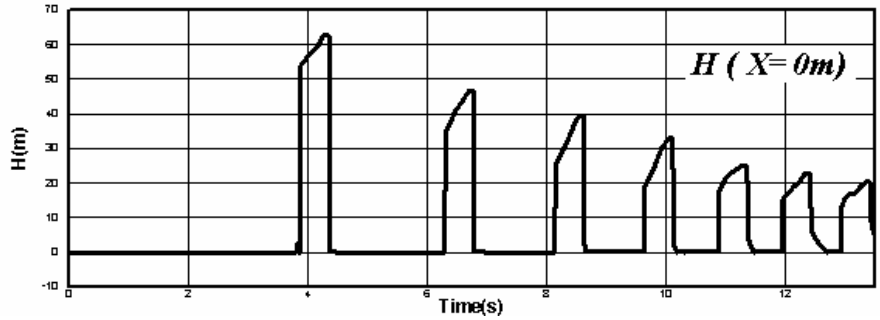

Fig. 4.4c The pressure history for upstream cavitating flow for Case 4.3.2 at x=0m by the Schmidt model.

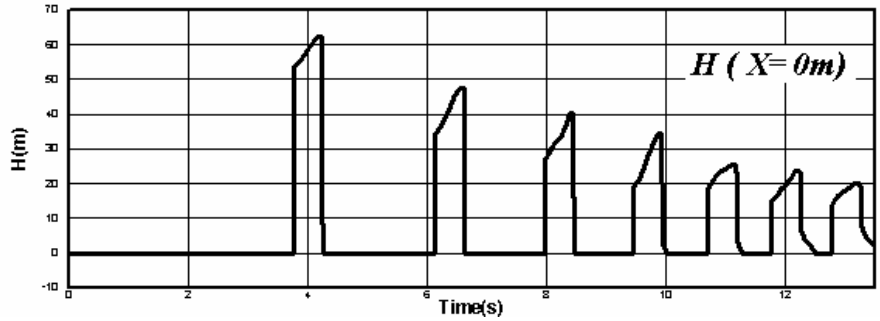

Fig. 4.4d The pressure history for upstream cavitating flow for Case 4.3.2 at x=0m by the modified Schmidt model.

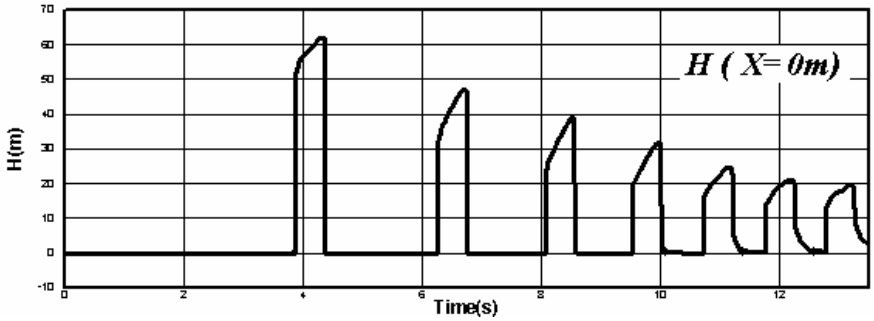

Fig. 4.4e The pressure history for upstream cavitating flow for Case 4.3.2 at x=0m by the Isentropic model.

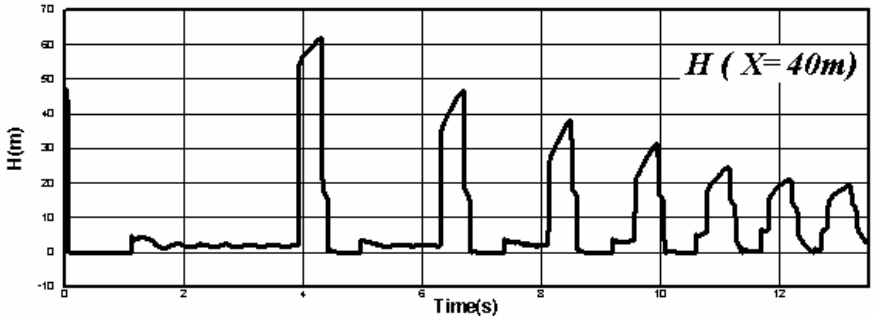

Fig. 4.4f The pressure history for upstream cavitating flow for Case 4.3.2 at x=40m by the Isentropic model.

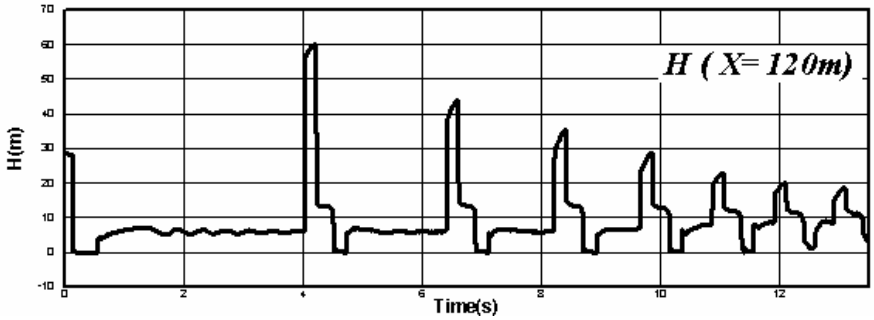

Fig. 4.4g The pressure history for upstream cavitating flow for Case 4.3.2 at x=120m by the Isentropic model.

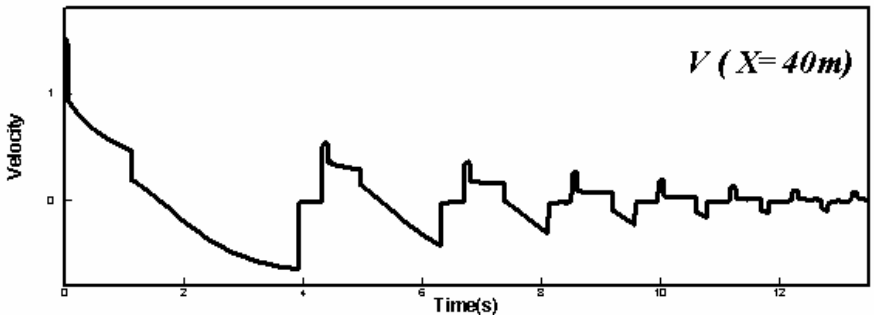

Fig. 4.5a The velocity history for upstream cavitating flow for Case 4.3.2 at x=40m by the Isentropic model.

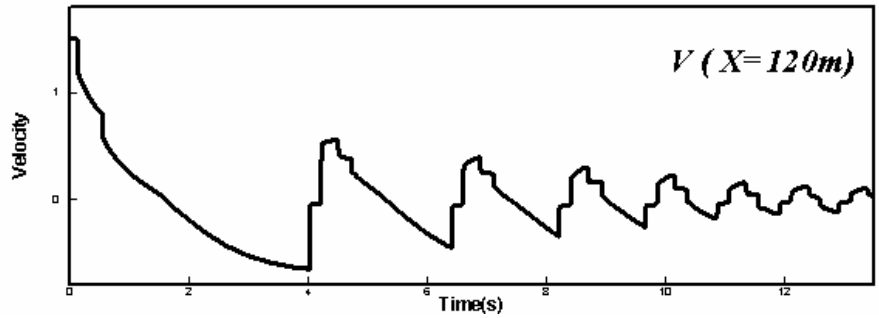

Fig. 4.5b The velocity history for upstream cavitating flow for Case 4.3.2 at x=120m by the Isentropic model.

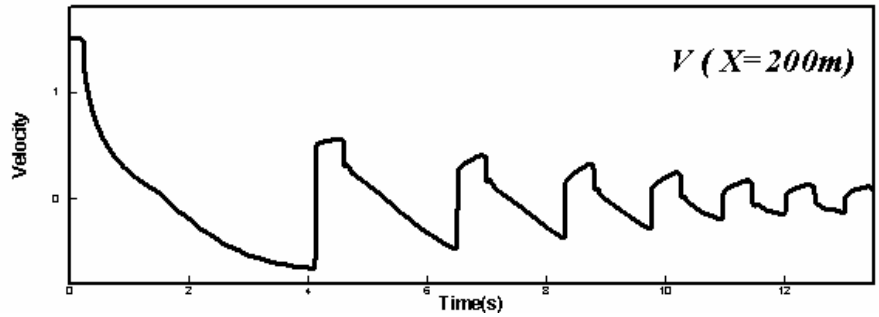

Fig. 4.5c The velocity history for upstream cavitating flow for Case 4.3.2 at x=200m by the Isentropic model.

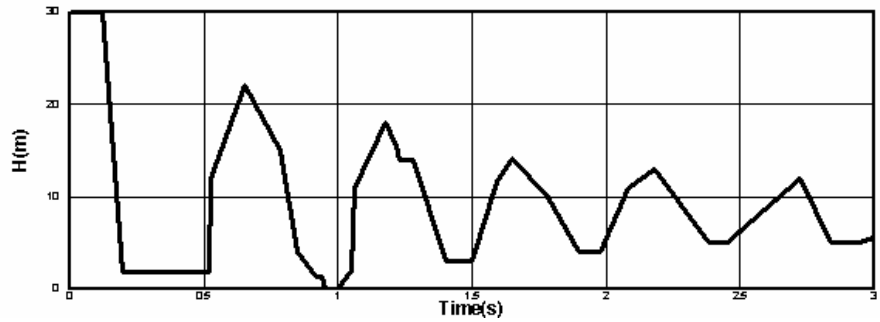

Fig. 4.6a The experimental pressure history for midstream cavitating flow for Case 4.3.2 at x=120m duplicated from (Sanada, 1990).

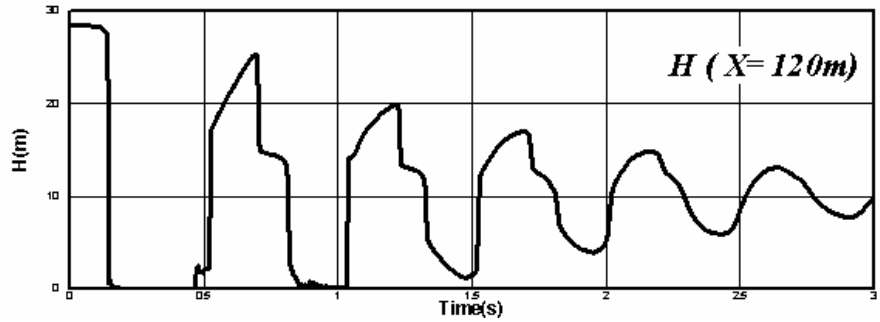

Fig. 4.6b The pressure history for midstream cavitating flow for Case 4.3.2 at x=120m by the Isentropic model.

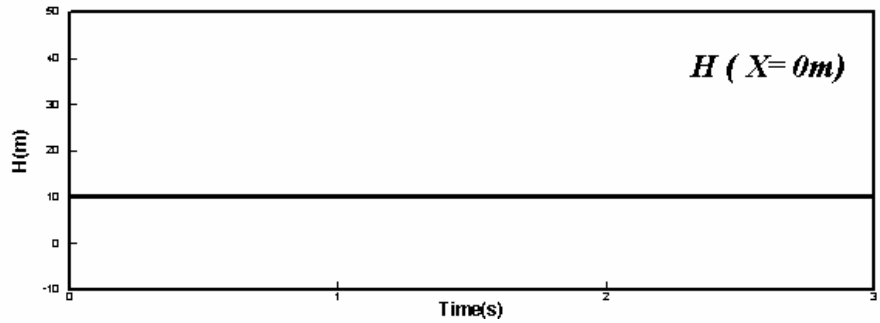

Fig. 4.6c The pressure history for midstream cavitating flow for Case 4.3.2 at x=0m by the Isentropic model.

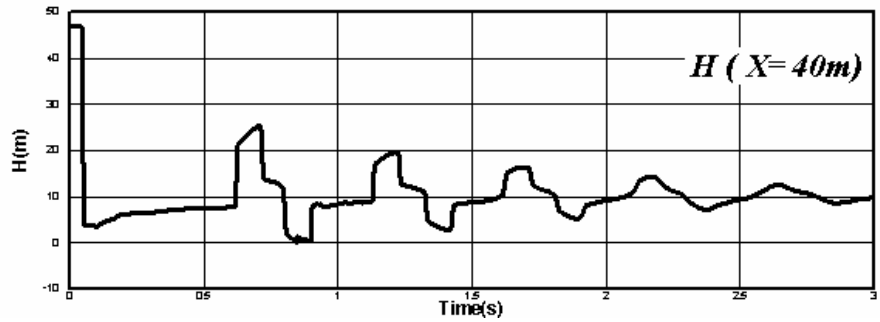

Fig. 4.6d The pressure history for midstream cavitating flow for Case 4.3.2 at x=40m by the Isentropic model.

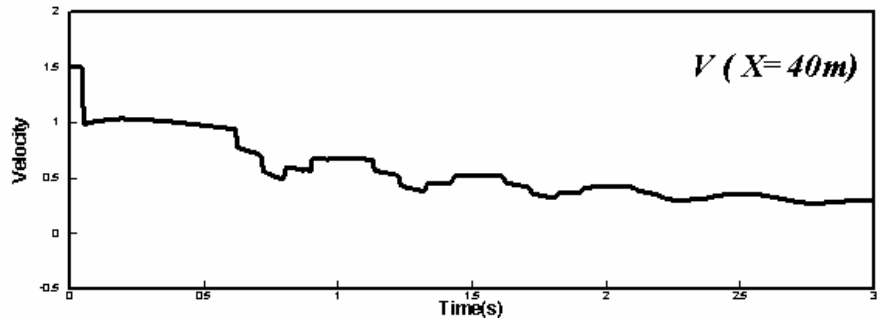

Fig. 4.7a The velocity history for midstream cavitating flow for Case 4.3.2 at x=40m by the Isentropic model.

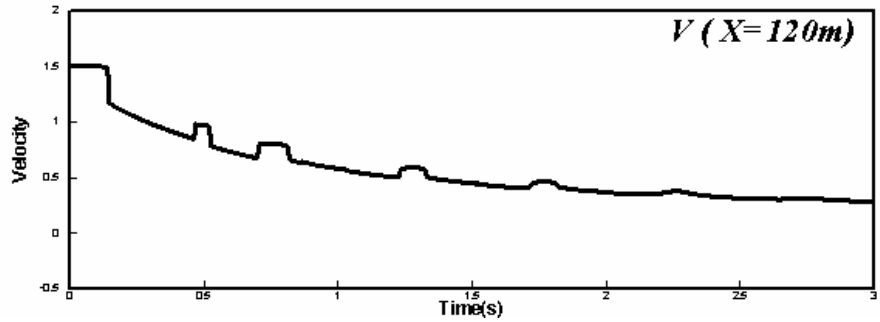

Fig. 4.7b The velocity history for midstream cavitating flow for Case 4.3.2 at x=120m by the Isentropic model.

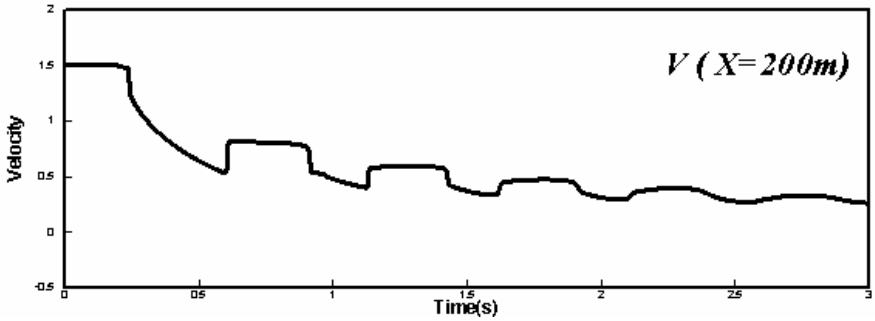

Fig. 4.7c The velocity history for midstream cavitating flow for Case 4.3.2 at x=200m by the Isentropic model.

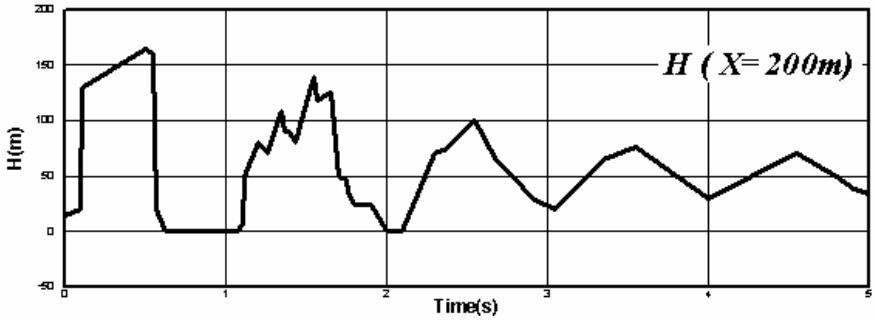

Fig. 4.8a The experimental pressure history for downstream cavitating flow for Case 4.3.2 at x=200m duplicated from (Sanada, 1990).

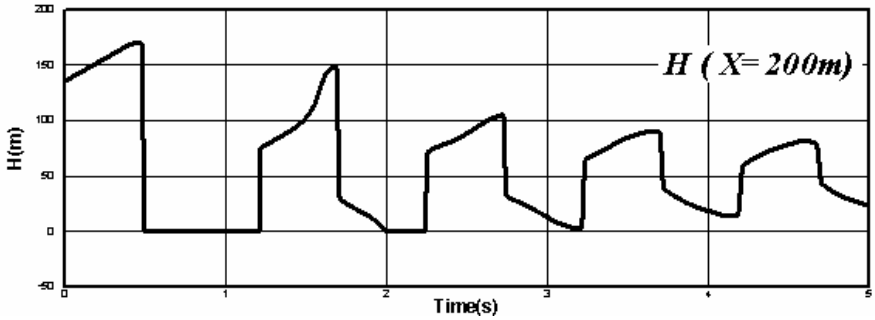

Fig. 4.8b The pressure history for downstream cavitating flow for Case 4.3.2 at x=200m by the Isentropic model.

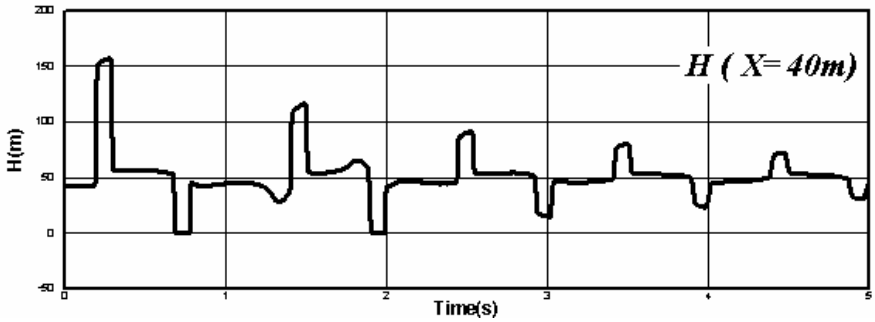

Fig. 4.8c The pressure history for downstream cavitating flow for Case 4.3.2 at x=40m by the Isentropic model.

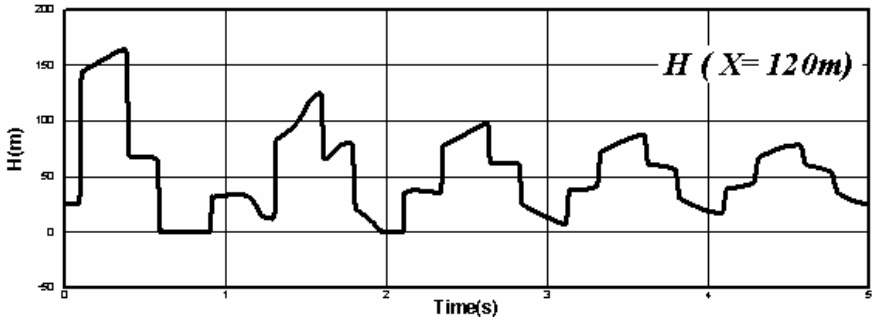

Fig. 4.8d The pressure history for downstream cavitating flow for Case 4.3.2 at x=120m by the Isentropic model.

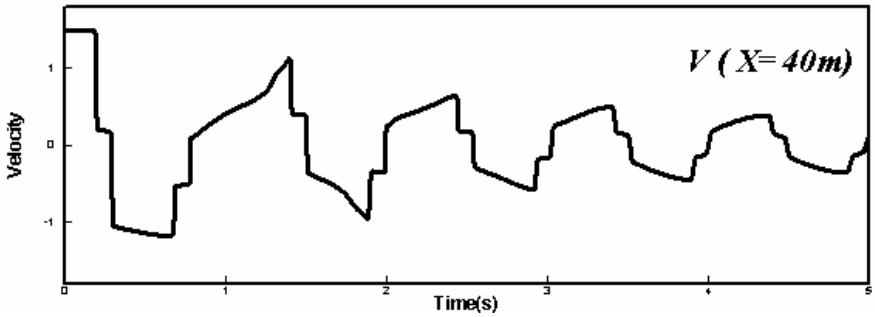

Fig. 4.9a The velocity history for downstream cavitating flow for Case 4.3.2 at x=40m by the Isentropic model.

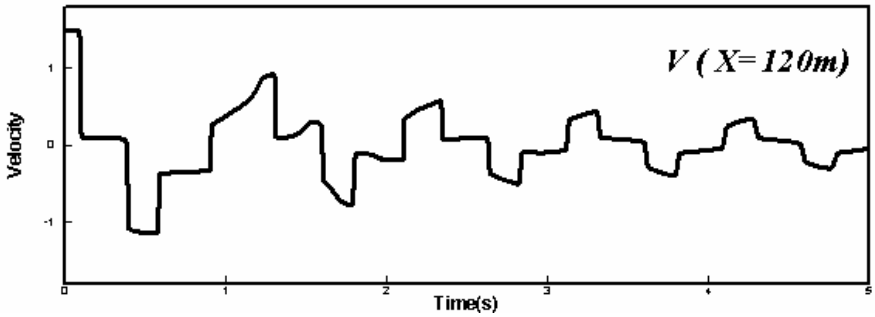

Fig. 4.9b The velocity history for downstream cavitating flow for Case 4.3.2 at x=120m by the Isentropic model.

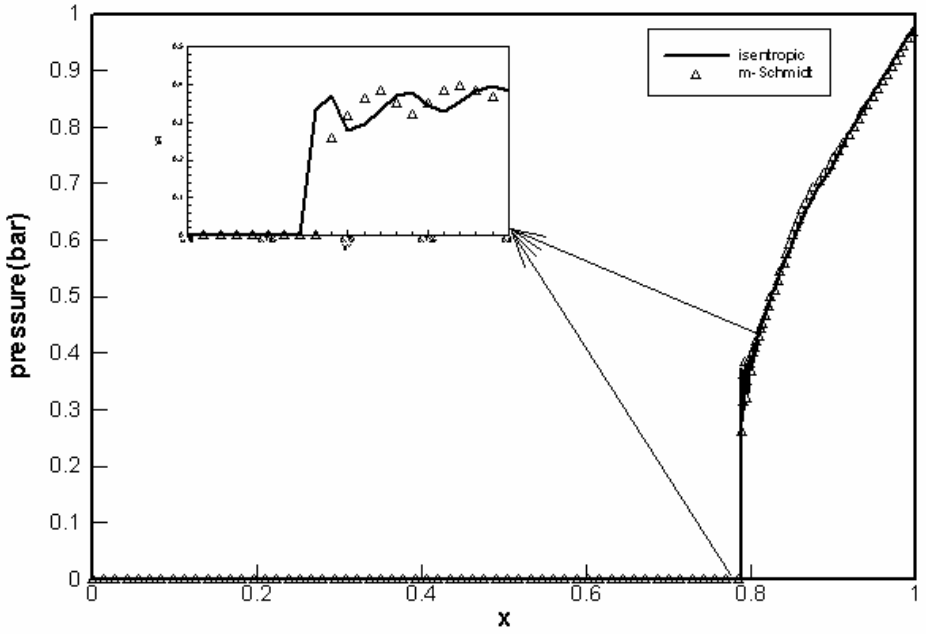

Fig. 4.10 The comparison of pressure profile for Case 4.3.2 by the modified Schmidt model to the Isentropic model before the first cavitation collapse at t=0.185s.

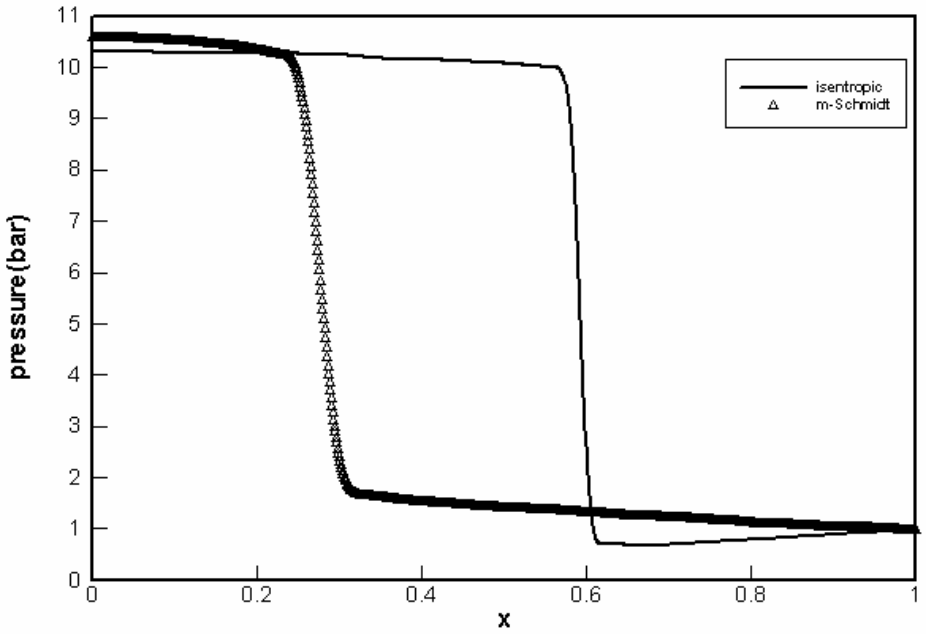

Fig. 4.11 The comparison of pressure profile for Case 4.3.2 by the modified Schmidt model to the Isentropic model after the first cavitation collapse at t=4.07s.

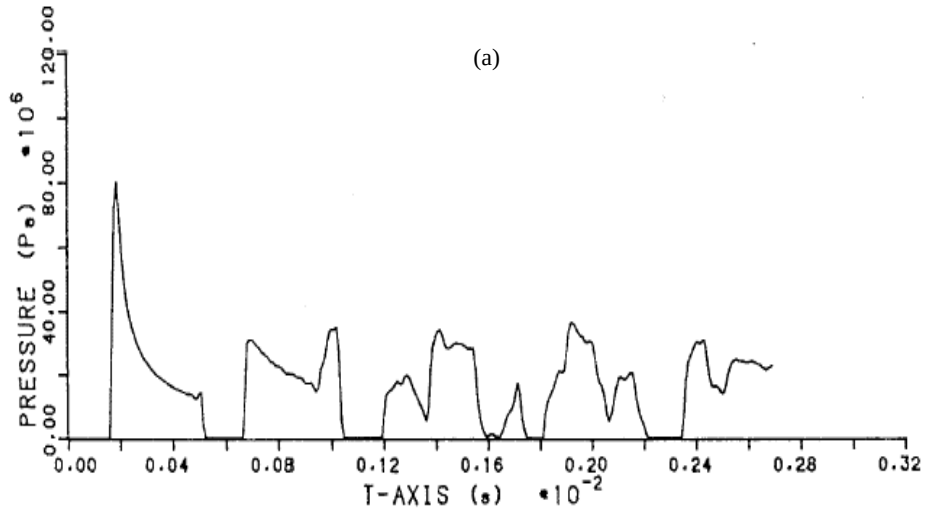

Fig. 4.12a Pressure histories at the right end wall for Case 4.3.3 by the Vacuum model (P_v =0.).

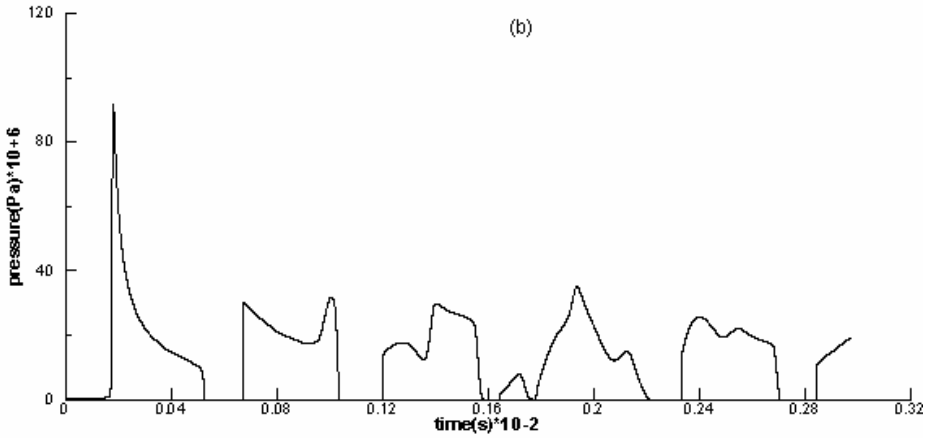

Fig. 4.12b Pressure histories at the right end wall for Case 4.3.3 by the Cutoff model.

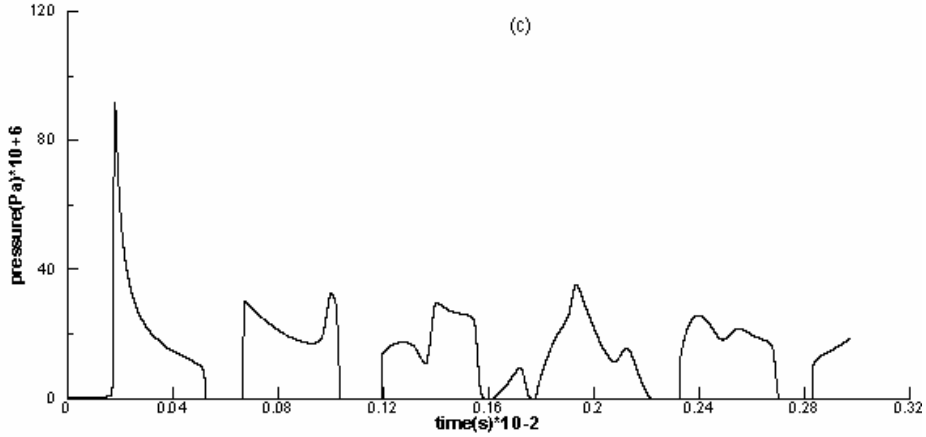

Fig. 4.12c Pressure histories at the right end wall for Case 4.3.3 by the Schmidt model.

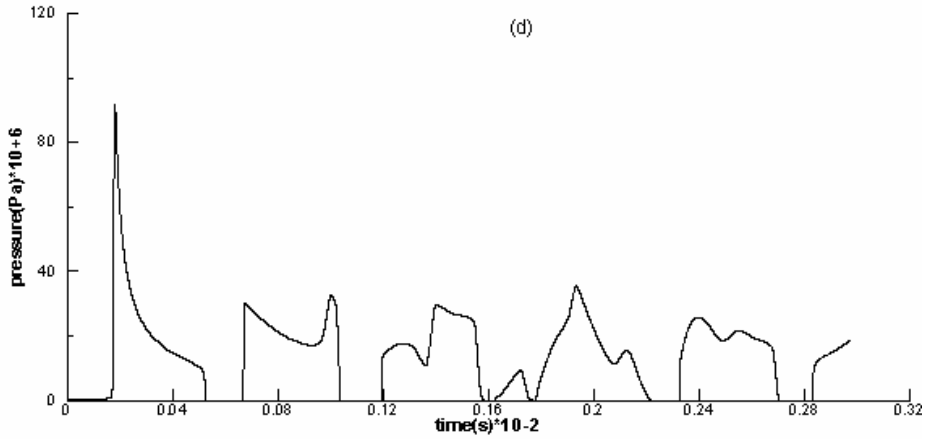

Fig. 4.12d Pressure histories at the right end wall for Case 4.3.3 by the modified Schmidt model.

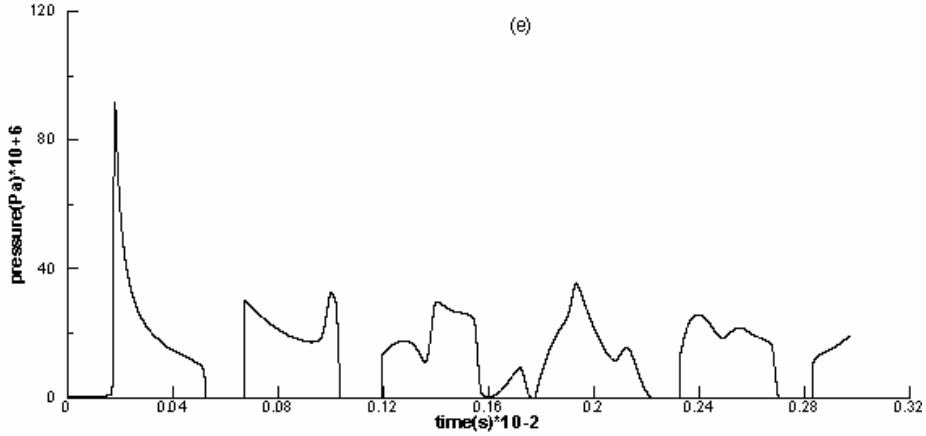

Fig. 4.12e Pressure histories at the right end wall for Case 4.3.3 by the Isentropic model.

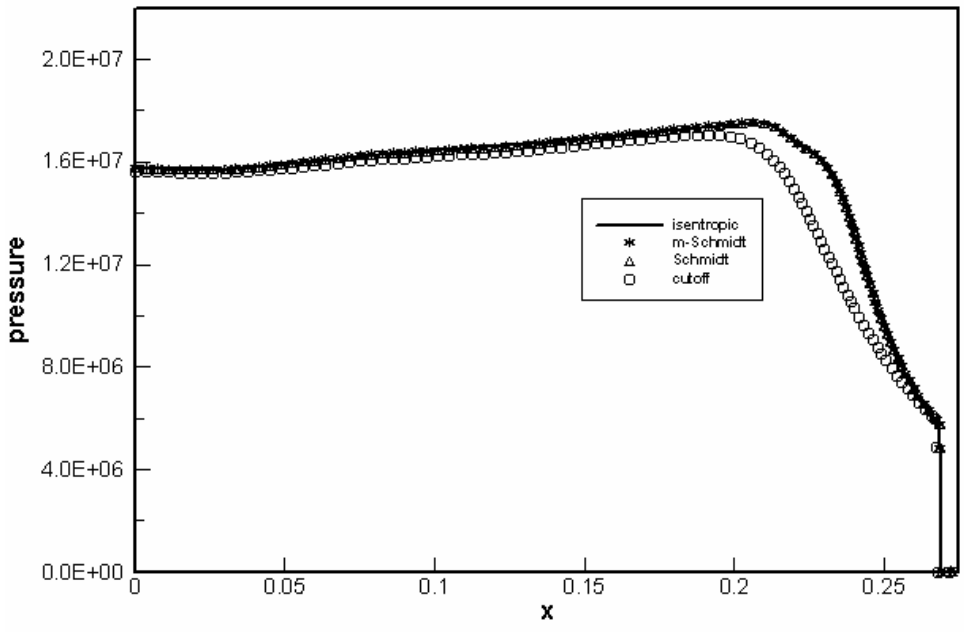

Fig. 4.13 Pressure profile for Case 4.3.3 at t=0.00065s by four models.

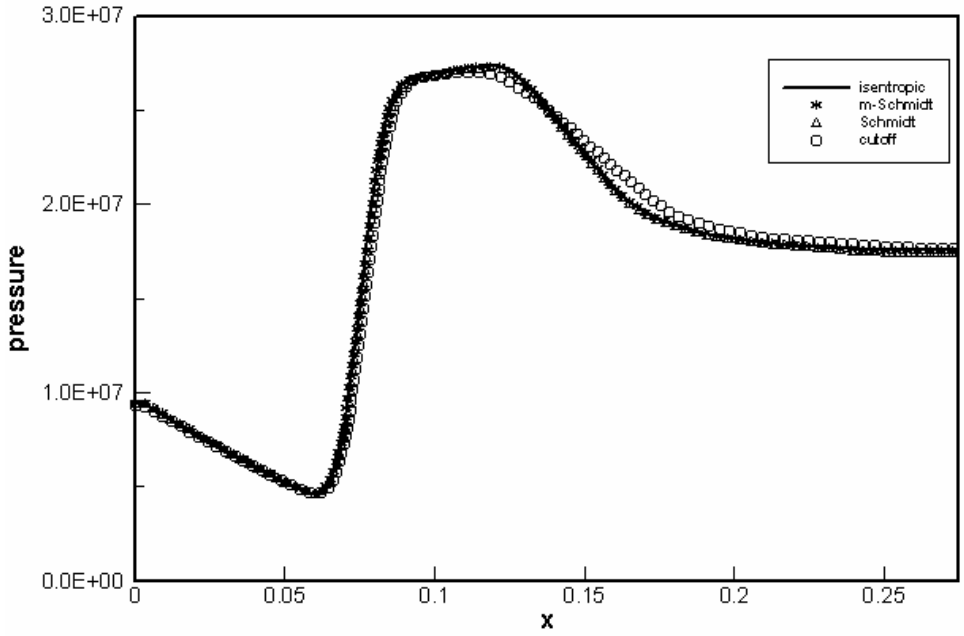

Fig. 4.14 Pressure profile for Case 4.3.3 at t=0.00090s by four models.

Chapter 5

Applications: 2D Cavitating Flows

In practical engineering application, problems considered are always multi-dimensions where more than one medium coexists in fluid flows initially. As such, the numerical methods and one-fluid cavitation models provided in Chapter 2 and Chapter 3 are extended for 2D applications in this chapter. A fix for treatment of water-solid interface where the negative pressure appears in solid side bordering the interface is also proposed. The cavitating flows arisen from underwater explosions are simulated and the shock-cavitation-structure interaction is analyzed in this chapter. More specially, two underwater explosion problems are considered and calculated here. The first one is a cylindrical underwater explosion near a planar wall. The planar wall is taken as rigid or flexible for analysis and comparison. In this problem, the impulse and net force exerted by the shock and cavitation collapse are also calculated to predict the damage effect of an underwater explosion on nearby structures. The other one is a spherical underwater explosion in a cylindrical container where the solid wall of the container may be rigid or flexible. For this problem, flow profiles are presented at a series of time instances to investigate the whole process. Similar to the 1D simulation, the various one-fluid cavitation models are used for calculations and comparisons.

5.1 Introduction

A non-contact underwater explosion near a structure consists of shock loading and and cavitation reloading (pressure impulse). To simulate faithfully the flow dynamics and hence the prediction of these loadings are important considerations in the design of submerged structures able to withstand or mitigate the damage effect of an underwater explosion. For the shock loading, a lot of numerical studies can be found in literature

as mentioned in Chapter 1. Some experimental studies are also carried out (Brett et al, 2000; Rajendran and Narasimhan, 2001;Ramajeyathilagam and Vendhan, 2004). In those works, the response of plate/cylinder subjected to an underwater explosion, in both the linear and non-linear regime, was experimentally investigated and analyzed. Needless to say, it is found that the deformation of the plate can be significant if the shock loading is sufficiently strong. Such shock loading can, obviously, lead to structural failure when the deformation is beyond some critical values. For further and detailed analysis of shock loading, Houlston et al (1985) and McCoy and Sun (1997) carried out numerical analysis of underwater shock on structures via finite element method (as employed in commercial software). Such calculations can provide broad and overall understanding of shock loading as occurred in underwater explosions. The commercial software like ABAQUS and DYNA, however, are not very inaccurate in the treatment of wave interactions at the material interface like explosive gas-water and water-flexible structure interfaces.

In the evaluation of an underwater explosion near structure, it is imperative for one to consider the effect of cavitation which is initiated primarily by the pressure drop across cavitation interface and the said sudden pressure change may very well be comparable to the initial shock loading. The damage effect of cavitation collapse on nearby plate was experimentally investigated by Jin et al (1996) with different ratios of the distance from the boundary. It had been also shown by Tomita et al (2002) and Lindaw and Lauterborn (2003) that boundary shapes significantly affects the growth and collapse of cavitation bubbles. For investigation of curved target damage generated by underwater explosions, Brett et al (2000) conducted a series of experiments to investigate cylinder deformation associated with underwater explosions. The reloading of structure arising from the cavitation collapse can be

clearly observed in their experiments. Although the peak pressure produced from the cavitation collapse is lower than that of shock loading, the duration of pressure pulse from the former is well comparable to or even a little longer than that of shock loading. As a result, the pressure impulse generated from cavitation collapse is in the same magnitude and comparable to the pressure impulse associated with the major shock loading. The shock-cavitation-structure interaction is a transient event and invariably complex to be adequately studied and analyzed via experiments where usually only pressure measurements at a few selected locations are made. A numerical study can definitely serve to complement our understanding of the transient shock-cavitation-structure phenomenon. The commonly used cavitation model in past multidimensional studies is the Cutoff-like model. Mäkine (1998) developed a cavitation model called pressure criterion (PC) to simulate planar shock wave-structure interaction. The pressure in cavity is assumed as the vapor pressure and the motion of the cavitation is driven by the difference between the surrounding flow pressure outside the cavity and the vapor pressure inside the cavity. This model is essentially a Cutoff-like model. The constant pressure model developed by Galiev (1997) is similar to the PC model. The Cutoff-like model is easy to be incorporated into the commercial software due to its simplicity (Philemon et al, 2000; Sprague and Geers, 2004). However, this model is not so accurate and certainly non-conservative as analyzed in Chapter 3. To overcome such difficulties, other one-fluid cavitation models like the modified Schmidt model and the Isentropic model have been developed to achieve higher level of accuracy while still about maintaining the simplicity of the Cut-off like model. The one-fluid models can be applied to simulate the unsteady multiphase compressible cavitating flow and is employed in the present study of shock-cavitation-structure interaction associated with an underwater explosion.

The rest of this chapter is organized as follows. The numerical methodology for 2D Euler system is presented in Section 5.2. The shock loading and cavitation reloading on structures are analyzed in Section 5.3. A note on present computation is presented in Section 5.4. The solution procedures and two case problems are shown in Section 5.5, followed by a brief summary in Section 5.6.

5.2 Methodology for 2D Euler System

5.2.1. The Present GFM for 2D Applications

For 2D or 3D axis-symmetric inviscid flow, we have

$$\frac{\partial U}{\partial t}+\frac{\partial F(U)}{\partial r}+\frac{\partial G(U)}{\partial z}=S(U). \tag{5.1}$$

The respective expressions of *U*, *F*, *G* and *S* for gas flow (not vapor) are given as

$$U=\begin{bmatrix}\rho\\ \rho u\\ \rho v\\ \rho E\end{bmatrix}\quad F=\begin{bmatrix}\rho u\\ \rho u^2+p\\ \rho uv\\ (E+p)u\end{bmatrix}\quad G=\begin{bmatrix}\rho v\\ \rho uv\\ \rho v^2+p\\ (E+p)v\end{bmatrix}\quad S=-\frac{(n-1)}{r}\begin{bmatrix}\rho u\\ \rho u^2\\ \rho uv\\ (E+p)u\end{bmatrix}. \tag{5.2a}$$

Here ρ is the gas flow density, *p* is the pressure, *u*, *v* are the flow velocities in the *r* and *z* directions, *E* is the total energy and given as $E=e+0.5\rho(u^2+v^2)$, where *e* is the internal energy per unit volume as mentioned in Chapter 2. *n* is a system parameter which takes on a value of 1 or 2. If *n* is set equal to 1, System (5.1) is for planar 2D flow; if *n* is set equal to 2, it is for 2D axis-symmetric flow. Similar to 1D flow as mentioned in Chapter 2, as the liquid, solid and cavitation mixture are assumed to be barotropic, the total energy equation is not required to be solved directly, and thus the ensuing expressions for *U*, *F*, *G* and *S* valid for liquid, solid and cavitating flow are

$$U=\begin{bmatrix}\rho\\ \rho u\\ \rho v\end{bmatrix}\quad F=\begin{bmatrix}\rho u\\ \rho u^2+p\\ \rho uv\end{bmatrix}\quad G=\begin{bmatrix}\rho v\\ \rho uv\\ \rho v^2+p\end{bmatrix}\quad S=-\frac{(n-1)}{r}\begin{bmatrix}\rho u\\ \rho u^2\\ \rho uv\end{bmatrix}. \tag{5.2b}$$

As such, ρ is the flow density, u and v are the flow velocities in the r and z directions, and p is the flow pressure. In this chapter, n is set equal to 1 for the first problem (Case 5.5.1) and 2 for the second problem (Case 5.5.2). Equation (3.2) as presented in Chapter 3 is taken as the equation of state for closure of System (5.1).

The 1D characteristic methods developed in Chapter 2 can be directly extended for system (5.1) in the normal direction. The unit normal at every grid point, $\vec{N}$, is defined via level set function ($\vec{N}=\nabla\phi/|\nabla\phi|$) where ϕ is the level set function. The characteristic equations in the normal direction at the interface for (5.1) are then defined as

$$\frac{dp_I}{dt}+\rho_{IL}c_{IL}\frac{du_I}{dt}+\frac{n-1}{r}\rho_{IL}u_{IL}c_{IL}^{\ 2}=0,\ \text{along}\ \frac{dx}{dt}=u_I+c_{IL}, \tag{5.3a}$$

$$\frac{dp_I}{dt}-\rho_{IR}c_{IR}\frac{du_I}{dt}+\frac{n-1}{r}\rho_{IR}u_{IR}c_{IR}^{\ 2}=0,\ \text{along}\ \frac{dx}{dt}=u_I-c_{IR}. \tag{5.3b}$$

System (5.3) can be discretized at the normal direction of the interface as

$$p_I-p_{IL}+\rho_{IL}c_{IL}(u_I-u_{IL})+\frac{n-1}{r}\Delta t\rho_{IL}u_{IL}c_{IL}^2=0, \tag{5.4a}$$

$$p_I-p_{IR}-\rho_{IR}c_{IR}(u_I-u_{IR})+\frac{n-1}{r}\Delta t\rho_{IR}u_{IR}c_{IR}^2=0, \tag{5.4b}$$

Solve (5.4a) and (5.4b) to get the interface pressure and (normal) velocity as follows

$$p_I=\frac{p_{IL}\rho_{IR}c_{IR}+p_{IR}\rho_{IL}c_{IL}+\left(u_{IL}-u_{IR}-\frac{n-1}{r}\Delta t(u_{IL}c_{IL}+u_{IR}c_{IR})\right)\rho_{IL}c_{IL}\rho_{IR}c_{IR}}{\rho_{IL}c_{IL}+\rho_{IR}c_{IR}}, \tag{5.5a}$$

$$u_I=\frac{p_{IL}-p_{IR}+\rho_{IL}u_{IL}c_{IL}+\rho_{IR}u_{IR}c_{IR}-\frac{n-1}{r}\Delta t\left(\rho_{IL}u_{IL}c_{IL}^2-\rho_{IR}u_{IR}c_{IR}^2\right)}{\rho_{IL}c_{IL}+\rho_{IR}c_{IR}}, \tag{5.5b}$$

where the values of p_{IL} (p_{IR}), ρ_{IL} (ρ_{IR}), u_{Il} (u_{IR}) and c_{IL} (c_{IR}) are taken from the left (right) side of the interface in the normal direction. The application range of the present GFM is investigated in Chapter 2. For multidimensional problems, the velocity field in the tangential plane has to be defined. Here a method developed by Fedkiw et al (1999b) is adopted and summarized below. Similar to the isobaric fix as mentioned in Chapter 2, the tangential velocity is expected to be extrapolated (extended) as a constant in the normal direction. A basis free projection method (Fedkiw et al, 1998) is employed to define tangential velocity for 2D problem via extrapolation. Firstly, a velocity is defined as $\vec{V} =< u, v, w >$ and then a propagation equation,

$$V_t \pm \vec{N} \cdot \nabla \vec{V} = 0, \tag{5.6}$$

is solved. Now two velocity fields are obtained for each ghost cell, one is from the real fluid and the other one is from the ghost fluid. For each velocity field, the normal component of the velocity is $V_N = \vec{V} \cdot \vec{N}$; it can be put into a vector as $V_N \vec{N}$. Thus the tangential component of the velocity can thus be expressed as a vector, say $\vec{V} - V_N \vec{N}$.

For multidimensional applications, the definition of ghost fluid status involves more grid cells because more than one velocity has to be defined for ghost fluids as mentioned above. Similar to Liu et al (2003), an identification matrix S_K, which is dependent on level set function, is defined for each medium to determine which medium is to be taken by each grid point. We assume that there are K mediums in the fluid flows. If $S_K(i, j, k) = 1$ the grid (i, j, k) is occupied by *Kth* medium, otherwise $S_K(i, j, k) = 0$. The update of S_K is determined by the new level set function.

After the interface locations are obtained by the level set method, we define a rectangular band $[i_1, i_2] \times [j_1, j_2] \times [k_1, k_2]$ in which an interface lies. There are 8-10 grid

points in the normal direction for this rectangular band. Assuming that the interface is located at x_I, thus the two grid points located at $x = x_I \mp 1.5\min(\Delta x, \Delta y, \Delta z)$. For the grid point of real fluid bordering the interface, the density is obtained via the predicted interface entropy. Such fix is used to suppress the "overheating" phenomenon. For the ghost point bordering the interface (ghostp1) and the ghost point next to the ghostp1, the pressure and normal velocity are copied from the predicted interface quantities, and the density is determined by predicted interface entropy while the tangential velocity is calculated by (5.6), say $\vec{V} - V_N \vec{N}$; this is the tangential component of the velocity field from the ghost fluid as mentioned above. For the ghost points not bordering the interface but still lying within the band, the pressure and velocity are kept unchanged while the density is defined by the isentropic fix as mentioned in Chapter 2.

It is clearly shown that the extension of the present GFM to 2Ds is fairly straightforward. (5.5) is an algebraic equation, thus no iteration is needed when the predicted interface status is calculated. Therefore, the present GFM is able to keep to the simplicity and low computational cost as for the original GFM.

5.2.2. A Fix for Simulation of Water-Solid Interface

Note that the application of (5.5) is conditional on the positive pressure predicted from (5.5a). It has been found in Chapter 2 that (5.5a) may on occasions predict a negative pressure quantity especially when the low pressure region appears near the water-solid interface. In the simulation of water-solid compressible flows, both the EOS for water and solid are very stiff. That means that a small density change can correspondingly lead to a large pressure change. This may be especially severe for the solid medium due to the large B and γ in the solid EOS. To verify this point, we assume a problem where the cavitation in water occurs in the region bordering the

water-solid interface. In this problem, the calculated solid density next to the water-solid interface by the numerical scheme may become a little less than the initial density due to propagation of rarefaction waves. Thus, the calculated solid pressure from this density may become negative. Unlike the water medium, the solid is able to sustain large negative pressure and thus the computation in the solid medium continues on. The system (5.5), however, cannot be used to predict the interface pressure and velocity under such conditions where negative pressure appears in the solid medium because it may result in negative interface pressure. As mentioned in Section 2.4.4, a fix can be incorporated to the present GFM into overcome such possible difficulty. Based on the same assumptions as in Section 2.4.4, such fix can be extended to 2D computations. Similar to 1D analysis, (5.5) can be rewritten as

$$p_I = \frac{\dfrac{p_{IL}}{\rho_{IL}c_{IL}} + \dfrac{p_{IR}}{\rho_{IR}c_{IR}} + u_{IL} - u_{IR} - \dfrac{n-1}{r}\Delta t\left(u_{IL}c_{IL} - u_{IR}c_{IR}\right)}{\dfrac{1}{\rho_{IL}c_{IL}} + \dfrac{1}{\rho_{IR}c_{IR}}}, \tag{5.7a}$$

$$u_I = \frac{\dfrac{p_{IL} - p_{IR}}{\rho_{IL}c_{IL}\rho_{IR}c_{IR}} + \dfrac{u_{IL}}{\rho_{IR}c_{IR}} + \dfrac{u_{IR}}{\rho_{IL}c_{IL}} - \dfrac{n-1}{r}\Delta t\left(\dfrac{u_{IL}c_{IL}}{\rho_{IR}c_{IR}} - \dfrac{u_{IR}c_{IR}}{\rho_{IL}c_{IL}}\right)}{\dfrac{1}{\rho_{IL}c_{IL}} + \dfrac{1}{\rho_{IR}c_{IR}}}. \tag{5.7b}$$

With $\left|u_{IL} - u_{IR}\right| < \varepsilon$, $\left|p_{IL} - p_{IR}\right| < \varepsilon$ and $\rho_{IR}c_{IR} >> \rho_{IL}c_{IL}$ as denoted in Section 2.4.4, (5.7a, b) can be rewritten as

$$p_I \approx p_{IL} + \rho_{IL}c_{IL}\left(u_{IL} - u_{IR}\right) - \frac{n-1}{r}\Delta t\rho_{IL}c_{IL}\left(u_{IL}c_{IL} + u_{IR}c_{IR}\right), \tag{5.8a}$$

$$u_I = u_{IR} + \frac{n-1}{r}\Delta t u_{IR}c_{IR}. \tag{5.8b}$$

The pressure calculated via (5.8a) is positive because the product of the second term minus the third term at the right hand of (5.8a) is always a small positive quantity. System (5.8) is thus able to suppress the possible negative interface pressure. The

detailed definition of ghost fluids in the application of (5.8) can be found in Section 2.4.4.

5.2.3. The One-fluid Cavitation Models for Multi-dimensions

The main advantage of a one-fluid cavitation model is that it can be directly applied to multidimensional problems without any additional numerical treatment. Obviously, all the cavitation models as presented in Chapter 3 are easily implemented for multi-dimensions. We assume a grid point (i, j, k) in a multidimensional computational domain, and the application of a one-fluid cavitation model can be simply expressed as follows

$$p(i,j,k) = \begin{cases} Tait's \quad EOS & p(i,j,k) > p_{sat} \\ Cavitation \quad Model & p(i,j,k) < p_{sat} \end{cases}, \tag{5.9}$$

where p_{sat} is the physical saturated pressure and the cavitation model can be one of the Cutoff model, the Schmidt model, the modified Schmidt model and the Isentropic model in present computation. One may note strictly in (5.9) the pressure criterion is solely is employed to determine if a cavitation occurs. As Tait's EOS is very stiff such that the calculated pressure may not be so accurately determined, both the pressure and density are therefore employed in the present work to evaluate if a cavitation occurs in the flow. In the implementation, it is apparent that the one-fluid cavitation model for multi-dimensions is the same as for 1D application without any additional treatment. Other cavitation models like the multiphase model (Saurel and Abgrall, 1999) do not possess such advantage.

5.2.4. 2D Boundary Treatment

Two main types of boundary conditions are involved in 2D computation. One is the complete reflecting boundary and the other is the non-reflecting boundary. It should be

noted that the source term in (5.1) has to be incorporated into the boundary computation. For all stationary rigid walls (boundaries), the complete reflecting boundary condition is employed where a wave impacting a solid wall will reflect with a wave of equal strength. Non-reflecting boundary is extensively used in simulation of the underwater explosion because the shock wave is physically considered to propagate outside of the computational domain without reflection. Here we only consider the end boundary associated with the system (5.1) in the *r*-direction; the end boundary in the *z*-direction can be obtained in a similar way. The characteristic form of system (5.1) can be expressed as

$$\frac{\partial v}{\partial t}+u\frac{\partial v}{\partial r}+S_{t1}=0, \tag{5.10a}$$

$$c\frac{\partial \rho}{\partial t}+\rho\frac{\partial u}{\partial t}+(u+c)\left(c\frac{\partial \rho}{\partial r}+\rho\frac{\partial u}{\partial r}\right)+\frac{n-1}{r}\rho uc+S_{t2}=0, \tag{5.10b}$$

$$c\frac{\partial \rho}{\partial t}-\rho\frac{\partial u}{\partial t}+(u-c)\left(c\frac{\partial \rho}{\partial r}-\rho\frac{\partial u}{\partial r}\right)+\frac{n-1}{r}\rho uc+S_{t3}=0, \tag{5.10c}$$

where

$$\begin{bmatrix} S_{t1} \\ S_{t2} \\ S_{t3} \end{bmatrix}=\begin{bmatrix} v\dfrac{\partial(\rho v)}{\partial z}-\dfrac{\partial\left(\rho v^2+p\right)}{\partial z} \\ (c-u)\dfrac{\partial(\rho v)}{\partial z}+\dfrac{\partial(\rho uv)}{\partial z} \\ (c+u)\dfrac{\partial(\rho v)}{\partial z}-\dfrac{\partial(\rho uv)}{\partial z} \end{bmatrix}, \tag{5.10d}$$

(5.10d) is obtained from the production of the left eigenvector and $\dfrac{\partial G(U)}{\partial z}$, and is treated as a source term. The differential operator in (5.10d) is discretized by a second-order accurate central difference method as

$$\frac{\partial M}{\partial z}=\frac{M_{i,j+1}-M_{i,j-1}}{2\Delta z}, \tag{5.10e}$$

where *M* express the various terms given in (5.10d). Based on system (5.10), we denote the following

$$\begin{cases} \Pi_1 = u\dfrac{\partial v}{\partial r} \\ \Pi_2 = (u+c)\left(c\dfrac{\partial \rho}{\partial r} + \rho\dfrac{\partial u}{\partial r}\right) \\ \Pi_3 = (u-c)\left(c\dfrac{\partial \rho}{\partial r} - \rho\dfrac{\partial u}{\partial r}\right) \\ \Pi_4 = \dfrac{n-1}{r}\rho u c \end{cases} \tag{5.11}$$

for the outgoing wave. For the incoming wave, Π_1 to Π_4 are set equal to zero. The non-reflecting boundary conditions are then written as

$$\frac{\partial v}{\partial t} + \Pi_1 + S_{t1} = 0, \tag{5.12a}$$

$$c\frac{\partial \rho}{\partial t} + \rho\frac{\partial u}{\partial t} + \Pi_2 + \Pi_4 + S_{t2} = 0, \tag{5.12b}$$

$$c\frac{\partial \rho}{\partial t} - \rho\frac{\partial u}{\partial t} + \Pi_3 + \Pi_4 + S_{t3} = 0, \tag{5.12c}$$

The system (5.12) then leads to

$$\frac{\partial v}{\partial t} = -(\Pi_1 + S_{t1}), \tag{5.13a}$$

$$\frac{\partial \rho}{\partial t} = \frac{-(\Pi_2 + \Pi_3 + 2\Pi_4 + S_{t2} + S_{t3})}{2c}, \tag{5.13b}$$

$$\frac{\partial u}{\partial t} = \frac{-(\Pi_2 - \Pi_3 + S_{t2} - S_{t3})}{2\rho}, \tag{5.13c}$$

The pressure at the boundary can also be solved from density via EOS for each medium. For outgoing waves, the derivative of Π_k is discretized by a second-order one-sided upwind scheme. In doing so, the open boundary at $t = t^{n+1}$ can be solved from the primitive variables at $t = t^n$.

5.3 The Shock Loading and Cavitation Reloading on Structure

In engineering application, the shock loading is always taken as the main or primary effect on structure. The cavitation reloading which has been usually or traditionally neglected as of secondary importance, however, was found to be comparable to shock loading (Brett et al, 2000). To evaluate the effect of an underwater explosion on structure, both the shock loading and cavitation reloading have to be considered. Generally, the pressure impulse exerted on a salient point of the structural surface and/or overall force exerted on the affected structure surface can be calculated to evaluate the respective contributions.

5.3.1. Pressure Impulse on Structure Surface

The interaction of an underwater explosion with structure is sometimes illustrated or shown as a series of pressure history plots contributed in a large way by how the measurements invariably in terms of the pressure transducers mounted on the structure are employed for data acquisition; to a lesser extent accelerometers may be employed too. This practice in experiments is deemed reasonable since in an underwater explosion near a structure, the pressure at a point on the structural wall (normally taken to be at the center point of the wall) changes abruptly and therefore serves as a proxy to observe the effect of an underwater explosion on structure. Of course, another very important consideration is the matured development and well tested pressure transducer technology which is coupled to relatively low cost implementation. The pressure impulse on the surface can be expressed as

$$I_C = \int_{T_E} p_C dt \,, \tag{5.14}$$

where I_C is the pressure impulse at the center point of the solid wall. Here p_C is the associated pressure at this center point and T_E is the integrated final time. Equation

(5.14) is integrated from the arrival of the shock wave to cavitation occurrence. By cavitation occurrence, one takes it to be cavitation inception till its collapse and there can be a series of cavitation occurrences. As such, the pressure impulse associated shock wave can be directly compared to the pressure impulse associated with cavitation collapse.

5.3.2. Overall Force on Structure Surface

For ease of analysis, the force acting in the direction perpendicular and towards a planar wall is to be postive. The overall force on a structure surface can be expressed as

$$F_S = \int_S p dS , \tag{5.15}$$

where F_S are the overall forces exerted on the surface of a solid wall S . By recording the overall force on a solid surface, the comparison of shock loading and cavitation reloading can be clearly shown. In Section 5.5, it will be presented the overall force on the solid surface calculated separately for the rigid wall and flexible wall to observe and determine the effect of solid deformation on cavitation physics.

5.4 A Note on Present 2D Computation

Numerical examples in Section 5.5 will show that the present method performs well if the solid wall is taken as rigid where the complete reflecting boundary condition is used. It is also found that the present computation is valid for the problem if the solid wall is taken as flexible but the wall is thick enough to treat the outer-boundary as fixed while the inner boundary of the wall is captured by level set method. The present computation, however, may fail to simulate the deformation of a thin flexible wall because the outer-boundary and inner-boundary are moving together in such case.

Figure 5.1 shows the schematic diagram for an inner explosion in a closed cylinder with a thin flexible wall where the upper and bottom boundaries are fixed while the left and right boundaries are free to move. Physically, the thin wall will be deformed when shock wave impacts the inner-boundary of the solid wall and transmits through the solid wall and thus makes the outer-boundary deformed. After that, the fixed top and bottom solid boundaries will drag the solid wall back. This means that the top and bottom solid boundaries always sustain large force. The present computation, however, treats the top and bottom solid boundaries by using complete reflecting conditions and fixes the top and bottom solid boundaries by setting the velocity in *r*-direction equal to zero. Therefore, we have

$$\begin{cases} u_{TB} = 0, v_{TB} = 0 \\ u_{BB} = 0, v_{BB} = 0 \end{cases}, \tag{5.16}$$

where subscripts "*TB*" and "*BB*" stand for the top solid boundary and the bottom solid boundary, respectively. With (5.16) and (5.1), the pressure and density at solid boundaries are constant. This is obviously nonphysical because the force exerted on the top and bottom solid boundaries are changing as time progresses. Therefore, the present system is unable to model this kind of problems. One possible method to overcome such difficulty is to use the different system for liquid and solid. The Navier equation can be employed as governing equation for solid and then the fluid is coupled to the solid by providing a pressure. This is a potential work in the future and not discussed in the present computation.

5.5 2D Applications to Underwater Explosions

If we assume the flow variables at $t = t^n$ are known, the numerical procedures to obtain flow variables at the next time step t^{n+1} can be summarized as follows:

1. Initialize level set functions and identification matrix S_K in Section 5.2.1.
2. Initialize the flow field and calculate the initial time step-size.
3. Obtain the computational domain (band) for the first medium.
4. Obtain the interface status using (5.5) and (5.6) and define the ghost fluids. If negative pressure appears in solid medium, (5.5) is ignored and the ghost fluid is defined using (5.7).
5. Obtain the flow variables using (5.1) for one medium.
6. Evaluate the value of pressure (p) to check if the pressure is less than the *physical* saturated pressure (p_{sat}) for the water medium. If $p \geq p_{sat}$, pressure can be solved from EOS for water with known density. Otherwise, the selected one-fluid cavitation model is employed to calculate the pressure in the cavitation point/region.

Steps 4 to 6 will be repeated until each medium has been solved.

7. Update the boundary points using complete reflecting boundary condition or non-reflecting boundary condition (5.13).
8. Obtain the flow field for each medium using identification matrix S_K .
9. Update the level set functions and thus identification matrix S_K .
10. Calculate new time step-size and go back to step 3 if necessary.
11. Stop the computation when the expected run time is achieved.

In this section, two problems are investigated in detail. The first is a cylindrical underwater explosion near a planar wall and the second is a spherical underwater explosion in a cylinder. These two problems have much practical engineering applications in designing submerged structures. For the former, the pressure contours at various time instances are presented and the pressure histories at the center point of

the planar wall are recorded. The pressure impulse and overall force exerted on the planar wall are also calculated by (5.14) and (5.15) in the application of various one-fluid cavitation models for comparisons. The compressibility of the thick solid wall is also considered in this problem. The comparisons of pressure histories at the center of planar wall which is respectively taken as rigid and flexible are then carried out to observe the effect of solid deformation on cavitation physics. Similar to the first problem, the solid wall is also taken as rigid and flexible in the second problem and then the pressure histories at the center of the side wall are recorded for comparison. The pressure contours are presented to observe the wave propagations in the cylinder. To better compare various one-fluid cavitation models, the pressure profiles along the central direction of wall before and after the cavitation collapse are also presented.

The present GFM is employed to treat the material interfaces of gas-water and water-solid while the various one-fluid cavitation models are used to simulate the evolution and collapse of 2D cavitation if any. For both problems, p_{sat} is set to *0.05bar*. The CFL number is set to 0.45 and the mesh is uniformly distributed in computational domain. The time step-size is calculated using the following stability condition:

$$\Delta t = CFL \frac{\min(\Delta x, \Delta y)}{\max\left(\left|u_{i,j}\right| + \left|v_{i,j}\right| + c_{i,j}\right)} \tag{5.17}$$

Case 5.5.1: 2D Cylindrical Underwater Explosion near a Planar Wall. A cylindrical underwater explosion near a flat free surface has previously been studied by Liu et al (2003a). Case5.5.1 is to investigate the shock-structure interaction associated with possible cavitation near the water-solid interface. For ease of description and comparison, this case is divided into two Sub-cases, Case5.5.1a and Case5.5.1b where a rigid planar wall is used for Case5.5.1a and a thick flexible wall is used for

Case5.5.1b. Figure 5.2 shows the schematic diagram for Case1b where P is the center point of the planar wall. If the solid is taken as rigid, the water-solid interface is treated as an outer-boundary and hence Fig. 5.2 is also the schematic diagram for Case5.5.1a. The initial conditions for Case5.5.1a are given as follows. A high pressure air cylinder of unit radius is located at the origin (0.0, 0.0) in water and the initial flow parameters inside the air bubble are $\rho_g = 1270 kg/m^3$, $p_g = 8290 bar$, $u_g = 0.0\, m/s$, $v_g = 0.0\, m/s$ and $\gamma_g = 2.0$. The initial flow parameters for water are $\rho_l = 1000\, kg/m^3$, $p_l = 1 bar$, $u_l = 0.0\, m/s$, $v_l = 0.0\, m/s$ and $\gamma_l = 7.15$. The computational domain is a rectangular region with $x \times y \in [-6m, 6m] \times [-6m, 3m]$ and the planar wall is located at the straight line y=3m. A total of 361×271 grid nodes are uniformly distributed in the respective x and y directions and the CFL number is set to 0.45. (This case is calculated based on equation (2.2) with $n = 1$.) For this problem, the cylindrical explosion is strong and the explosion center is close to the planar wall. The resultant flow pressure, therefore, is so high that the cavitation pressure becomes less significant to the overall (fluid) flow field. Numerical results demonstrate that the four one-fluid cavitation models produce very similar results. Figures 5.3a-5.3f show that the pressure contours at various time instances. Figure 5.3a shows that the shock generated by the explosion has been reflected from the planar wall at t=1.5ms. Such reflected shock interacts with the air bubble, resulting in a strong rarefaction wave moving towards the planar wall at t=2.0ms as shown in Fig. 5.3b. After this said rarefaction wave impacts the wall and reflects from the wall at t=3.0ms, a low pressure region forms near the planar wall as shown in Fig. 5.3c. With pressure continues to decrease, at t=4.0ms, the cavitation appears at this low pressure region as shown in Fig. 5.3d. Simultaneously, the main shock is propagating outside of the computational domain. The cavitation, as shown in Fig. 5.3e at t=5.5ms, collapses

from the center of the cavitation zone, leading to a water-jet near and directed towards the planar wall and a relatively strong compression wave propagating towards the bubble. The cavitation collapses completely at t=6.5ms as shown in Fig. 5.3f. Pressure contours depict the inception, evolution and collapse of the cavitation clearly. Also, the shock-cavitation-structure and shock-bubble interaction are well captured by the present GFM and cavitation models.

Similar to 1D application, the pressure at P is recorded to analyze the effect of the underwater explosion on the structure as shown in Fig. 5.4. It is discerned that the structural loading consists of shock loading and cavitation collapse reloading where the peak pressure of shock is much larger than peak pressure of cavitation collapse while the duration of cavitation collapse is substantially longer than that of shock. The pressure impulses calculated via (5.14) for shock and cavitation collapse are 865850 $P_a.s$ and 196030 $P_a.s$, respectively. Obviously, the pressure impulse of cavitation collapse is comparable to that of shock. For engineering application, the overall force on the structural surface is sometimes calculated to evaluate structural loading. Figure 5.5 shows the history of overall force on a quadrate region with area of $16\,m^2$ around the P. The overall force at the time of cavitation collapse is also in the same order of magnitude as that at the time of shock impacting the wall. It should be noted that the four models provide close pressure histories and overall force for this problem due to much higher flow pressure than cavitation pressure.

Replaceing the rigid wall with a flexible wall affects the resultant fluid-structure interaction. The flexible wall is deformed to create a low pressure region very near the surface of the wall while the shock-bubble interaction creates another low pressure lying between the bubble and solid. These two low pressure regions then interact with each other and finally create an overall lower pressure cavitation region. To observe

the deformation of solid wall on the cavitation, the solid wall in Case5.5.1b is considered as flexible and the hydro-elasto-plastic EOS (EOSS3) as presented in Chapter 2 is employed for the solid. The initial conditions for such a flexible solid are $p_s = 1.0bar$, $\rho_s = 7800\,kg/m^3$, $u_s = 0.0\,m/s$ and $v_s = 0.0\,m/s$. Other solid parameters are shown in Table 2.1 while the intial conditions for explosive gas and water are kept the same as for Case5.5.1a. The computational domain of Case5.5.1b is set as $x \times y \in [-6m, 6m] \times [-6m, 6m]$, and 361×361 uniform grid points are distributed. The non-reflective boundary condition is used for all four boundaries. Figures 5.6a-5.6e show the pressure contours up to 5.5ms. The shock-solid interactions and wave propagations through the water-solid interface can be observed from these pressure contours. The physical process of cavitation evolution and collapse is similar to the Case5.5.1a except for the occurrence of wave interaction at the water-solid interface. Figure 5.6a shows that the shock generated by explosion reflects from and transmits through the solid wall at t=1.5ms. It is apparent that the present GFM can track the water-solid interface. Close examination of Figs. 5.6b-5.6c reveals the deformation of the solid while wave propagating in the solid can also be clearly observed. The cavitation appears at t=4.0ms as shown in Fig. 5.6d. This occurs when the rarefaction wave generated from the shock-bubble interaction is reflected from the water-solid interface. At this time, the calculated pressure on the solid medium becomes negative thereby resulting in the breakdown of the explicit characteristic method. As discussed in Section 5.2.2, a numerical fix which effectively leads to the new version GFM (Fedkiw et al, 2002) is employed to ensure that such negative pressure is well suppressed. Figure 5.6e shows the cavitation collapses completely at t=5.5ms.

Similar to Case 5.1.1a, the pressure histories and overall force histories provided by four cavitation models look similar as shown in Figs. 5.7 and 5.8 due to the very high

surrounding flow pressure. Figure 5.9 depicts pressure histories at the center of solid surface for the rigid wall (Case 5.5.1a) and flexible wall (Case 5.1.1b). Here the predicted time instances of cavitation creation and collapse, as well as the predicted peak pressure of cavitation collapse, are different for Case 5.1.1a and Case 5.1.1b. As we are aware, the strength of shock generated from cavitation is determined by the cavitation size as well as the pressure jump across the cavitation boundary. In Case 5.1.1b, a portion of the flow energy is dissipated via the solid medium, thereby resulting in a lower corresponding flow pressure and speed in the water medium. Therefore, the rarefaction wave generated from the shock-bubble interaction is weaker than that for Case 5.1.1a. This explains that Case 5.1.1b provides for a later time instance of cavitation creation and lower peak pressure of cavitation collapse as shown in Fig. 5.9. It is also found that Case 5.1.1b gives a faster cavitation collapse than Case 5.1.1a. The cavitation for Case 5.1.1a is usually incepted when the rarefaction wave is reflected from the solid surface while the cavitation for Case 5.1.1b is incepted at the middle region between bubble and water-solid interface as mentioned above. This causes the surrounding flow to move towards and fill in the cavitation region more quickly for Case 5.1.1b, resulting in an earlier time instance of cavitation collapse. Figure 5.10 shows the history of overall force as calculated via (5.15) on a quadrate region with an area of $16\,m^2$ around the center of the planar wall. Once again, the overall force at the time of cavitation collapse is in the same order of magnitude with that at the time of shock impacting the wall.

Case 5.5.2: A Spherical Underwater Explosion in a Cylindrical Container. A spherical explosion in a rigid cylindrical container has been previously investigated in (see also Liu et al, 2004a; Xie et al, 2005a) where the physics of cavitation inception, evolution and collapse is analyzed in detail. In the present computation, a flexible thick

wall is employed to replace the rigid solid wall for investigating wave interactions between water and solid as well as the effect of solid deformation on cavitation physics. Similar to Case 5.5.1, this case is divided into two sub-cases, Case5.5.2a and Case5.5.2b. Figure 5.11 shows the schematic diagram for Case 5.5.2 where the center locations of the left/right cylinder walls are marked as P1 and P2, respectively. For the Case5.5.2a, the computational domain is the inner cylinder as shown in Fig. 5.11 where the completely reflecting boundary condition is employed for the inner boundary. The diameter and height of the cylinder are 0.0889m and 0.2286m, respectively. The explosive gas sphere is located at the center of the cylinder full of water. The inner diameter of the gas sphere is 0.03m. The initial pressure and density inside the gas sphere are respectively 20000 bar and 1770kg/m^3, and γ_g is set to 2.0 for the explosive gas. There are 71×361 grid-points uniformly distributed on one-half of the computational domain since the problem is symmetric. It is interesting to note that there is no non-physical oscillation encountered for the Schmidt model for this problem. This is because the cylinder size is relatively small and the initial flow is under very high pressure condition; the Schmidt model faces no difficulty when applied to such a small-size and high pressure situation as verified by Schmidt et al (1999). The cylinder walls are treated using completely reflecting boundary condition. Case5.5.2 is not exactly the same as but very similar to the problem studied by Wardlaw and Luton (2000). The difference lies in the present explosion is initiated by a highly-pressurized gas sphere in a rigid cylinder while it was by real explosive in a cylinder of flexible wall in Wardlaw and Luton (2000). We are unable to obtain the "exact" equivalent of initial pressure and explosive bubble size for Wardlaw and Luton's case from that article. Therefore, we only try to obtain the "broad" equivalent of initial total energy inside the bubble with the PETN explosive as employed in

Wardlaw and Luton (2000). However, the basic physics of flow studied here is essentially the same as that studied by Wardlaw and Luton; the associated flow physics has been discussed in some great details by Wardlaw and Luton. In general, all the major physics disclosed and analyzed in Wardlaw and Luton (2000) has been qualitatively identified and matched to the present computation. Once the explosion is initiated, a strong spherical shock is generated and propagates symmetrically outwards with an exponentially decaying strength. The reflected shock from the container side wall with a decreasing strength impacts the expanding explosion bubble, resulting in a rarefaction wave reflected from the gas bubble surface (Liu et al, 2001b). The rarefaction wave can be so strong that cavitation may be created next to the bubble surface. The rarefaction wave also makes a reflection at the cylinder side wall and then cavitation is created next to the wall. The cavitation subsequently collapses due to the compression from compressive wave, which is generated by the wave-bubble surface interaction (Liu et al, 2001b). Figure 5.12a-5.12d show a series of pressure contours at the respective times of 30, 60, 90 and 120μs. At t=30μs, the underwater shock has already been reflected from the cylinder wall, and the reflected shock wave has interacted with the expanding bubble surface. A rarefaction wave is generated due to the shock-bubble interaction and a low pressure region is created next to the bubble surface. At t=60μs, a large size cavitation region has been created next to the wall. The reflected shock waves from the top/bottom of the cylinder interact with those reflected from the side walls, resulting in a complicated shock-shock interaction. The transmitted shocks of the reflected shock waves from the side wall inside the gas bubble have already made reflection at the gas bubble surface and caused shock focusing on two points inside the oval shaped bubble. At t=90μs, with the decrease of shock strength, the shock-shock interaction results in two nearly plane shocks

propagating towards the bubble from the top and bottom. The cavitation next to the side walls is shrinking and on the verge of going into collapse stage. At t=120μs, the cavitation has collapsed and the resultant flow field becomes very complicated. For this problem, the Cut-off model and the Schmidt model provide fairly similar gross features as those obtained by the modified Schmidt model and the Isentropic model.

For comparison, the pressure profiles along the line of P1-P2 before and after cavitation collapse are also presented in Fig. 5.13 and 5.14, respectively. Before the cavitation collapse at t=50μs (Fig. 5.13), the Schmidt model, the modified Schmidt model and the Isentropic model provides almost identical results while the Cutoff model also compares favorably with the other three models with little discrepancy. After the cavitation collapses t=100μs (Fig. 5.14), the results by the first three models still look fairly similar but there is a small difference discerned on the left/right wall region towards the side wall locally. On the other hand, the pressure profile obtained by the Cutoff model shows that the wave has been reflected from the side wall which is obviously faster than the results provided by the other three models. This shows that the different cavitation pressure has some effects, although limited, on the surrounding flow and hence the pressure profiles. It should be reiterated that the cavitation in this problem occurs under a very high pressure situation and the cavitation size is relatively small. The Schmidt model is found to work fairly well for this problem (Schmidt et al, 1999). As a result, the modified Schmidt model is quite equivalent to the Schmidt model. This also shows that the modified Schmidt model can work consistently from small size to large dimension cavitation in either high or low surrounding pressure situations, and the simple modification for the Schmidt model effectively removes the limitation of the original Schmidt model.

The pressure history at the P2 is recorded for comparison up to 120μs as shown in Fig. 5.15, where the results by four models are presented for comparison. It can be observed that the pressure histories provided by the respective four models are almost the same before the cavitation collapse. The Cut-off model provides a different time instance of cavitation collapse and a lower pressure surge, while the Isentropic model, the Schmidt model and the modified Schmidt model provides similar results. It takes about 25μs for the flow pressure at the surface of the wall changing from peak shock pressure to approach the physical cavitation pressure (decay of shock). The cavitation appears from the surface of cylinder at about 43μs. The collapse of the first cavitation begins around 90μs and the second cavitation appears at about 120μs. As a result, the effect of the first cavitation collapse lasts about 30μs (120μs minus 90μs). This duration of first cavitation collapse (30μs) is obviously comparable with the decay time of the shock wave (23μs). The peak pressure during the cavitation collapse is about 4500 bar which is about 60% of that of the shock wave. The pressure impulse obtained from (5.14) is 340 $P_a.s$ for cavitation collapse and 990 $P_a.s$ for shock wave. Similar to Case 5.5.1, the two pressure impulses generated from initial shock and cavitation collapse are in the same order of magnitude and thus the effect of the cavitation has to be taken into account if the overall damage effect of underwater explosion is considered.

Until now, the underwater explosion in a rigid cylindrical container has been investigated in detail. If the solid wall of the container is taken as a thick flexible boundary (Case 5.5.2b), the effect of solid deformation on cavitation flow dynamics can be further studied in the following. The initial conditions for solid medium are $p_s = 1.0bar$, $\rho_s = 7800\,kg/m^3$, $u_s = 0.0\,m/s$ and $v_s = 0.0\,m/s$ and other parameters of the hydro-elato-plastic EOS for solid can be found in Table 2.1. The initial

conditions for gas and water are kept the same as for Case 5.5.2a. The inner diameter of the cylinder is 0.0889m while the outer diameter is 0.1143m. All four boundaries are treated using the completely reflecting boundary condition. There are 181×361 grid-points are uniformly distributed in one half of the computational domain. The pressure contours at five time instances are shown in Figs. 5.16a-5.16e, respectively. At the time instance of 20μs (Fig. 5.16a), the main shock generated by the explosion is reflecting from the side walls while it is transmitting through the solid wall. It is clearly shown that the present GFM can capture the water-solid interface well. At the time instance of 30 μs (Fig. 5.16b), the reflected main shock has interacted with the explosive bubble resulting in a strong rarefaction wave travelling through the side wall. The obvious deformation of the inner boundary can be observed from Fig. 5.16b due to strong shock impacting; At the time instance of 50μs (Fig. 5.16c), the rarefaction generated from the shock-bubble interaction has been reflected from the inner boundary and thus the cavitation occurs at the surface of the side wall. Such cavitation has developed to a relatively large dimension as shown in Fig. 5.16c. In the whole domain, the contours lines are concentric which shows that flow symmetry is maintained by the present methods. Figure 5.16d shows that the cavitation is compressed and shrinks to a small dimension at the time instance of 70 μs. At this time, the waves in the domain become very complicated. The present method still can maintains a good flow symmetry. The cavitation collapses completely at the time instance of 90 μs.

For comparison of the four cavitation models, the pressure profiles along the line of P1-P2 before and after the cavitation collapse are provided as shown in Figs. 5.17 and 5.18, respectively. It should be noted that the interface pressure becomes negative when the cavitaion occurs near the surface of the solid wall. Thus, the fix as proposed

in Section 5.2.2 is used to overcome such difficulty in the implementation of the present GFM method. After the cavitation collapses at the time instance of 90 μs (Fig. 5.18), the pressures differences near the water-solid interface provided by the four models are partly attributed to the different calculated cavitation pressure. The pressure histories at the P2 are recorded for comparison up to 120μs and shown in Fig. 5.19; the results by the four models are presented for comparison. It can be observed that the pressure histories provided by the respective four models are almost the same before the cavitation collapse. The Cut-off model provides a different time instance of cavitation collapse and a lower pressure surge, while the Isentropic model, the Schmidt model and the modified Schmidt model provides fairly similar results. This further verifies that the Cut-off model tends to provide not very accurate result when compared to the other models even for those problems with very high surrounding flow pressure. It is also found from Fig. 20 that a later time instance of cavitation inception, a faster cavitation collapse and a lower peak pressure of cavitation collapse are predicted by Case 5.5.2b in contrast to Case 5.5.2a. Such observations are consistent with Case 5.1.1 where the underlying physics has been analyzed in detail.

5.6 Summary for Chapter 5

The present GFM and one-fluid cavitation models developed in Chapter 2 and Chapter 3, respectively, are further extended to simulate 2D underwater shock-cavitation-structure interaction. In particular, the underwater explosion near a planar solid wall and the underwater explosion in a closed cylindrical container have been studied. In the study of the cylindrical underwater explosion near a planar solid wall, the computation is carried out for a long time to capture the interactions of the underwater shock, cavitation, and solid wall. The water-jet-like collapse of cavitation and a strong shock generated by the cavitation collapse have been observed. The

collapse of cavitation is so violent that the pressure impulse and overall force are fairly comparable to those generated from the main shock. When the solid wall is taken as flexible, the obvious deformation of solid wall and its effect on the periods and peak pressures of the cavitation has also been investigated in this chapter. The deformation of solid wall leads to a faster collapse of the cavitation and lower peak pressure of the collapse when compared to a rigid wall simulation.

In the computation of the spherical underwater explosion in a closed cylindrical container with rigid solid walls, the present results are compared to the numerical results by Wardlaw and Luton (2000) which is based on a commercial code associated with the Cutoff model. All the physical phenomena put forth by Wardlaw and Luton are exhibited in the present computation. When the wall is taken as a thick flexible wall, a fix is required to treat the possible negative (water-solid) interface pressure. Such fix is able to suppress the negative interface pressure associated with the use of the present GFM. The wave motion in solid is clearly shown in a series of pressure and density contours. The spherical shock-cavitation-solid interactions, as well as water-solid interface, are reasonably captured and simulated.

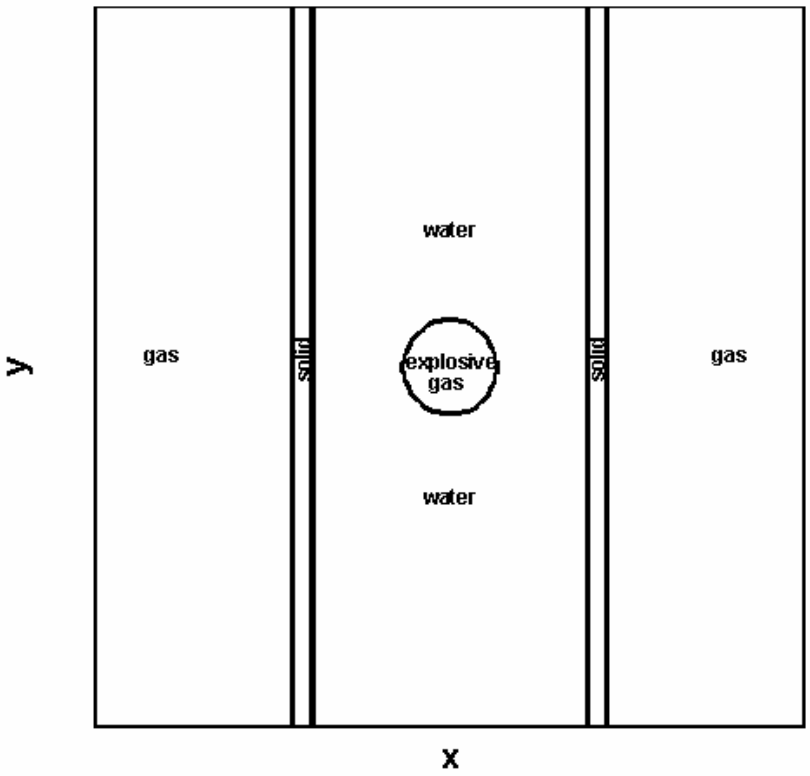

Fig. 5.1 Schematic diagram for an inner explosion in a closed cylinder with a thin flexible wall.

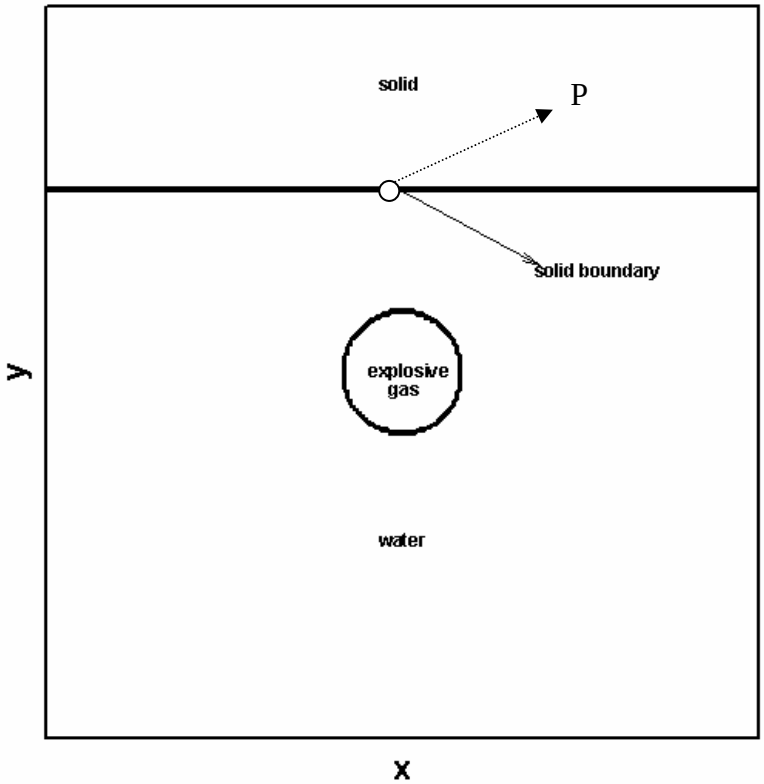

Fig. 5.2 Schematic diagram for a under water explosion near a planar wall (P is center point of the planar wall).

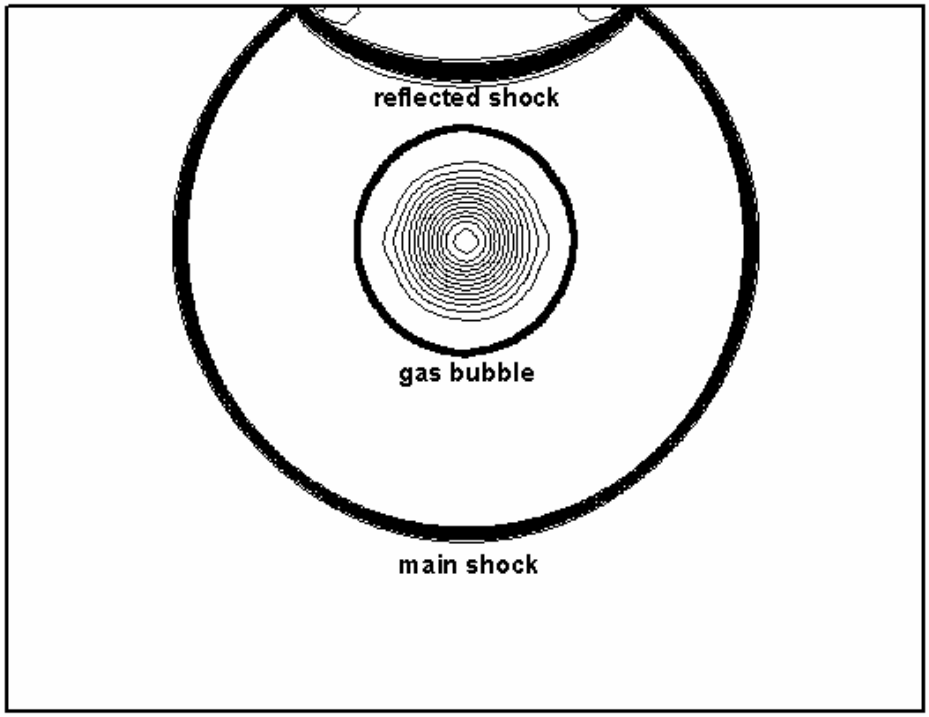

Fig. 5.3a Pressure contour for Case 5.5.1a at t=1.5ms.

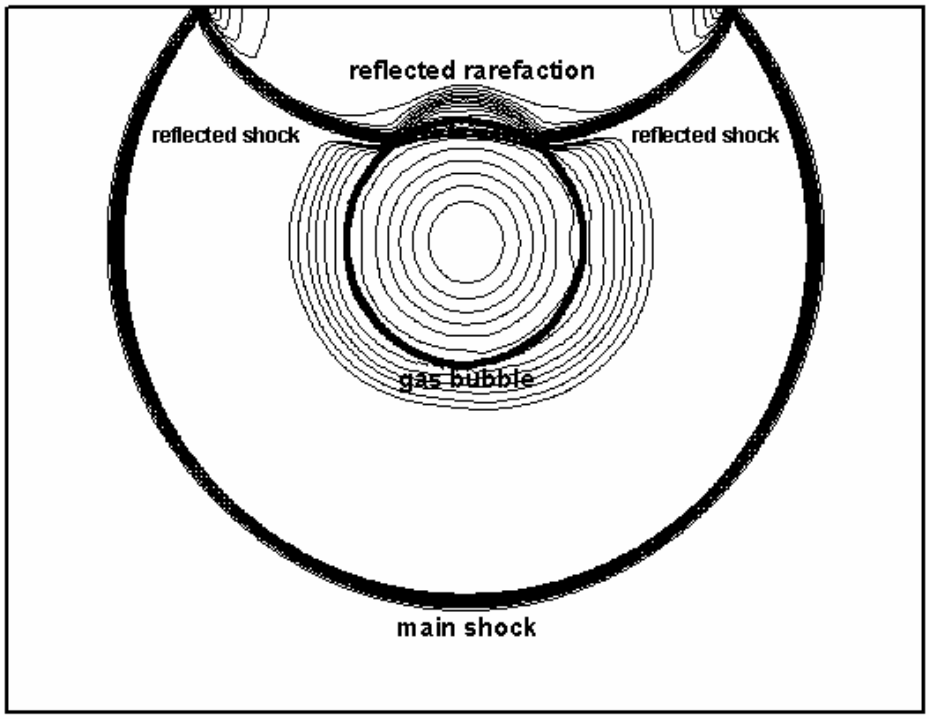

Fig. 5.3b Pressure contour for Case 5.5.1a at t=2.0ms.

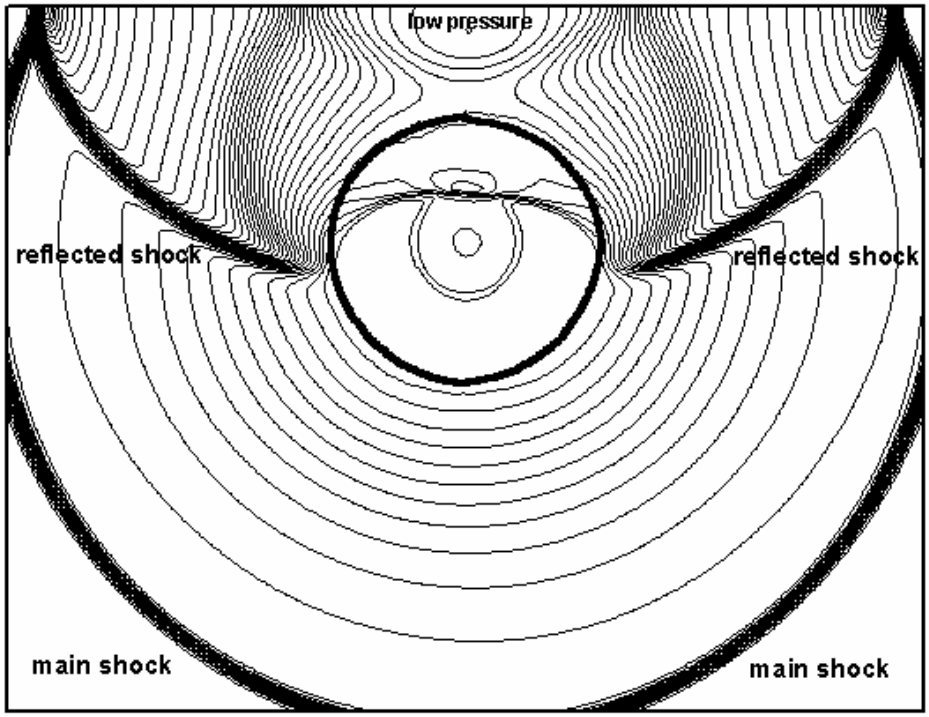

Fig. 5.3c Pressure contour for Case 5.5.1a at t=3.0ms.

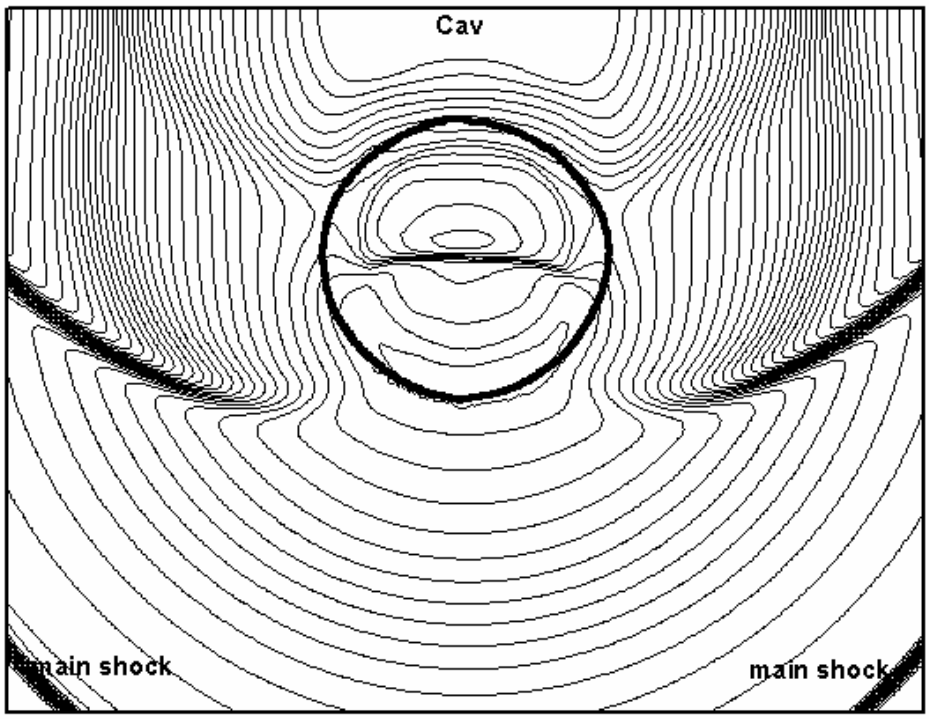

Fig. 5.3d Pressure contour for Case 5.5.1a at t=4.0ms.

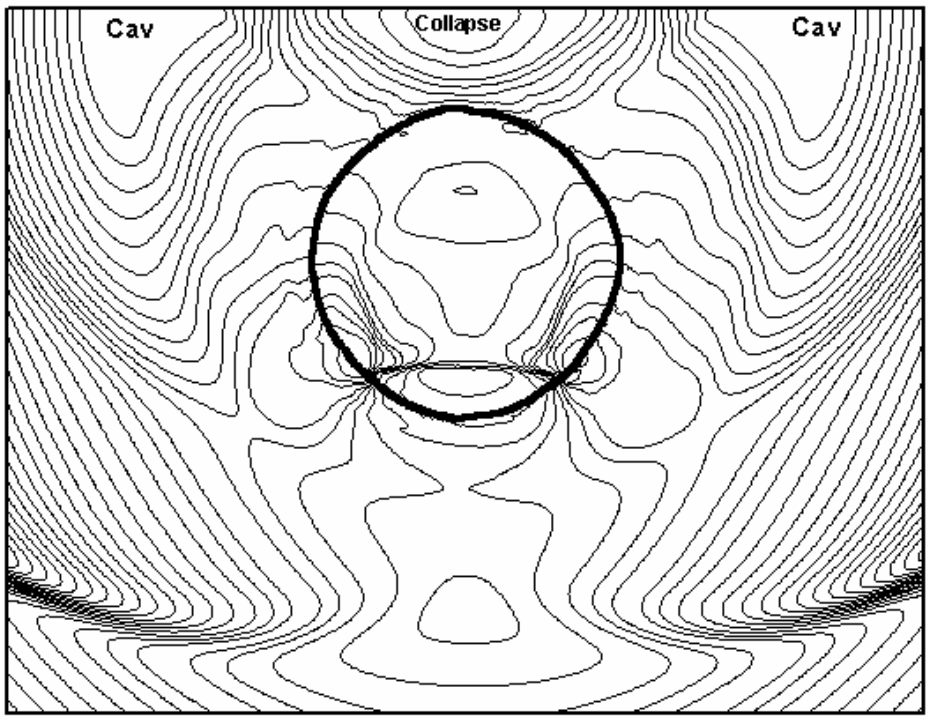

Fig. 5.3e Pressure contour for Case 5.5.1a at t=5.0ms.

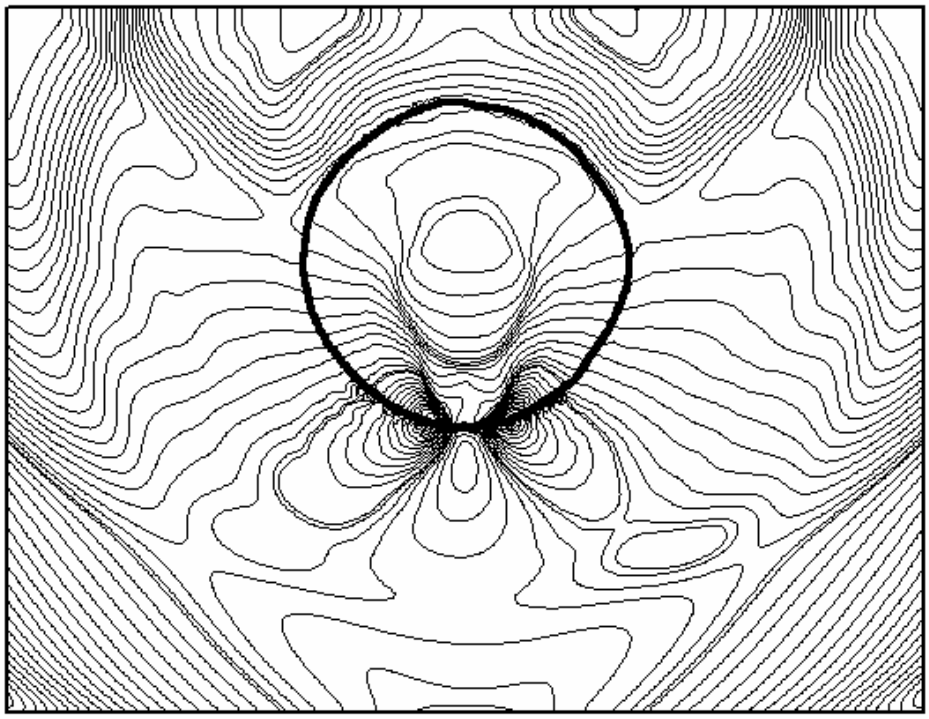

Fig. 5.3f Pressure contour for Case 5.5.1a at t=6.5ms.

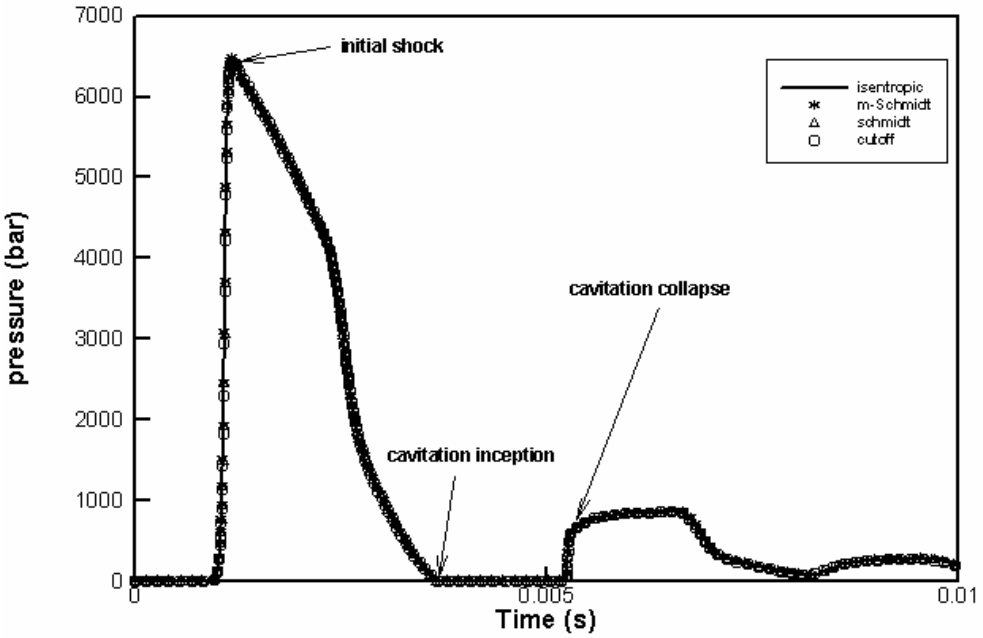

Fig. 5.4 Pressure history for Case 5.5.1a at the center location of the planar wall (P).

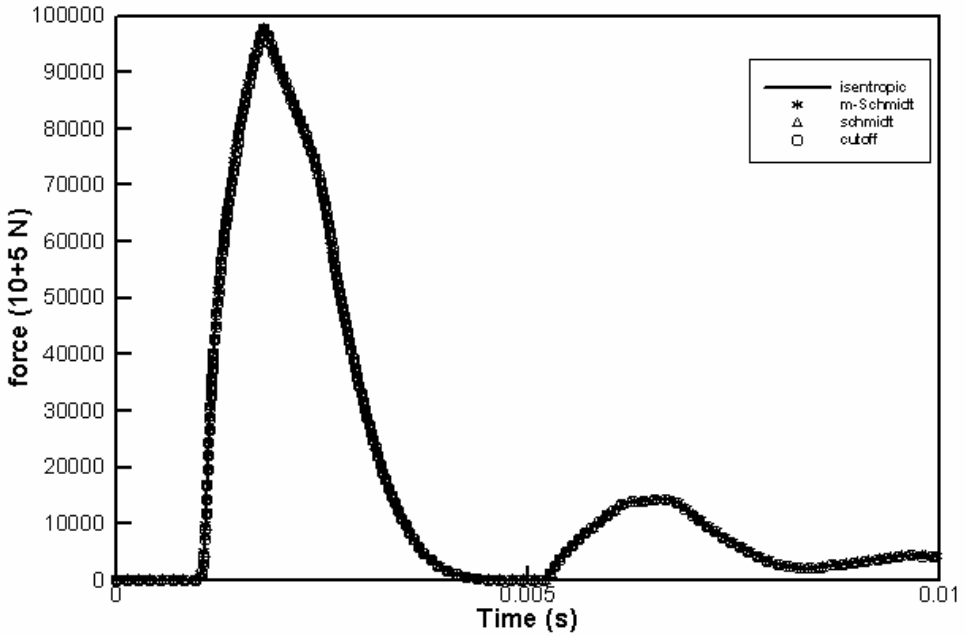

Fig. 5.5 Overall force history for Case 5.5.1a on a quadrate region at the center of the planar wall (P).

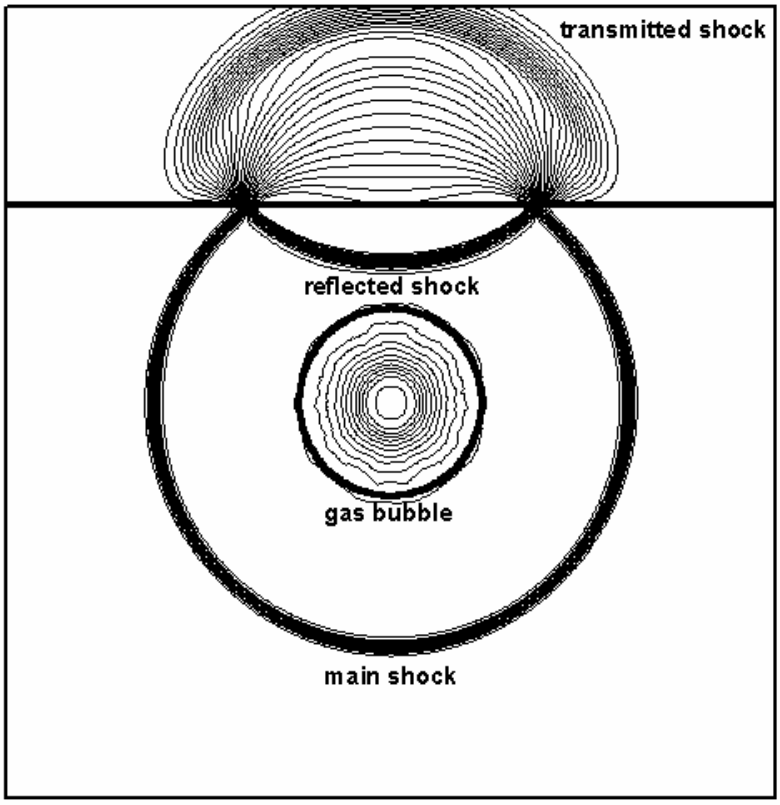

Fig. 5.6a Pressure contour for Case 5.5.1b with flexible wall at t=1.5ms.

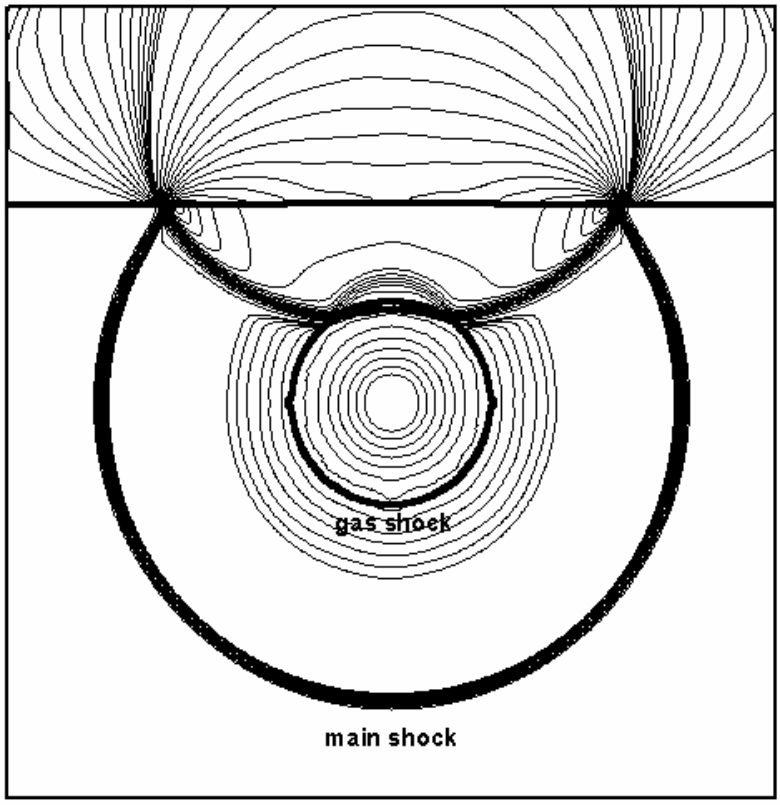

Fig. 5.6b Pressure contour for Case 5.5.1b with flexible wall at t=2.0ms.

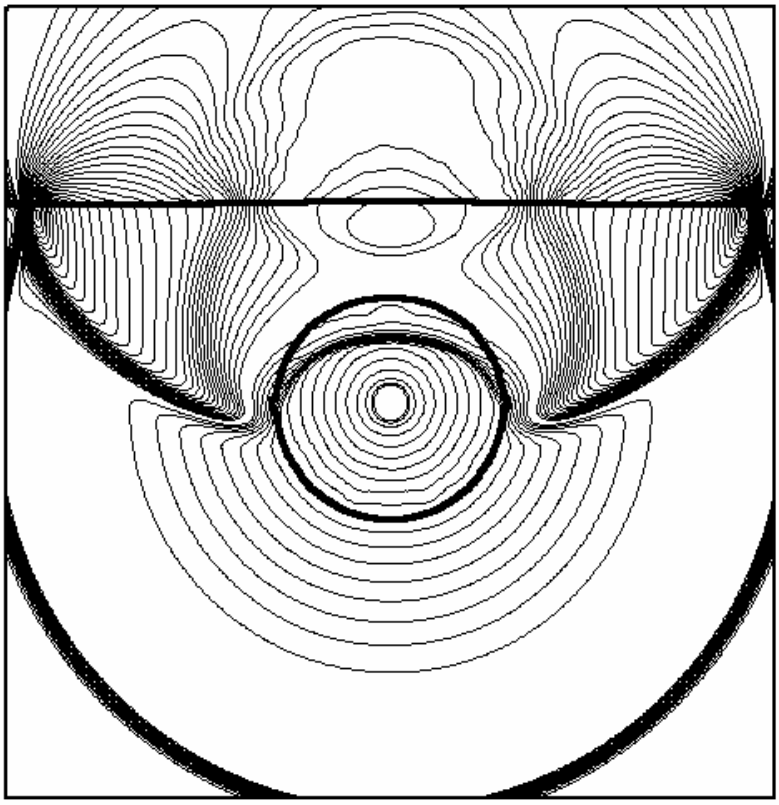

Fig. 5.6c Pressure contour for Case 5.5.1b with flexible wall at t=3.0ms.

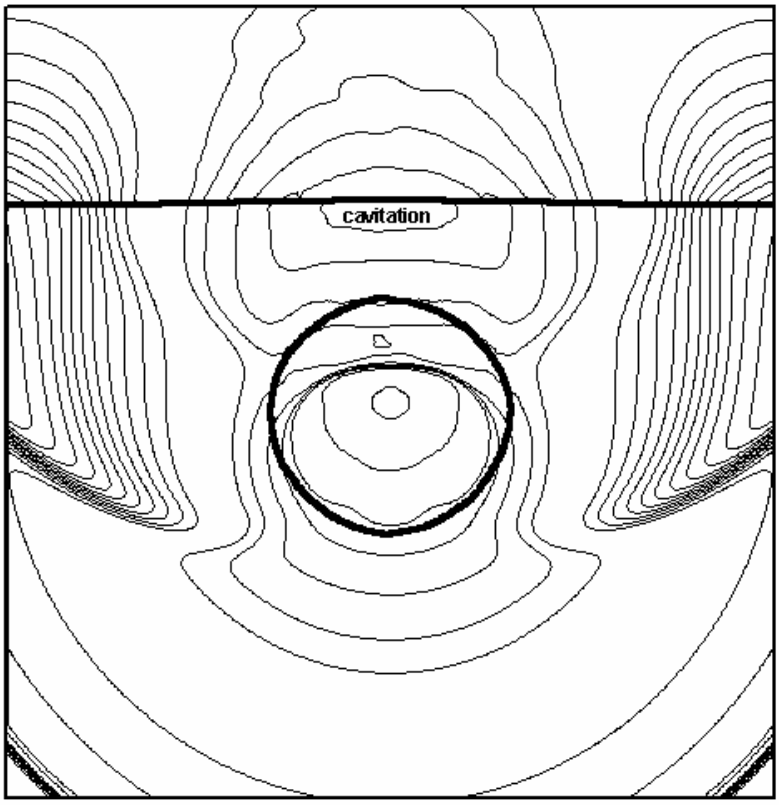

Fig. 5.6d Pressure contour for Case 5.5.1b with flexible wall at t=4.0ms.

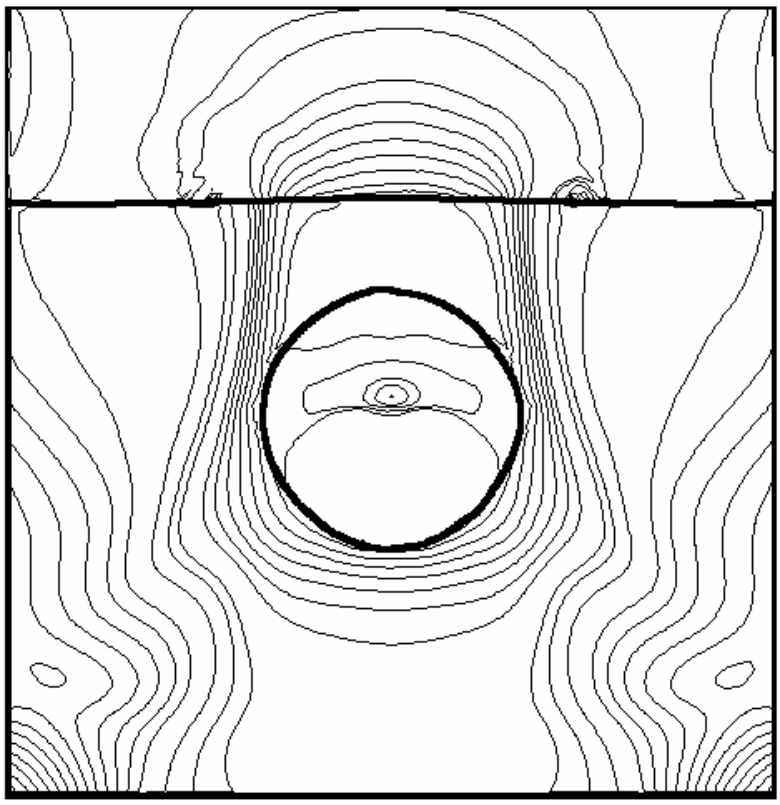

Fig. 5.6e Pressure contour for Case 5.5.1b with flexible wall at t=5.5ms.

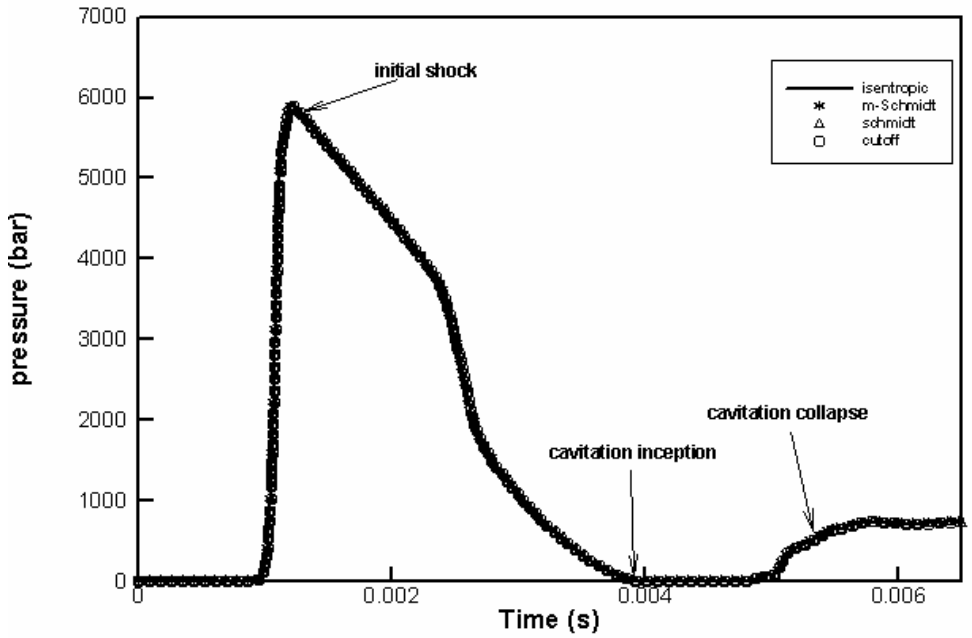

Fig. 5.7 Pressure history for Case 5.5.1b at the center location of the flexible planar wall (P).

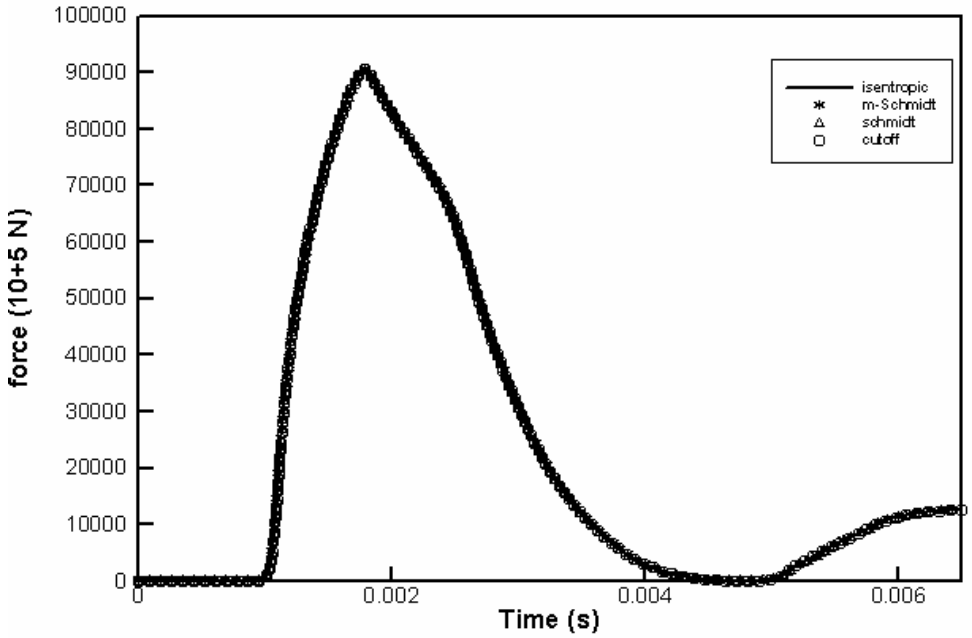

Fig. 5.8 Overall force history for Case 5.5.1b at the center location of the flexible planar wall (P).

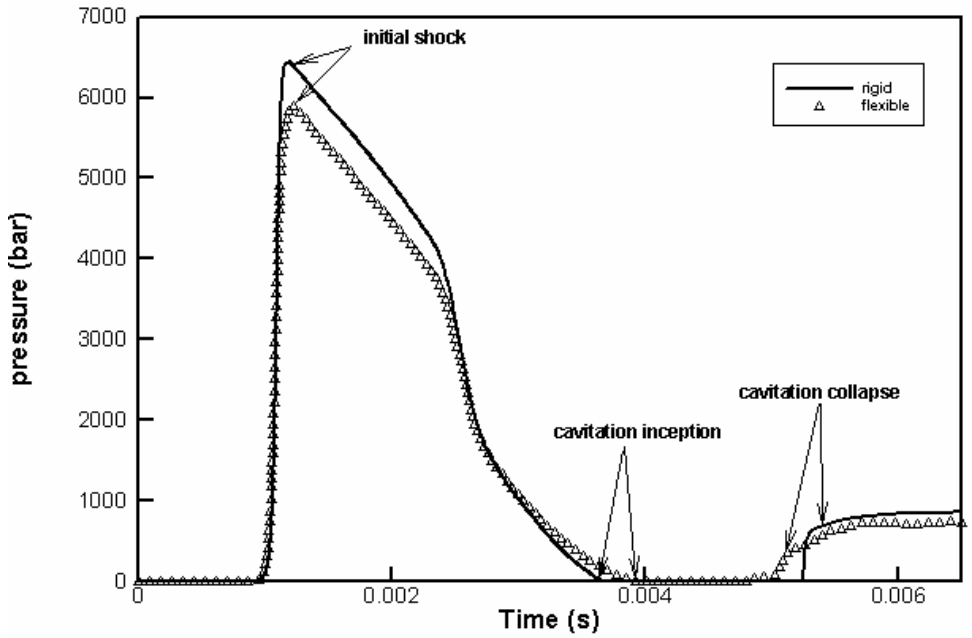

Fig. 5.9 The comparsion of pressure histories for Case 5.5.1 at the center location of the rigid and flexible planar wall (P).

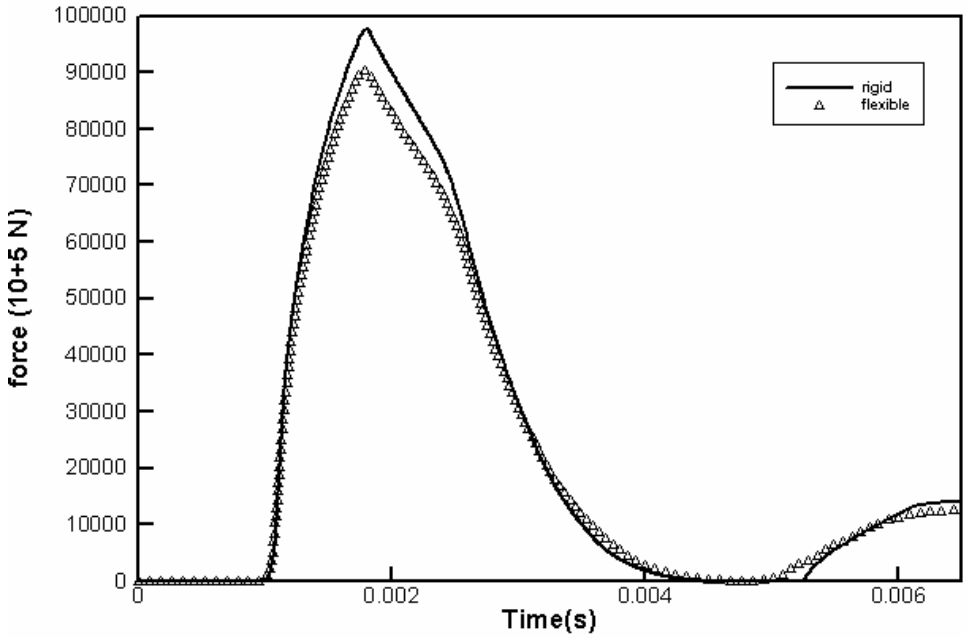

Fig. 5.10 The comparsion of overall force for Case 5.5.1 exerted on the rigid and flexible planar wall.

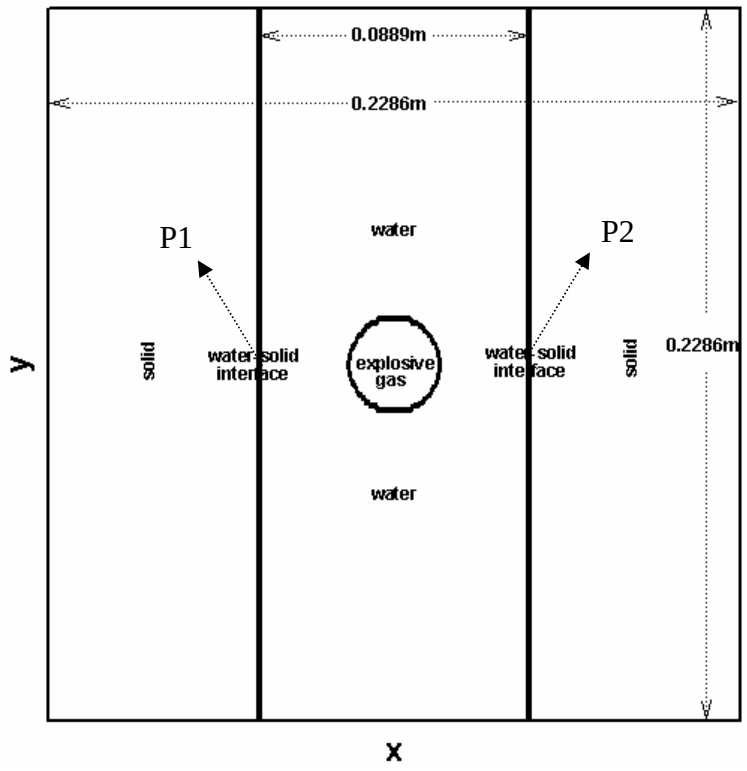

Fig. 5.11 Schematic diagram for an inner explosion in a closed cylinder where P1 and P2 are center points of the cylinder wall.

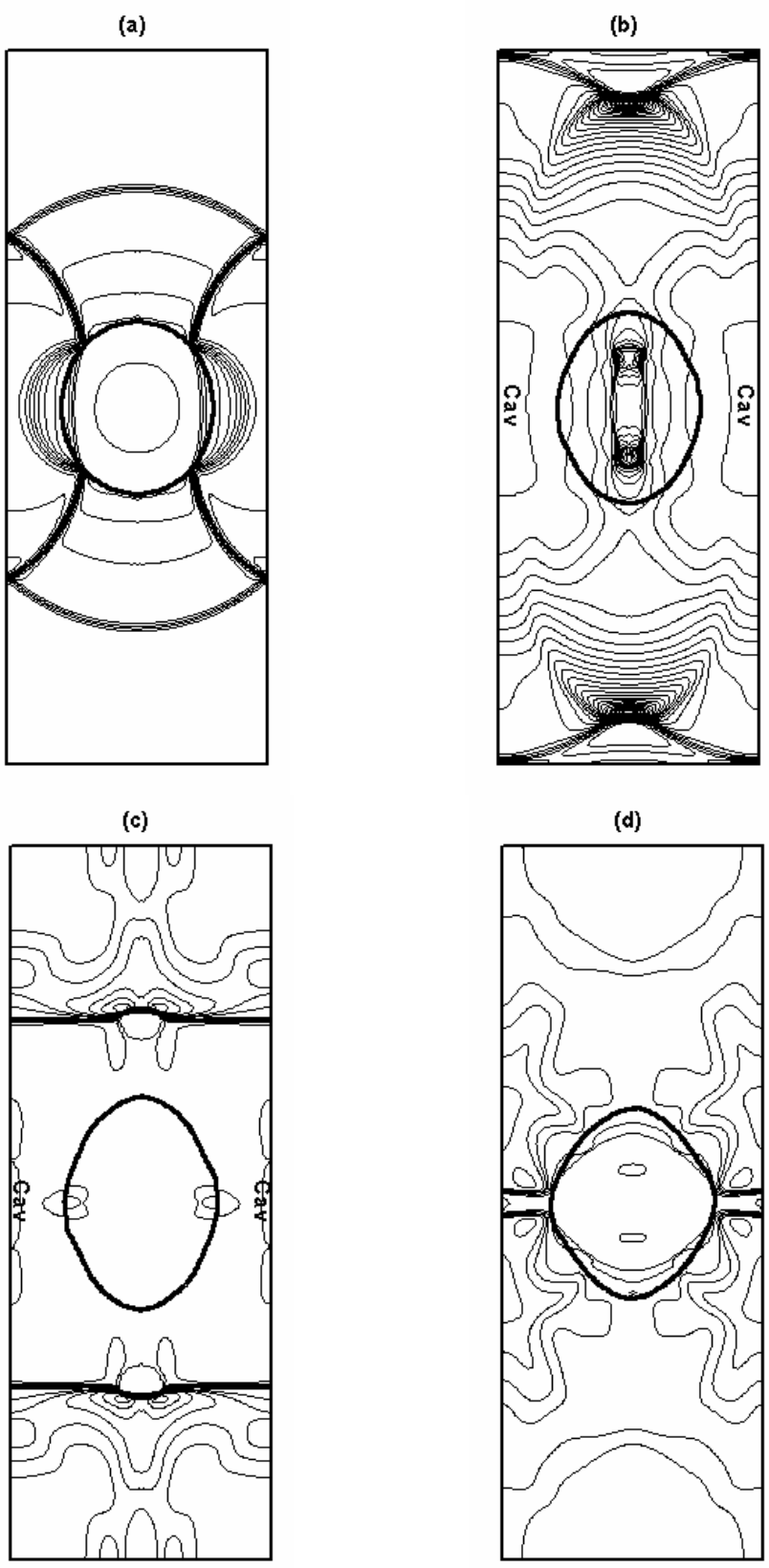

Fig. 5.12 Pressure contours for Case 5.5.2a at (a) t=30μs; (b) t=60μs; (c) t=90μs; (d) t=120μs. “Cav” indicates the cavitation region.

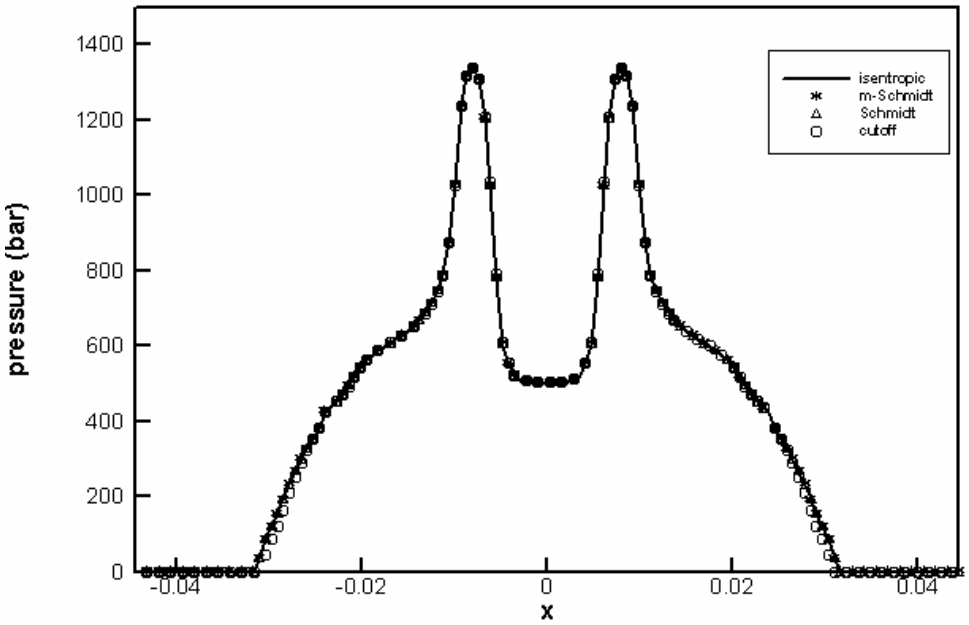

Fig. 5.13 Pressure profiles for Case 5.5.2a by the four cavitation models along the left/right wall (P1-P2) before cavitation collapse at t=50μs.

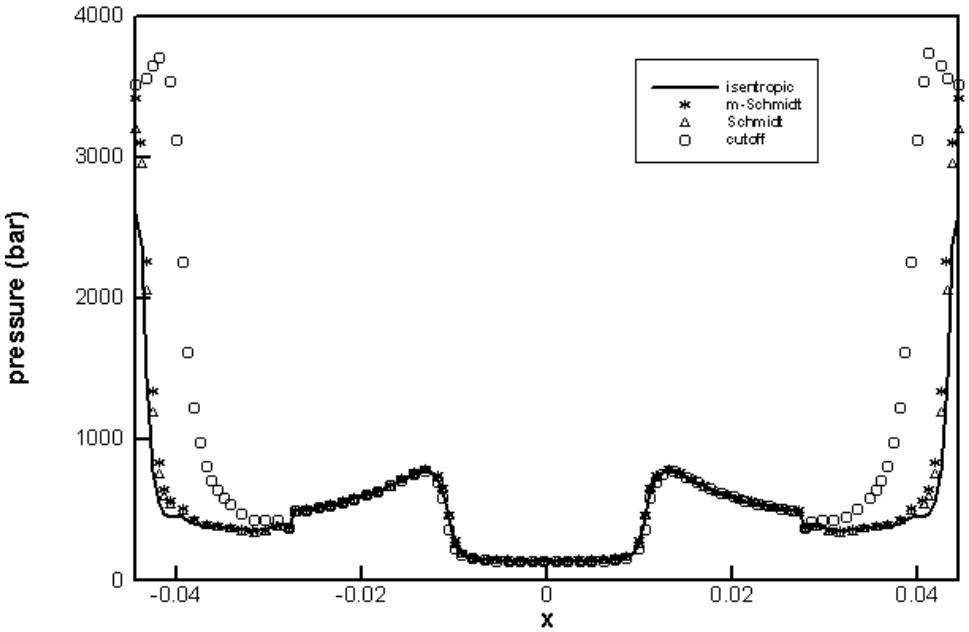

Fig. 5.14 Pressure profiles for Case 5.5.2a by the four cavitation models along the left/right wall (P1-P2) after cavitation collapse at t=100μs.

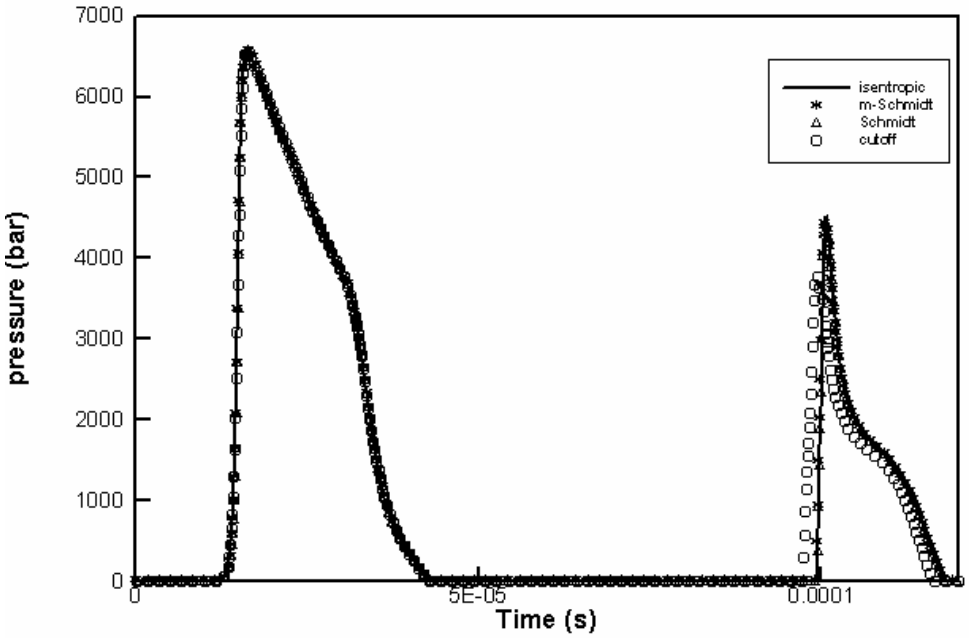

Fig. 5.15 Pressure history for Case 5.5.2a at the center location of the right side of flexible wall (P2).

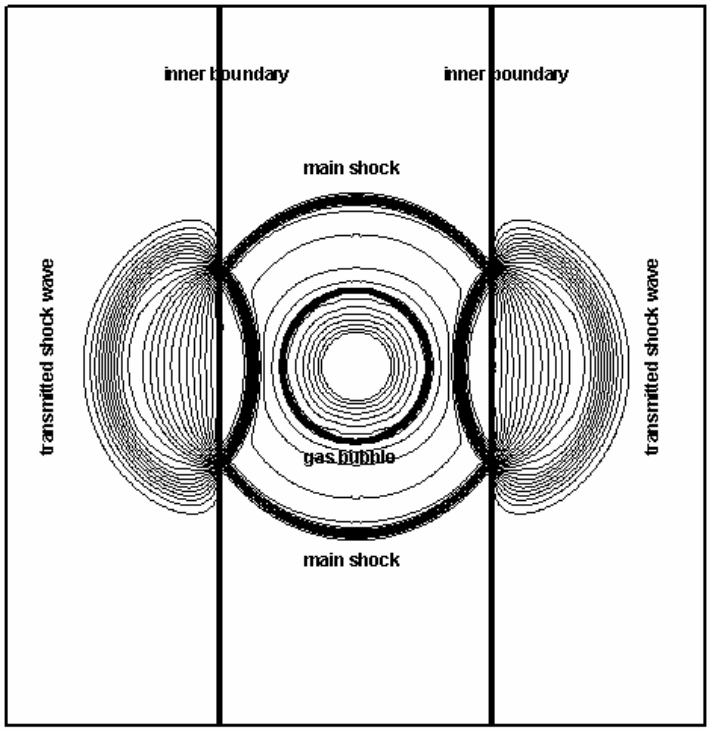

Fig. 5.16a Pressure contour for Case 5.5.2b with flexible wall at t=20μs.

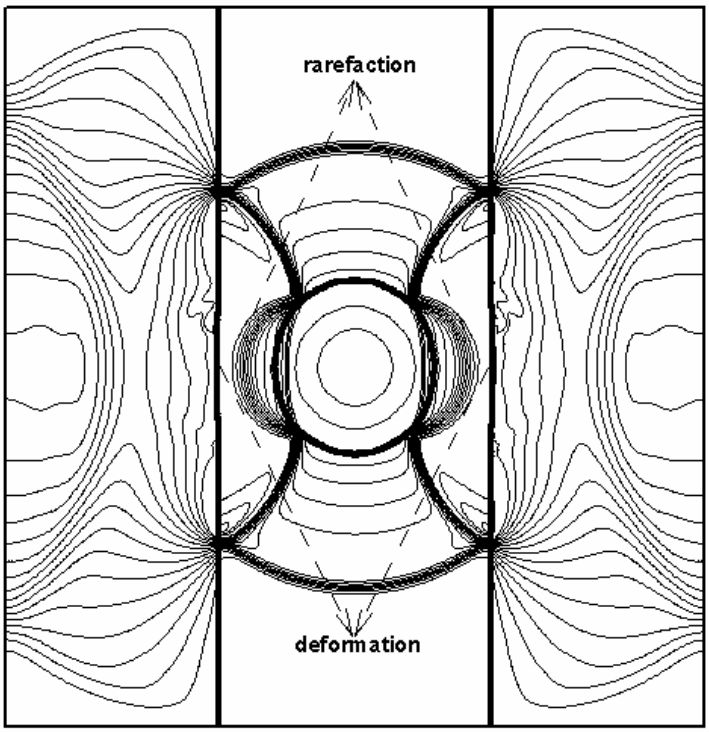

Fig. 5.16b Pressure contour for Case 5.5.2b with flexible wall at t=30μs.

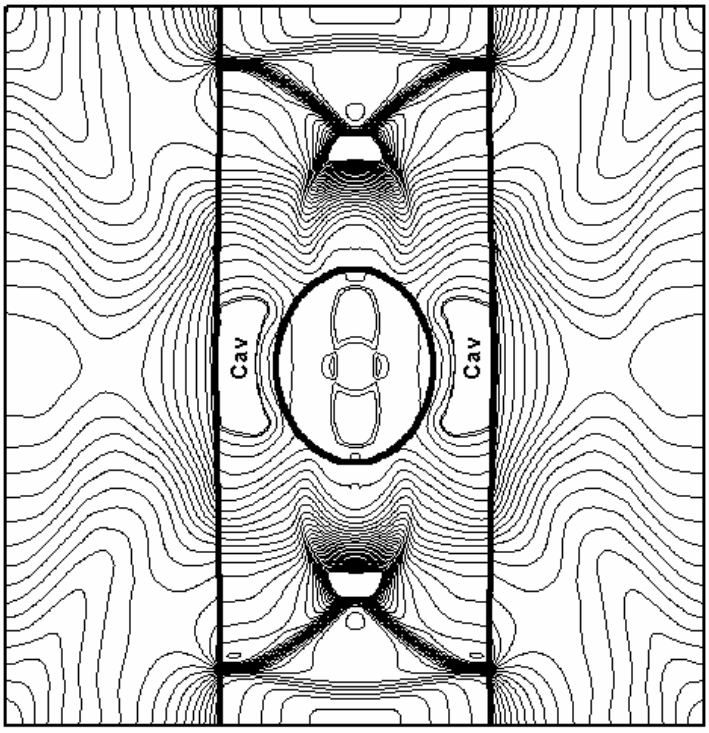

Fig. 5.16c Pressure contour for Case 5.5.2b with flexible wall at t=50μs.

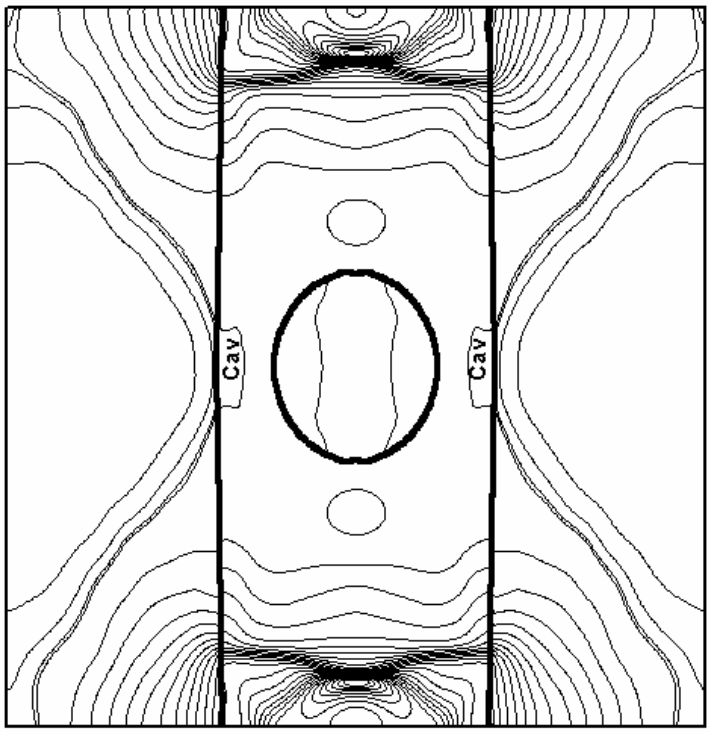

Fig. 5.16d Pressure contour for Case 5.5.2b with flexible wall at t=70μs.

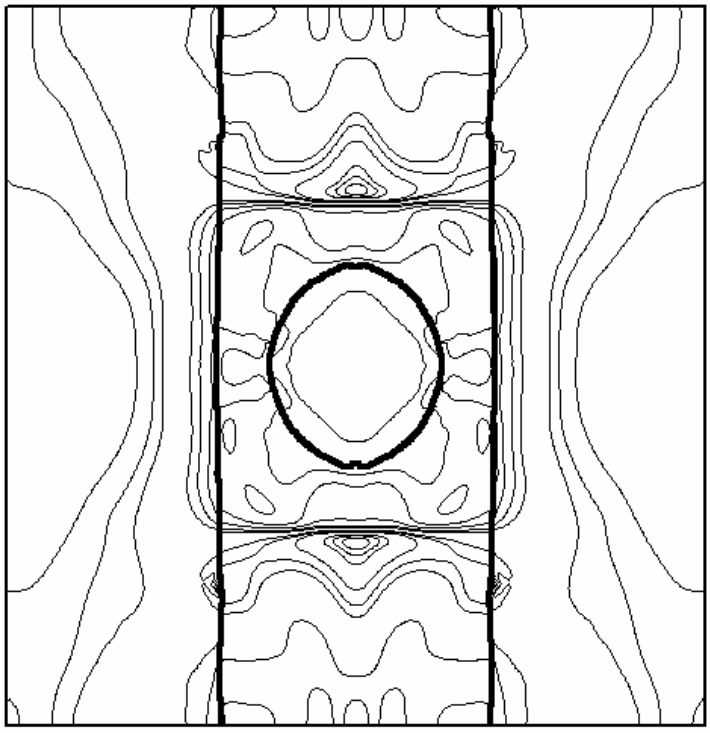

Fig. 5.16e Pressure contour for Case 5.5.2b with flexible wall at t=90μs.

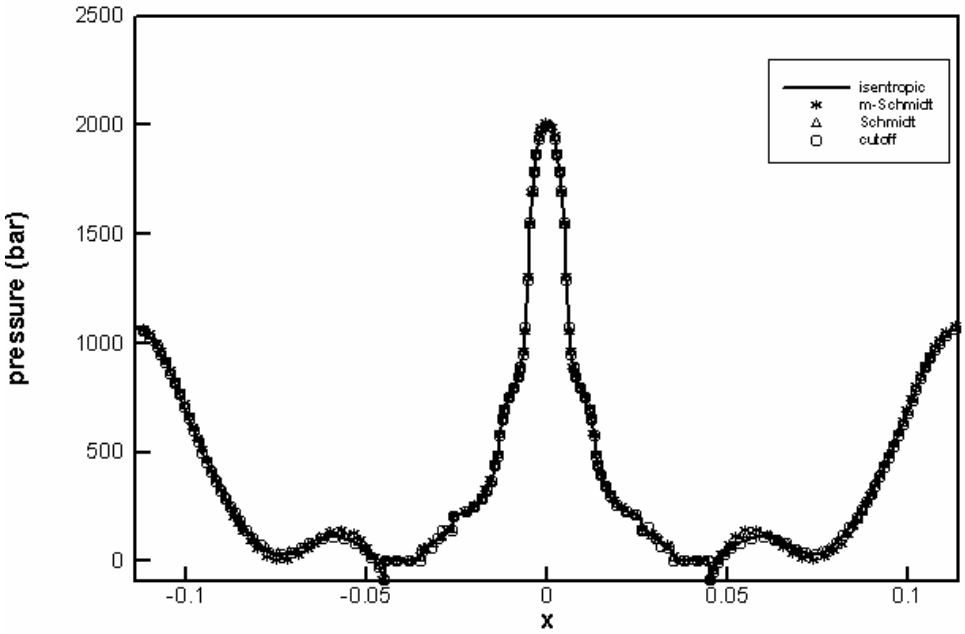

Fig. 5.17 Pressure profiles for Case 5.5.2b by the four cavitation models along the left/right wall (P1-P2) before cavitation collapse at t=60μs.

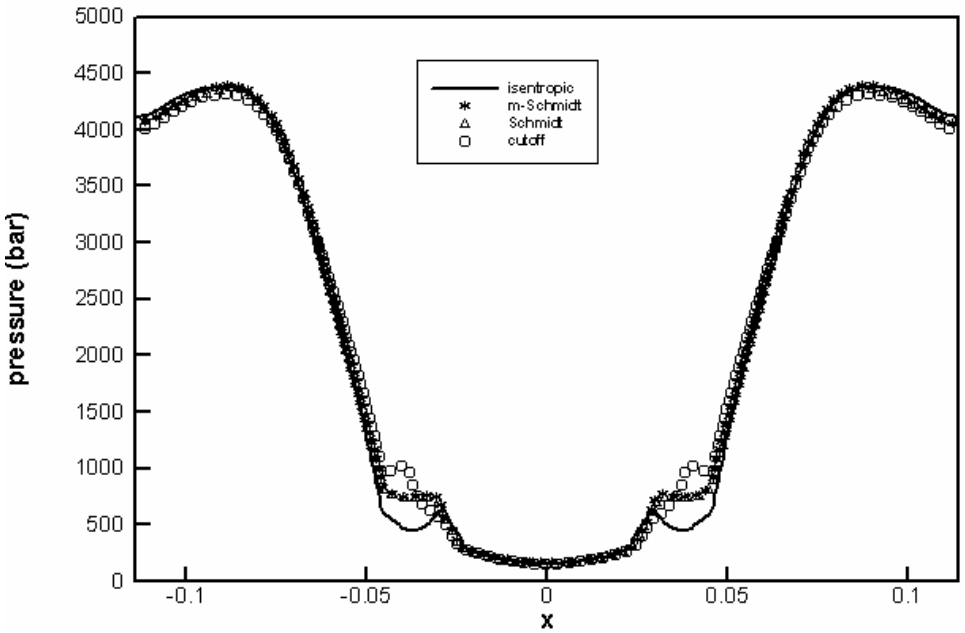

Fig. 5.18 Pressure profiles for Case 5.5.2b by the four cavitation models along the left/right wall (P1-P2) after cavitation collapse at t=90μs.

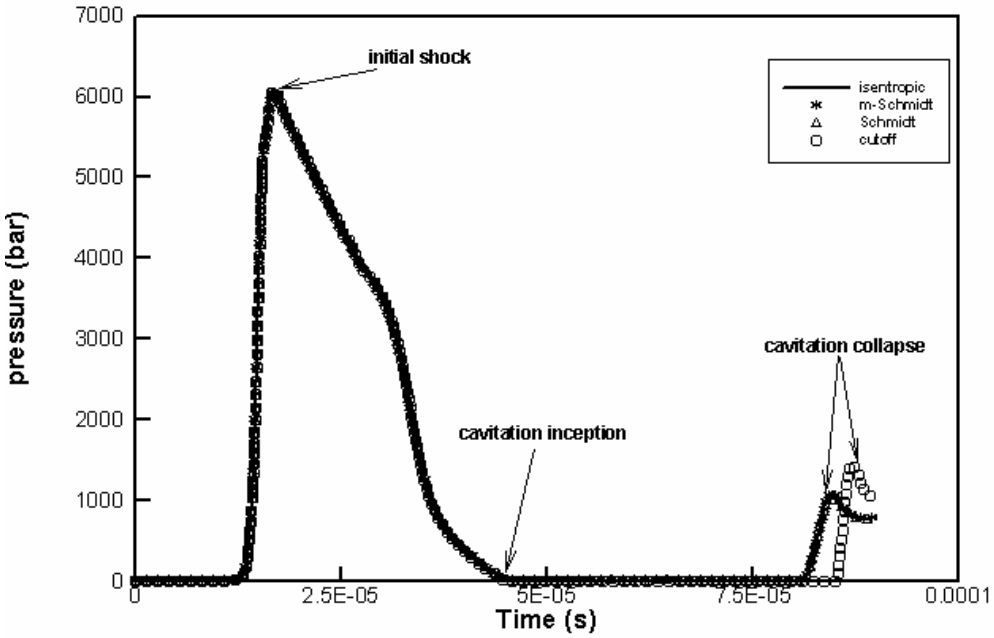

Fig. 5.19 Pressure history for Case 5.5.2b at the center location of the right side of flexible wall (P2).

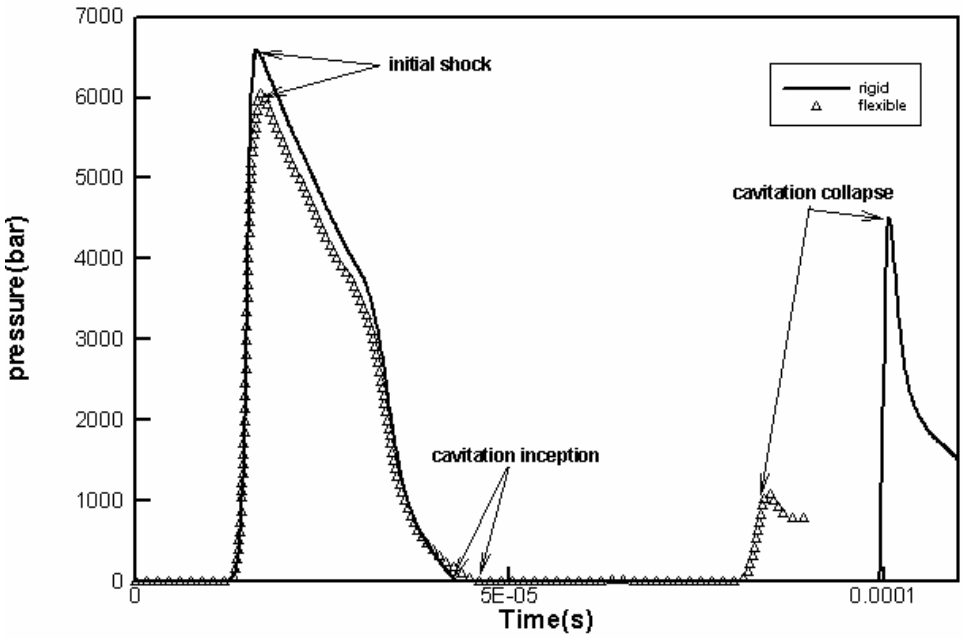

Fig. 5.20 The comparsion of pressure histories for Case 5.5.2 at the center location of the rigid and flexible cylindrical wall (P2).

Chapter 6

Conclusions and Recommendations

6.1 Conclusions

Two parts of simulations are involved in the simulation of an underwater explosion near a structure. The first one is the treatment and simulation of the material interface of multi-medium/multiphase compressible flows. The other one is the simulation and modeling of cavitation. For the former, to capture a sharp material interface and suppress possible numerical oscillation at the interface are always challenging. For this purpose, the analysis is carried out for various multi-medium/multiphase compressible flows via the existing GFM-based algorithms like the original GFM and new version GFM as developed by Fedkiw et al (1999b, 2002) and the MGFM as developed by Liu et al (2003) where an Approximate Riemann problem (ARPS) is solved via iteration to obtain the interface status. Based on the analysis, the present GFM associated with an explicit characteristic method for predicting the interface information is developed. The ARPS in the MGFM is replaced by such explicit characteristic method where only an algebraic equation is solved and no iteration is needed.

For simulation of the cavitation, a few commonly employed one-fluid cavitation models, the Cut-off model, the Vacuum model and the Schmidt model, have been found to be mathematical inconsistent or complicated. In this work, we present two recently developed one-fluid cavitation models, the mathematical self-consistent Isentropic model (see also Liu et al, 2004a) and the modified Schmidt model (see also Xie et al, 2005a). Extensive analysis and comparisons are carried out to define the application ranges of these one-fluid cavitation models. The test cases are listed in Table 6.1.

Chapters	Test cases	Purposes
Chapter 2	1. Gas-water flows 2. Gas-solid flows 3. Water-solid flows	1. Compare GFM-based algorithms 2. Support the analysis.
Chapter 3	Various single-phase cavitating flows	1. Compare one-fluid cavitation models. 2. Support the analysis.
Chapter 4	1. Single-phase cavitating flow in a closed tube 2. Water-hammer problem 3. Gas-water cavitating flow	1. Observe the cavitation inception, evolution and collapse. 2. Compare one-fluid cavitation models to experiments. 3. Test the proposed GFM and one-fluid cavitation models together.
Chapter 5	1. UNDEX near a planer wall 2. UNDEX inside a cylinder	1. 2D applications of the proposed methods. 2. UNDEX in an open region like a floating ship. 3. UNDEX in a closed region like a closed tank.

Table 6.1 The lists and purposes of test cases in each chapter.

For application of the present GFM and one-fluid cavitation models to the test cases as shown in Table 6.1, the main findings can be summarized as follows:

1. The original GFM and new version GFM do not work well when applied to simulate compressible multi-medium flows involving strong shock wave or jet impact; the iteration needed by the MGFM is found to take quite many steps and sometimes may fail to converge especially in the low pressure situation of the multi-medium/multi-phase flows involving fluid-structure interaction. The present GFM is robust and very cost-effective in such situations. On the other hand, the present GFM is not very effective for cases where strong rarefaction waves are propagating in fluid mediums. This is because the explicit

characteristic method as used in the present GFM approximates exact interface Riemann Solver with only first order accuracy.

2. The one-fluid models as presented in this work can capture different cavitation sizes and have different application ranges (i.e. density ratio of liquid to vapor). The Isentropic model, as well as the modified Schmidt model, works much more consistently than other one-fluid models and are applicable for various flow conditions. There is no mathematical and physical inconsistency in the Isentropic model.
3. Four one-fluid models as presented in this work are employed to simulate cavitating flows in pipeline systems with accompanying water-hammer phenomena. The predicted pressure by the Isentropic model and modified Schmidt model histories at various locations of the pipeline are in substantial agreement with experiment data by Sanada et al (1990) both for the periods and peak pressure while the Cutoff model fails to provide reasonable periods and numerical oscillation is observed using the Schmidt-II models (see section 3.3.2).
4. Four one-fluid models provide similar pressure histories on time at the surface of the right end wall when applied to simulate 1D gas-water cavitating flows in a closed tube where the surrounding flow pressure is sufficiently high to provide a large pressure jump across the cavitation boundary.
5. The explicit characteristic method for multidimensional Euler system is derived and one-fluid cavitation models are directly applied to 2D axis-symmetric problems generated by underwater explosions where there is the presence of large surrounding flow pressure. The multidimensional material interface is

accurately captured and the inception, evolution, and collapse of cavitation near the solid wall are well simulated.

6. The deformation of solid wall is clearly captured by the present GFM. The deformation of the solid wall alters the periods and peak pressure of cavitation collapse; a faster cavitation collapse and lower peak pressure relatively to the rigid wall counterpoint. The possible negative pressure occurred in the solid side bordering the water-solid interface is successfully suppressed via the proposed fix as detailed in Section 5.2.3.

6.2 Recommendations

The present GFM and proposed one-fluid cavitation models provide reasonable results for cavitating flows in pipe/tube and underwater shock-cavitation-structure interactions. All these computations are based on the assumption that the cavitation is generated by pressure drop. Therefore, the thermal non-equilibrium can not be addressed by the present one-fluid cavitation models. It is desirable to develop a one-fluid model for incorporation of the thermal energy exchange; the present cavitation models are only used for simulation of compressible flows. The application of these models for incompressible flows based on an N-S solver is also desirable. For this purpose, the simulation of flow passing a hydrofoil will be carried out. As mentioned in Chapter 5, the present system is inapplicable for the simulation of shock-thin flexible wall interaction. The present method to be coupled with a Navier equation can be used for modeling such interaction. Thus further work is needed to couple the solid equation to the Euler system. Finally, the present computational domains are regular. Therefore, it is desirable to simulate the cavitation generated from irregular and coarse material surface. For example, an underwater explosion near a structure with a complex surface shape will be simulated.

Reference

Aanhold, J. E., G. J. Meijer and P. P. M. Lemmen. Underwater Shock Response Analysis on a Floating Vessel, Shock and Vibration, 5, pp.53-59.1998.

Abgrall, R. and S. Karni. Computations of compressible multifluids, J. Comp. Phys, 169, pp.594-623. 2001.

Abgrall, R. How to prevent pressure oscillations in multicomponent flow calculations: A quasi conservative approach, J. Comp. Phys, 125, pp. 150-160. 1996.

Ahuja, V., A. Hosangadi and S. Arunajatesan. Simulations of cavitating flows using hybrid unstructured meshes, J. Fluid Eng,123, pp.331-340.2001.

Ahuja, V., H. Ashvin and A. Srinivasan, Simulations of Cavitating flows Using Hybrid Unstructured Meshes, JFE Trans ASME, 123, pp.331-340. 2001.

Allaire, G., S. Clerc and S. Kokh. A five-equation model for the simulation of interfaces between compressible fluids, J. Comp. Phys, 181, pp. 577-616. 2002.

Avva, R. K. and A. K. Singhal. An enthalpy based model of cavitation, ASME FED summer meeting, Hilton Head Island, August 13-18. 1995.

Brennen, C. E. Cavitation and Bubble Dynamics. Oxford University Press. 1995.

Brett, J. M., G. Yiannakopoulos and Paul J. Van der Schaaf. Time-resolved measurement of the deformation of the submerged cylinders subjected to loading from a nearby explosion, Int. J. Impact Eng, 24, pp.875-890. 2000.

Chaiko, M. A., and K. W. Brinckman. Models for Analysis of Water Hammer in Piping With Entrapped Air, J. Fluid Eng, ASME, 124, pp. 194-204. 2002.

Chen, Y. and S. D. Heister. A numerical treatment for attached cavitation, J. Fluid Eng, 116, pp.613-618. 1994.

Clerc, S. Numerical Simulation of the homogeneous equilibrium model for two-phase flows, J. Comp. Phys, 161, pp. 354-375. 2000.

Cochran, G. and J. Chan. Shock initiation and detonation models in one and two dimensions, Lawrence Livermore National Laboratory Report. 1979.

Cole, A. H. Underwater Explosion. Dover, New York. 1965.

Coutier-Delgosha, O., J. L. Reboud and Y. Delannoy, Numerical simulation of the unsteady behaviour of cavitating flows, Int. J. Numer. Meth. Fluids, 42, pp. 527-548. 2003.

Coutier-Delgosha, O., R Fortes-Patella, J. L. Reboud., Simulation of unsteady cavitation with a two-equation turbulence model including compressibility effects, J. Turbulence, 3, pp.1-20. 2002.

Coutier-Delgosha, O., R. Fortes-Patella. On Evaluation of the turbulence model influence on the numerical simulations of unsteady cavitation, JFE Trans ASME, 125, pp.38-45. 2003.

Delannoy and J. L. Kueny. Two phase flow approach in unsteady cavitation modelling, Cavitation and Multiphase Flow Forum, *ASME, FED*, 98, pp.152-158 .1990.

Deshpande, M., J. Feng and C. L. Merkle. Cavity flow predictions based on the Euler equations, J. Fluid Eng, 116, pp.36-44 .1994.

Deshpande, M., J. Feng and C. L. Merkle. Numerical Modelling of the thermodynamic effects of cavitation, J. Fluid Eng, 119, pp.420-427 .1997.

Duncan R., van der Heul, C. Vuik and P. Wesseling. Efficient computation of flow with cavitation by compressible pressure correction. European Congress on Computational Methods in Applied Sciences and Engineering Barcelona, 2000.

Einfeldt, B., C. D. Munz., P. L. Roe and B. Sjogreen. On Godunov-type methods near low densities, J. Comp. Phys, 92, pp.273-295. 1991.

Evje S, Fjelde KK. Hybrid flux-splitting schemes for a two-phase flow model, J. Comp. Phys, 175, pp.674-701. 2002.

Falcovitz, J. and A. Birman, A singularities tracking conservation laws scheme for compressible duct flows, J. Comp. Phys, 115, pp. 431-439. 1994.

Farhat, C. and F. X. Roux. A method for finite element tearing and interconnecting and its parallel solution algorithm, Int. J. Numer. Meth. Engng, 32, 1205-1227.1991.

Fedkiw, R. P. Coupling an Eulerian Fluid Calculation to a Lagrangian Solid Calculation with the Ghost Fluid Method, J. Comp. Phys, 175, pp.200-224. 2002.

Fedkiw, R. P., A. Marquina and B. Merriman. An isobaric fix for the overheating problem in multimaterial compressible flows, J. Comp. Phys, 148, pp. 545-578. 1999a.

Fedkiw, R. P., A.Marquina and B.Merriman., A non oscillatory eulerian approach to interfaces in multimaterial flows (The ghost fluid method), J. Comp. Phys, 152, pp.457-492. 1999b.

Fedkiw, R. P., B.Merriman and S. Osher., Efficient characteristic projection in upwind difference schemes for hyperbolic systems (the Complementary Projection Method), J. Comp. Phys, 141, pp.22-36. 1998.

Felipe, B. Freitas Rachid. A thermodynamically consistent model for cavitating flows of compressible fluids, Int. J. Non-Linear Mech, 38, pp.1007-1018. 2003.

Fellipa, C.A. and J.A. Deruntz. Finite element analysis of shock-induced hull cavitation, Comput. Meth. Appl. Mech. Eng, 44, pp. 297–337.1984.

Franc, J. P, F. Avellan, B. Belahadji, J. Y. Billard, L. Briancon, Marjollet, D. Frechou, D. H. Fruman, A. Karimi, J. L. Kueny and J. M. Michel. La Cavitation: Mecanismes Physiques et Aspects Industriels, Presses Universitaries de Grenoble, Grenoble (EDP Sciences), pp. 28-449, France. 1995.

Freitas Rachid F.B. and H. S. Costa Mattos. Modeling the damage induced by pressure transients in elasto-plastic pipes, Mechanica, 33, pp.139–160.1998.

Freitas Rachid, F. B. and H. S. Costa Mattos Modeling of pipeline integrity taking into account the fluid–structure interaction, Int. J. Numer. Meth. Fluids, 1, pp. 21–39.1998.

Galiev, S. U. Influence of cavitation upon anomalous behaviour of a plate liquid underwater explosion system, Int. J. Impact Eng, 19, pp. 345-359. 1997.

Gavrilyuk, S. and R. Saurel. Mathematical and numerical modelling of two-phase compressible flows with micro-inertia. J. Comp. Phys, 175, pp.326-360. 2002.

Glaister, P. An approximate linearized Riemann solver for the Euler equations for real gas, J. Comp. Phys, 74, pp.382-408. 1988.

Glimm, J., O. Mcbryan, R. Melnikoff and D. H. Sharp. Front tracking applied to Rayleigh-Taylor instability, SIAM. J. Sci. Stat. Comput, 7, pp. 230-251. 1998.

Godunov, S. K., A. Zabrodine, M. Ivanov, A. Kraiko and G. Prokopov. Resolution numerique des problemes multidimensionnels de la dynamique des gaz, Moscow. 1979.

Gopalan, S. and J. Katz. Flow Structure and Modeling Issues in the Closure Region of Attached Cavitation, Phys. Fluids, 12(4), pp. 895-911. 2000.

Guillard, H. and C. Viozat. On the behaviour of upwind schemes in the low Mach number limit, Comp.& Fluids, 28, pp.63-86. 1999.

Harten, A. and S. Osher. Uniformly High-Order Accurate Non-Oscillatory Schemes I, SIAM. J. Numer. Anal, 24, pp. 279-309. 1987.

Harten A., P. D. Lax and B. Van leer. Upstream Differencing and Godunov-type Schemes for Hyperbolic Conservation Laws. SIAM. Review, 25, pp. 35-61. 1983.

Harten, A. High resolution schemes for hyperbolic conservation laws, J. Comp. Phys, 49, pp.357-393. 1983.

Harten, A. On a Class of High Resolution Total Variation Stable Finite Difference Schemes, SIAM. J. Numer. Anal, 21, pp. 1-23. 1984.

Hilditch, J. and P. Colella. A front tracking method for compressible flames in one dimension, SIAM. J. Sci. Comput, 16, pp.755-772. 1995.

Hirt, C. W., and B. D .Nichols. Volume of Fluid (VOF) method for the dynamics of free boundaries, J. Comp. Phys, 39, pp.201-255. 1981.

Holt, M. Underwater Explosion, Annu. Rev. Fluid Mech, 1, pp.187. 1977.

Houlston, R., J. E. Slater, N. Pegg and C. G. Desrochers. On Analysis of Structural Response of Ship Panels Subjected to Air Blast Loading, Comput & Struct, 21, pp. 273-289. 1985

Hung, C. F., P.Y. Hsu and J.J. Hwang-Fuu. Elastic shock response of an air-backed plate to underwater explosion, Int. J. Impact Eng, article in press. 2004.

Hyman, J. M. Numerical methods for tracking interfaces, Physica D, 12, pp.396-407. 1984.

Iben, U. and F. Wrona. Cavitation in hydraulic tools based on thermodynamic properties of liquid and gas, JFE Trans ASME, 124, pp.1011-1017. 1994.

Jacqmin, D. Calculation of Two-Phase Navier-Stokes Flows Using Phase-Field Modeling, J. Comp. Phys, 155, pp. 96-127. 1999.

Jamet, D., O. Lebaigue, N. Coutris and J. M. Delhaye. The second gradient method for the direct numerical simulation of liquid-vapour flows with phase change, J. Comp. Phys, 169, pp.624-651. 2001.

Jin, Y. H., S. J. Shaw and D. C. Emmony. Observations of a cavitation bubble interacting with a solid boundary as seen from below, Phys. Fluids, 8, pp.1699-1701. 1996

Karni, S. Hybrid multifluid algorithm, SIAM J. Sci. Comput, 17, pp.1019-1039. 1996.

Karni, S. Multi-component flow calculations by a consistent primitive algorithm, J. Comp. Phys, 112, pp. 31-43. 1994.

Kirschner, I. N. Results of Selected Experiments Involving Supercavitating Flows, VKI Lecture Series on Supercavitating Flows, VKI Press, Brussels, Belgium. 2001.

Knapp, R. T., W. D. James and G. H. Frederick. Cavitation. McGraw-Hill. 1970.

Kubota, A., H. Kato and H. Yamaguchi. A new modelling of cavitating flows: a numerical study of unsteady cavitation on a hydrofoil section, J. Fluid Mech, 240, pp. 59-96. 1992.

Kunz, R. F., D. A. Boger, D. R. Stinebring, T. S. Chyczewski, J. W. Lindau, H. J. Gibeling, S. Venkateswaran and T. R. Govindan. A preconditioned Navier-Stokes method for two-phase flows with application to cavitation prediction, Comp. & Fluids, 29, pp.849-875. 2000.

Lafauie, B., C. Nardone, R. Scardovelli, S. Zaleski and G. Zanetti. Modeling merging and fragmentation in multiphase flows with SURFER, J. Comp. Phys, 113, pp. 134-147. 1994.

Larrouturou, B. How to preserve the mass fractions positivity when computing compressible multi-component flow, J. Comp. Phys, 95, pp.31-43. 1991.

Lecoffre, Y. Cavitation Bubble Trackers. Brookfield, VT, 1999.

Lindau, J. W, R. F. Kunz, D. Boger,. A, D. R .Stinebring, and H. J .Gibeling. High Reynolds Number, unsteady multi-phase CFD modeling of sheet cavitation, J. Fluid Eng. 124(3), pp. 607-616. 2002.

Lindaw, O and W. Lauterborn. Cinematographic observation of the collapse and rebound of a laser-produced cavitation bubble near a wall, J. Fluid Mech , 479, pp.327-348. 2003.

Liu, T. G., B. C. Khoo and C. W. Wang. The Ghost Fluid Method for Compressible Gas-Water Simulation, J. Comp. Phys., 204, pp.193-221. 2005.

Liu, T. G., B. C. Khoo and W. F. Xie. Isentropic One-Fluid Modelling of Unsteady Cavitating Flow, J. Comp. Phys, 201, pp. 80-108. 2004a.

Liu T. G., B. C. Khoo, K. S. Yeo and Wang, C., Underwater shock-free surface-structure interaction, Int. J. Numer. Meth. Engng., 58, pp. 609-630. 2003a.

Liu, T. G., B. C. Khoo and K. S Yeo. Ghost Fluid Method for strong shock impacting on material interface, J. Comp. Phys., 190, pp.651-681. 2003b.

Liu, T. G., B. C. Khoo and K. S. Yeo. The simulation of compressible multi-medium flow. Part I: A new methodology with test applications to 1D gas-gas and gas-water cases. Comp. & Fluids. 30(3), pp.291-314. 2001a.

Liu, T. G., B. C. Khoo and K. S. Yeo. The simulation of compressible multi-medium flow. Part II: Applications to 2D underwater shock refraction. Comp. & Fluids. 30(3), pp.315-337. 2001b.

Liu, T. G. A high-resolution method for multi-medium compressible flows and its application. PhD thesis, National University of Singapore. 2000.

Lohrberg, H., B. Stoffel, R. Fortes-Patella, O. Coutier-Delgosha and J.L. Reboud. Numerical and experimental investigations on the cavitating flow in a cascade of hydrofoils, Exp. Fluids, 33, pp. 578–586.2002.

Makine, K. Cavitation Models for Structures Excited by a Plane Shock Wave, J. Fluid Struct, 12, pp. 85-101. 1998.

Mao, D.-K. A shock tracking technique based no conservation in one space dimension, SIAM. J. Numer. Anal, 32, pp.1677-1703. 1995.

Mazel, P., R. Saurel., J. C. Loraud and P. B. Butler. A numerical study of weak shock wave propagation in a reactive bubbly liquid. Shock Waves, 6, pp. 287-300. 1996.

Massoni, J., R. Saurel, G. Demol and G. Baudin. A mechanical model for shock initiation of solid explosives, Phys. Fluids, 11, pp.710-736. 1999.

McCoy, R. W. and C. T. Sun. Fluid-structure interaction analysis of a thick-section composite cylinder subjected to underwater blast loading, Compos. Struct, 31, pp. 45-55. 1997;

Merkle, C.L., J. Z. Feng, and P. E. O. Buelow, Computational modeling of the dynamics of sheet cavitation, The 3rd International Symposium on Cavitation, Grenoble, France. 1998.

Molin B., L. Dieval., R. Marcer and M. Amaud. Modelisation instationnaire de poches de cavitation par la methode VOF. 6eme Journees de l'Hydrodynamique. Ecole Centrale de Nantes: ISSN 1161-1847. 1997.

Mulder, W., S. Osher and J. A. Sethian. Computing interface motion in compressible gas dynamics, J. Comp. Phys, 100, pp. 209-228. 1992.

Osher, S. and J. A. Sethian. Fronts propagating with curvature dependent speed. Algorithms based on Hamilton-Jacobi formulations, J. Comp. Phys, 79, pp 12-49. 1988.

Owis, F. M. and Ali H. Nayfeh. Computations of the compressible Multiphase Flow over the Cavitating High-Speed Torpedo, JFE Trans ASME, 125, pp.459-468. 2003.

Philemon, C. Chan, K. K. Kit and H. S. James. A Computational Study of Bubble-Structure Interaction, J. Fluids Eng, 122, pp.783-790. 2000.

Qin, J. R. Numerical Simulation of Cavitating Flows by the Space-Time Conservation Element and Solution Element Method, PhD Thesis, Wayne State University. 2000.

Qin, J. R., S. T. J .Yu and M.-C. Lai. Direct calculations of cavitating flows by the Space-Time CE/SE method, SAE Paper 1999-01-3554. 1999.

Qin, J. R., S. T. J. Yu., Z-C. Zhang and M-C. Lai. Direct Calculations of Cavitating Flows by the Space-Time CE/SE Method, AIAA 2001-1043, Reno, Jan. 8-11. 2001.

Rajendran, R., K. Narasimhan. Linear elastic shock response of plane plates subjected to underwater explosion, Int. J. Impact Eng, 25, pp.493-506. 2001.

Ramajeyathilagam, K. and C. P. Vendhan. Deformation and rupture of thin rectangular plates subjected to underwater shock, Int. J. Impact Eng, 30, pp. 699-719. 2004.

Sanada K, A. Kitagawa and T. Takenaka. A study on analytical methods by classification of column separations in water pipeline. Transaction of Japanese Society of Mechanical Engineers, Series B, 56/523, pp.585-593.1990.

Saurel, R. and O. Lemetayer. A multiphase model for compressible flows with interfaces, shocks, detonation waves and cavitation. J. Fluid Mech, 431, pp.239-271. 2001.

Saurel, R. and R. Abgrall. A multiphase Godunov method for compressible multifluid and multiphase flows, J. Comp. Phys, 150, pp.425-467. 1999b.

Saurel, R. and R. Abgrall. A simple method for compressible multifluid flows, SIAM. J. Sci. Comput, 21(3), pp.115. 1999a.

Schmidt D. P., J. R. Christopher and M.L. Corradini. A Fully Compressible, Two-Dimensional Model of Small, High-Speed, Cavitating Nozzles, Atomization and Sprays, 9, pp.255-276. 1999.

Schmidt, D. P. Cavitation in diesel fuel injector nozzles. PhD thesis, Wisconsin University. 1997.

Schmidt, D., T.-F. Su, K. Goney, P.V. Farrell and M.L. Corradini. Detection of Cavitation in Fuel Injector Nozzles, In S. H. Chan (ed.), Transport Phenomena in Combustion, 2. pp. 1521.1996.

Sedov, L. I. Similarity and Dimensional Methods in Mechanics. New York: Academic Press. 1959.

Senocak, I. and W. Shyy. A pressure-based method for turbulent cavitating flow computations, J. Comp. Phys., 176, pp. 363-383. 2002.

Senocak, I. Computational Methodology for the Simulation of Turbulent Cavitating Flows, PhD Thesis, University of Florida, 2002.

Shin, B. R., Y. Iwata and T. Ikohagi. Numerical simulation of unsteady cavitating flows using a homogenous equilibrium model, Computational Mechanics, 30, pp.388-395. 2003.

Shu, C. W. and S. Osher. Efficient implementation of essentially non-oscillatory shock-capturing schemes, J. Comp. Phys, 77, pp. 439-471. 1988.

Shu, C. W. and S. Osher. Efficient implementation of essentially non-oscillatory shock-capturing schemes II, J. Comp. Phys, 83, pp. 32-78. 1989.

Shyue, K. M. A fluid-mixture type algorithm for compressible multicomponent flow with Mie-Gruneisen equation of state, J. Comp. Phys, 171, 678-707. 2001.

Shyue, K. M. An efficient shock-capturing algorithm for compressible multicomponent problem, J. Comp. Phys, 142, pp.208-242. 1998.

Shyy, W., H. S. Udaykumar, M. M. Rao and R. W. Smith. Computational Fluid Dynamics with Moving Boundaries, Taylor & Frnacis, 1996.

Song, C. S. C. A virtual single-phase Natural Cavitation Model And its Application to Cav2003 Hydrofoil, Fifth International Symposium on Cavitation, Osaka, Japan, 2003.

Song, C. S. C. and X. Chen, Numerical simulation of cavitating flows by single-phase flow approach, The 3rd International Symposium on Cavitation, Grenoble, France.1998

Soteriou, C., R. Andrews and M. Smith. Direct Injection Diesel Sprays and the Effect of Cavitation and Hydraulic Flip on Atomization, SAE Paper 950080, pp. 27-51. 1995.

Sprague, M. A., T. L. Geers. A spectral-element method for modelling cavitation in transient fluid–structure interaction, Int. J. Numer. Meth. Engng, 60, pp. 2467-2499. 2004.

Tang, H. S. and D. Huang. A second-order accurate capturing scheme for 1D inviscid flows of gas and water with vacuum zones, J. Comp Phys, 128, pp.301-318. 1996.

Tang, H. S. and F. Sotiropoulos. A second-order Godunov method for wave problems in coupled solid-water-gas systems, J. Comp. Phys, 151, pp.790-815. 1999.

Tomita, Y., P. B. Robinson, R. P. Tong and J. R. Blake. Growth and collapse of cavitation bubbles near a curved rigid boundary, J. Fluid Mech, 466, pp. 259-283. 2002.

Toro, E. F. Riemann solvers and numerical methods for fluid dynamics. Springer Publication Company. 1997.

Vaidyanathan, R., I. Senocak, J. Y. Wu and W. Shyy. Sensitivity evaluation of a transport-based turbulent cavitation model, JSME Trans ASME, 125, pp. 447-458. 2003.

Van, Brummelen EH and B. Kolen. A pressure-invariant conservative Godunov-type method for barotropic two-fluid flows, J. Comp. Phys, 185, pp.289-308. 2003.

Venkateswaran, S., J. W. Lindau, R. F. Kunz and C. L. Merkle. Computation of multiphase mixture flows with compressible effects, J. Comp. Phys., 180, pp.54-77. 2002.

Venkateswaran, S., J.W. Lindau, R. F. Kunz and C. L. Merkle. Computation of multiphase mixture flows with compressibility effects, J. Comp. Phys, 180, pp.54-77. 2002.

Ventikos, Y. and Tzabiras. A numerical method for the simulation of steady and unsteady cavitating flows, Comp. & Fluids, 29, pp.63-88. 2000.

Wallis, G. B. One-dimensional two-phase flow, McGraw-Hill Book Company. 1969.

Wardlaw, A. B. and H. U. Mair. Spherical solutions of an underwater explosion bubble, Shock and Vibration, 5, pp.89-102. 1998.

Wardlaw, A. B. and J. A. Luton. Fluid-structure interaction mechanisms for close-in explosions, Shock and Vibration, 7, pp. 265-275. 2000.

Wesseling, P. Non-convex hyperbolic systems. VKI lecture Series, von Karman Institute for Fluid Dynamics, Rhode Saint Genese, Belgium, 1999-03, 1999.

Xie, W. F., T. G. Liu and B. C. Khoo. Application of a one-fluid Model for Large Scale Homogeneous Unsteady Cavitation: the modified Schmidt model, Comp. & Fluids, revised for publication. 2005a.

Xie, W. F., T. G. Liu and B. C. Khoo. The Ghost Fluid Method for Fluid- (flexible) Structure Interaction, J. Comp. Phys, submitted for publication. 2005b.

Xie, W. F., T. G. Liu and B. C. Khoo. The Simulation of Underwater Shock-Cavitation-Structure Interaction, Int J Multiphas Flow. Submitted for publication. 2005c.

Xie, W. F., T. G. Liu and B. C. Khoo. Homogeneous Simulation of Cavitating Flows, 5th International Conference on Multiphase Flow, Yokohama, Japan, May. 31-Jun. 3 2004.

Yee, H. C. A class of high-resolution explicit and implicit shock-capturing methods. Von Karment Institute for Fluid Dynamics, Lecture series 1989-04. 1989.

Yee, H. C. Upwind and symmetric shock-capturing schemes. Technical Report-TM-89464, NASA, 1987.

Youngs, D. L. Time-dependent multimaterial flow with large fluid distortion. In numerical Methods for Fluid Dynamics, pp. 273-285, New York: Academic Press. 1984.

Zalesak, S. T. A preliminary comparison of modern shock-capturing schemes: linear advection, in Computer Methods for partial Differential Equations, pp. 15-22, VI, IMACS. 1987.

Appendices

Appendix A

This is the proof for the unity of model constant in Qin's model. Assuming the flow is isentropic we have

$$\frac{dP}{d\rho} = a^2, \tag{A1}$$

$$dP = \frac{\left(\rho_g - \rho_l\right)}{\left[\rho_l + \left(\rho_g - \rho_l\right).\alpha\right].\left[\left(\frac{1}{\rho_g.a_g^2} - \frac{1}{\rho_l.a_l^2}\right).\alpha + \frac{1}{\rho_l.a_l^2}\right]} d\alpha \quad , \tag{A2}$$

We set

$$\begin{cases} \rho_g - \rho_l = A, \rho_l = B \\ \frac{1}{\rho_g.a_g^2} - \frac{1}{\rho_l.a_l^2} = C, \frac{1}{\rho_l.a_l^2} = D \end{cases}, \tag{A3}$$

Then we have

$$P = \frac{A}{D.A - B.C}\log\frac{B + A.\alpha}{D + C.\alpha} + N\,. \tag{A4}$$

Since $P = P^{sat}$ if $\alpha = 0$, we have

$$N = P_l - \frac{A}{D.A - B.C}.\log\frac{B}{D} \Rightarrow P = \frac{A}{D.A - B.C}\log\frac{\left(B + A.\alpha\right).D}{\left(D + C.\alpha\right).B} + P_L \,, \tag{A5}$$

Thereafter, Equations (A.3), (A.4) and (A.5) can lead to

$$P = P^{sat} + P_{gl}.\log\left[\frac{\rho_g.a_g^2.(\rho_l + \alpha.\left(\rho_g - \rho_l\right)}{\rho_l.\left(\rho_g.a_g^2 - \alpha\left(\rho_g.a_g^2 - \rho_l.a_l^2\right)\right)}\right]. \tag{A6}$$

This concludes the proof.